2023

A Source-to-Sink Analysis of the Pantanal Basin (Brazil): Implications for Weathering, Erosion, and Landscape Evolution in the World's Largest Wetland

Edward L. Lo

University of Kentucky, edward_lo@aol.com

Author ORCID Identifier:

https://orcid.org/0000-0003-3299-4495

Digital Object Identifier: https://doi.org/10.13023/etd.2023.405

Right click to open a feedback form in a new tab to let us know how this document benefits you.

STUDENT AGREEMENT:

I represent that my thesis or dissertation and abstract are my original work. Proper attribution has been given to all outside sources. I understand that I am solely responsible for obtaining any needed copyright permissions. I have obtained needed written permission statement(s) from the owner(s) of each third-party copyrighted matter to be included in my work, allowing electronic distribution (if such use is not permitted by the fair use doctrine) which will be submitted to UKnowledge as Additional File.

I hereby grant to The University of Kentucky and its agents the irrevocable, non-exclusive, and royalty-free license to archive and make accessible my work in whole or in part in all forms of media, now or hereafter known. I agree that the document mentioned above may be made available immediately for worldwide access unless an embargo applies.

I retain all other ownership rights to the copyright of my work. I also retain the right to use in future works (such as articles or books) all or part of my work. I understand that I am free to register the copyright to my work.

REVIEW, APPROVAL AND ACCEPTANCE

The document mentioned above has been reviewed and accepted by the student's advisor, on behalf of the advisory committee, and by the Director of Graduate Studies (DGS), on behalf of the program; we verify that this is the final, approved version of the student's thesis including all changes required by the advisory committee. The undersigned agree to abide by the statements above.

<div align="right">

Edward L. Lo, Student

Dr. Michael M. McGlue, Major Professor

Dr. Kevin M. Yeager, Director of Graduate Studies

</div>

A SOURCE-TO-SINK ANALYSIS OF THE PANTANAL BASIN (BRAZIL):
IMPLICATIONS FOR WEATHERING, EROSION, AND LANDSCAPE EVOLUTION
IN THE WORLD'S LARGEST WETLAND

_____

DISSERTATION
_____

A dissertation submitted in partial fulfillment of the
requirements for the degree of Doctor of Philosophy in the
College of Arts and Sciences
at the University of Kentucky

By

Edward Limin Lo (羅力明)

Lexington, Kentucky

Director: Dr. Michael M. McGlue, Alumni Endowed Professor

Lexington, Kentucky

2023

ABSTRACT OF DISSERTATION

A SOURCE-TO-SINK ANALYSIS OF THE PANTANAL BASIN (BRAZIL):
IMPLICATIONS FOR WEATHERING, EROSION, AND LANDSCAPE EVOLUTION
IN THE WORLD'S LARGEST WETLAND

Large back-bulge retro-arc basins have limited information about the sediment composition, yet they comprise important parts of the stratigraphic rock record. The exorheic Pantanal Basin is the world's largest continental wetland that regulates many valuable ecosystem services (water storage, nutrient cycling, agriculture, ranching, tourism, and transportation). This dissertation is composed of three studies that utilize a suite of tools to examine the most fundamental basin-wide source-to-sink sediment processes and controls that affect the characteristics and distribution of modern sediments.

The first paper consists of a metadata analysis of 76 shallow tropical floodplain lakes in the literature with bathymetric data and age models developed from ^{210}Pb, ^{14}C, or optically stimulated luminescence. The assessment revealed an exponential increase in sediment accumulation rate since the 1960s, sometimes by as much as an order of magnitude compared to the historical sedimentation. Short-term sedimentation showed that the average lake infill time is 100-1,000 years, well within the time span of a few human generations. We highlighted the importance of lake bathymetry surveys because computing lake volume based on average depth tends to overestimate the true volume of the lake. Tropical lakes with steeper slopes and higher population density are at risk of more rapid infill rates, which implies accelerating sedimentation rates resulting from anthropogenic land use change.

The second paper presents a petrographic investigation of 97 modern fluvial sands across the Pantanal, coupled with a pour point analysis for each sampling station. The sands were prepared as grain mount thin sections, and 500 grains were counted for every sample following the Gazzi-Dickinson point counting method. We defined six provenance regions across the Pantanal Basin: lowlands, Amazon craton, Rio Apa craton, plateau, Southern Paraguay Belt, and Northern Paraguay Belt. The most commonly occurring grain was non-orogenic quartzose detritus (%Quartz\Feldspar\Lithic 88\5\7). Lithic grains were most concentrated in rivers draining the Paraguay Belt highlands, whereas K-feldspars were frequently observed in sands in rivers of the Rio Apa craton. Finer K-feldspar sands were found in the medial Taquari River megafan caused by channel avulsion and exhumation of more feldspar-rich floodplain deposits. The main control on sand is bedrock lithology, followed by mean annual precipitation.

The third paper is a study of the mineralogy and geochemistry of 74 distinct modern fluvial clays in the Pantanal Basin to assess the controls on clay composition. We used wavelength-dispersive X-ray fluorescence to measure major elemental abundance in silt + clay samples, and we used X-ray diffraction to obtain semi-quantitative clay proportions. The abundance of clay is as follows: kaolinite > vermiculite > illite > smectite. We identified the Taquari River weathering hinge, where kaolinite is most abundant in northern

Pantanal muds and vermiculite is most abundant in southern Pantanal muds. The controls on clay compositions are as follows: hydroclimate > soils > lithology. The geochemistry of the silt + clay reveals the influence of quartz addition from parent rocks. In the context of the Plata River watershed, the kaolinite-dominant fluvial clays from the Pantanal Basin are diluted by illite-dominant clays from the sub-Andean foreland basin.

Edward Limin Lo 羅力明

(Name of Student)

08/24/2023

Date

A SOURCE-TO-SINK ANALYSIS OF THE PANTANAL BASIN (BRAZIL):
IMPLICATIONS FOR WEATHERING, EROSION, AND LANDSCAPE EVOLUTION
IN THE WORLD'S LARGEST WETLAND

By
Edward Limin Lo (羅力明)

<div style="text-align:center">

Dr. Michael M. McGlue
Director of Dissertation

Dr. Kevin M. Yeager
Director of Graduate Studies

08/24/2023
Date

</div>

DEDICATION

To my loving parents who gave me the gifts of a lifetime: curiosity in my Taiwanese ancestry and pride in my Brazilian cultural heritage, as well as a curiosity for all worldly things and for instilling much compassion for a more just and equitable society. I thank my extended family in Curitiba, who inspired me to contribute to humanity and to think beyond the confines of national borders and identities.

ACKNOWLEDGMENTS

TABLE OF CONTENTS

LIST OF TABLES

LIST OF FIGURES

LIST OF ADDITIONAL FILES

CHAPTER 1. INTRODUCTION

Source-to-sink analyses are conceptual frameworks used to decipher all processes that affect sediment generation, transport, storage and deposition in an exorheic tropical basin. Large-scale basin stratigraphy is fundamentally a product of the rate of sediment delivery into the depositional basin (Allen & Allen, 2013). A number of factors affect sediment routing systems: uplift, subsidence, precipitation, and anthropogenic activity (Romans et al., 2016). Vegetation and their associated soil development may also play a role in modifying sediment flux (Heins & Kairo, 2007; Ivory et al., 2017). Source-to-sink studies are important tools to understand how sediments record timescale dependent environmental signals over geologic time (Covault et al., 2010; Armitage et al., 2011). Here, we employ this framework to understand the Pantanal Basin, the world's largest continental wetland.

The global continental tropics are characterized by high year-round temperature and humidity. The higher annual temperatures are generated by the oblong shape of the Earth, which concentrates incoming solar radiation around the equator (Ruddiman, 2001). This solar radiation plus low albedo in areas with dense green forests produces longer and more humid growth seasons. The water cycle is controlled by large-scale atmospheric circulation, tied to Hadley cells driven by solar heating, evaporation, and trade winds. The Intertropical Convergence Zone (ITCZ) is a low-pressure band that lies at the confluence of the northern and southern trade winds, bringing intense seasonal rainfall as it migrates. This annual migration pattern has created the South American Convergence Zone and the South American Summer Monsoon (SASM), where the majority of the annual precipitation falls in the months of December, January, and February (Garreaud et

al., 2009; Schneider et al., 2014; Syvitski et al., 2014). Monsoons are driven by land-ocean heat contrasts common to continental sub-tropics that change in speed and direction seasonally (Chiang & Friedman, 2012).

Sediment routing systems begin in the uppermost hinterland, with decay and disintegration of primary minerals in parent rocks into sedimentary products (Allen & Allen, 2013). The rate of disintegration depends on the lithology and the climate, where chemical weathering is enhanced by high mean annual temperature in the tropics (Prothero & Schwab, 2004). The resulting high kinetic thermal energy increases weathering reactions to include hydrolysis, dissolution, oxidation, and hydration. These processes facilitate the development of deeply weathered soil profiles such as laterites, which is evidence of the great extent of chemical leaching. As an example of this principle, White et al. (1999) demonstrated that weathering rates of granitoid rocks increases with increasing temperatures. Intense vegetation growth further enhances sediment generation due to root activity, which breaks down rock through root wedging and releasing organic acids (Keller & Frederickson, 1952; Drever, 1973; Pawlik et al., 2016).

Sediment transport primarily through fluvial systems is the primary means of filling intermediate basins such as the Pantanal Basin. Large, meandering rivers feed into the Pantanal lowlands, a tectonically active Quarternary basin located mostly in western Brazil that formed from subsidence and basement faulting that generated accommodation due to the Andean orogeny. Up to ~500 m of alluvial, fluvial, and lacustrine sediments have accumulated in this low slope (0.015 m/km along the N-S axis) region. A detailed provenance analysis of the modern sediments in the basin will be critical for accurately

interpreting environmental signals in the rock record. Here, we present three chapters evaluating distinct components of the modern fluvial and lacustrine sediments. We first completed a meta-analysis of sedimentation in tropical floodplain lakes to determine how rapidly the lakes were infilling and controls on rates. Following this first step, we examine a snapshot of the mineralogical and geochemical composition of the sand, silt, and clay in the Pantanal's fluvial system to document the properties of the sediments generated and transported into the Pantanal lowlands.

1.1   Lacustrine sedimentation rates

In Chapter 2, a meta-analysis of published infill rates of shallow tropical floodplain lakes was completed to test whether observations of accelerating sedimentation in the Pantanal is representative of the broader tropics defined by the Köppen climate classification (Beck et al., 2018). We focused only on lakes with reported depth <10 m and sediment cores age dated with ^{14}C, ^{210}Pb, or optically stimulated luminescence. Infill time of each lake was most commonly estimated using the linear accumulation rate and the average or maximum depth. Additionally, the watershed size, slope, distance to trunk river, tree loss, and population density were considered using principle components analysis for 76 lakes that could best explain the rapid changes to sediment accumulation. The analysis demonstrated that the largest acceleration in sedimentation was observed across the global tropics for the past 100 years, particularly in lakes with watersheds that were steeper and more densely populated. Our findings carry important implications for the loss of ecosystem services in the tropics as climate change impacts intensify. This paper is an article published in *Frontiers in Earth Science* on May 19, 2022, available online: https://doi.org/10.3389/feart.2022.875919.

1.2   Fluvial sediment composition

In Chapter 3, we shifted our focus to what the sediment composition could reveal about landscape evolution and weathering of different lithologies across the basin. What is the composition and distribution of the petrology of modern sands in the Pantanal, and what are the determinants of the mineralogical composition? The Pantanal Basin was divided into six provenance regions, and we used pour point analyses to determine the best sampling points to ensure adequate coverage of diverse environments and lithologies. Ninety-seven samples were collected in 2019-2021 from sand bars or from the channel axis where accessible. All samples were sieved to obtain the sand fraction (54-2000 microns) and treated with hydrogen peroxide in a hot water bath to remove organic matter. Grain mount thin sections were made at Wagner Petrographic (Lindon, UT), and 500 grains were counted in each slide following the Gazzi-Dickinson method. The catalog of data revealed that parent rocks are the primary control on sand mineralogy, where Mesozoic sandstones in the hinterland produce quartz-rich sands. The Rio Apa craton and the Southern Paraguay Belt were the source of more sedimentary lithic grains than anywhere in the basin, creating a unique compositional signal. This is an Accepted Manuscript of an article published in *Sedimentologika* in August 2023.

In Chapter 4, we collected clay plus silt samples from 74 distinct sampling sites to examine the fine-fraction mineralogy and geochemistry. The objective of this study was to test whether mean annual precipitation controlled modern clay mineralogy in an extant tropical back-bulge basin. We used X-ray fluorescence to measure major elemental chemistry for the <53 µm clay plus silt fraction. X-ray diffraction was used to produce diffractograms used for semi-quantitative clay mineralogy for the <2 µm clays. The abundance of clays was kaolinite > vermiculite > illite > smectite in the Pantanal.

Kaolinite was more abundant in the north-central Pantanal than in the southern Pantanal, defined by the Taquari River weathering hinge. Illite was most common downstream of the Northern Paraguay Belt and limited parts of the Southern Paraguay Belt, suggesting weathering-limited erosion where transport forces exceed the rate of clay mineral authigenesis. Vermiculite was a dominant constituent of the southeastern Pantanal watershed, downstream of dacitic rocks and rhodic ferralsols. Smectite was unequivocally identified at three locations. Fine-fraction geochemistry revealed the overlapping effects of quartz addition and clays inherited from the parent rocks, with the most quartzose sediments in the medial Paraguay River indicating maximal chemical weathering resulting from the long hydroperiod. Downstream of the Pantanal, sub-tropical clays derived from Andean megafan systems dilute the kaolinite-dominant clay assemblage. This study illustrates how clay and silt in back-bulge basins filled with non-orogenic detritus are controlled by climate > soils > parent rocks.

CHAPTER 2. SEDIMENT INFILL OF TROPICAL FLOODPLAIN LAKES:
RATES, CONTROLS, AND IMPLICATIONS FOR ECOSYSTEM SERVICES

2.1 Introduction

Tropical floodplain lakes provide important ecosystem services that are often overlooked (Street & Semenov, 1990). Less than 10% of all lakes are situated in the tropics, but their importance is disproportionately large compared with their number or aggregate surface area (Lewis, 1996). Tropical floodplain lakes provide supporting, provisioning, regulating, and cultural services that are critical to regional livelihoods and add to the natural heritage of low latitude regions (Apitz, 2011; Settele et al., 2014). For example, floodplain lakes in the Pantanal Basin in central South America, the world's largest tropical wetland, showcase a wide variety of valuable ecosystem services (McGlue et al., 2011, 2015; Assine et al., 2015). Supporting services consist of primary and secondary productivity, which contribute to biodiversity and form the base of food webs. Aquatic plant biomass is high in many tropical floodplain lakes due to the extended growing season and high mean annual air temperature (Talling, 2001); such is the case in several of the Pantanal's large floodplain lakes (Lo et al., 2017; Silio-Calzada et al., 2017). Provisioning services include natural resources, such as fisheries, or irrigation water for agriculture that directly support economic assets and development. For example, saline-alkaline lakes in the Pantanal of Nhecolândia precipitate mineral-rich sediments that support traditional cattle ranching and sustainable organic beef production

(Guerreiro et al., 2019). Regulating services include the storage, transformation, and transportation of nutrients and other biochemical compounds that sustain the healthy functioning of the broader ecosystem (Settele et al., 2014). Recently, Rasbold et al. (2021) argued that an important regulating service of the Pantanal's lakes is long-term atmospheric carbon sequestration. Cultural services include the aesthetic and educational value that lakes bring to a region and its people, including opportunities for ecotourism (e.g., Street & Semenov, 1990; Schulz et al., 2019). The "Large Lakes of the Pantanal" have served as trade corridors for the fishers, hunters, and gatherers among pre-colonial indigenous populations, and continue to provide ecotourism and sport fishing opportunities today (Peixoto, 2009; Oliveira & Milheira, 2020).

Ecosystem services tied to lakes are dependent on the maintenance of pelagic (open water) environments and the presence of a water column. When aquatic environments shift to alternative states due to changes in climate or human engineering, so too may ecosystem services transform, or in some instances, be lost entirely (e.g., Colloff & Baldwin, 2010; Nobre et al., 2020). For example, excessive summer rainfall can impact the rate of river avulsions in the plains of the Pantanal (Bergier et al., 2018), whereas extreme drought can lead to reduced water availability, resulting in fish stock depletion and food insecurity for ribeirinhos, local people living closer to floodplains (Marengo et al., 2020). Floodplain lakes and wetlands associated with meandering rivers can permanently transform into dry landforms over decades or centuries with avulsions (Assine et al., 2015), fundamentally altering the spatial distribution of open water environments and ecosystem services (Louzada et al., 2020, 2021).

Sedimentation influences the persistence of open water environments and the lifespan of tropical floodplain lakes. Natural or human-driven changes that increase sediment loads to lakes, through distinct inlet channels, overbank sedimentation, or from overland flow, may reduce open water persistence. In the Pantanal, Lo et al. (2019) observed accelerating sediment accumulation over the past 100 years in Lake Uberaba that has resulted in a shoaling and contraction of the Pantanal's largest floodplain lake. Shallow floodplain lakes in the Pantanal are relatively well-studied compared with other tropical lowland lakes. However, it remains unknown if observations from the Pantanal are representative of tropical floodplain lakes more broadly. Out of 422 lakes in a recent global study of lake sedimentation, < 5% were in tropical climates (Baud et al., 2021).

Here, a meta-analysis of floodplain lake data from the tropics attempts to address this knowledge deficit. Three questions motivate this work: 1) At what rates do tropical floodplain lakes accumulate sediment? 2) How rapidly will extant tropical floodplain lakes completely fill with sediment, given current trajectories in sedimentation and environmental conditions? 3) What environmental factors control sediment accumulation rates in these settings? To address these questions, data from tropical floodplain lakes (e.g., sediment core-based accumulation rates, morphometrics, bathymetry) were compiled using the peer-reviewed literature, supplemented where necessary with new bathymetric modeling and remote sensing data.

2.2   Materials and Methods

The criteria used to establish an internally consistent database that allows for the analysis of tropical floodplain lake attributes are described as follows. The database was compiled using published papers on lake studies that were electronically searched using

keywords including "tropics lake sediment [place]," "lake sediment tropics ^{14}C," "lake sediment core tropics ^{210}Pb," "lake paleoclimate [country]," and "geochronology floodplain lake [location]." The tropical lowland floodplain lakes considered here were classified as one of five types, all of which are present in the Pantanal wetlands, however, the classes of lakes were not used as keywords. The Pantanal region (western Brazil) was used as the main reference due to the availability of raw data and the presence of different types of lakes (Figure 2.1). Wetzel (2001) defined three classes of floodplain lakes based on morphology, including (channel, dish, and oxbow lake types). Here, two additional floodplain lake types were included: distal lakes and blocked valley lakes. Channel lakes experience high hydraulic throughflow during river flooding and are often characterized by seasonal or perennial tie channels to a major river. A subset of the channel lakes is oxbow lakes, which occur where a meander is cut off from an active river channel. Distal lakes are a subclass of channel lakes defined by their location on the terminal fringe of a distributary fluvial system (e.g., Hartley et al., 2010). Blocked valley lakes extend away from the floodplain, and their outlets have been restricted by levee buildup or resistant channel-margin lithologies that help to pond water. Dish lakes are typically isolated from river channels and are sustained by a combination of flood waters, precipitation, and groundwater input. Dish lakes often experience fluctuations in water level and hydrochemistry stemming from their closed hydrology and evaporation. Many dish lakes are found in the Nhecôlandia region of the central Pantanal, an abandoned lobe of the Taquari River megafan (Figure 2.1) (Furian et al., 2013; McGlue et al., 2017).

To be included in the database, lakes needed to meet the criteria defined here. Lakes needed to be located in tropical rainforest (Af), tropical monsoon (Am), or tropical

savanna (Aw) Köppen climate regions (Beck et al., 2018). Shallow depths are typical for floodplain lakes; a ~13 m threshold was selected for this study, though other authors have set lower maximum values (Hamilton & Mitchell, 1996; Hayashi & van der Kamp, 2000; Padisák & Reynolds, 2003). Lowland environments consist of areas affected by annual river flooding (Erenstein, 2006) and with elevation ≤500 m above mean sea level (a.m.s.l.). In order to be included in the database, lakes that met the environmental criteria described above needed at least one sediment core that was dated using radiocarbon (^{14}C), optically stimulated luminescence (OSL), or lead-210 (^{210}Pb). In most cases, lakes in the database lack published bathymetric maps (a common limitation in other studies; see also Ang et al., 2021; Liu & Song, 2022). However, average lake depth values were commonly available, and these data were employed in the calculation of lake volume. Lakes without any depth information were excluded. Artificial lakes, reservoirs, and impoundments were also not considered in this study (Figure 2.2).

2.2.1   *Linear and Mass-Based Sediment Accumulation Rates*

Linear sediment accumulation rates (LAR, mm/yr) were computed by dividing the length of a sediment core section by the time interval established by ^{14}C or OSL to provide a long-term context to the more recent changes in accumulation rates. For lakes with sediment cores dated with ^{210}Pb, age models were computed using unsupported or "excess" ^{210}Pb (^{210}Pb$_{xs}$) and the constant rate of supply (CRS) model, which provides information on sediment accumulation over the last ~100–150 years depending on ^{210}Pb$_{xs}$ activity concentrations and allows for variability in sedimentation rates over time (Appleby & Oldfield, 1978, 1992; Ritchie & McHenry, 1990). In contrast, lake studies that utilized the constant initial concentration (CIC) or constant flux:constant

sedimentation (CF:CS) models only reported one mean sedimentation rate for entire cores. To facilitate a comparison of rates among studies/cores whose ^{210}Pb data were modeled with CRS, CIC, and CF:CS, we calculated a mean rate for each core modeled by CRS using linear regression (Binford et al., 1993). This mean rate encompassed all data points available in the published literature.

Where older sediment was recovered in relatively long cores, ^{14}C and OSL age dates were used to calculate long-term sediment accumulation rates over hundreds or thousands of years from the core basal age. Several studies published in the 1980s and 1990s that were included did not report calibrated ^{14}C age dates; in those cases, ^{14}C dates were converted to calendar ages using the online software Calib 8.20 and Calibomb (R. Reimer & Reimer, 2004; Stuiver et al., 2021). The SHCal20 curve was selected for lakes in the Southern Hemisphere, whereas the IntCal20 curve was used for lakes in the Northern Hemisphere (Hogg et al., 2013; Reimer et al., 2020). The median of the calibrated age range was used as the calendar age at a given core depth. Although Blaauw and Christen (2005) reported tradeoffs associated with using the median ^{14}C age, most cores have fewer than five dated horizons each, thereby minimizing the potential error of this approach. Age inversions were excluded from rate calculations. We adopted the framework of Sadler (1981) for comparisons among cores with ^{14}C or OSL age-depth models. This technique afforded the opportunity to test the influence of measurement duration on sediment accumulation rate among sites.

Mass accumulation rates (MAR, g/cm^2/yr) were determined by multiplying the LAR by sediment dry bulk density (g/cm^3), which was estimated based on grain size when such information was unavailable in the original reference (Verstraeten & Poesen,

2001; Avnimelech et al., 2001; Shi et al., 2003). Sediment accumulation rates must be

reported as a volumetric rate ($g/cm^2/yr$) to obtain the most accurate, quantitative

estimates of infill (Clemens et al., 1987). When the dry bulk density was not reported, we

approximated sediment lithologic composition and clay content based on the core details

presented in the study and applied the conversion of Shi et al. (2003) for non-marine

sediments. Such an assumption is a potential source of uncertainty in the calculations but

is unavoidable for reasonable estimates of lake infill time.

2.2.2 *Lake infill*

Lake infill is defined here as the amount of time needed to entirely fill a lake and

create a new aquatic environment (e.g., a marsh or river floodplain) and assuming that the

sediment accumulation rate will continue unchanged into the future. In order to estimate

lake infill time, it is important to have accurate data on lake basin volume. Lake volume

was determined by multiplying the lake surface area by the mean depth, or depth of the

coring station when mean depth was unavailable. For lakes that experience a large

seasonal change in surface area, we selected the annual mean lake extent from cloud-free

satellite imagery. In contrast, we imported a point cloud of individual depth

measurements or digitized isobaths to QGIS 3.4 if detailed bathymetric data were

available. A Delaunay triangular interpolated network (TIN) was then calculated and

converted into raster format to derive surface volume in ArcMap 10.7.1. The infill time

estimates were determined by dividing the lake volume by the MAR.

2.2.3 *Statistical analysis*

The database of sedimentation rate versus duration of measurement was plotted

on a log scale and the linear regression was associated with a power law. These

regression analyses provided the most straightforward interpretation in log-log plots to accommodate the large range of values. In addition, regression analysis is widely applied when the response variable and the explanatory variable are continuous (Crawley, 2012). However, exponential functions were more suitable to describe accelerating rates of change for ^{210}Pb-derived sediment accumulation rates.

Lake surface areas, elevations, numbers of inlet channels, and distances to the dominant river channel were compiled for all lakes in the database, either from the literature or measured directly from Google Earth™ images. The lake watershed area, including potential riverine input during the wet season, was delineated in QGIS 3.4 using shuttle radar topography mission data (SRTM; 30 m resolution). The watershed variables were calculated by: 1) converting the digital elevation model (DEM) to a projected and equal-area coordinate system, 2) filling in sinks (Wang & Liu, 2006), 3) extracting a channel network and drainage basins (Conrad et al., 2015), 4) calculation of upslope area (O'Callaghan & Mark, 1984), 5) conversion to polygon, and 6) calculation of zonal statistics. The average and maximum slopes were derived from the same DEM using the slope function in the Raster Terrain Analysis toolbox of QGIS 3.4. Average annual rainfall and temperature were derived from the WorldClim data set (Fick & Hijmans, 2017).

In order to aid in the interpretation of controls on sediment accumulation in these lakes, ten environmental and human factors (lake depth, surface area, elevation, distance to the dominant river channel, average slope of watershed, annual rainfall, short-term accumulation rate, infill time, watershed human population density, and tree loss) were compiled using Paleontological Statistics (PAST) software (Hammer et al., 2001). In the

[210]Pb dataset (see Supplementary Material), we applied multivariate statistics through the principal components analysis (PCA) technique using the "correlation" option, which normalizes all variables using division by their standard deviations; this is appropriate given that the matrix contains variables with many different units and has been applied successfully in other tropical lake environments (e.g. Parinet et al., 2004). The PCA finds a small number of linear combinations in the variables to capture most of the variation in the data frame (Crawley, 2012). Tree loss and population density were utilized in this study to approximate the anthropogenic influence on shallow lake sediment accumulation. Tree loss was calculated from publicly available University of Maryland data over 2000 to 2012 (Hansen et al., 2013, version 1.0). This value (0–1, where 1 is complete loss of forest cover) does not specify land uses but rather expresses whether a given area lost tree cover (≥5 m canopy) between 2000 and 2012. The population density information was taken from a publicly available global shapefile and averaged across each watershed (Center for International Earth Science Information Network - CIESIN - Columbia University, 2018). Multivariate statistics was not possible for long-term MAR dataset, because variables such as land use are not available over the thousands of years that the ^{14}C age models span.

2.3 Results

2.3.1 *Lake Morphometry*

Seventy-six (76) lakes met the selection criteria and were included in the database. Most lakes ($n = 61$) are situated in the southern hemisphere, but the full range falls within 18°N and 25°S (Figure 2.2). Most lakes in the database are in tropical

savanna regions, fewer in the tropical rainforest and tropical monsoon climate regions. The altitude of all lakes ranged between <1 and 391 m a.m.s.l., and the average annual precipitation at the lakes ranged between 780- and 6,323-mm. Watershed size varied from 17 to 5×10^6 km^2, with a median of 21,750 km^2, and the average watershed slope ranged from 0.5° to 13.4°, with a median of 3.2°. Maximum lake depths ranged from 1.0 to 13.0 m, with a median of 2.6 m. The deepest lakes were channel and blocked valley types. Lake surface areas ranged from 0.02 to 2,500 km^2, with a median of 1.70 km^2. Lake volumes ranged from 4×10^{-5}–19 km^3, with a median of 0.006 km^3. Channel lakes ($n = 38$) comprised 50% of the data set, whereas blocked valley ($n = 15$) and dish lakes ($n = 12$) were less common. Oxbow lakes ($n = 9$) were found near the hinterlands of the Pantanal and the Amazon River basins, and therefore these lakes are situated on relatively high elevation floodplains. Only two examples of distal lakes were available: Lake Uberaba (Pantanal) and Lake Pemerak (Borneo). Most lakes in the database ($n = 46$) are hydrologically open, whereas the remaining lakes are closed at the surface and lack active channel connections to a proximal river. Many lakes in the database had only one inlet channel ($n = 24$) or lacked inflowing streams altogether ($n = 25$). In most cases ($n = 49$), the distance from the sediment coring station to the nearest inlet channel was ≤2 km. The straight-line distance from the coring station to the nearest major river channel, excluding tie channels, was ≤5 km for most lakes in the database ($n = 43$).

2.3.2 Lake Sediment Accumulation Rates

2.3.2.1 Long-Term Sediment Accumulation Rates (^{14}C and OSL Dating).

The range of ^{14}C-derived sediment accumulation rates, referred to herein as long-term rates, was 0.02–8.20 mm/yr. (Table 2.1). Similar to Sadler (1981), long-term rates

for each lake core were plotted against the duration of measurement (Figure 2.3). The fitted power functions for this study ($n = 74$) and for global lakes ($n = 860$) from Sadler (1981) were significantly different with a 99% confidence interval. When plotting the LARs of discrete intervals between two adjacent dated core samples, the dish and blocked valley lake data sets were each characterized by power function slopes > -0.9 (Figure 2.4). The channel and oxbow lake data sets were approximately -0.7, so over durations of measurement of 10^2–10^4 years, their average LARs increase rapidly in the last century but less so compared with the dish and blocked valley lakes. Distal lakes (here only Lake Melintang, Indonesia) experienced the least change in sediment accumulation but consistently accumulated sediment on the upper end of all long-term LARs in this study.

2.3.2.2   Short-Term ^{210}Pb-Derived Sediment Accumulation Rates.

The range of ^{210}Pb-derived sediment accumulation rates, referred to herein as short-term rates, was 1.06–5.18 mm/yr. (Table 2.1; Figure 3). On tropical floodplains, lake LARs have increased exponentially by five-to six-fold in the past century. Most of these increases occurred from the 1960s onward across all lake types (Figure 2.5). Prior to 1960, the dish and blocked valley lakes recorded LARs that were higher than the LARs of channel, oxbow, and distal lakes. After the 1960s, channel and oxbow lakes notably recorded more sediment influx and deposition. Though consistent with the pattern of increasing sedimentation rates through time, the distal lakes class records the most modest increase of all lakes in the database (Figure 2.5). Among three cores (Lakes Negra, Castelo, Caranã) where both ^{210}Pb and ^{14}C were available, the average ^{14}C -based

linear accumulation rate was one order of magnitude lower than the averaged [210]Pb

accumulation rate.

2.3.3 Lake Infill Chronology

Lake infill times estimated from long-term MARs and lake volumes are between

1,000 and 100,000 years; MARs are on the order of 0.01–0.10 $g/cm^2/yr$. using ^{14}C or

OSL datasets (Figure 2.6A). Alternatively, the infill time based on short-term ([210]Pb$_{xs}$-

based) rates ranged from 100 to 10,000 years, with MARs on the order of 0.1–1.0

$g/cm^2/yr$. (Figure 2.6B).

Volume estimates for lakes where both average depth and detailed bathymetry

were available were used to estimate the potential error arising from the use of

generalized depth information (Figure 2.7). In the ten lakes where bathymetric data were

available (Table 2.2), the lake volume estimates were consistently lower than those

determined using only a single mean lake depth, indicating that the application of average

depth values artificially increases lake volume. Our comparisons using TINs of

bathymetry in ArcGIS resulted in calculations that were consistently lower than those of

simple volumes, in some cases >80% lower (Figure 2.7).

2.3.4 Statistical Analysis

The linear regression shows a negative correlation between ^{210}Pb-derived

sedimentation rates and time (Figure 2.3). When compared with a global lakes study

published by Sadler (1981) ($y = 2.2732x^{-0.21\pm0.036}$), our results show that tropical lakes

present a lower negative correlation ($y = 19.486x^{-0.48\pm0.147}$), meaning that lake infill has

accelerated through time. With respect to the long-term ^{14}C-derived rates, the distal lake

type presented the highest negative correlation ($y = 48.919x^{-0.402}$) and the blocked valley

17

lake type presented the lowest negative correlation ($y = 600.49x^{-0.985}$) (Figure 2.4). The

most extreme trajectory towards fast sedimentation rates occurs in the dish lake setting,

most specifically after 1960 CE (Figure 2.5).

The PCA of lake depth, surface area, elevation, distance to the dominant river

channel, average watershed slope, annual rainfall, short-term LAR, infill time, population

density, and tree loss revealed that PC1 and PC2 account for ~46% of the total variance

(Figure 2.8). Principal component 1 accounted for 27% of the variance and loaded

positively on lake depth, annual rainfall, tree loss, short-term LAR, average slope, and

population density (Figure 2.8). The distance to the dominant river channel, elevation,

and infill time loaded negatively in the PC1. Thus, PC1 reflects key controls on lake

sedimentation and infill time. We interpret that the lakes in low elevation, deforested

watersheds marked by high annual rainfall infill with sediment comparatively faster than

those at higher elevations with native vegetation or intact managed forests. The lack of

orthogonality of infill time, however, suggests that PC2 is an equally important control.

Watershed average slope and population density loaded positively on PC2 and negatively

for lake depth and infill time. Such a pattern emerging from PC2 may reflect erosion

within the watershed, accelerated by the landscape gradient, human settlement, and land-

use changes. This result suggests that lakes found in steeper watersheds with higher

populations are susceptible to more rapid infill than those located in low gradient,

sparsely populated watersheds. These results have important implications for the

effective management of lake resources at the watershed scale.

2.4 Discussion

2.4.1 *Recent Sediment Accumulation Rates Increasing in Tropical Lowland Lakes*

The multivariate and linear regression analyses of tropical floodplain lake datasets conducted in this study suggest that deforestation and human population densities may explain the onset of increasing rates of sedimentation in the second half of the 20th century independent of soil type. There is a large body of literature that implicates land-use changes by humans, particularly deforestation, as causal agents of erosion not only in the tropics but in other climatic regions (e.g., Owens et al., 2005; Syvitski & Kettner, 2011; Restrepo et al., 2015). For example, Ivory et al. (2021) reported that deforestation and reduction of tree cover have led to increased sediment input into Lake Tanganyika in the last few decades. Similarly, Baud et al. (2021) found that global lake sedimentation rates have increased by nearly four times since the "Great Acceleration" (post-1960s). Schiefer et al. (2013) reported a steadily increasing lake sedimentation rate in the late 20th century in western Canada linked to the oil, gas, and timber extraction industries. Deforestation in much of the rest of the world increased rapidly during the late 20th century, which has frequently been recorded in lacustrine records (e.g., Roulet et al., 2000; Dearing & Jones, 2003; Long et al., 2021). Now, the Global South, consisting of many developing nations in the tropics, has overtaken developed nations in population growth and resource consumption (Chant & McIlwaine, 2009; Adams et al., 2020; Archer et al., 2020). Population density in the tropics is projected to increase rapidly (e.g., Laurance et al., 2014), hence >50% of the world's population is expected to reside in the tropics by 2050. Land conversion for livestock and agriculture has intensified in the tropics since the "Green Revolution" in the second half of the 20th century (e.g.,

Evenson & Gollin, 2003; Huong & Son, 2020; Sinha et al., 2020; Jankowski et al., 2021; Alavez-Vargas et al., 2021), leading to increased sediment supply to some lowland lakes. Owens (2020) describes that greater sediment accumulation rates have become a threat to water security. Increased sedimentation is likely to continue strengthening with the tree loss that often accompanies population growth (Wolman & Schick, 1967; Walling, 1999; Papangelakis et al., 2019).

Another mechanism by which tropical floodplain lakes may lose areas of open water is through colonizing vegetation (Barlow et al., 2018). Abundant rainfall and warm temperatures year-round contribute to the rapid proliferation of aquatic macrophytes (P. A. Chambers et al., 2008). Lakes with sediment accumulation rates >4 mm/yr. (e.g., Lake Uberaba, Brazil; Laguna La Tembladera, Peru; and Waigani Lake, Papua New Guinea) commonly develop marshy littoral zones leading to terrestrialization at the expense of open water environments (Osborne et al., 1993; López-Blanco et al., 2017; Lo et al., 2019). This phenomenon has been documented for the Paraguay River, as large floating islands of Cyperaceae (baceiros) were found to constrict channel margin environments (Costa & Telmer, 2006; Pott & da Silva, 2015; Coutinho et al., 2018). Floating Cyperaceae mats grow and die rapidly, forming an aggrading, organic-rich soil that woody vegetation can colonize (Prado et al., 1994; Pivari et al., 2008). Recent studies have suggested that this process influences floodplain lakes as well, resulting in considerable basinward expansion of the shoreline and shallow littoral zones at the expense of pelagic environments (Lo et al., 2017; Rasbold et al., 2021). Similarly, Ryken et al. (2015) found that sedge wetlands have a first-order control in retaining sediments and excess nutrient runoff from land-use changes.

Seasonally intense rainfall is another key characteristic of tropical climates that enhances erosion, sediment transport, and export to lake basins. For example, sediment accumulation patterns in the lake-wetland continuum are highly dependent on flood frequency and intensity (e.g., Silio-Calzada et al., 2017). Rainfall erosivity combined with high intensity of land use changes or total removal of vegetation cover produce increased sediment delivery downstream (Krishnaswamy et al., 2001; Carlson et al., 2014). Recent data suggest that pulses of sediment export may become stronger with wetter rainy seasons and drier dry seasons in sub-Saharan Africa (Salerno et al., 2019). Similar severity of increased droughts and unprecedented flooding linked to Atlantic Ocean warming has been demonstrated for Amazonia (Barichivich et al., 2018). This suggests that floodplain lakes without perennial tie channel connections to a dominant river (e.g., oxbow lakes, dish lakes) may experience higher sediment influx.

The lacustrine sedimentary record in the Pantanal Basin illustrates the continuous impacts of population growth and deforestation. For example, the upper Taquari River oxbow lakes experienced increased sedimentation rates related to the expansion of planted pastureland and croplands (e.g., Leite et al., 2012). These unnamed oxbow lakes have sandy sediments that were likely derived from the upper watershed, which is part of the cerrado biome (composed of savannas and grasslands amid humid and dry forests), where the agricultural activity has been most severe, in evidence by large gullies, soil loss, and increased avulsions (e.g., Gomes et al., 2019; Louzada et al., 2020).

Our study results suggest that increased sediment transport, perhaps linked to deforestation and other land-use changes for agriculture that started in the 1950s–1970s, maybe driving rapid sediment accumulation in tropical floodplain lakes. The

environmental variables that seem to most affect tropical floodplain lake infill time are annual rainfall and landscape features (including tree loss, elevation, and distance to the dominant fluvial channel). This outcome is consistent with Ndehedehe et al. (2021) results, who reported that anthropogenic activities and climate change have resulted in the accelerating decline of permanent open water features in tropical fluvial environments. Indeed, cropland density in temperate and high latitude lake watersheds has been implicated as the most direct predictor of accelerated sediment accumulation rates (Baud et al., 2021). This correlates closely with tree loss because the density of cropland frequently comes at the expense of tree cover (e.g., Gibbs et al., 2010). Globally, lowland areas have been more exploited for agricultural, and pastoral uses than relatively elevated hinterland regions, but highland cropland expansions in Southeast Asia are also increasing sediment inputs to lowland areas (Zeng et al., 2018). The distance to the dominant river channel controls the rate of overbank sedimentation, as hydrological connectivity is the main control of floodplain sediment accumulation rates (Walling & He, 1998; Rodríguez et al., 2019). The net cumulative effect of these factors is that the short-term sediment accumulation rates are much higher than those integrated over longer periods. Yet this two-dimensional infill requires consideration of three-dimensional space vis-à-vis lake volume.

2.4.2   *Completion of Lake Infill*

When comparisons were possible, our data (*n = 13*) showed that lake volumes calculated from single depth measurements produced inaccurate (overestimated) lake volumes. This has been reported previously for lakes in other climatic settings. Cross and Moore (2014) compared the volume estimates from variable bathymetric transect spacing

and found that increased spacing produced lower volume estimates relative to a modeled

volume for four lakes and one reservoir. None of Cross and Moore's (2014) lakes are in

floodplain environments, and so they likely function differently. This may help to explain

the higher lake volume estimates relative to modeled volumes based on bathymetric data,

which were on average 49% lower. Lakes in floodplains are complex open-water systems

(Crisman et al., 2005). For example, paleotopography and the shape of the basin in

shallow lakes can influence the infill pattern, which is clearly not captured by an average

depth approximation (e.g., Debret et al., 2014; Bennett & Buck, 2016). The complex

spatiotemporal distribution of sediments can vary with depth and distance to the nearest

major river channel, such that completion of infill is best reported as a range (e.g.,

Kossoni & Giresse, 2010).

The infill times given in this study are maximum estimates because the true lake

volumes are likely to be lower than current approximations based on a single reported

depth at the coring site. Published studies of shallow tropical lakes, where completion of

infill is expected on the order of hundreds or a few thousand years, further lend support to

the accelerating infill process (e.g., Räsänen et al., 1991; Horbe et al., 2011; Aleman et

al., 2013; Bremond et al., 2017). In the Pantanal Basin, five of the nine lakes with data

are predicted to infill in <1,000 years, and four lakes will infill in <10,000 years

according to this study. A similar pattern is predicted for shallow tropical lakes outside of

the Pantanal, where lakes infill within 10^2–10^3 years (e.g., Kossoni & Giresse, 2010). The

actual sediment accumulation rates in all lakes considered in this study may be higher

considering the land use/land cover changes recorded in the tropical lowlands (e.g.,

Biswas & Dhara, 2019). We can be confident that the rate of accumulation of sediment volume is increasing throughout the lake basins (Bennett & Buck, 2016).

We show that some tropical floodplain lakes may infill in ≤150–200 years and demonstrate that small changes in lake depths have major implications for calculations of lake volume. Although recent middle-lower Amazon lake models have improved bathymetric estimates (e.g., Park et al., 2020; Ang et al., 2021), ground-truthing or field validation using hydrographic surveying remains extremely valuable as a snapshot of actual conditions at the time of the survey. An average depth or the depth at the lake depocenter continues to be a crude estimate of the true lake volume, which our meta-analysis reveals to be standard for most lake core studies and consequently, a significant source of error when attempting to quantify infill timescales. The Global Surface Water Explorer has been an important assessment tool for lake surface areas (Busker et al., 2019), so predictive modeling has improved for parts of the world with extensively published studies and high-resolution LiDAR data. Where limnogeology is a nascent field, as is the reality in the world's tropical floodplain lakes with limited remote sensing, bathymetric surveys are sorely needed to validate lake volume estimates based on laser and radar altimetry (e.g., Carabajal & Boy, 2021). The lack of published depth data for small, shallow lakes remains a key limitation (e.g., Webster et al., 2022), but several remote sensing products have attempted to refine predictive bathymetric modeling. HydroLAKES include volume estimates for lakes >10 ha, and the GLOBathy repository provides a refined model for estimating bathymetry in lakes (Messager et al., 2016; Khazaei et al., 2022). This study did not include GLOBathy data because the 1,503 lakes with observational data that were used to validate the model were outside of the tropics.

The HydroLAKES database assumes that the average depth can be reasonably predicted from surrounding topography, but the low gradient of floodplain environments betrays subtle but important variations of actual lake depth.

2.4.3 Aquatic Ecosystem Services

Lake volume reduction has an outsized impact on shallow small lakes, which are common in tropical floodplain environments (Nõges, 2009). Hydrological changes have large impacts because small changes will dramatically alter the submerged lake margins where the ratio of lake area to depth is high. The effects of lake surface area reduction have been reported in tropical mountain lake districts (Mosquera et al., 2017) and in semi-arid Brazilian lakes and reservoirs (Rocha Junior et al., 2018; Nobre et al., 2020), but the impacts on fisheries, irrigation, and other ecosystem services remain unclear for tropical floodplain lakes (e.g., Tan et al., 2020). Quantitative estimates of the loss of ecosystem services in global shallow lakes are in the early stages of development (Xu et al., 2018; Janse et al., 2019), and existing datasets pertain to localized sites such as Lake Malombe, Malawi (Makwinja et al., 2022).

In the Pantanal, the intensive land use changes owing to cattle ranching and settlements that expanded in the 1970s have been implicated in higher rates of gully formation and land surface degradation of the upper Taquari River Basin (Louzada et al., 2020, 2021). The Pantanal's large floodplain lakes Gaíva, Mandioré, and Baía Vermelha, are directly connected to the Paraguay River via tie channels, and while these lakes are far from urban areas, they are immediately downstream of areas that have been deforested (McGlue et al., 2011; Schulz et al., 2019). The terrestrialization process can lead to conditions in which the extant flora and fauna struggle to thrive, which can

influence local biodiversity (Lo et al., 2019; Abel et al., 2021). These changes in tropical lowlands are particularly critical given their traditional role as a sustainable support system for local populations both presently and historically (e.g., Shepard Jr. et al., 2020).

Varying resolution of global datasets of land use and soil type precluded their consideration in this study. Global anthropogenic land-use shows extensive development of pasture and cropland in areas outside of the tropics, except on the Indian subcontinent (Goldewijk et al., 2011). Large swaths of South America were not systematically modified until the 20th century, so changes in land use that occurred in the 20th century are captured in the ^{210}Pb core chronologies. One variable not specifically considered in our analysis was soil type. Soil types are cataloged in the United Nations Food and Agriculture Organization Soil Map of the World, but the scale of that map (1:5 million) is not adequate for small-scale watershed analyses (e.g., Reynolds et al., 2000; Selcer, 2015). Future refinement of the database could include soil information if it can be obtained at the watershed scale.

2.5   Conclusion

Since the 1960s, the rate of sediment accumulation in tropical floodplain lakes has increased by as much as an order of magnitude relative to previous periods. This outcome aligns with other studies that have noted shallow lakes are rapidly losing resilience to climate change, as documented by annual lake area decreases (e.g., Havens et al., 2016; Silio-Calzada et al., 2017; Bartczak et al., 2019; Lo et al., 2019). The infill times for tropical floodplain lakes are between 1,000–10,000 years when using long-term sediment accumulation rate information, but the average infill times for these lakes decrease to 100–1,000 years when using the short-term sediment accumulation rates calculated using

26

[210]Pb data, and therefore warrant consideration in water and sediment management planning. We show that ^{14}C, ^{210}Pb, and OSL data help form expanded age-depth models to compare temporal changes to sediment accumulation, bypassing the temporal limitations of using only ^{210}Pb models. Simple geometric lake volume estimates based on an average depth overestimated the true volume calculated from detailed bathymetry, which was available for <20% of the lakes in this study. Hence, the infill times are conservative maximum estimates in most cases and are likely to be much faster given that most lake volumes were overestimated when an average depth was assumed. Where possible, locally measured lake and watershed characteristics will provide an improved context for evaluating sediment infill time and the utility of remotely sensed global data sets. Importantly, the rapid loss of these tropical lowland floodplain lakes due to sediment infilling and terrestrialization could alter or eliminate ecosystem services supporting diverse species, fisheries, nutrient cycling, and water resources.

2.6 Acknowledgments

2.7   Tables and Figures

Table 2.1 Summary and comparison of ^{14}C-based infill rates and ^{210}Pb rates for lake type

Lake type	Long-term avg. (mm/yr)	Short-term avg (mm/yr)	Long-term avg ($g/cm^2/yr$)	Short-term avg ($g/cm^2/yr$)
Oxbow	**2.41**	**4.98**	**0.27**	**0.80**
Dish	**0.40**	**3.10**	**0.05**	**0.42**
Channel	**0.73**	**4.51**	**0.08**	**0.52**
Blocked valley	**0.96**	**6.72**	**0.12**	**0.76**
Distal	**2.24**	**2.32**	**0.29**	**0.37**

Table 2.2 Comparison of modeled 3-dimensional lake volume and simple volume for selected lakes

Lake	Simple Volume (km^3)	Modeled 3D volume (km^3)	Difference	Depth (m)	MAR time to fill simple vol (yrs)	MAR time to fill 3D vol (yrs)	Lake type
Uberaba	0.903	0.47	-48%	3.5	1,250	650	Distal
Negra	0.021	0.018	-14%	2.3	16,430	14,290	Channel
Gaíva	0.44	0.24	-46%	4.7	47,000	25,530	Channel
Mandioré	0.44	0.35	-22%	3	15,000	11,720	Channel
Cáceres	0.1	0.07	-27%	3.2	18,820	13,850	Channel
Caçó	0.025	0.004	-83%	10	66,670	10,670	Channel
Tembladera	0.008	0.003	-59%	8	2,310	960	Channel
Bera	0.002	0.001	-48%	3.5	550	290	Channel
Lago Grande Curuai	13	5.27	-60%	6.5	490	200	Channel
Lago Santa Ninha	0.85	0.41	-52%	5.5	11,460	5,520	Channel
Salina da Ponta	0.00048	0.00016	-66%	2.5	12,500	4,140	Dish
Salina Babaçu	0.00035	0.00021	-39%	2.5	16,670	10,130	Dish
Salina do Meio	0.00035	0.00009	-75%	3.5	590	150	Dish
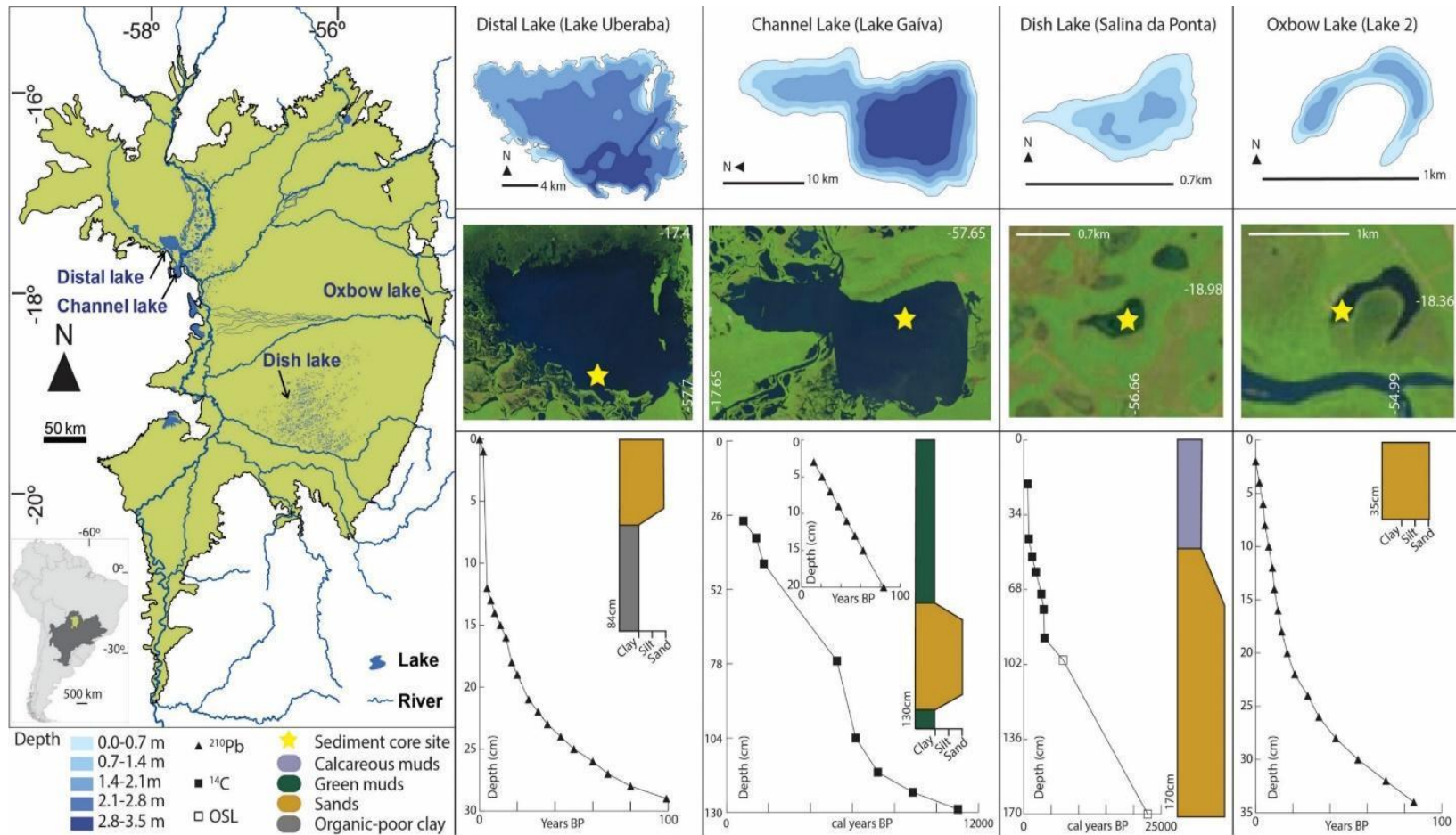
Figure 2.1 Map of the Pantanal lowlands (green shaded area, left) and endmember floodplain lake types present in the basin. Accompanying age-depth models, stratigraphy, and bathymetry were collated from source articles and matched with satellite images (Sentinel 2, 10 m resolution, January 22-24, 2019).
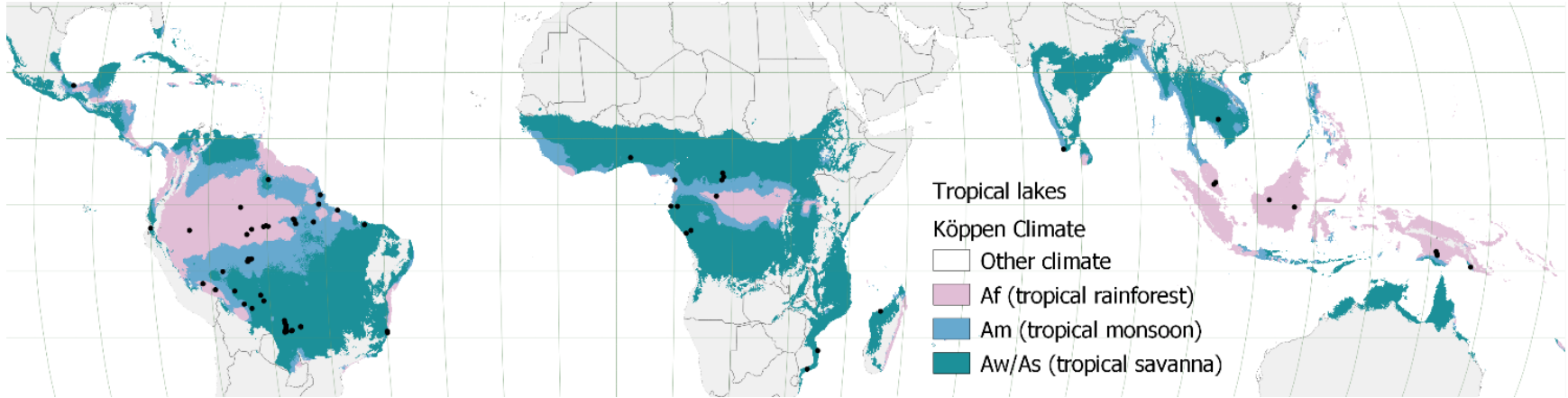
Figure 2.2 Mapped distribution of 76 lakes across the global Köppen tropical climate using the Robinson projection.
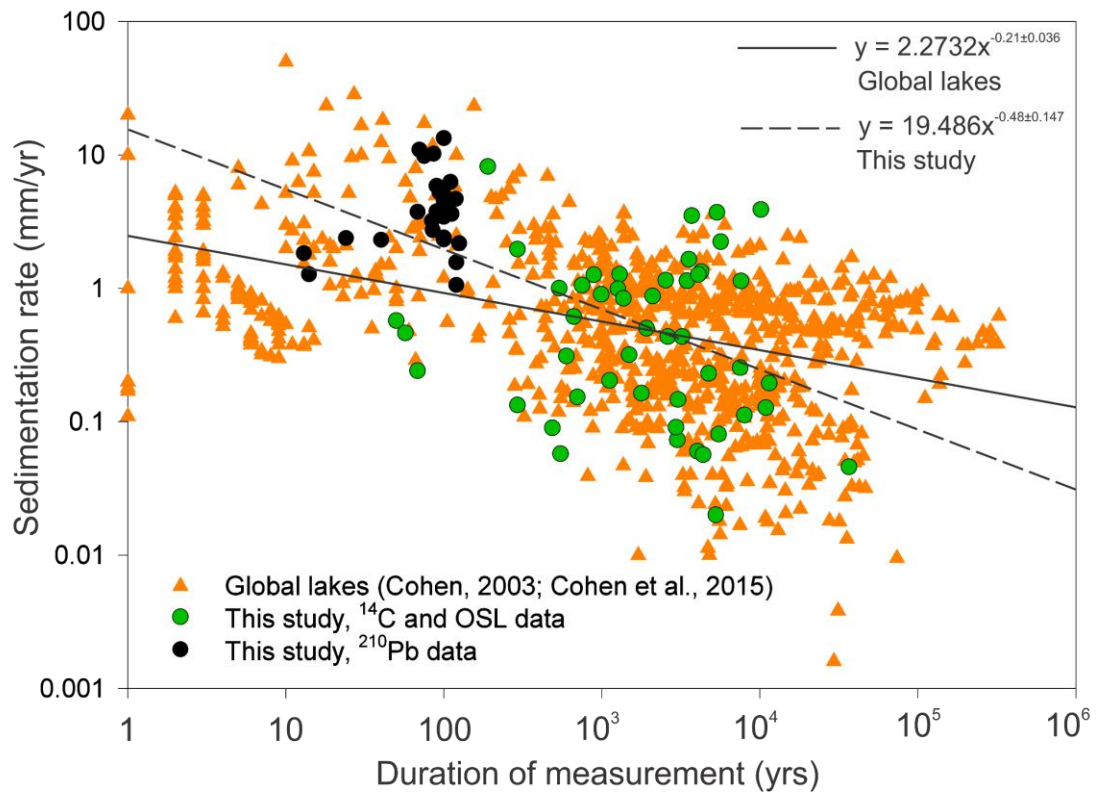
Figure 2.3 Global lacustrine sediment accumulation rates are shown with 99% confidence intervals against the rates found in this study (modified from Sadler, 1981). Each lake with ^{210}Pb chronology is represented by one black circle, including CRS, CIC, and CF:CS models. The inverse power law function for this study shows greater sediment accumulation rates for periods of < 1,000 years than for the global lakes data set.
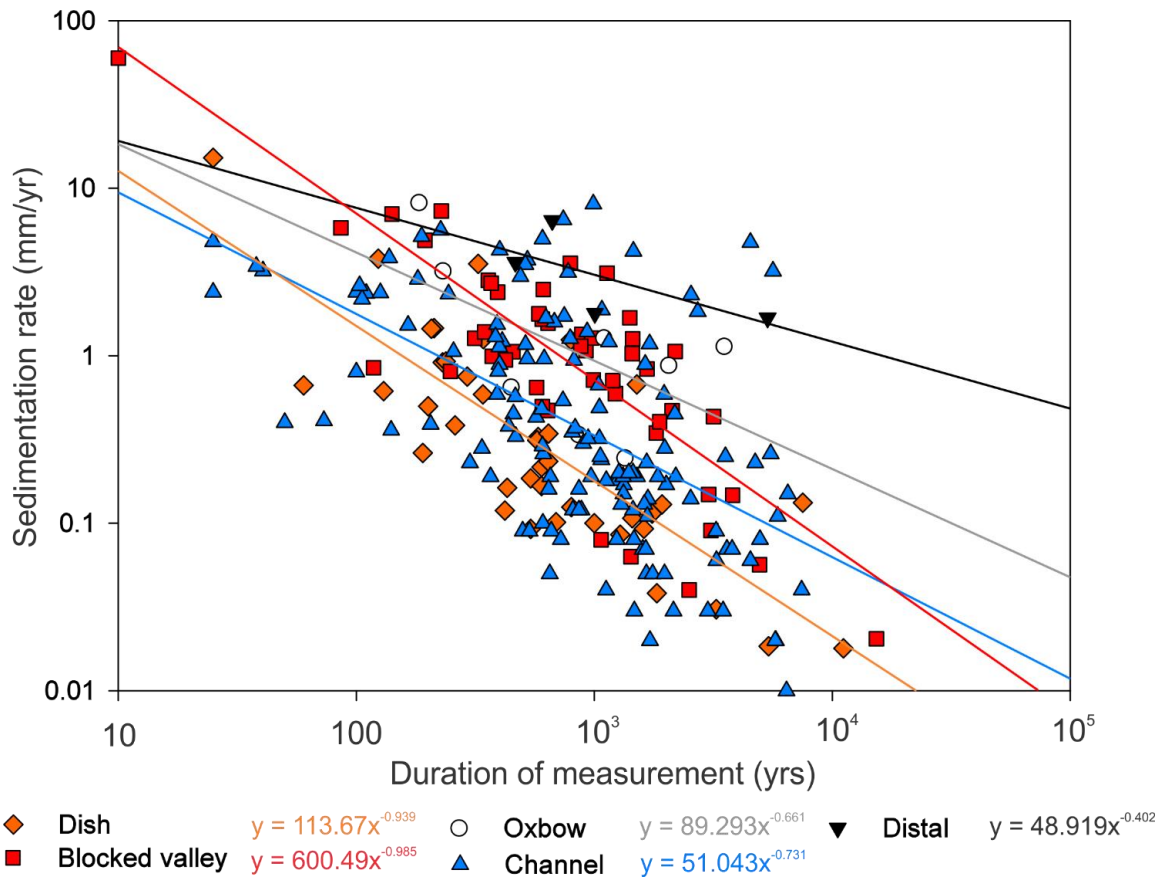
Figure 2.4 All ^{14}C age dates for every available core are plotted here. Dish and blocked valley lake data indicate that their rates of change are faster than those of oxbow and channel lakes. The distal lake trend suggests a higher but constant sediment accumulation rate over time, independent of duration of measurement.
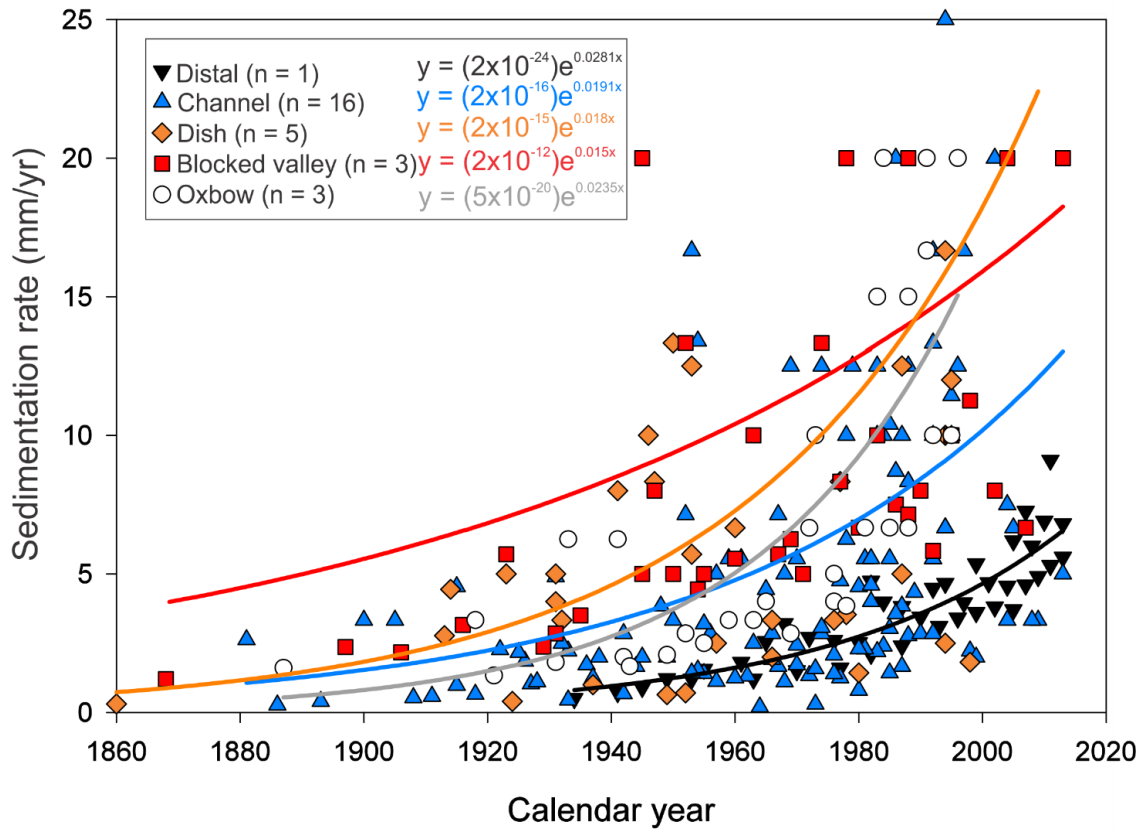
Figure 2.5 The ^{210}Pb data from every available core interval including CRS, CIC, and CF:CS models illustrate an exponential acceleration in sediment accumulation rates over the last ~50 years. Lake sediment accumulation rates dated with CIC and CF:CS models are represented by one point. The dish and blocked valley lakes have experienced more rapid increases in sediment accumulation compared with the other Wetzel lake types.
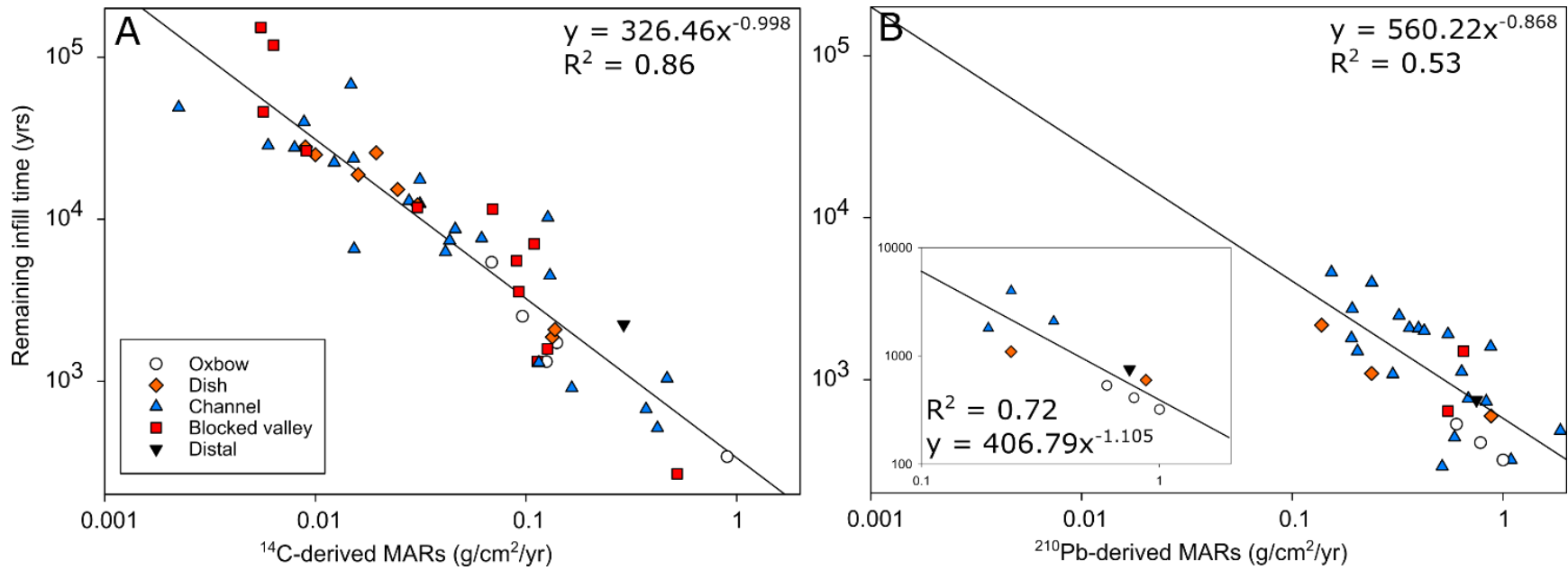
Figure 2.6 Whole-core average sediment accumulation rates are plotted to illustrate how ^{210}Pb-derived and ^{14}C-derived mass accumulation rates affect lake infill times. The ^{210}Pb-derived Pantanal data set was placed in an inset figure in panel B to highlight the 0.72 coefficient of determination.
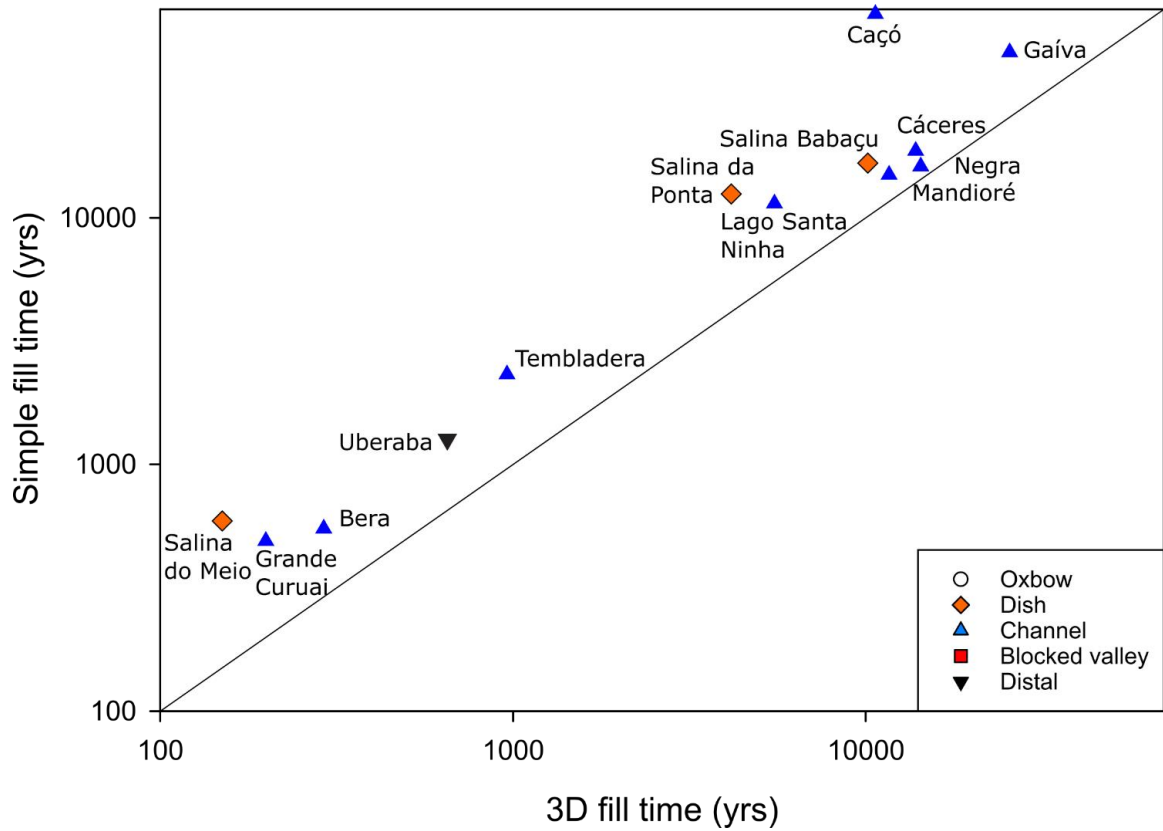
Figure 2.7 The different infill times from Table 2.2 are visually compared. The diagonal 1:1 line denotes identical fill time for simple and 3D volumes, so values above the line occur when the simple fill time overestimates the 3D fill time.
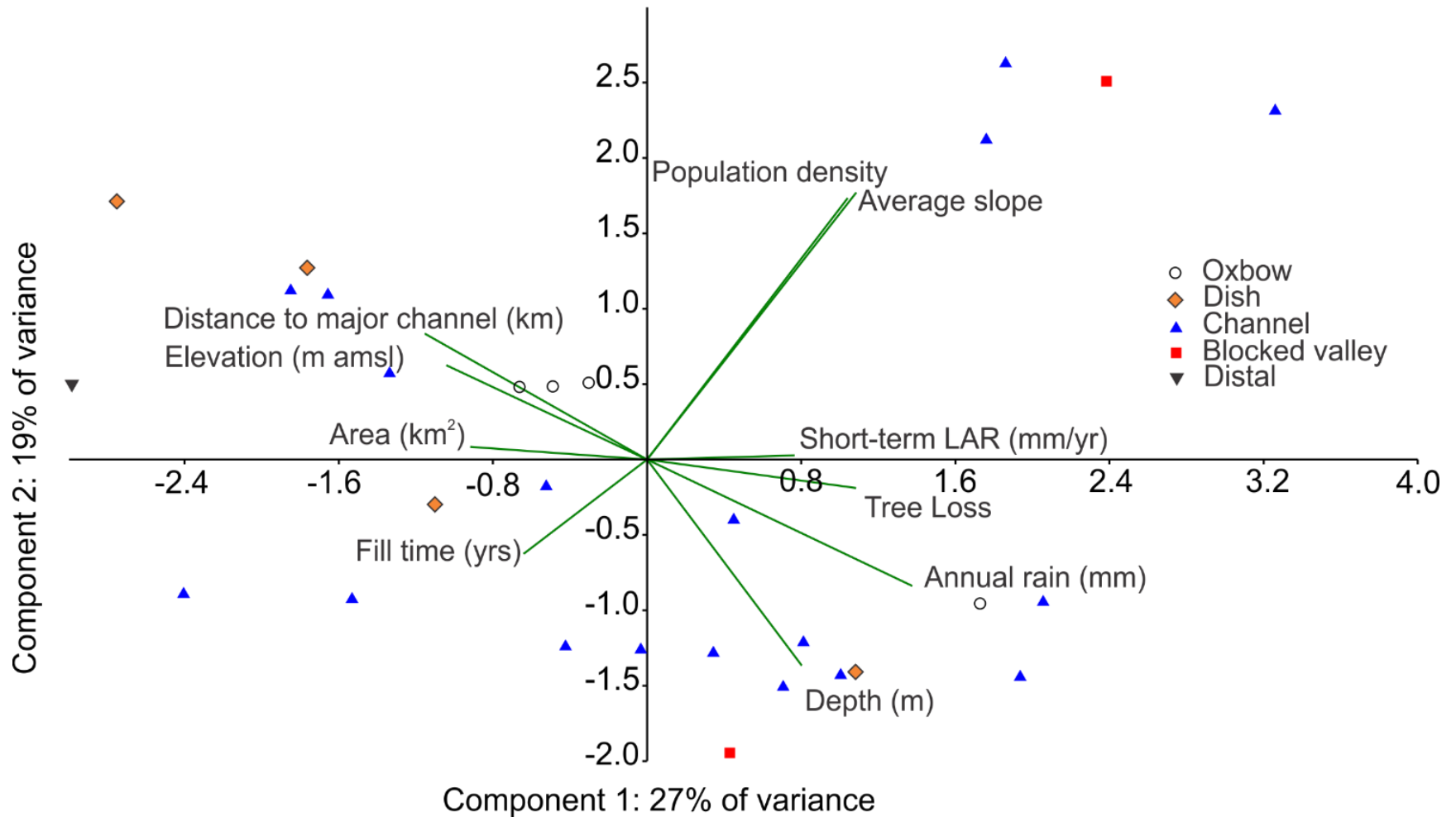
Figure 2.8 Biplot of the 1st and 2nd principal component axes, which collectively account for 46% of the total variance based on the 29 lakes with available ^{210}Pb chronology in our dataset.

CHAPTER 3. SOURCE-TO-SINK CONTROLS ON MODERN FLUVIAL SANDS IN THE PANTANAL BACK-BULGE BASIN (BRAZIL)

This is an Accepted Manuscript of an article in *Sedimentologika* accepted on August 16, 2023.

3.1   Introduction

The purpose of this study is to describe the composition of modern river sediments collected from a broad spatial network of stations in the Pantanal Basin of western Brazil (Figure 3.1). The Cenozoic Pantanal Basin is the back-bulge depozone of the central Andean retro-arc basin (DeCelles & Giles, 1996; Horton & DeCelles, 1997; Horton, 2022). Known for its strongly seasonal flood pulse that helps to form one of the largest and most biodiverse tropical wetland systems in the world, the Pantanal remains understudied from the perspective of sedimentary geology and the source-to-sink processes of sediment generation, transport, and deposition (Assine et al., 2016). Like many continental back-bulge depozones, the Pantanal is dominated by low-gradient meandering rivers, vast megafan floodplains, shallow lakes, and heavily vegetated swamps (Assine, Merino, et al., 2015). The Pantanal forms the headwaters of the Paraguay River. The Upper Paraguay River flows from north to south along the basin's western margin and sets the regional base level. Numerous lateral drainages, including several that form large and prominent distributive systems such as the Taquari, Paraguay, and Cuiabá megafans (Assine & Silva, 2009; Zani et al., 2012; Pupim et al., 2017), enter the Pantanal from northern and eastern plateaus. The plateaus are regionally known as *planalto*, which was formed from erosion of the Paraná Basin rocks prior to final basin

development (Assine et al., 2016). From the perspective of Andean tectonics, the Pantanal sits between a broad flexural forebulge that is dominantly covered by alluvium and the Brazilian craton (Chase et al., 2009; McGlue et al., 2016). Drainages flowing east across the low-amplitude forebulge appear to contribute little sediment to the Pantanal, as the Amazon craton acts as a topographic barrier (Kuerten & Stevaux, 2021). Therefore, rivers draining the craton, as well as the Paraguay River itself, dominate with respect to sand delivery to the Pantanal.

Modern provenance studies have examined river sands from several areas of the modern Andean foreland basin, particularly in the wedgetop and foredeep depozones (Johnsson, 1990; Savage & Potter, 1991; Johnsson et al., 1991; McGlue et al., 2016; Capaldi et al., 2019). Much of the Andean modern provenance research has focused on individual drainages or sets of major tributaries, whereas basin-scale studies are less common. The existing modern sand provenance database from Latin America has been used to characterize the influence of collisional mountain building on sediment generation near the thrust front, which has proven valuable for calibrating tectono-stratigraphic models and interpreting ancient mountain building processes and timelines from the ancient sedimentary record (Carrapa et al., 2011; McGlue et al., 2016; Tineo, 2020; Papa et al., 2021; Garzanti et al., 2021a). Because recognition of ancient forebulge and back-bulge deposits in the rock record are often crucial for establishing the history of orogenesis and flexural basin development, petrographic data from modern rivers in these depozones provide the potential for improving paleoenvironmental interpretations. A paucity of such data exists for the distal depozones of the Andean foreland, and consequently, the processes that influence sediment generation, transport, storage, and

deposition are poorly known. Here, we provide the first comprehensive description of sand composition in a modern back-bulge basin, using the Pantanal and its rivers as the focus.

Relatively diverse bedrock characterizes the hinterland of the Pantanal Basin today, whereas the conditions that influence weathering such as temperature and precipitation gradients are more muted. We therefore hypothesize that geological gradients, in particular parent lithology, control river sand composition in this basin. Provenance lithotypes have been shown to determine the composition and texture of the sand-sized fraction across diverse climatic and tectonic environments (Heins, 1993; Heins & Kairo, 2007). We employed optical petrographic analysis and Gazzi-Dickinson point counts on a database of river sand samples that were tied to hinterland lithology using geographic information systems (GIS) to test the hypothesis.

3.2 Geologic setting

The name *Pantanal* is derived from the Portuguese words *pântano* (meaning wetland or swamp) and the suffix *-al* (meaning abundance, agglomeration, or collection). The lowlands are ~150,000 km^2 but the watershed known as the Upper Paraguay River Basin spans ~465,000 km^2 across Brazil, Bolivia, and Paraguay (Paz et al., 2010; Bravo et al., 2012). The Pantanal is a Cenozoic-age basin that has accumulated ~500 m of sediment (Horton & DeCelles, 1997; Ussami et al., 1999). The basin formed from the flexure of the continental crust in response to the Andean orogeny (Horton & DeCelles, 1997; Assine, 2005; Assine et al., 2016). The crust is thin, ranging from 38-43 km on the west and thinning to ≤35 km on the eastern margin of the basin (Rivadeneyra-Vera et al., 2019; Cedraz et al., 2020; Shirzad et al., 2020). The Pantanal has been a site of intraplate

seismicity, with notably large earthquakes in 1964 and 2009 (Dias et al., 2016). The Transbrasiliano lineament runs NE-SW along the southeastern flank of the basin, but seismic events have not been explicitly related to reverse or strike-slip motion on this structure.

In the context of fluvial sediment transport, the Upper Paraguay River Basin watershed extends eastward from the Andean forebulge (Bravo et al., 2012). Within the Upper Paraguay River Basin in Brazil, the point of highest elevation is in the plateau at 1260 m above sea level (m.a.s.l.), and the lowest point is 70 m.a.s.l. near the Pantanal Basin outlet at the confluence of the Apa River and Paraguay River (Figure 3.1). The average watershed slope is greatest at the transition out of the plateau, but within the lowlands, the slope is much reduced (Zani et al., 2012).

We consider the Pantanal to be supplied with sediment from six distinct provenance regions (Figure 3.1). Much of the unconsolidated alluvium lies in the lowlands (Figure 3.2) (Assine, Merino, et al., 2015). The Pantanal is bounded by the Amazon craton in the northwest and consists of the Sunsás and Rondônia-San Ignacio provinces with granites, granodiorites, schists, and dikes of quartz-diorite and quartz-gabbro composition (Rizzotto & Hartmann, 2012; Horbe et al., 2013; Braga et al., 2019). The southwestern Pantanal hosts the Rio Apa craton, consisting of gneisses, granites, granodiorites, amphibolites, schists, and quartzites (RadamBrasil, 1982; Alvarenga et al., 2011). The eastern Pantanal is bounded by the Pantanal plateau composed of Phanerozoic sedimentary lithotypes derived from the Paraná Basin (Figure 3.2B). The southern Paraguay Belt hosts phyllites, schists, metarenites, quartzites, and dolomitic and calcitic marble in the Serra da Bodoquena (Figure 3.1C). The Northern Paraguay Belt includes

the Província Serrana with phyllites, schists, calcitic limestones, siltites, and arenites (RadamBrasil, 1982).

Mean annual rainfall is ~1800 mm in the northern and eastern Pantanal, but it reduced to ~1200 mm along the western and southern margins (Figure 3.3B). The hydroclimate of the Pantanal Basin is defined by a distinct wet and dry season; most of the annual rainfall occurs in the months of December, January, and February. The dry season reaches its apex in the months of June, July, and August. The annual migration of the Intertropical Convergence Zone is responsible for this seasonality of precipitation and patterns in floodplain inundation and phytogeography (Ivory et al., 2019). For the Paraguay River, this style of precipitation results in a flood pulse effect, which manifests as a several month delay in peak discharge at the southern end of the basin near its outlet (Junk et al., 2006). The annual temperature range is 21-27°C with a mean value of ~25°C and is described by tropical savanna climate in the Köppen climate system (McGlue et al., 2011). The mean annual precipitation across the basin is ~1444 mm with an average annual temperature of 25°C (Fick & Hijmans, 2017). Overall, the northern Pantanal experiences higher maximum temperature and precipitation amounts than does the southern Pantanal, where evaporation is higher (Figure 3.3B). The soil and vegetation composition provide important context for understanding the sediment routing system (Figures 3.2A, 3.3A). The soils are dominantly planosols in the lowland flooded savanna, whereas the *cerrado* region contains mostly ferralsols and arenosols plus luvisols in the southern *cerrado* (Benedetti et al., 2011). Lithosols, planosols, vertisols, and solonetz are present in limited geographic extent in the Pantanal Basin (Figure 3.2A). Much of the Pantanal consists of flooded savanna and *cerrado* (tropical savanna) environments; dry

forest and dry Chaco make up the balance of the basin (Figure 3.3A). C*errado* and dry

forest ecotones occupy the hinterland, and flooded savanna occupies the lowlands. Some

areas of the basin along the western margin are dry *cerrado*, and very minor parts are

humid Chaco and Atlantic Forest (Figure 3.3A).

3.3   Methods

The Pantanal remains mostly undeveloped, with vast tracts of wilderness that are

difficult or impossible to access across large portions of the year. To obtain a

representative sample set, pour point analyses were conducted using GIS to identify

viable sample collection sites in accessible locations. A pour point is the lowest point in a

given watershed to which all of the waters drain (Gleyzer et al., 2004). Sample sites were

selected to maximize coverage across the Pantanal and its hinterland lithological

diversity, as well as reconciling access points. A total of 97 samples were collected in

total across the six provenance regions (Figure 3.1). We used Shuttle Radar Topography

Mission (SRTM) digital elevation models (DEMs) from the USGS EarthExplorer website

(https://earthexplorer.usgs.gov) with 30 m resolution for slope calculations, watershed

area delineation, and pour point analysis (Tables B.1 and B.2). Where the watershed

exceeded 250,000 km^2, we utilized a DEM with 3-arc second resolution (Verdin, 2017).

Analyses were completed using built-in algorithms within QGIS 3.4.6. Elevation for each

sampling station was derived from Google© Earth, and precipitation and temperature

data were obtained from WorldClim (Fick & Hijmans, 2017) (Table B.1).

Samples were collected directly from the river channel axis, or from point bars

where accessible. We waded into the river up to 1 m depth or used a ponar grab sampler

deployed from bridges. In the laboratory, each sample was air dried, sieved through a 2

mm sieve to remove grains larger than sand and 63 μm sieve to remove clays and silts, treated with 30% hydrogen peroxide, rinsed with deionized water, and air dried prior to thin section fabrication. Sand aliquots were sent to Wagner Petrographic (Lindon, Utah) for embedding in epoxy resin. Each slide was stained for calcite, plagioclase, and potassium feldspar. Five hundred (500) grains were counted in each sample following the Gazzi-Dickinson method (Figure 3.4, Table 3.1) (Ingersoll et al., 1984). Counts were completed on a Zeiss Photomicroscope equipped with a Swift point counter, with the spacing interval adjusted based on the average grain size in each thin section. Common grains were tabulated, and summary statistics were calculated for the full dataset. The data were normalized and plotted on ternary diagrams using the provenance fields of Dickinson *et al.* (1983) and Dickinson (1985). The ratio Quartz/(Feldspar + Lithics) or Qt/(F+L) was calculated for each sample; larger values indicate greater intensity of weathering (Pettijohn, 1954).

Canonical correspondence analysis (CCA) was employed to examine the competing controls on sand composition. We considered the primary components of the point counts, total quartz (Qt), total feldspar (F), and total lithic clasts (L), along with the major hinterland lithologies and environmental variables. To facilitate this analysis, we grouped the hinterland lithologies into seven categories. Sedimentary rocks were simplified and binned into siliciclastic or carbonate types. Metamorphic rocks were grouped into foliated or non-foliated lithotypes, and igneous rocks were divided into plutonic and volcanic lithotypes. We also considered the unconsolidated alluvium in the lowlands, which occupy a large proportion of the Pantanal Basin. Key environmental parameters were included in the assessment, such as in-channel distance to the

confluence with the Paraguay River (a relative proxy of transport distance), elevation at the sampling site, and average precipitation, temperature, and slope in each pour point defined sub-watershed.

3.4   Results

The average basin-wide sample composition was %QtFL 88\5\7, and the average Qt/(F+L) was 44 (Table B.3). The pour point analyses across the Pantanal Basin (Figure 3.5) showed that siliciclastic sedimentary rocks and unconsolidated surficial deposits dominated most of the watersheds, particularly when the sampling station was situated in the lowlands or the plateau. The most lithologically diverse outcrops were found in the watersheds draining the cratons and the Paraguay Belt.

3.4.1   Lowlands (Region A)

The lowland provenance domain is largely made up of low-elevation plains west of the plateau. The mean annual precipitation in the lowlands is 1430 mm, with average annual temperature of 25°C. Lowland samples were derived from the largest watersheds (average 93,608 km^2) in the basin with large components of surficial alluvium and siliciclastic sedimentary lithotypes (A1-A39, Figure 5); only five of the 39 samples had >30% foliated metamorphic parent rocks in their sub-watersheds, all of which were derived from the smallest lowland watersheds.

The samples from the Lowlands (**Region A;** n = 39) had the highest percentage of quartz grains for any of the Pantanal's provenance regions, with an average QtFL of 93\5\2 with a Qt/(F+L) range of 3 to >100 (average = 58) (Table B.3). The lowland samples are most enriched in monocrystalline quartz, and all but three stations were

quartzose (Figures 3.4, 3.6) (Dickinson, 1985). Lithic grains in lowland samples were predominantly sedimentary (Figure 3.4A). Considering the spatial variance of grain types in the lowlands, monocrystalline quartz grains were most common in proximity to the medial Paraguay River, near the geographic center of the Pantanal Basin (Figure 3.7).

3.4.2   Amazon craton (Region B)

The Amazon craton provenance domain consists of hilly remnants of the Precambrian formations in the Jauru terrane in the northwest Pantanal Basin and the Sunsás province in eastern Bolivia. The mean annual precipitation is 1536 mm, with average annual temperature of 26°C. Amazon craton samples were derived from relatively small watersheds (average 1,318 km^2) with extensive volcanic, plutonic, and foliated metamorphic lithotypes (B1-B9, Figure 5); only two of the nine samples had >50% siliciclastic sedimentary rocks in their sub-watersheds. The areal extent of the most common lithotypes was composed of siliciclastic rocks 31%, plutonic igneous rocks 22%, volcanic igneous rocks 18%, and foliated metamorphic rocks 18% averaged across the 9 Amazon craton sample watersheds (Table B.2).

For samples from the Amazon craton provenance region (Region B; n = 9), the average QtFL was 92\5\3 with a Qt/(F+L) range of 6 to 69 (average = 22). Most Amazon craton samples were quartzose (Figure 3.6). Amazon craton samples belonged to three tributaries that originated from the northwestern Pantanal Basin. The spatial patterns of grain types showed that feldspar counts were ~5% and lithic grains were 2-3% except for one sample site where the Qt/(F+L) was >30 (Figure 3.7). The feldspathic grains were further transported to the Paraguay River lowland samples immediately downstream of the confluences of the tributary rivers draining the Amazon craton.

3.4.3 Rio Apa craton (Region C)

The Rio Apa craton is the southernmost exposure of the Amazonian craton and consists of outcrops covered by Quaternary sediments (Cordani et al., 2010; Faleiros et al., 2016). The mean annual precipitation is 1260 mm, with average annual temperatures of 25°C. Rio Apa craton samples were derived from an average watershed size of 2,774 km^2 draining foliated metamorphic lithologies and plutonic igneous rock. Only two of the eight samples contained $\geq$50% surficial sediments. The most common lithologies were foliated metamorphic rocks 43%, surficial alluvial deposits 22%, and plutonic igneous rocks 16%.

Samples from the Rio Apa craton provenance region (Region C; n = 8) had an average QtFL of 57\28\15, with a Qt/(F+L) range of 0 to 6 (average = 2). These samples are characterized as feldspatho-quartzose sands (Figure 3.4B). Rio Apa craton sands are the most enriched in potassium feldspar of any samples in the Pantanal Basin (Figure 3.6). The Qt/(F+L) decreased to <12 in the Paraguay River stations downstream of the confluence with tributary supply of feldspars sourced from the adjacent craton. Lithic grains are enriched to 20-89 grains/sample and Qt/(F+L) decreases to <20 in the downstream Paraguay River lowland samples.

3.4.4 Plateau (Region D)

The plateau river samples primarily drain Phanerozic-aged siliciclastic formations and volcanic igneous rock (mainly dacite) and are characterized by deep, rapidly eroding gullies. The mean annual precipitation is 1516 mm, with average annual temperature of 24°C. The plateau samples are derived from an average watershed size of 14,240 km2. All but five samples have >50% siliciclastic lithologies in their watersheds. The areal

extent of siliciclastic rocks was 76% and volcanic igneous rocks 15% averaged across the plateau sample watersheds (Table B.2).

Sand from the plateau provenance region (Region D; n = 21) show an average QtFL of 94\2\4 with a Qt/(F+L) range of 4 to >100 (average = 60). Like the lowland sands, the plateau sands were chiefly quartzose (Figure 3.6). With respect to spatial variance, a hinge in quartz enrichment was observed, with samples from the plateau south of the Taquari River being less quartzose than plateau samples north of the Taquari River. The southern plateau samples had lower Qt/(F+L) and higher abundances of lithic and feldspar grains (Figure 3.7) (Barboza et al., 2018).

3.4.5   Southern and Northern Paraguay Belt (Regions E and F)

Both regions of the Paraguay Belt consist of a fold-thrust belt covered by Phanerozoic sediments. The mean annual precipitation is ~1314 mm in Region E and ~1493 mm in Region F, with average annual temperatures of 24°C and 25°C, respectively. Region E sample watersheds had an average watershed size of 384 km2 and Region F watershed average size was 6,816 km2 draining Neoproterozoic metasediments and granites (Barboza et al., 2018).

The Southern Paraguay Belt samples Region E (n = 7) show an average QtFL of 52\3\45, with a Qt/(F+L) range of 0 to 21 (average = 4), and the Northern Paraguay Belt samples Region F (n = 13) were 96\0\4, with a Qt/(F+L) range of 9 to 160 (average = 41). The most commonly occurring lithologies in the Southern Paraguay Belt were carbonate sedimentary rocks 43% and non-foliated metamorphic rocks 28%. The common lithologies in the Northern Paraguay Belt were siliciclastic rocks 45% and biochemical sedimentary rocks 17%. The Northern Paraguay Belt sands had nearly double the quartz

content of the Southern Paraguay Belt sands. Southern Paraguay Belt samples were characterized as litho-quartzose sand (Figure 3.4E). In contrast, Northern Paraguay Belt samples were depleted in feldspars (<2%) and lithic sediments (<4%).

3.4.6 Spatial distribution and statistical data

The canonical correspondence analysis (Figure 3.8) considered how a suite of environmental variables including precipitation, temperature, elevation, slope, and distance from the Paraguay River and surficial extent of lithotypes influence riverine sand composition. Rainfall, temperature, average slope, and metamorphic and sedimentary lithologies were important controls along component 1. The average watershed slope and metamorphic lithologies exerted the strongest control on samples in the southern Paraguay Belt and the Rio Apa craton. These environmental and lithological characteristics translated into greater feldspar counts in Rio Apa sands and sedimentary lithic grains from southern Paraguay Belt sands. Most of the closely grouped samples from the lowlands, Amazon craton, plateau, and Northern Paraguay Belt regions loaded negatively on component 1, where the mean annual precipitation was a strong predictor for sand composition. Component 2 was most influenced by sampling station elevation, proportion of sedimentary parent rocks, and distance from the Paraguay River.

3.5 Discussion

3.5.1 The modern Pantanal back-bulge in the Andean retroarc context

Modern sediments in the Pantanal Basin are assumed to originate entirely from the interior craton. Several westward directed fluvial fans occupy the Pantanal Basin, with their apices defined by the transition from plateau to lowland provenance domains.

The largest examples of these are the Paraguay, Cuiabá, São Lourenço, and Taquari fans

with smaller examples in the inter-megafan area (e.g., Weissmann *et al.*, 2015). The

smaller fluvial fans such as the Miranda River fan are adjacent to interfan plains (Merino

& Assine, 2020). These rivers all discharge into the Paraguay River, which serves as the

trunk or axial fluvial system. The dominance of sand in all of these areas suggests a low

accommodation to sediment supply ratio (Weissmann et al., 2015). As a result of this

basin configuration, practically no Andean syn-orogenic sediment is transported by rivers

into the Pantanal Basin, which is instead filled with non-orogenic cratonic debris.

Contributions of wind-blown sand to the Pantanal are unknown, but given prevailing

wind directions at the latitude of the basin, the effects of eolian deposition are presumed

to be minimal.

The Pantanal Basin sediments were considered in the context of the modern

regional Andean river sands studied closer to the extant fold-and-thrust belt (Decelles &

Hertel, 1989; Savage & Potter, 1991; Vezzoli *et al.*, 2013; McGlue *et al.*, 2016; Garzanti

et al., 2021a). The sands downstream of four of the six provenance regions were highly

quartzose (>90 % quartz) (Figure 3.9), consistent with a cratonic interior source

(Dickinson et al., 1983; Dickinson, 1985). This contrasts with other areas of the Andean

back-bulge that are connected to the thrust front by rivers that traverse the forebulge

crest, such as the Pilcomayo and Bermejo Rivers, which discharge into the Paraguay

River (Cohen et al., 2015; McGlue et al., 2016). Both the Pilcomayo and Bermejo Rivers

have similarly quartzose compositions at their confluence with the Paraguay River, but in

those cases, sediments were derived from recycling of Subandean Belt siliciclastic rocks.

The key exceptions to high quartz content in the Pantanal Basin were the sands from the

Rio Apa craton and the southern Paraguay Belt, reflecting compositionally distinct Precambrian sources of sediment generation. These relatively diverse sand compositions can be attributed to tributaries draining crystalline basement. The modern Pantanal Basin fluvial sands provide key data to improve our understanding of back-bulge sedimentary processes, particularly as sand petrology datasets are used to train predictive machine learning models (Johnson et al., 2022).

3.5.2 *Lithology as the primary control on sand generation*

Sands from the Pantanal Basin are quartzose, which is consistent with the source lithologies of siliciclastic sedimentary rocks and alluvium occupying ~80% of the basin's surface area. The large fluvial megafans of the Paraguay, Taquari, and Cuiabá fans are responsible for most of the alluvial cover and drain fine- to medium-grained quartz arenites of fluvial or eolian origins in the plateau region (Fantin-Cruz et al., 2020). The Bauru, Botucatu, and Aquidauana formations were the most likely origins of these sediments based on their composition (Wu & Caetano-Chang, 1992; Schiavo et al., 2010; Fernandes & Magalhães Ribeiro, 2015). Commonly sub-rounded and rounded grains in the Paraguay River samples suggested that a proportion of the sands originated from the Botucatu Formation eolian sands (Bertolini et al., 2021). Taking the Bauru Formation as a representative contributing unit, soils developing over these lithologies are quartz-rich ferralsols influenced by intense chemical weathering associated with prolonged exposure to high temperature and precipitation (Balbino et al., 2002). Given these extensive weathering conditions and source areas composed of arenites, multiple phases quartz recycling is very likely to have occurred in the sediment-generating hinterland.

For most rivers, quartz sand counts generally increased towards the lowland region, as the distance to the Paraguay River confluence decreased. Some exceptions to this trend are present, however. Litho-feldspatho-quartzose sand originated from Rio Apa foliated metamorphic rocks in the Alto Tererê Group and the Amoguijá Group (Figure 3.9) (RadamBrasil, 1982). Litho-quartzose sand originated from the southern Paraguay Belt biochemical sedimentary rocks and non-foliated metamorphic rocks in the Corumbá Group and the Cuiabá Group, respectively (Figure 3.9) (RadamBrasil, 1982). The size of the watershed may also play an important role, because only sands from small watersheds (on average <2000 km^2) preserved lithic grains. By analogy, changes to the quartz percentage was observed in the equatorial Kagera River in east Africa due to dilution (e.g., Garzanti et al., 2013). Dilution with quartz may increase with watershed size in the Pantanal Basin, and therefore influence river sand composition.

Within the Paraguay River, sands become increasingly fine and quartzose traveling from north to south. However, the composition of Paraguay River sand was modified as the river flowed adjacent to the Rio Apa craton south of the Miranda River confluence (Figure 3.7). The Paraguay River samples near the Rio Apa craton have greater counts of feldspars by virtue of their proximity to the foliated metamorphic rocks and plutonic igneous rocks in the hinterland outcrops. Additional samples from the Paraguay River in Paraguayan territory may help clarify the spatial influence of the Rio Apa craton on sand composition beyond the initial confluence with the Paraguay River. Studying the Paraguay River terraces would also help to constrain the history of sediment generation and export (Jonell et al., 2017).

3.5.3   *Chemical weathering as a secondary control on sand composition*

Differences in hydroclimate may constitute a feedback mechanism on sediment generation processes and help to explain the higher counts of lithic sedimentary grains and feldspars in the southern half of the Pantanal Basin. Chemical weathering in the Pantanal Basin is moderated by seasonally and spatiotemporally variable precipitation and temperature (Figure 3.3B). The mean annual precipitation appears to be a secondary influence on the modern river sand composition in the Pantanal Basin based on the multivariate statistics (Figure 3.8). The southern Pantanal region, where the Rio Apa and Southern Paraguay Belt provenance regions are situated, has a shorter dry season of 1-3 months and reduced mean annual precipitation, resulting in less efficient weathering and transport of sediments. We inferred that >1300 mm/y of precipitation coupled with a dry season of 4-5 months in the plateau provenance region led to more effective weathering and flushing of quartz-rich sand (Latrubesse et al., 2012). The export of quartz grains from the siliciclastic lithotypes is therefore interpreted to be an important control on lowland, Amazon craton and plateau sample composition, reflecting polyphase recycling and elevated tropical weathering rates.

One area of the basin that showed a divergence in the quartzose sand was the medial Taquari River megafan, which contained slightly higher abundances of fine-grained feldspar (up to 17% of the composition). We interpret that feldspars are concentrated in the finest sand size fraction because weaknesses in bond strength along cleavage planes rapidly reduce feldspar grain size, especially for plagioclase grains (Suttner & Dutta, 1986; Islam et al., 2002). Hence, most fine sand size feldspars were potassium feldspars from siliciclastic lithologies. This abundance of feldspar on the

megafan is consistent with quartz-rich cratonic sandstones that have greater feldspar concentrations in either the very fine sand fraction or in the coarse silt fraction (Odom, 1975; Odom et al., 1976; Blatt, 1985).

The extent of soil development can produce sand compositions that are skewed towards higher quartz content from the hinterland regions. The steeper areas in the Serra da Bodoquena and Província Serrana have comparatively thin, poorly weathered lithosols, which facilitates an increased volume of sediment exported to the lowlands (Figure 3.1C) (Brosens et al., 2020). Fluvial sediments downstream of these steeper fold-thrust regions should contain more feldspar and lithic grains, which was observed for Rio Apa and Southern Paraguay Belt samples (Figure 3.7). The Northern Paraguay Belt samples downstream of the Província Serrana did not record as many feldspar and lithic grains, due to higher rainfall. Feldspar and lithic grains are rapidly weathered in the soils where the Pantanal's tropical climate prolongs chemical weathering (Berner & Holdren, 1979).

For the plateau region, the most strongly weathered soils (i.e., ferralsols) developed on the gently sloping areas of the plateau are known to generate more quartz-rich sediments (Deckers et al., 2003; Strey et al., 2016; Terra et al., 2018). The arenosols are poorly developed soils with high sand content and in fluvial deposits (Grossman, 1983). Where sandy soils form, the removal of feldspars likely occurs during periods of prolonged subaerial exposure. In contrast, the planosols are characterized by hydromorphized conditions and develop in the lowland regions (Benedetti et al., 2011). Both arenosols and ferralsols favor the generation of quartz-rich sediments, especially when combined with high temperature and precipitation encountered in the north and

central areas of the basin (Sileshi et al., 2022). We observed this effect in the São

Lourenço and Piquiri Rivers, where total quartz exceeds 93%.

Calcite grains observed in a few samples of the Southern Paraguay Belt rivers

suggest two simultaneous processes that are unique to specific localities in the Pantanal

Basin. First, breakdown of carbonate lithologies generates carbonate rock fragments. The

carbonate formations consist of Xaraiés and Pantanal de Miranda limestones and the

Serra da Bodoquena tufa deposits and other biogenic carbonates (Boggiani et al., 1995;

Ribeiro et al., 2001; Oste et al., 2021). The sands of the Salobra River in the Southern

Paraguay Belt region contain many (~66%) weathered carbonate grains, interpreted to be

the result of weathering of the original limestone outcrops comprising >80% of the

watershed surface area (Figure 3.4B, E, F). This finding was consistent with the

underrepresentation of carbonate grains relative to their areal extent (Garzanti et al.,

2021b). Second, the reduced annual rainfall coupled with the carbonate formations help

sustain high calcium concentrations in the surface waters, leading to

penecontemporaneous calcite precipitation (Arribas & Arribas, 2007). Bicarbonate waters

flow through these areas, and the occurrence of limestone deposits overlying Holocene

sands likely facilitated the bicarbonate solution to precipitate ooids (Ribeiro et al., 2001;

Silva et al., 2017). Freshwater ooids have been documented to form with microbial

activity where shallow ponded water occurs (Davaud & Girardclos, 2001; Pacton et al.,

2012). Although rarely reported, fluvial ooids have formed in areas that receive calcium

carbonate-rich springs (Geno & Chafetz, 1982). The Formoso River near Bonito, Mato

Grosso do Sul is filled with calcareous bioclastic sediment, counted as carbonate lithic

grains (Oste et al., 2021).The E1, E3, E5, and E7 sampling stations contained >16%

carbonate lithic sedimentary grains and 2% up to 10% feldspars. Hence, very localized

processes influence sand compositions but become rapidly diluted by quartzose sands

downstream of the confluence with the Miranda River.

3.5.4   *Other landscape factors and implications*

Vegetation composition can play an important role in sediment retention or

export. The Apa craton, plateau, and Southern and Northern Paraguay Belt regions were

historically dominated by savannas, with small areas of forest and grassland (Rodrigues

et al., 2022). Their density and root structures help to retain sediments in the plateau

regions and reduce sediment export to the lowlands both in the *cerrado* and the dry forest

ecotones (Figure 3.3A). However, as humidity increased in the late Quaternary, the

highly weathered ferralsols and arenosols would have been susceptible to eroding into the

lowlands. The land-use transitions have converted large swathes of the plateau into

cropland and pasture (Godoy et al., 2002; Rodrigues et al., 2022). In order to determine

the timing and volume of sediment export into the lowlands, the acquisition and dating of

sediment cores from paleochannels is needed, such as the Cuiabá River study that

identified decreased vegetation cover during the last glacial maximum (Pupim et al.,

2017).

Two possibilities may explain the increased concentration of feldspar grains in the

medial Taquari River megafan: exhumation of buried floodplain sediments at the channel

avulsions or unusual hydrodynamic sorting. Here, we focus on the exhumation process.

The Caronal avulsion is actively shifting the downstream half of the river to a new

channel (Buehler et al., 2011; Louzada et al., 2020, 2021). The A26 and A27 sampling

stations are located at the Caronal avulsion node where the Taquari River is constructing

a new lobe and illustrate that very fine feldspars are rapidly redirected to the newly constructed channel, more than doubling the feldspar grains counted in the abandoned channel stations. The feldspar grains in the Cuiabá River (sample A10) comparable to those in the Taquari River might be explained by the sampling station's proximity to abandoned distal channel lobes that may supply exhumed feldspathic grains. Because the downstream concentration of feldspars was observed primarily in or near these fluvial fans, we propose that channel avulsions and the subsequent incision of a new channel into the floodplain exhume feldspars. These feldspar grains may have been deposited during the drier conditions of the early Holocene (Novello et al., 2017; McGlue et al., 2017).

The composition of fluvial sand along rivers depends in part on the grain size but why this occurs remains debated (Garzanti et al., 2009; Miller et al., 2014). It is useful to consider how grain size may influence the sand composition (63-2000 µm). The Taquari River contained moderate amounts of potassium feldspar grains and chert, but in the medial Taquari megafan, the raw count of feldspar grains increased due to a grain size effect where feldspathic grains are commonly reduced to very fine sand size (Odom, 1975; Garzanti et al., 2008). Much of the surface sediment in the Pantanal is reworked by fluvial channel processes (Assine, Merino, et al., 2015; Pupim et al., 2017). Hydraulic sorting effects has been shown to change grain size distribution and can be identified by a few characteristics (Kroonenberg, 1992; Barshep & Worden, 2023). We propose that selective entrainment of finer, less dense grains such as feldspars compared with quartz grains is a common process in the Pantanal (Komar, 1987). Although sorting and grain size were not explicitly measured, Taquari River sands became finer from the plateau

57

towards the Caronal avulsion. When the Taquari distributary channels discharge into the Paraguay River, the high Qt/(F+L) values where quartz content is >90% and increasingly fine sands suggest that grain size and composition are linked.

Slope is an important factor related to the potential for sediment generation, particularly along the hinterland plateau regions. The siliciclastic formations in the plateau regions are friable and moderately consolidated, which eases and hastens the development of dendritic drainage and erosion. The old, weathered soils such as arenosols and ferralsols on these lithologies can be a critical source of fine grains observed in the lowlands. In contrast, the steeper gradient of the Paraguay Belt precludes deeper soil profiles and instead facilitates the export of comparatively poorly weathered feldspathic and lithic grains. Low gradient in the floodplains can help increase the possibility that the grains are diluted or incorporated into soil-forming processes (Hatzenbühler et al., 2022).

3.6 Conclusions

We evaluated lithologic and hydroclimate controls on sand production in the modern rivers of the Pantanal Basin, the largest extant example of a back-bulge basin. Petrographic data was combined with remotely sensed datasets to determine the factor(s) that influence modern sand composition. The compositions of the river sands were predominantly quartzose in the Pantanal and consisted of non-orogenic debris. The other two endmembers were feldspatho-quartzose sand and litho-quartzose sand from the Rio Apa craton and the Southern Paraguay Belt, respectively. Intensive weathering was evident from the conditions of the minerals in thin section, as lithic fragments were only present in smaller, steeper watersheds draining the Rio Apa and the Southern Paraguay

Belt. The presence of carbonate lithic sands was spatially limited to small, upland regions in bicarbonate waters.

We found that parent rock lithology was the primary control on modern sand composition in the Pantanal Basin, with secondary effects from climate variability. The average slope helped to explain the presence of lithic grains, where areas of greater average watershed slope had more lithic fragments. Areas of lower slope and increased storage capacity in the floodplain had a greater presence of quartz grains. Lithic compositional signals were rapidly lost in areas with steep topography and felsic volcanic rocks. Chemical weathering driven by variable precipitation and seasonality acted as a secondary control that enhanced physical weathering in the Pantanal Basin. In modern sand compositions, this was most evident in the rapid reduction of less durable sand-sized grains such as feldspars and lithics as the dilution effect from tributary supply increased downstream. Most of these lithic grains were present when the sampling site was in an area with adjacent geologic outcrops to supply these freshly weathered grains. Critically, the increased feldspar counts in the fine fraction of the Taquari River megafan was interpreted to occur from the exhumation of floodplain deposits as avulsions incise new channels.

The lithologies of the Pantanal Basin demonstrate the usefulness of the Qt/(F+L) ratio as an overall indicator for the influence of different provenance regions. Regions south of the Taquari River and along the Taquari River have Qt/(F+L) <30, contrasting with areas that have Qt/(F+L) >120 north of the Taquari River apart from the Amazon craton. Refining our models of back-bulge basin environments in the sedimentary record will require cautious assessment of subtle changes in the sand compositions. The three

stations A1, A2, and A3 sampled closest to the confluence between the Apa and Paraguay Rivers demonstrates that the river's bedload sands record the tributary supply of feldspathic and lithic sands eroded from the Rio Apa craton lithologies.

3.7   Acknowledgments

3.8   Tables and Figures

Table 3.1 Point counting parameters

Symbol	Definition	Symbol	Definition
Qm	Monocrystalline quartz	Qpq	Polycrystalline quartz
P	Plagioclase feldspar	K	Potassium feldspar
Cht	Chert	M	Phyllosilicates (biotite, muscovite, chlorite)
F	Total feldspar grains (P + K)	U	Unidentifiable grains
Ls	Sedimentary lithic grains	Qt	Total quartz grains (Qm + Qpq + Cht)
Lm	Metamorphic lithic grains	Qp	Polycrystalline quartz grains (Qpq + Cht)
Lv	Volcanic lithic grains	Lt	Total lithic grains (Qpq + Lm + Lv + Ls)
L	Ls + Lm + Lv	Acc	Accessory (Cpx, Hem, chalcedony, Hbl)

Note: Cpx= clinopyroxene, Hem= hematite, Hbl= hornblende
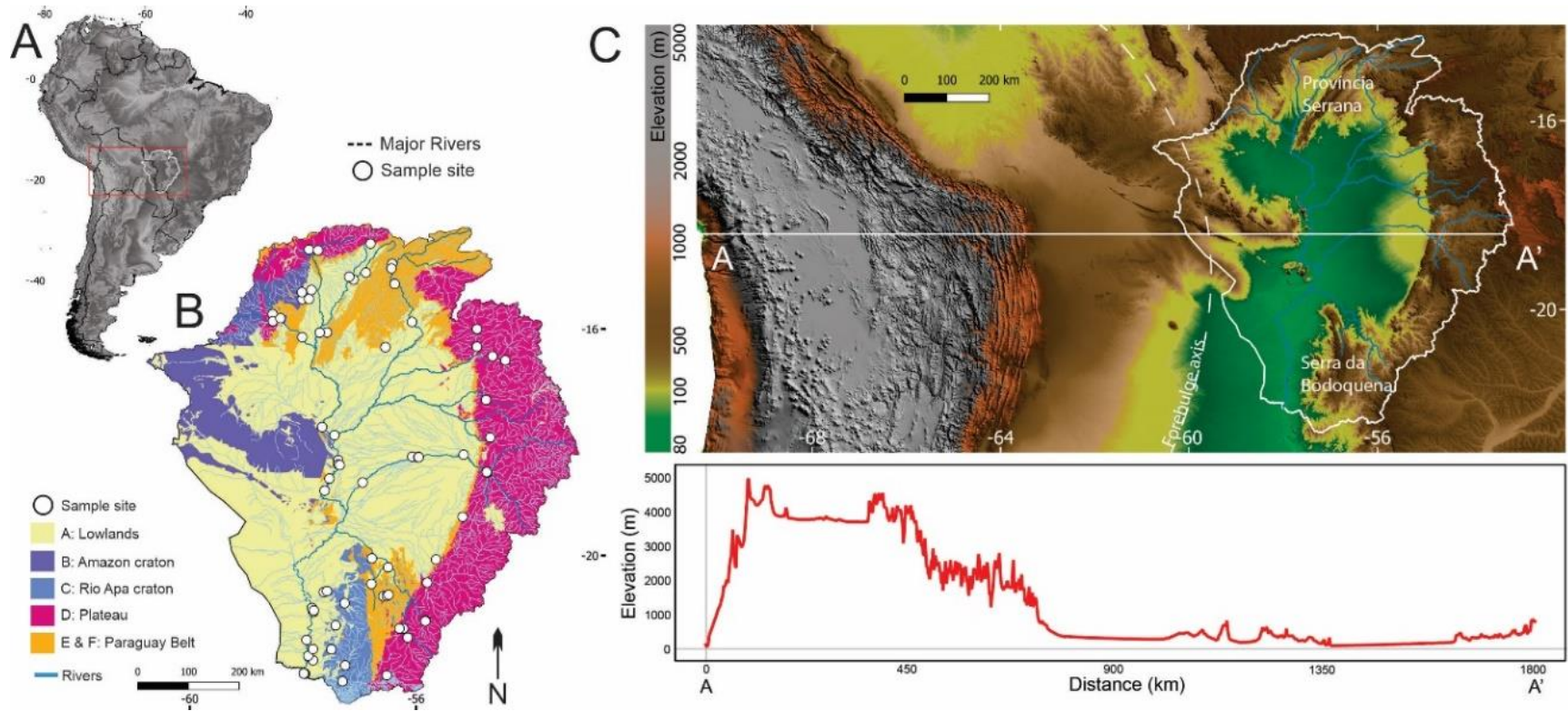
Figure 3.1 Pantanal Basin provenance regions and topography. A) Upper Paraguay River Basin (white outline) in South America with major rivers (blue lines). B) Pantanal Basin sediment generation (provenance) regions with hydrologic map, referenced throughout the text. Much of the areas covered at the surface by wetlands are designated as lowlands, in contrast with the fringing cratons and the plateau. C) GTOPO30 digital elevation model of South America (USGS, 1996), including a simplified tropographic cross-section A-A' from Google Earth©. The forebulge axis and the Província Serrana and Serra da Bodoquena mountain ranges are labeled.
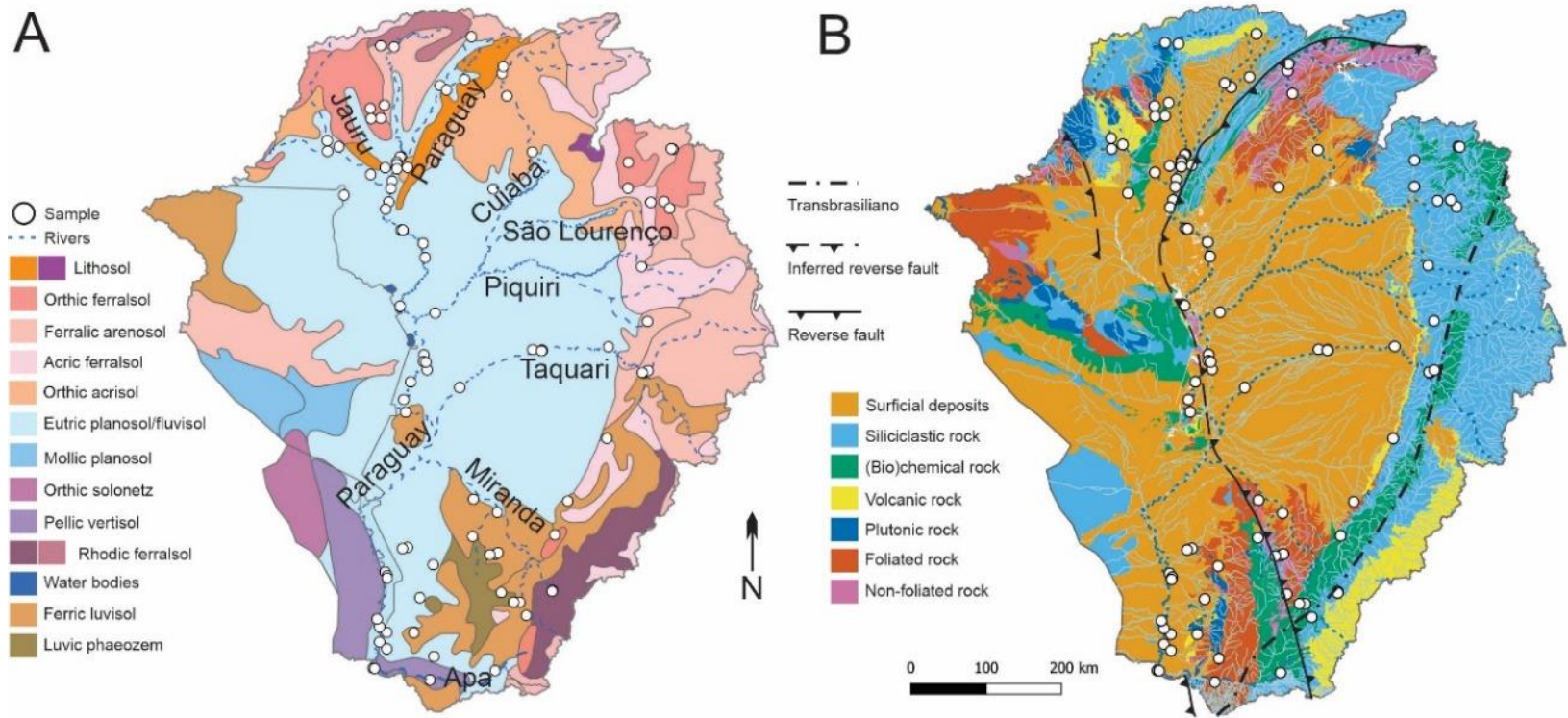
Figure 3.2 Soil and geological maps. Figure 3.2 A) Soil map for the Pantanal Basin (FAO, 1970). The primary soil classes are eutric planosol/fluvisol (Benedetti et al., 2011). B) Geology of the Pantanal Basin and drainage network, with major faults in the region. The plateau is dominated by siliciclastic sedimentary rock, whereas metamorphic rocks are restricted to the cratons and Paraguay Belt. Geologic information was obtained for Bolivia (Dirección de Ordenamiento Territorial, Gobierno Autónomo Departamental de Santa Cruz), Paraguay (Vice Ministerio de Minas y Energía), and Brazil (Serviço Geológico do Brasil, CPRM). Faults were drawn based on published studies (Rizzotto & Hartmann, 2012; Warren et al., 2015; Faleiros et al., 2016; Barboza et al., 2018; Rivadeneyra-Vera et al., 2019; Cedraz et al., 2020).
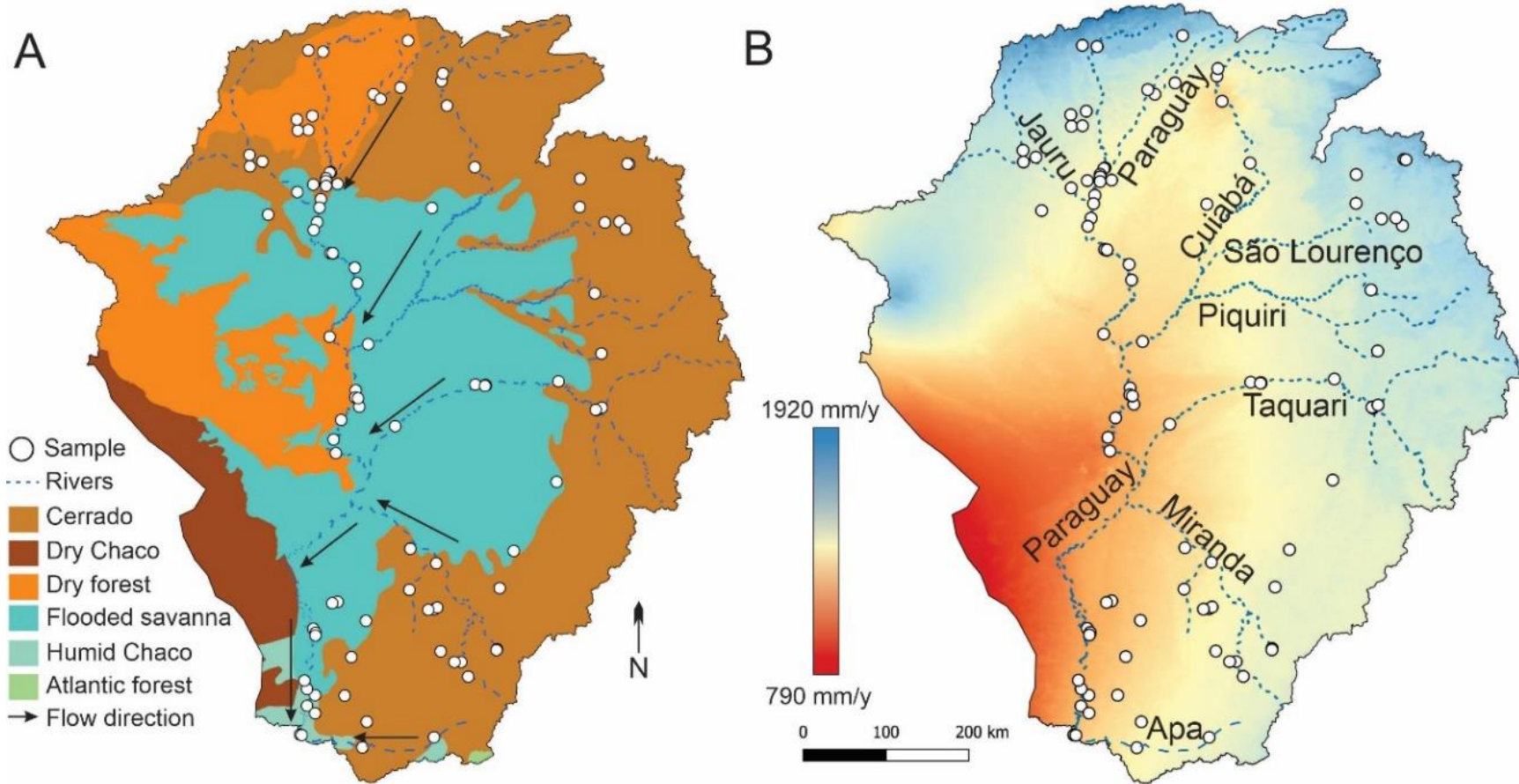
Figure 3.3 Vegetation and mean annual precipitation maps. A) Vegetation ecoregions of the Pantanal Basin (Olson et al., 2001). The primary vegetation of the Pantanal consists of flooded savanna and cerrado (tropical savanna). B) Mean annual precipitation (mm/y) from WorldClim database (Fick & Hijmans, 2017).
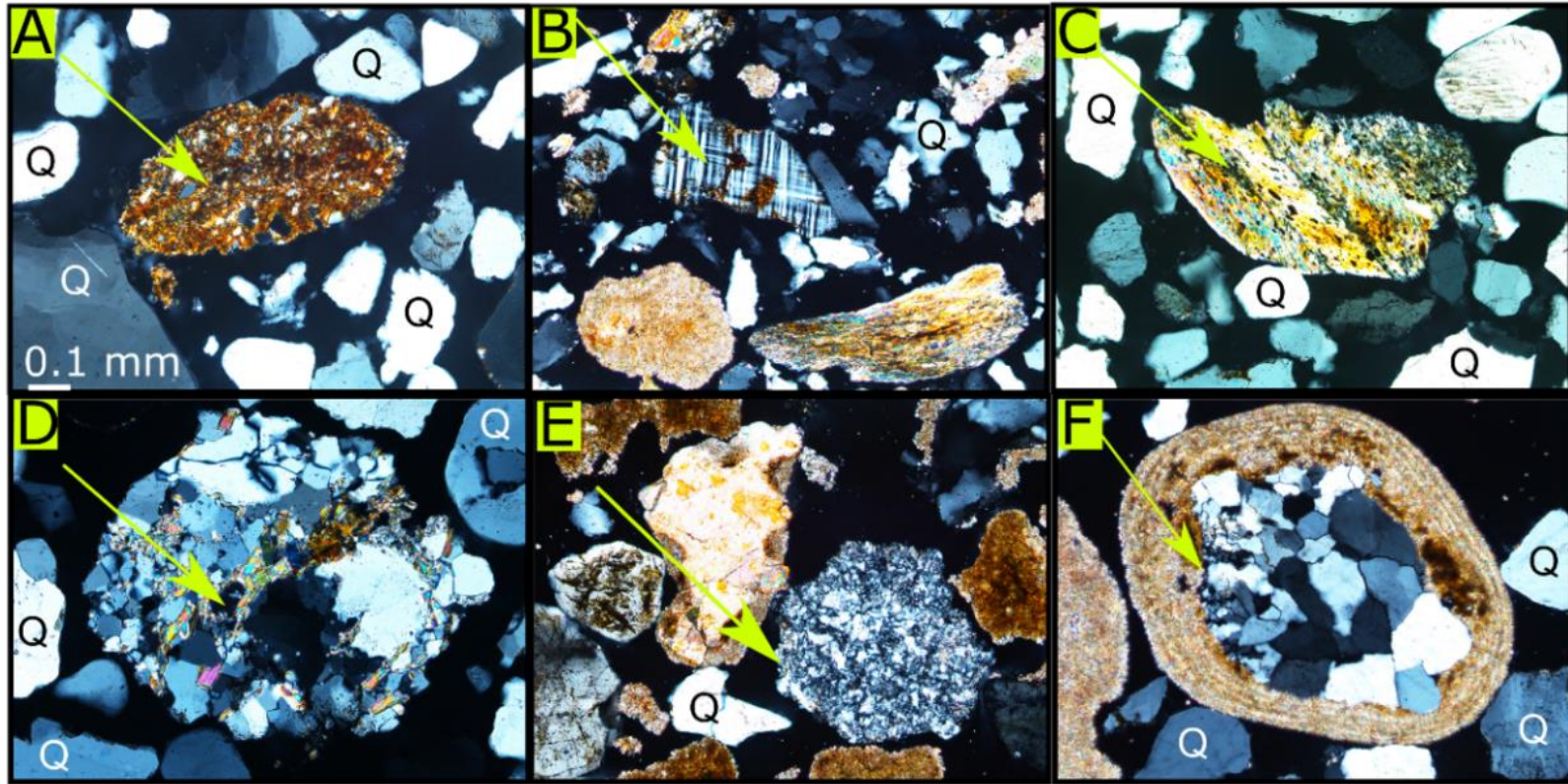
Figure 3.4 Common framework grains identified with yellow arrows in thin sections from Pantanal Basin river sands. A) detrital siltstone clast, B) microcline, C) lithic metamorphic grain, D) polycrystalline quartz, E) chert, and F) ooid with polycrystalline quartz nucleus. Note the abundance of monocrystalline quartz grains (Q) in each panel and the calcite grains in B) and E).
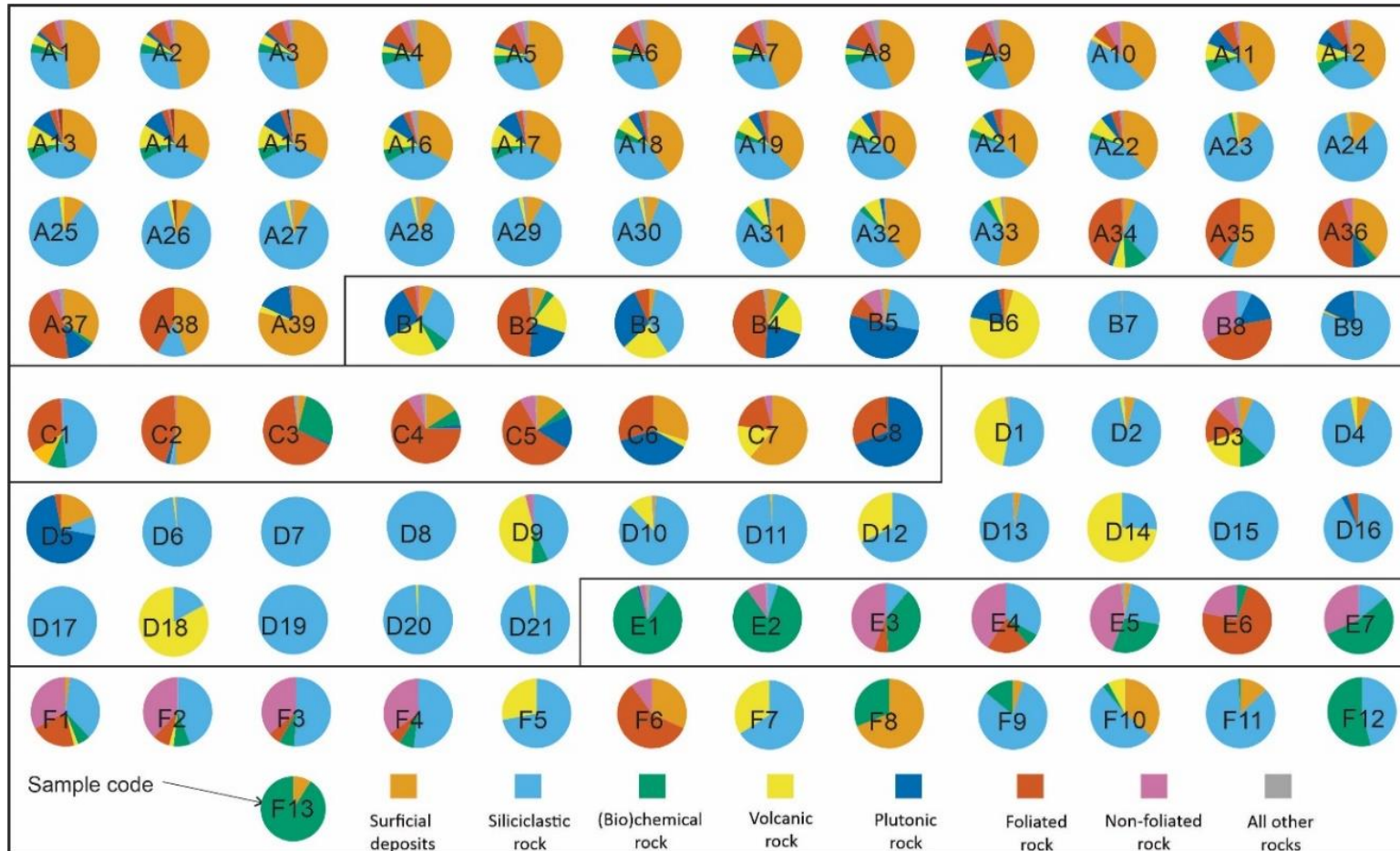
Figure 3.5 Pie charts showing relative percentages of lithologies (see Figure 2B) in each sample sub-watershed resulting from pour point analysis. For each region, samples were organized by decreasing watershed size ordered left to right and top to bottom. Regions are A, Lowlands; B, Amazon craton; C, Rio Apa craton; D, Plateau; E, Southern Paraguay Belt; F, Northern Paraguay Belt.
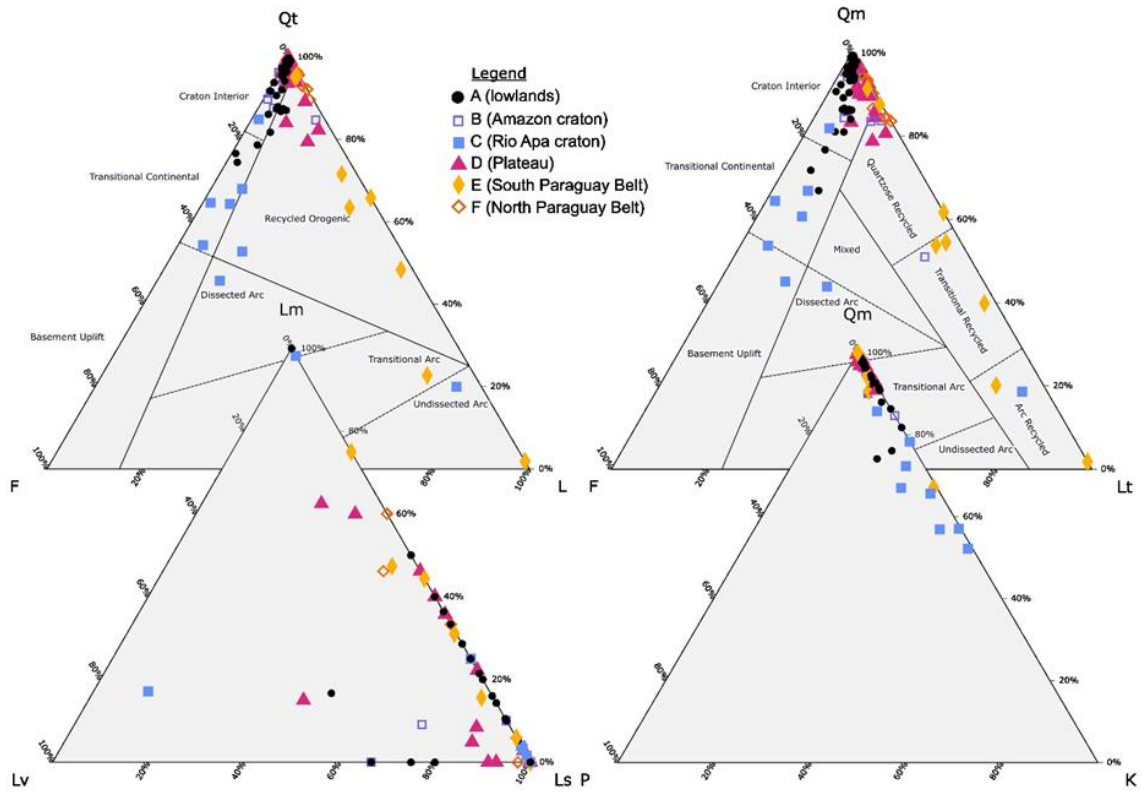
Figure 3.6 Ternary plots of sand composition in the Pantanal Basin and its provenance regions (Dickinson, 1985). The vertices were Qt (sum of monocrystalline quartz, polycrystalline quartz, and chert), F (sum of plagioclase and potassium feldspar), and L (sum of lithic igneous, metamorphic, and sedimentary grains). Qm (monocrystalline quartz), F (plagioclase and potassium feldspar), and Lt (polycrystalline quartz and lithic igneous, metamorphic, and sedimentary grains). Lm (lithic metamorphic), Lv (lithic volcanic), and Ls (lithic sedimentary). Qm (monocrystalline quartz), P (plagioclase) and K (potassium feldspar).
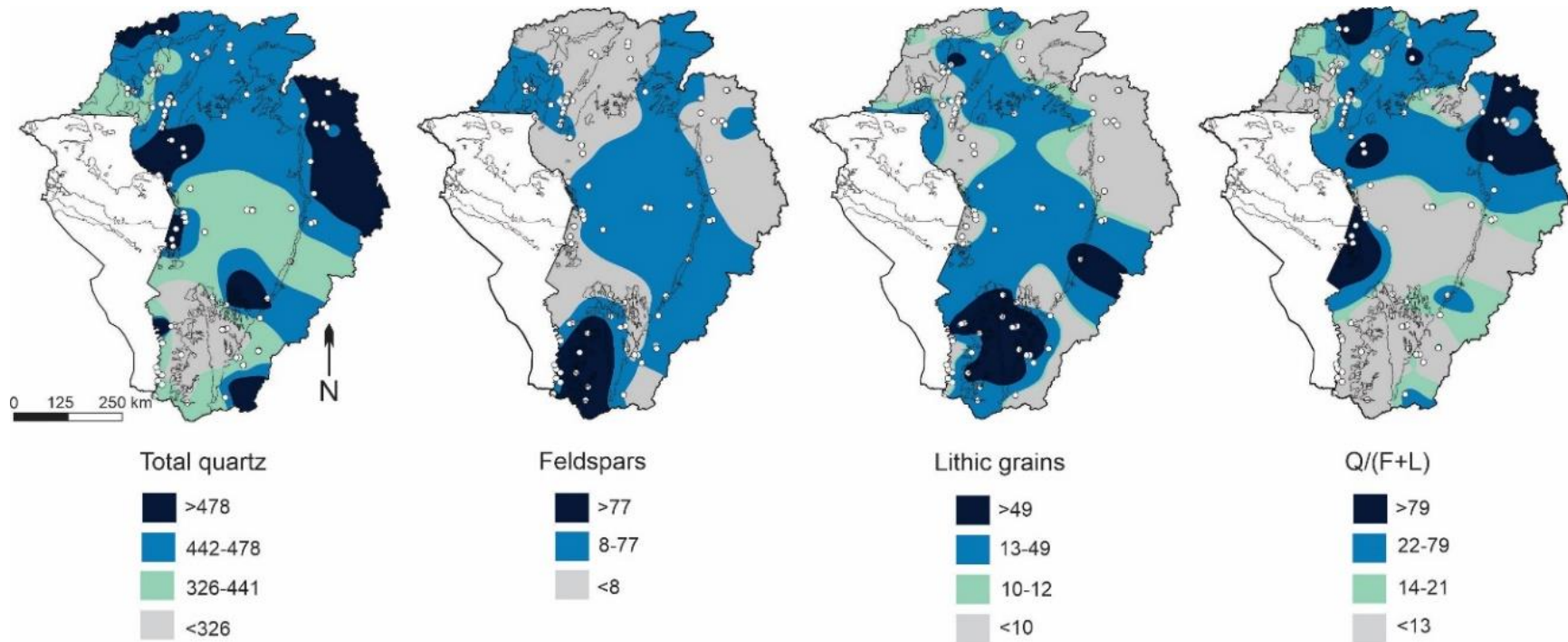
Figure 3.7 Spatial interpolation maps of the Upper Paraguay River Basin showing raw point counts for Qt (sum of monocrystalline quartz, polycrystalline quartz, and chert), F (sum of plagioclase and potassium feldspar), and L (sum of lithic igneous, metamorphic, and sedimentary grains) and Qt/(F+L). Blank areas have no data.
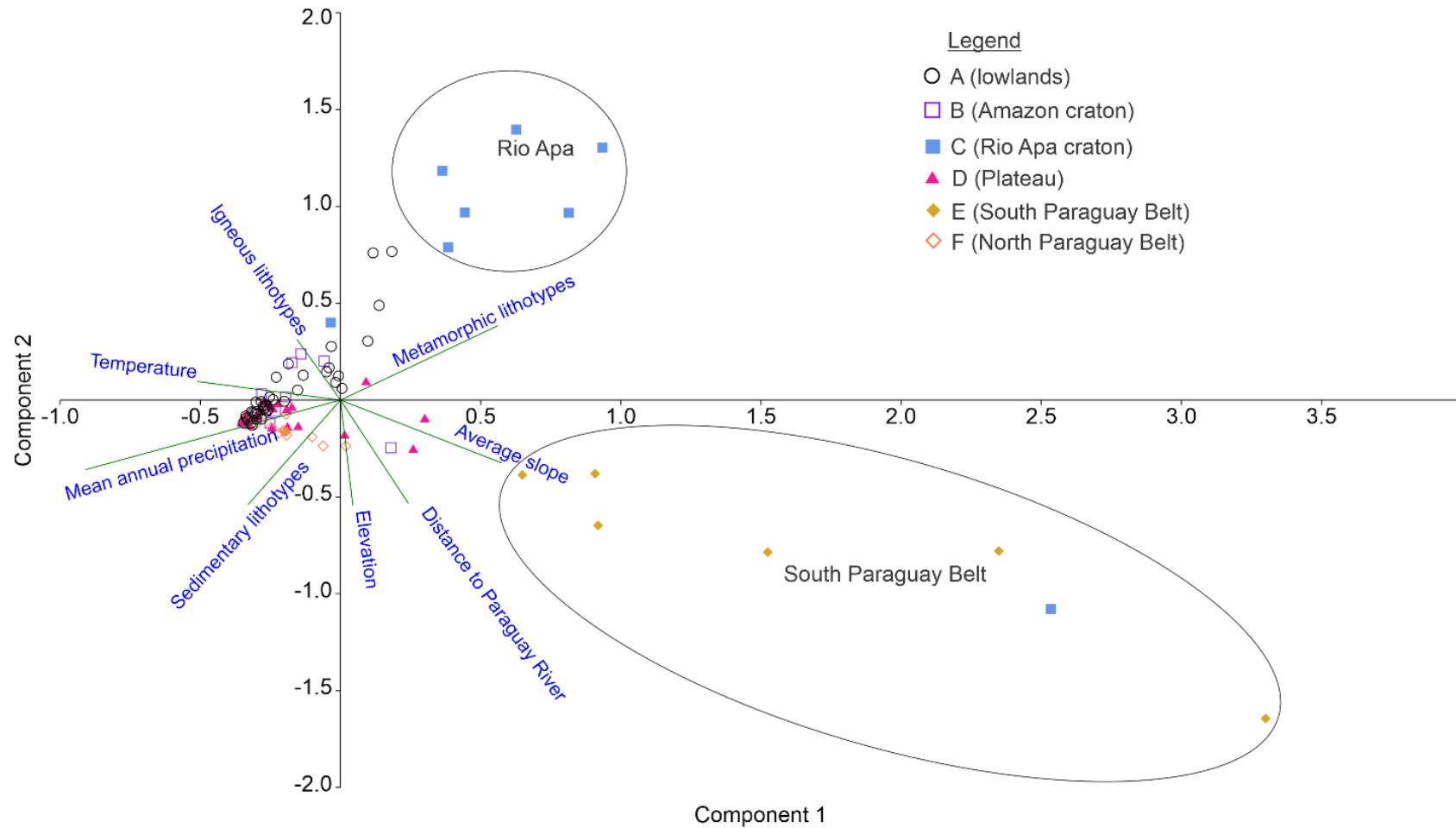
Figure 3.8 Canonical correspondence analysis (CCA) plot showing how distance to the Paraguay River, temperature, average slope, elevation, igneous rock, metamorphic rock, and sedimentary rock/alluvium affect Qt, F, L. The compositional biplot shows sample stations (points) and variables (green rays). Longer rays are proportional to the variance of the corresponding element in the data set.
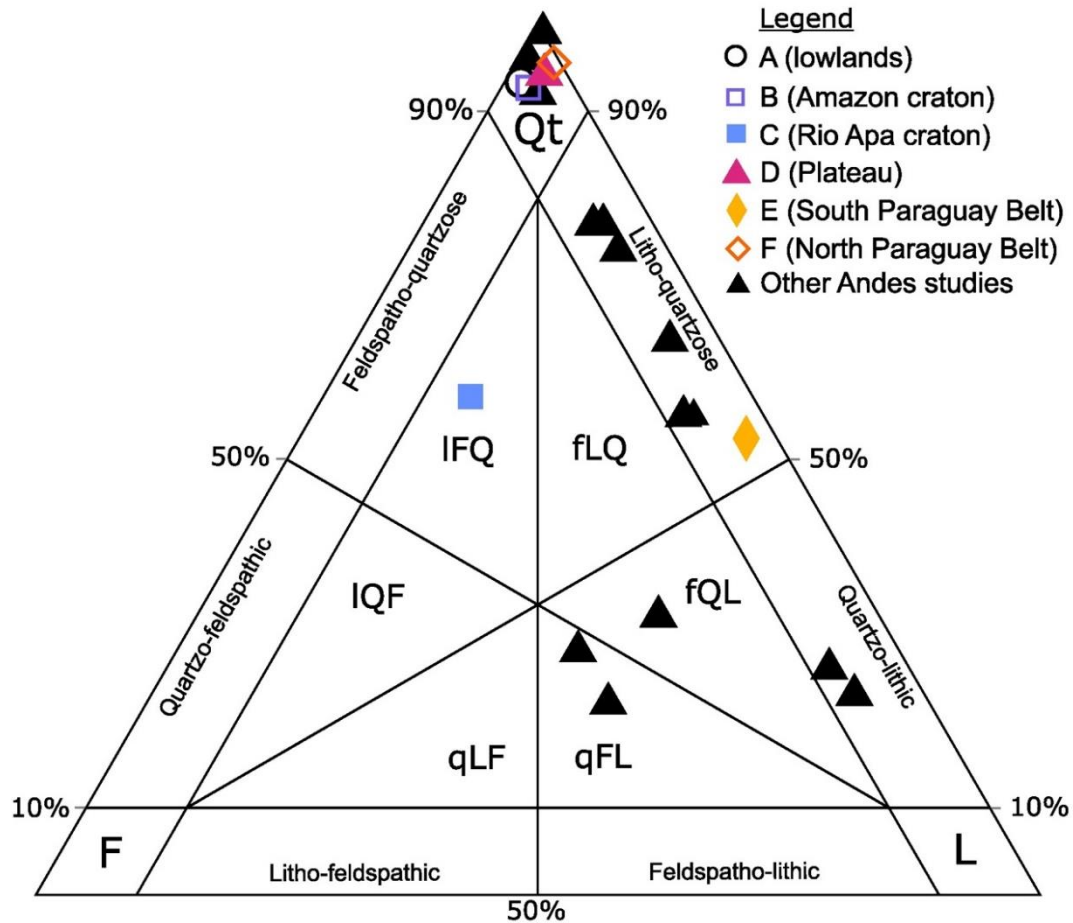
Figure 3.9 Qt/F/L ternary plot **Qt** (sum of monocrystalline quartz, polycrystalline quartz, and chert), **F** (sum of plagioclase and potassium feldspar), and **L** (sum of lithic igneous, metamorphic, and sedimentary grains) plot containing the average value for each of the six provenance regions as well as average QtFL values represented as black triangles reported from studies that used the Gazzi-Dickinson point counting protocol (Decelles & Hertel, 1989; Savage & Potter, 1991; Vezzoli et al., 2013; McGlue et al., 2016; Garzanti et al., 2021a). Abbreviations are defined lFQ = litho-feldspatho-quartzose, lQF = litho-quartzo-feldspathic, qLF = quartzo-litho-feldspathic, qFL = quartzo-feldspatho-lithic, fQL = feldspatho-quartzo-lithic, fLQ = feldspatho-litho-quartzose (Garzanti, 2019).

70

CHAPTER 4. PANTANAL BASIN RIVER MUDS FROM SOURCE TO SINK: COMPOSITIONAL CHANGES IN A TROPICAL BACK-BULGE DEPOZONE

4.1 Introduction

Back-bulges are usually low-gradient depozones in convergent orogenic systems that store sediment and preserve important environmental signals over geologic time (Horton & DeCelles, 1997; Assine et al., 2016; Brewer et al., 2020; Caracciolo, 2020). The Pantanal Basin (Brazil/Bolivia/Paraguay) forms the back-bulge depozone of the Cenozoic Andean foreland basin (Chase et al., 2009; Cohen et al., 2015; Horton, 2022). The Pantanal is a tropical savanna extending from the Amazon drainage divide to the Brazilian border with Paraguay (Figure 4.1A) (Beck et al., 2018). Most hinterland (i.e., basin margin) lithologies surrounding the Pantanal are siliciclastic sedimentary rocks, with some pre-Cambrian igneous and metamorphic exposures; these lithologies were recently grouped into six provenance regions (Figures 4.1B, C; Lo et al., *in review*). Silt plus clay preservation is considerable in low-gradient back-bulge depositional environments (e.g., in floodplains, lakes, and wetlands), and therefore the potential for representation by siltstones and mudstones in the continental geological record is high (Quartero et al., 2015; McGlue et al., 2016; Tineo et al., 2022). Syn-orogenic mudstones are useful for environmental and ecological reconstructions of the earth in deep time and in some cases for inferring tectonic processes (Macquaker et al., 2007; Li et al., 2012). Therefore, one of the motivations of this research is to examine the processes that control mud mineralogy and chemistry in a modern tropical setting where the environmental gradients (i.e., climate, soils, vegetation, relief) are relatively well-understood, in order to

71

provide insights that may improve interpretations of the geological record. The mud composition can also reflect differences between transport-limited erosion and weathering-limited erosion (Stallard et al., 1991).

Modern sands and fine-fraction sediments in large watersheds have been examined to reveal the interactions among parent lithology, climate, and tectonics that influence sediment composition (Johnsson, 1993; Jonell et al., 2017; He et al., 2020; Garzanti, Pastore, et al., 2021). For instance, quartz enrichment and kaolinite abundance in lowland settings or intense mechanical weathering on hillslopes are often linked to hot, humid conditions characteristic of the tropics (Oliva et al., 1999; Viers et al., 2000; Aristizábal et al., 2005; Garzanti et al., 2019). Tardy et al. (1973) show that montmorillinite is concentrated in the lowlands downstream of granites in humid tropical environments. Tropical and sub-tropical climates commonly result in under-representation of mafic lithologies relative to their areal extent in modern fluvial sediments (Garzanti et al., 2014; Hatzenbühler et al., 2022). Sediment erosion can be considered as transport-limited erosion where weathering creates more clays than can be transported, resulting in deeply weathered soil profiles (Stallard et al., 1991). Weathering-limited erosion occurs when the bedrock is partially weathered before the sediment is removed, concentrating micas and feldspars (Stallard et al., 1991). Further understanding of these and other source-to-sink processes requires close examination of weathering intensity, as recorded in clay mineral composition and elemental geochemistry (He et al., 2020; Cruz et al., 2022). Although studies on clay minerals have been conducted worldwide (e.g., Chamley, 1989), many questions about the relationships among fluvial transport, climate, tectonics, and chemical weathering on clay mineralogy

72

are site-specific and require localized sediment sampling. Folkoff and Meentemeyer (1987) illustrate that mean annual precipitation is an important control on clay mineral assemblages in the continental United States. Modern fluvial sediment compositions have not been systematically assessed in most continental back-bulge basins, with limited research focused on the composition of the suspended sediment load in a few major rivers of South America (Potter, 1994; Guyot et al., 2007; McGlue et al., 2016; Repasch et al., 2020).

In this study, modern muds in the rivers of the Pantanal were collected to evaluate their mineralogy and chemical composition. We employed X-ray diffraction (XRD) for semi-quantitative clay mineralogy and wavelength-dispersive X-ray fluorescence (WD-XRF) to deduce major elemental geochemistry (Moore & Reynolds, 1989). These data were analyzed along with environmental characteristics of the watersheds (e.g., slope, lithology, precipitation, elevation) to elucidate the processes that control clay composition. We tested the hypothesis that differences in mean annual precipitation control the clay mineral assemblage in modern fluvial silt plus clay in the Pantanal. This article is a companion study to a petrographic analysis of modern river sands in the Pantanal (Lo et al., *in review*), with the end goal of identifying major patterns in sediment generation and transport in this back-bulge setting. Plata River samples were integrated with this study to evaluate the influence of Pantanal Basin clay composition on downstream sediments. Ultimately, our objective is to improve interpretations of ancient sedimentary rocks in similar settings through a detailed set of actualistic observations and a database of mineralogical and chemical measurements.

4.2   Geological setting

The Cenozoic Pantanal Basin formed from flexure of the crust as the Andes range arose from the subduction of the Pacific plate beneath the South American plate (Horton & DeCelles, 1997; Assine et al., 2016). The Pantanal Basin has accumulated ~500 m of sediment, with the depocenter located near the geographic center of the basin in the area of the Taquari River (Ussami et al., 1999). The Pantanal Basin is occupied by large distributary fluvial systems also known as fluvial megafans (Assine, 2005; Zani et al., 2012; Hartley et al., 2013; Weissmann et al., 2015). Unconsolidated sediments fill the lowlands, which span ~150,000 km^2 within the Upper Paraguay River watershed covering ~465,000 km^2 of Brazil, Bolivia and Paraguay. The Pantanal Basin can be divided into six hinterland provenance regions: lowlands, Amazon craton, Rio Apa craton, plateau, and the southern and northern Paraguay Belt (Lo et al., *in review*) (Figure 4.1B). Bedrock in the northwestern Pantanal consists of Amazon craton, with granites, granodiorites, schists, and dikes of quartz-diorite and quartz-gabbro making up the bedrock (Figure 4.2B) (Rizzotto & Hartmann, 2012; Horbe et al., 2013; Braga et al., 2019). The Rio Apa craton in the southwestern Pantanal consists of gneisses, granites, granodiorites, amphibolites, schists, and quartzites (RadamBrasil, 1982; Alvarenga et al., 2011). The plateau region hosts Phanerozoic sedimentary rocks derived from the Paraná Basin: the Aquidauana Formation (arenites, diamictites, siltites, shales), Botucatu Formation (eolian arenites), Serra Geral Formation (basalts), Caiuá Group (arenites), and Paraná Group (shales, siltites, arenites, arkose) (Lacerda Filho et al., 2004; 2006). The southern Paraguay Belt hosts phyllites, schists, metarenites, quartzites, and dolomitic and calcitic marble in the Serra da Bodoquena. The northern Paraguay Belt includes the Província Serrana, with phyllites, schists, limestones, siltites, and arenites (RadamBrasil,

74

1982). The point of highest elevation is 1260 m above sea level (m.a.s.l.) on the eastern

plateau, and the lowest point is 70 m.a.s.l. at the basin outlet near the confluence of the

Apa and Paraguay Rivers (Figure 4.1C).

The hydrologic configuration of the Pantanal is responsible for the diversity of

lowland environments and the contrast between wet-dry seasons (Figure 4.3B). The

Paraguay River flows along the basin's western margin and is the trunk river of the

Pantanal. The Paraguay River is joined by the Jauru River west of the Província Serrana

in the northern Paraguay Belt provenance region. The Cuiabá River discharges into the

Paraguay River at 17.9°S latitude, followed by the Taquari River's numerous distributary

channel discharging just north of 19°S latitude. The Miranda River joins the Paraguay

River at ~19.4°S latitude. The Paraguay River flows along the Rio Apa craton between

21°S and 22°S latitude before flowing out of the basin. The waters that flow to the trunk

river annually depend on the migration of the Intertropical Convergence Zone, which

concentrates rainfall in the months of December, January, and February and strongly

influences patterns of flooding and vegetation (Ivory et al., 2019). The peak dry season

occurs in June, July, and August, but the dry season varies from 1-2 months north of the

Taquari River to 4-5 months south of the Taquari River (IBGE, 2002). This seasonality of

rainfall coupled with the minimal gradient of the lowlands results in a flood pulse effect,

such the rains that fall in the plateau and northern Pantanal delay 2-3 months to reach the

basin outlet (Junk et al., 2006). This results in broad areas of inundation in the lowlands

that lasts for several months annually. Mean annual rainfall is ~1800 mm in the northern

and eastern Pantanal but diminishes to ~1200 mm along the western and southern

Pantanal (Figure 4.3B). The average annual temperature is ~25°C basinwide (Fick & Hijmans, 2017).

Clay minerals can be transformed in contemporary soils depending on climate, slope gradients, and vegetation (Hillier, 1995; Velde & Meunier, 2008) (Figures 4.2A, 4.3A). The soils of the Pantanal are dominated by eutric planosols and fluvisols in the lowlands, but the plateau provenance region is more variable (Figure 4.2A). The plateau region contains mostly ferralsols and arenosols in addition to luvisols in the south (Benedetti et al., 2011). Lithosols are present in the Província Serrana region, and the western Pantanal contains mollic planosols, rhodic ferralsols, and orthic solonetz. Figure 3A illustrates the general patterns of vegetation, but additional floral diversity relates to the spatial distribution of soil types (de Souza et al., 2021). Broadly, the soils are divided into forest formations, arboreal *cerrado*, herbaceous *cerrado*, chaco (woody steppic savanna), monodominant formations, and mixed vegetation (dos Santos Vila da Silva et al., 2021). For example, semideciduous (*capão*) and deciduous forests thrive in vertisols, whereas the savanna woodlands (*cerradão*) grow best in arenosols (de Souza et al., 2021).

4.3 Methods

4.3.1 Initial design and fieldwork

Paired sand and silt plus clay samples were collected from river margin bars in the Pantanal in 2019-2021. Sample sites were chosen to maximize spatial coverage and lithological diversity and for ease of access. Each site was treated as a pour point, which is the endpoint of a streamflow network (Gleyzer et al., 2004). Pour point analysis was

completed with QGIS 3.4.6 to define each sample's contributing watershed using Shuttle

Radar Topography Mission (SRTM) digital elevation models (DEMs) from USGS

EarthExplorer (https://earthexplorer.usgs.gov). Pour point analysis for watersheds >

250,000 km^2 was completed with 3-arc second resolution DEM (Verdin, 2017). The

average watershed slope was calculated from these DEMs, whereas elevation and

distance from the Paraguay trunk river were extracted from Google© Earth. The

precipitation and temperature for each sample site were measured from WorldClim (Fick

& Hijmans, 2017) (Table C.1). Soils were identified in each watershed from global FAO

(1970) data and converted to the United States Department of Agriculture classification

for the purposes of literature review (Deckers et al., 2003; Souza et al., 2018). Vegetation

ecoregions were identified from (Olson et al., 2001), and geologic data were extracted

from national geologic maps (Lacerda Filho et al., 2004, 2006; SERGEOMIN, 2005;

Spinzi & Ramírez, 2014) (Table C.2). Seventy-four (74) distinct silt plus clay sampling

stations were studied, and of these, 71 samples have mineralogy data, 66 have

geochemical data, and 63 have both mineralogy and geochemistry data.

4.3.2 XRD clay mineralogy

The silt plus clay fraction was separated by wet sieving using a 53 µm sieve. We

treated each sample with 1N sodium acetate (NaOAc) with pH 5 adjusted using glacial

acetic acid (HOAc) to dissolve carbonates and replace the exchange sites for Ca and Mg

with Na. We used 30% hydrogen peroxide (H_2O_2) to dissolve organic matter, followed by

washing once with 200 mL NaOAc and 200 mL with 1M sodium chloride (NaCl)

(Jackson, 1969). To obtain the <2 µm fraction, we centrifuged the samples first at 750

rpm for 3 minutes and decanted the supernatant (liquid >2.5 cm from bottom of a 250mL

bottle) containing the <2 µm clays into a separate container for settling. The bottle was refilled with sodium carbonate (Na_2CO_3) and the process repeated until a relatively clear supernatant was achieved. The remaining material was separated as the silt fraction (2-54 µm). Several days to weeks was allowed for the clays to settle, and 50mL of the clays were transferred to a centrifuge tube for freeze drying.

Oriented slides of clay fractions were prepared using the filter peel method (Drever, 1973), with diagnostic treatments of magnesium (Mg), Mg-glycerol, and a potassium (K)-saturated slide. Briefly, we measured 200 mg of freeze-dried clay (<2 µm) for each slide and transferred the sample to 50 mL centrifuge tubes. We added 25 mL 0.5M magnesium chloride ($MgCl_2$), mixed well, and sonicated. In a separate centrifuge tube, we added 25 mL 0.5M potassium chloride (KCl) to 200 mg of freeze-dried clay, mixed well, and sonicated. The tubes were centrifuged at 2000 rpm for 5 minutes, the supernatant was discarded, and the process was repeated twice more. We added deionized water, mixed, sonicated the sample, and poured the mixture onto a Millipore 0.45 µm membrane filter mounted to a vacuum flask. With the clay still moist, we removed the filter and placed the filter clay side down on a glass slide. We lightly rolled a 20 mL glass vial across the back of the filter as we peeled away the filter, leaving behind a uniformly thick oriented clay mount.

The mineralogy of the oriented clays was determined using XRD. A PANalytical X'Pert diffractometer with a Cu tube at 45 kV and 40 mA from 2°-40° with a step size of 0.03 °2θ step size and scan step time of 10 seconds was employed for the analysis. Total scan time was ~3.5 hours for each treatment: Mg-saturated, K-saturated, Mg-glycol solvated, and K-550°C. When the first two treatments were scanned, we solvated the Mg-

saturated slide with glycol to identify if smectite was present, and the K-saturated slide was heated to 550°C for one hour to collapse the kaolinite structure. The major constituent clays identified in X-ray diffractograms used established 2-theta peak (2θ) positions (e.g., Moore & Reynolds, 1989). All data were analyzed using X'Pert HighScore software. Semi-quantitative calculation of clay mineral compositions was accomplished by multiplying the height (counts) by the full width at half maximum (FWHM, °2θ) in the Mg-saturated plot divided by the sum of the calculated areas for the predicted clay minerals and multiplied by 100 (Biscaye, 1965; Moore & Reynolds, 1989) (Table C.3). These clay abundances were cross checked in NEWMOD II, in order to confirm the reliability of this semi-quantitative method (Yuan & Bish, 2010). Spatial interpolation of the three primary clay minerals (kaolinite, illite, vermiculite) was performed using the "Spline with barriers" tool in ArcGIS Pro. Smectite, goethite, and gibbsite were reported based on presence or absence at each sampling station. The iron content in illite was calculated using the intensity of the illite (001) and (002) peaks: I (001)/I (002) (Brown & Brindley, 1980; Deconinck et al., 1988; Furquim et al., 2010; A. F. Nascimento et al., 2015).

4.3.3 WD-XRF geochemistry

WD-XRF measurements completed with a Bruker AXS Inc. S4 Pioneer device were used to determine chemical elemental abundances for the <53 µm fraction of samples with sufficient material ($n = 66$). Eight duplicate samples were measured to assess the repeatability of the analysis. Following the loss-on-ignition protocol, each sample was heated to 550°C for four hours to remove organic matter and 950°C for two hours to remove carbonate (Heiri et al., 2001). Samples were disaggregated and

homogenized in a mortar and pestle, mixed with borate flux GF-9010 (90% lithium

tetraborate and 10% lithium fluoride) in an 8:1 ratio and two drops of lithium tetraborate

($Li_2B_4O_7$), and made into glass discs using a Katanax X-300 or K1 automatic fusion

fluxer machine. The samples were calibrated with a set of eight certified reference

samples using linear regression. Molar proportions were utilized to calculate the chemical

weathering indices, including the chemical index of alteration (CIA) and the Weathering

Index of Parker (WIP) (Parker, 1970; Nesbitt & Young, 1982). Both indices are used to

determine the extent of weathering (Table C.4). The WIP acts as an index of quartz

recycling, whereas the CIA is unaffected by quartz dilution. Calculating the ratio of CIA

to WIP allows us to differentiate between weathering and quartz recycling (Garzanti et

al., 2019). The weathering indices were spatially interpolated using the "Spline with

barriers" tool and classified using geometric intervals in ArcGIS Pro.

$$WIP = 100 * (\frac{2Na_2O}{0.35} + \frac{MgO}{0.9} + \frac{2K_2O}{0.25} + \frac{CaO}{0.7})$$

$$CIA = \frac{100 * Al_2O_3}{Al_2O_3 + CaO + Na_2O + K_2O}$$

We evaluated the influence of source rock composition on fine-fraction sediment

chemistry using ACN, ACNK, ACNKFM plots and molar proportions of the major

elements (Nesbitt & Young, 1984; Nesbitt & Wilson, 1992; Fedo et al., 1995).

We examined environmental controls on clay mineralogy and chemistry using canonical correspondence analysis (CCA). The key advantage for using CCA was to distinguish how the environmental variables and major elements affected both the clay abundance and the sampling sites. We also explored other ordination analyses to examine their effectiveness in explaining the distribution of clay minerals in the Pantanal.

4.4   Results

4.4.1   Basin-wide clay mineralogy

At basin-scale, the rank order of clay mineral abundance is kaolinite > vermiculite > illite > smectite (Table C.3). Kaolinite was determined to be present if the 7 Å diagnostic (001) peak collapsed when the K-saturated slide was heated to 550°C for one hour. Illite was identified at 10Å for the (001) peak and 5Å for the (002) peak. Smectite was identified on the basis of the 14 Å diagnostic peak shifting to 18Å following Mg-glycerol (Figure 4.4). Vermiculite was distinguishable from smectite where the 14 Å peak did not shift to 17-18 Å following Mg-glycerol treatment. We identified goethite at the (110) peak at 4.18 Å and gibbsite at the (002) peak at 4.85 Å (Moore & Reynolds, 1989). The Cuiabá, Taquari, and Paraguay River muds are particularly enriched in kaolinite, representing ≥50% of the clay mineral composition (Figure 4.5). Substantial in-channel compositional variability was observed in the Taquari River, which is fed by two large tributary rivers carrying 71% kaolinite and 43% kaolinite in the plateau.

Spatial interpolation enabled additional basin-wide observations. The highest kaolinite percentages (>70%) were found in the medial Pantanal Basin, at the confluence of the Paraguay River with the distal distributary channels of the Taquari River (Figure

4.5). The medial Pantanal region is known to be regularly inundated with flood waters for some of the longest periods of the year (Ivory et al., 2019). The northernmost plateau sampling stations also produced similarly high kaolinite abundance. The northeastern plateau sampling sites were generally enriched in kaolinite downstream of orthic ferralsols and ferralic arenosols, while the southeastern plateau sampling sites in the Miranda River watershed were depleted of kaolinite, where ferric luvisols dominate (Figures 4.2A, 4.5). In contrast, the Miranda River watershed has the highest concentrations of vermiculite in the Pantanal. As the Paraguay River flows to the basin outlet in the south, the proportion of kaolinite in the river muds decreases noticeably. There, vermiculite was more common (>50%) in the clay assemblages, particularly at sampling sites fed by rivers draining the Rio Apa craton (Figure 4.5) and the southern Paraguay Belt. Both the Miranda and Apa rivers drain the Serra Geral Formation dacite, which produce rhodic ferralsols (Figure 4.2B) (Lacerda Filho et al., 2006). Illite was 40-60% in the <2 µm fraction in the Paraguay Belt region where phyllite and amphibolite schist parent lithologies dominate, producing lithosols and orthic acrisols. The Paraguay Belt contained the highest contributions of illite to the Pantanal Basin, followed by the São Lourenço River draining surfaces covered by lithosols, acrisols, and ferralsols (Figures 4.3B, 4.5).

The FWHM of the diagnostic peaks shows how crystallinity changes along the length of the Taquari River (Aparicio et al., 2006). The kaolinite (001) FWHM remained constant along the length of the megafan, indicating no changes to the crystallinity. The gibbsite diagnostic peak at 4.85 Å in the Taquari River sampling station also disappears from the proximal to the distal megafan regions. Chlorite was not found, and smectite

was identified only at limited sites such as sample A26 in the medial Taquari River megafan where the vermiculite and smectite peaks could be clearly disentangled. The average iron content in illite was 2.19, with most of the highest iron content located in the northern Pantanal in tributaries of the Jauru, Paraguay, and Cuiabá Rivers.

Gibbsite and goethite are not abundant clay minerals in samples from the Pantanal (25% of samples contained neither of these minerals), but they do constitute important minor components (Figure 4.6). Sample sites with both gibbsite and goethite were most frequently present in the north plateau region, where the mean annual precipitation in the basin is the greatest (Figure 4.3B). Gibbsite was most common in samples along the Taquari River megafan, whereas goethite occurred in samples from the southern plateau and in the medial lowlands (Figure 4.6A). Samples with neither mineral were common in the Rio Apa craton in southern Pantanal. Smectite was identified in ~30% of the 71 sampling stations (Figure 4.6B). The presence of smectite appeared to be distributed across the Pantanal Basin with no specific pattern.

4.4.2 Basin-wide geochemistry

Ternary diagrams showed that most samples exhibited >70% Al_2O_3, and all lowland samples >80% Al_2O_3 (Figures 4.7A, B). Most samples contained <10% Na_2O (Figure 4.7B) and 20-30% Fe_2O_3 + MgO (Figure 4.7C). Geochemically, all samples from watersheds in the southern Paraguay Belt provenance region and select samples from the Rio Apa craton provenance region were enriched in Ca, Na, and K and low in Al (Figure 4.7C). Average values for geochemical variables in the six provenance regions further show the greatest SiO_2 enrichment in the lowlands provenance region and the lowest average SiO_2 in the Southern Paraguay Belt (Table 4.1).

The geochemical discrimination plots show decreasing Al_2O_3 as SiO_2 increases, consistent with quartz addition relative to the UCC standard (Figure 4.8) (S. R. Taylor & McLennan, 1995). The lowland, Rio Apa craton, and Amazon craton samples followed this quartz enrichment trend closely, whereas the plateau and Paraguay Belt samples diverged from this quartz enrichment pattern. Approximately 50% of the samples (Figure 4.8C) contained less SiO_2 than the UCC and were mostly <5 $Na_2O+K_2O+MgO+CaO$. Most samples followed the quartz addition trend (Figures 4.8C, D). However, the CIA/WIP plot showed mostly a weathering trend concentrated at 70-90 CIA and <40 WIP (Figure 8B).

4.4.3   Weathering indices and statistical analysis

Table 4.1 provides summary statistics across all six provenance regions. The CIA and WIP values showed that samples from the lowlands provenance region were the most weathered, especially near the Taquari megafan where high values (83-94) of the CIA were recorded. Weathering intensities measured by WIP were more variable in the lowlands (10-36) (Figure 4.9). The Itiquira and Piquiri Rivers draining the plateau highlands immediately north of the Taquari River produced silt plus clay minerals that were consistently highly weathered as indicated by the CIA and WIP. The weathering indices reflected the clay mineral proportions deduced by XRD; the areas with the greatest kaolinite coincided with the highest CIA values and the lowest WIP values for the Piquiri, Cuiabá, São Lourenço, and medial Paraguay rivers (Figure 4.9). In contrast, the lowest CIA values and highest WIP values were recorded in the Rio Apa and southern Paraguay Belt regions (Figure 4.9).

Fe$_2$O$_3$ and metamorphic parent lithologies loaded positively on axis 1 of the canonical correspondence analysis (Figure 4.10). The SiO$_2$, K$_2$O, and average watershed slope loaded negatively on axis 1. The average watershed slope, MgO, and Fe$_2$O$_3$ loaded positively whereas watershed area, sedimentary parent rocks, and SiO$_2$ loaded negatively on axis 2. All lowland samples plotted in negative axis 2 space, while most of the Paraguay Belt samples plotted in positive axis 2 space. Two large clusters of data points are distinguishable. The first cluster is oriented diagonally along a continuum formed by the SiO$_2$ and Fe$_2$O$_3$ rays with $n = 44$ sampling sites. The samples with more SiO$_2$ are also closer to the abundance of kaolinite, and samples with more Fe$_2$O$_3$ are associated with vermiculite. The quadrant with vermiculite is characterized by significantly more MgO and slightly more Al$_2$O$_3$, as suggested by the length of the shorter ray for Al$_2$O$_3$. The second cluster of data is oriented perpendicular to the first cluster, composed mostly of Paraguay Belt samples and an association with illite, K$_2$O, average watershed slope, and elevation of the sampling stations.

4.5   Discussion

4.5.1   *Insights from clay mineralogy*

4.5.1.1   Climate control.

The Pantanal Basin is warm and seasonally wet with open *cerrado* savanna vegetation in the hinterland areas (Cole, 1960), where a pronounced hydroclimate gradient in rainfall and seasonality controls modern clay distribution. The Taquari River forms a weathering hinge between the increased weathering intensity to its north and reduced weathering intensity to its south. The greater rainfall and shorter dry season north

of the Taquari River results in high kaolinite production as bedrock and soils are leached (Goldich, 1938; Depetris & Griffin, 1968; Singer, 1980; Garzanti et al., 2014; Guinoiseau et al., 2021). Most neoformed kaolinite in soils is subsequently transported downstream towards the Paraguay River in the suspended sediment fraction (e.g., Depetris & Probst, 1998). The fluvial sediment samples in the medial Pantanal reflect the cumulative climate-driven weathering north of the Taquari River hinge. On the basis of greater kaolinite abundance in the northern Pantanal, our data broadly support the hypothesis that mean annual precipitation controls clay mineralogy.

As the clay minerals are carried as suspended loads, their composition is subsequently transformed (Setti et al., 2014). Detrital clays such as vermiculite and illite can be compared with transformed clays such as kaolinite and smectite as a measure of chemical weathering and mechanical erosion (Shover, 1963; Vanderaveroet et al., 2000; Setti et al., 2014). The Jauru and Paraguay River clays west of the Província Serrana are mostly kaolinite, plus illite from the northern Paraguay Belt. These clays likely originated from the Amazon craton and the Paraguay Belt lithologies, in addition to the siliciclastic plateau at the northernmost end of the basin. The illite ($> 60\%$) in the uppermost Cuiabá River and along small watersheds of the northern Paraguay points to rapid mechanical weathering (e.g., Selvaraj & Chen, 2006). Mechanical weathering breaks down outcrops of the muscovite-bearing Cuiabá Group rocks (Alvarenga et al., 2011; Vasconcelos et al., 2015). This interpretation is consistent with the lithosols, which are thin and poorly developed (Camargo & Bennema, 1966). Following the confluence with the Cuiabá River, the Paraguay River carries more kaolinite, similar to levels recorded in the tributaries of the Cuiabá River.

Lower kaolinite in samples from sites south of the Taquari River is interpreted to be linked to reduced rainfall (~1200 mm/y) and increased length of the dry season (4-5 months) compared to ~1800 mm/y and 1-2 month-long dry season north of the Taquari River. This agrees with our hypothesis. Reduced weathering intensity produces more detrital clays.

The 2:1 clays were primarily vermiculite, commonly a byproduct of incomplete weathering of biotite (Cleaves et al., 1970; Ojanuga, 1973; Johnsson & Meade, 1990). The Paraguay River clays downstream of the confluence with the Taquari and Miranda Rivers begin to incorporate substantial vermiculite. The Southern Paraguay Belt region and the plateau provenance region south of the Taquari River weathering hinge contain ferric luvisols overlying carbonate and foliated metamorphic rocks, a unique combination of geological factors in the Pantanal Basin. As the Paraguay River flows along the Rio Apa craton towards the basin outlet at the confluence with the Apa River, the clay composition is modified by the illite and vermiculite chemically and mechanically eroded from the craton. The intensity of weathering inferred from the relative proportions of 50% kaolinite and 50% illite + vermiculite would indicate incomplete weathering closer to the outlet (samples A2 and A3; Table C.1) than in the medial Pantanal Basin (samples A6-A9; Table C.1). The modification of the Paraguay River suspended clays attests to non-linear compositional changes downstream.

4.5.1.2 Soil control.

The composition of extant soils in the provenance regions is interpreted to be an important secondary control on modern clay mineralogy and chemistry. Although we did

not examine the mineralogy of soil profiles adjacent to each sample, we can infer soil properties and clays based on the soil classification map (Figure 4.2A).

The extensive availability of kaolinite in the dominant soils helps to explain higher proportions of kaolinite in modern fluvial samples north of the Taquari weathering hinge. Soils in the northern Pantanal Basin were described as acrisols, arenosols, and ferralsols. The acrisols and ferralsols are known to have high amounts of kaolinite and gibbsite clays in the topsoil and subsoil, whereas the arenosols contain kaolinite and illite primarily in the subsoil (Ito & Wagai, 2017). The abundant kaolinite usually occurs in lateritic soils (e.g., Truckenbrodt et al., 1991), which may appear as ferralsols or ferralic arenosols in the Pantanal (Figure 4.2A) (Righi & Meunier, 1995; Mathian et al., 2020). Some of the kaolinite formed from laterite is instead replaced by hematite (Ambrosi et al., 1986), as observed by the iron-rich concretions (~1 cm in diameter) on the armored, wind-deflated surface of the Taquari River's lateritic soils (Figure 4.11). Although not shown on the map, gleysols and plinthosols also contribute to the high occurrence of kaolinite in the northern Pantanal soils (Coringa et al., 2012).

Soils in the southern Pantanal Basin are distinguished by the extensive development of luvisols that contain greater proportions of illite in both the topsoil and subsoil (Ito & Wagai, 2017; Warr, 2022). The Southern Paraguay Belt soils are dominantly mollisols, containing primarily vermiculite, followed by illite (Warr, 2022). Mollisols are interpreted as key contributors to the higher proportions of vermiculite in the southern Pantanal.

The presence of gibbsite is an indicator of intense weathering and desilication (Certini et al., 2006; Reatto et al., 2008). Gibbsite is an aluminum hydroxide associated

with strong hydrolysis and bauxitization processes (Chamley, 1989; Velde & Meunier, 2008). Bauxitization, or the formation of aluminum ore, occurs when extensive hydrolysis leads to gibbsite authigenesis. We infer that the gibbsite was eroded primarily from the surrounding soil cover (phaeozems, luvisols, and ferralsols). The northeastern Pantanal including the São Lourenço and Cuiaba Rivers are sources of gibbsite. Gibbsite peaks were also identified in the Amazon craton rivers and the southern Paraguay Belt samples. The gibbsite identified in the medial Paraguay River, upstream of the confluence with the Taquari River, were likely derived from erosion of lateritic soils in the uppermost regions of the plateau provenance region. Iron-bearing minerals, particularly hematite and goethite, are common in lateritic soils (Madeira et al., 1997). However, the occurrence of gibbsite and goethite was not consistently related to higher or lower kaolinite proportions. This observation suggests that the highest proportions of kaolinite are independent of goethite and gibbsite occurrence.

4.5.1.3 Geological and slope control.

When illite is generated from metamorphic rocks, rapid removal of material is often implicated, which is expected in a tropical environment with heavy seasonal rainfall like the Pantanal (Selvaraj & Chen, 2006; Velde & Meunier, 2008; Wang et al., 2011). The close spatial relationship between illite abundances and the Northern and Southern Paraguay Belt provenance regions suggests a direct contribution from the muscovite-rich greenschist facies (Almeida et al., 1976). The broad spatial occurrence of illite in the Northern Paraguay Belt region is evidence of mechanical bedrock erosion observed in regions of high precipitation (e.g., Liu et al., 2012). Calculation of Fe in the mica structure yielded a relatively high average value of 2.19 (Brown & Brindley, 1980;

89

Deconinck et al., 1988). High Fe availability is a prerequisite for authigenesis of ferric illite (Furquim et al., 2010), consistent with tropical environments that generate extensive iron oxides (Liptzin & Silver, 2009). The largest values for Fe content in illite were mostly concentrated north of the Taquari weathering hinge. The increased distribution of illite in the Northern Paraguay Belt is consistent with present-day weathering conditions.

The weathering of phyllite and amphibolite schist outcrops along the Salobra River, the Miranda River, and the uppermost Apa River are the best candidates for vermiculite generation. Select sampling stations in the Miranda River contain as much as 90% vermiculite, which we attribute to the erosion of adjacent Cuiabá Group phyllites (Lacerda Filho et al., 2006). Dacites such as the Serra Geral Formation in the study area have generated vermiculite clays in other regions (Harvey & Beck, 1962). Illite may also be altered to vermiculite as K is released in the soils, creating an interlayered illite-vermiculite mineral similar to Amazon Basin soils and verified with NEWMOD fitting (Han et al., 2014; Delarmelinda et al., 2017). Sample E1 in the Southern Paraguay Belt region contained an intermediate peak at 11.9 Å suggesting the presence of hydroxy-interlayered vermiculite (HIV), implicating a mixed layer illite-HIV.

The average watershed slope regulates fluvial incision and channel behavior. Steeper slopes favor high weathering rates, incised river channels, and minimal pedogenic development. In contrast, the low-slope floodplains act as temporary sinks for unconsolidated, highly weathered fine sediment subject to fluvial channel migration. The Taquari River at the distal Zé da Costa avulsion (sample A25; Table C.1) contained greater amounts of vermiculite than at the medial Caronal avulsion (samples A26-A27; Table C.1), suggesting that reworked floodplain sediments may be an important

contribution of vermiculite in the distal Taquari River. The exhumation of floodplain deposits can remobilize clays that were deposited during drier Holocene climatic conditions where transformation of clays was less efficient (McGlue et al., 2015, 2017; Novello et al., 2017). Vermiculite is diluted by dominantly kaolinitic tributary inputs when the Taquari River discharges into the Paraguay River.

Clay minerals may represent inherited weathering phases from recycling of more ancient sedimentary rocks that are exhumed to the surface environment (Eberl et al., 1997; Wilson, 1999; Bhattacharyya et al., 2000). For example, inherited clays may come from clay coats that formed prior to lithification of eolian sands into arenites (Wilson, 1992). The Botucatu Formation in the plateau provenance region is an eolian arenite with amorphous silica and kaolinite grain coatings (França et al., 2003; Hirata et al., 2011; Bertolini et al., 2021). The Mesozoic Era was characterized by hothouse conditions (Holz, 2015) that contributed to the generation of kaolinite in the Botucatu Formation (Correa et al., 2021). This formation may have contributed an unknown amount of inherited kaolinite to the silt plus clay fraction recovered in modern river samples (Balan et al., 2007). Inherited kaolinite is commonly more ordered than neoformed kaolinite (Balan et al., 2007; Bauluz et al., 2008), such that higher crystallinity with lower FWHM can indicate inheritance. Samples with the most disordered (neformed) kaolinite (FWHM 0.45 °2θ) were located at the confluence of the Taquari and Paraguay Rivers, where elevations are very low and the annual floodwater inundation period is high (Ivory et al., 2019). Furian et al. (2002) likewise encountered kaolinite in poorly drained areas of the Pantanal. The high levels of kaolinite at the confluence of the distal Taquari River and the Paraguay River further attests to kaolinite authigenesis associated with strong hydrolysis

(Chamley, 1989). Estimating inherited versus neoformed kaolinite remains challenging, because studies such as Balan et al. (2007) examined these processes primarily in soil profiles, not in modern fluvial samples.

4.5.2   *Chemical weathering and mechanical weathering*

Clay minerals generated today across the Pantanal Basin are controlled primarily by climate-induced chemical weathering and secondarily by soil and parent lithology types. Nearly all Rio Apa craton samples were relatively enriched in Na, K, and Al compared to samples from rivers draining the other provenance regions. Similarly, the Amazon craton samples had high relative Na, K, and Al, but less than that of the Rio Apa craton samples. All southern Paraguay Belt samples were enriched in Fe and Ca. Most of the lowland samples were high in Si, reflecting the quartzose nature of muds where repeated cycles of flooding and channel avulsions enhance sediment reworking (e.g., Louzada et al., 2021). The rivers draining provenance regions with the lowest CIA values were the Rio Apa craton and the southern Paraguay Belt, suggesting that the weathering effect for these metamorphic and carbonate rocks was low, most likely due to the reduced mean annual rainfall (~1200 mm/y) (Fick & Hijmans, 2017). These two regions also had WIP >40, indicating reduced quartz recycling relative to the other four provenance regions. Most samples from the Pantanal had CIA 75-95 and had WIP <20, attesting to both high quartz recycling and extensive weathering effects (Figure 4.8B). Our spatial distribution maps show that this effect was most concentrated in the medial Pantanal Basin, supplied mainly by the Cuiabá, São Lourenço, and Piquiri Rivers (Figure 4.9). Maximum quartz recycling and weathering effects in the medial Paraguay River fine fraction samples were consistent with highest quartz compositions near the confluence of

the Paraguay River with the Cuiabá and Taquari Rivers. The lowest WIP values in the basin are linked to the Jurassic-Cretaceous Botucatu Formation and the Cretaceous Bauru Formation quartz arenites of the plateau provenance region, which were highly weathered during deposition. Because quartz arenite weathering contributes little to the clay fraction in extant river muds, we interpret that most of the depletion of mobile ions occurred through kaolinite authigenesis by transformation. This view is consistent with the presence of goethite and gibbsite in unconsolidated sediments of the Botucatu Formation (Fagundes & Zuquette, 2011).

4.5.3   Clay transformation in the Plata River

The clay composition of the Pantanal back-bulge is distinguishable from the Andean foreland basin clays. The Paraguay, Paraná, and Uruguay Rivers are the primary sources of kaolinite to the Plata River estuary (Table C.5), which ranges from 50-75% in the suspended load (Figure 4.12) (Depetris & Griffin, 1968; Manassero et al., 2008). Samples downstream of the Pantanal outlet were commonly 15-20% kaolinite, indicating dilution of the kaolinite by sub-Andes-derived illite. The Bermejo River is an example of concentrated illite supply to the Paraguay River (Bertolino & Depetris, 1992; McGlue et al., 2016; Repasch et al., 2021). Bermejo clays were <5% kaolinite near the thrust front, and the kaolinite remained <5% as far as 40 km downstream (Bertolino & Depetris, 1992). Illite comprised ~60% of clay composition throughout the length of the Bermejo River to its confluence with the Paraguay River. Other rivers such as the Pilcomayo and the Salado Rivers that drain the Andean thrust belt were similarly enriched in illite (Bertolino & Depetris, 1992; McGlue et al., 2016). We ascribe the dilution of kaolinite in the Paraguay and Paraná Rivers to these illite-rich clay compositions draining the Andean

foothillls. The back-bulge and interior craton are dominated by kaolinite, thereby creating ancient wetland deposits that are also rich in kaolinite (e.g., Tineo et al., 2022). In contrast, the thrust front sediments are dominated by illite and smectite, with the latter influenced by the dry climate of the Chaco Seco (McGlue et al., 2016).

We find that the dominantly kaolinite clay composition at the Pantanal outlet is controlled by climate > soil > lithology. We interpret that because vermiculite clays were not present in downstream clay fractions, this observation suggests that vermiculite might be diluted as it exits the Pantanal Basin. In addition to the illite dilution effect, we identify three potential factors for the rapid change in clay composition. First, the decreased kaolinite in the Paraguay and the Paraná Rivers roughly coincide with the boundary between tropical savanna climate (Aw) and the humid subtropical (Cfa) zones (Beck et al., 2018). Campodonico et al. (2016) demonstrate that the CIA decreases downstream in the higher latitude and sub-tropical climate regions. Second, the adjacent lithologies may be supplying illite locally to the fluvial clays. Locally eroded illite was added to the Paraguay River as it flowed past the Rio Apa craton, which diluted the sediment samples with more illite and vermiculite. The lower Paraguay River flows adjacent to the Carboniferous Coronel Oviedo Group, consisting of shale, arenite, diamictite, and glacial tills (Orué, 1996). Third, kaolinite-rich clays might be preserved near the wetland but not preserved in much farther downstream sediments. Further systematic investigations of downstream clay compositions and heavy mineral suites to constrain the controls on clay composition in the entire Plata River catchment is warranted. This study of modern fluvial clays is an important contribution to our understanding of the distribution of clays in modern river sediments provides a key

source of information to improve the accuracy of global clay distribution models (Ito & Wagai, 2017; Warr, 2022).

4.6   Conclusions

This study of modern fluvial clays plus silt from 74 sampling sites revealed the spatial distribution of clay minerals and major fine-fraction chemical elements across an extant tropical back-bulge basin. Mineralogy and chemical weathering indices (CIA and WIP) showed distinct areas of clay generation among the provenance regions. The controls on fine-fraction mineralogy were systematically assessed, and the implications for the downstream fine sediment in the Plata River were summarized.

1. The clay proportions were kaolinite > vermiculite > illite > smectite, but these clays are not evenly distributed. The Taquari River forms a prominent E-W trending hinge across the Pantanal Basin, where more intensive leaching and authigenesis produce more kaolinite north of the river. Vermiculite was more common south of the Taquari River, and illite was most common along the Northern Paraguay Belt. Gibbsite and goethite in the clay-sized fraction signaled contribution from heavily weathered soils such as laterites.

2. Major elemental geochemistry of the clay plus silt was used to calculate average CIA = 76.4 and average WIP = 27.6 throughout the Pantanal. The medial Pantanal Basin is highly weathered at the confluence of the Taquari and Paraguay Rivers, representing the cumulative weathering effects of the northern Pantanal. The southern Pantanal fine sediments along the Rio Apa craton and the Southern Paraguay Belt were poorly weathered, displaying

greater values of CaO, Na$_2$O, and K$_2$O consistent with climate and parent rocks.

3. The main controls on modern fluvial clay plus silt were climate > soil > parent rock. This interpretation was supported by the Taquari River weathering hinge, where kaolinite-rich clays north of the river were linked to greater precipitation and shorter dry season. This same region also contained more kaolinite-rich soils such as acrisols and ferralsols. In contrast, mollisols and luvisols coupled with reduced precipitation and longer dry seasons in the southern Pantanal allowed for more detrital clays: illite and vermiculite. Illite was especially linked to low-grade metamorphic lithologies present only in the Paraguay Belt.

4. The Pantanal Basin's clay mineral composition near the basin outlet is primarily kaolinite and vermiculite, contrasting sharply with detrital back-bulge clays from the sub-tropics (Bermejo, Pilcomayo, etc.), which are dominated by illite and smectite. The illite transported from the sub-Andean regions significantly dilutes the proportion of kaolinite in the Plata River. This composition likely generates distinct mudstones in the rock record, with implications for interpretations of the rock record.

4.7 Acknowledgments

4.8 Tables and Figures

Table 4.1 Summary statistics for the corresponding provenance regions: lowlands (A), Amazon craton (B), Rio Apa craton (C), plateau (D), Southern Paraguay Belt (E), and Northern Paraguay Belt (F). Average smectite values were not determined due to occurrence in specific sampling stations.

Area	SiO_2 wt%	Al_2O_3 wt%	Fe_2O_3 wt%	K_2O wt%	Na_2O wt%	CaO wt%	MgO wt%	Kao	Illite	Verm	CIA	WIP
A: Lowlands	71.8	15.0	5.6	1.7	0.1	0.4	0.8	56	5.6	35	85.0	18.0
Comments: kaolinite comprised 50-60% of the Paraguay River clays near the basin outlet. Vermiculite composed >30% of the lowland clays downstream of the Rio Apa craton.												
B: Amazon craton	64.1	18.4	7.4	2.1	0.4	1.1	0.9	51.3	16	32.6	78.7	27.2
Comments: vermiculite varied 15-59%, and illite ranged 7-36%.												
C: Rio Apa craton	64.8	18.2	5.7	3.3	0.8	1.5	0.8	31.4	18.9	38.8	71.3	41.2
Comments: smectite was common where volcanic rocks formed 16% of the watershed. Kaolinite was most common in the sample where foliated metamorphic rocks were the single largest constituent lithology.												
D: Plateau	66.6	13.5	9.5	1.6	0.1	1.0	0.9	41.5	12.1	46.7	79.4	19.2
Comments: Clay assemblages in the Miranda River watersheds were almost dominantly vermiculite. Two sampling stations may drain the same siliciclastic lithologies but produce vastly different proportions of kaolinite, for example.												
E: Southern Paraguay Belt	59.3	12.5	5.5	1.7	0.1	18.7	1.3	18.5	30.3	51.2	34.6	66.4
Comments: kaolinite reached the lowest proportions of any area in the Pantanal. Biochemical lithologies were the main parent rock of the watersheds, but clay assemblages were more commonly controlled by the adjacent metamorphic lithologies.												
F: Northern Paraguay Belt	68.1	15.3	7.2	2.5	0.1	0.3	1.1	37.3	42.6	20.2	81.4	25.8
Comments: many simples contained >50% illite, which exceeds all other regions in the Pantanal.												
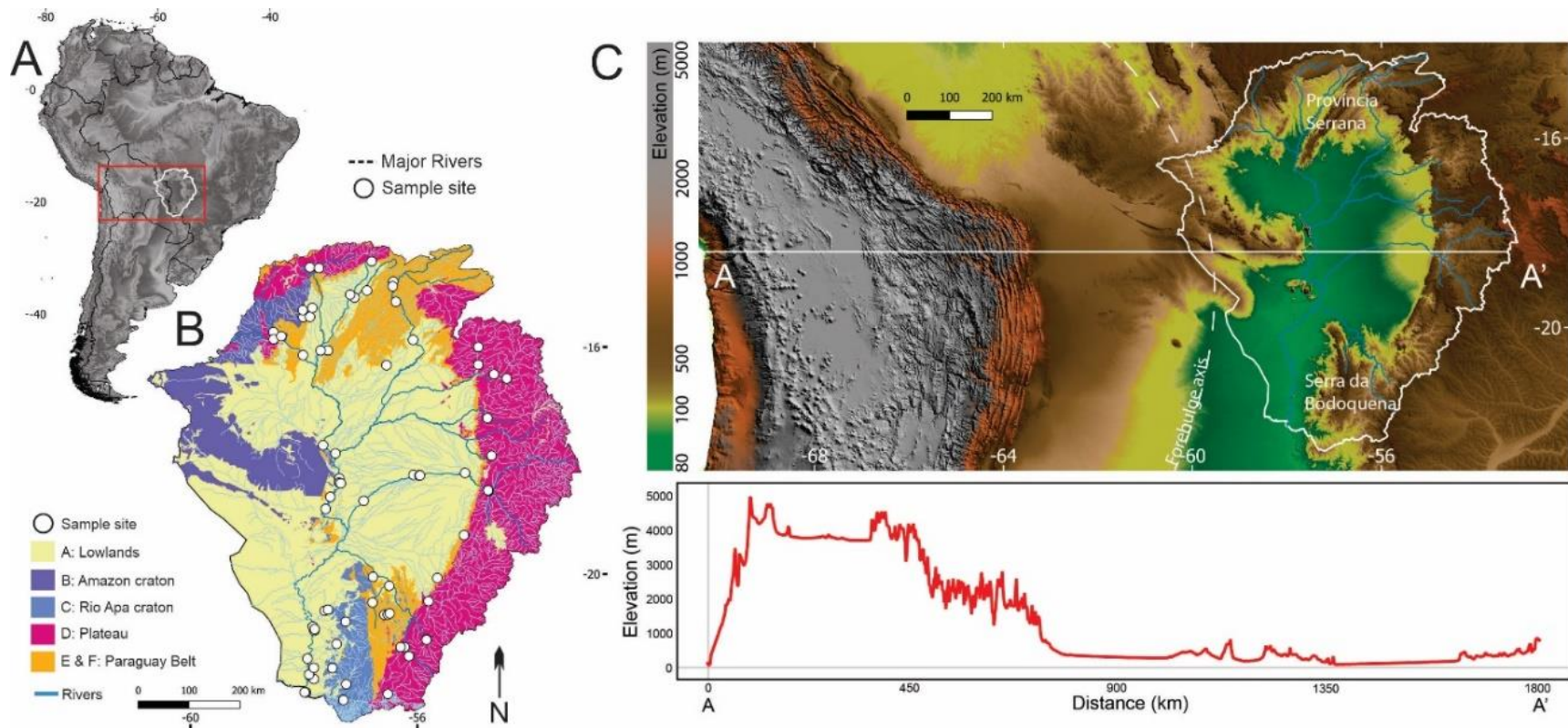
Figure 4.1 Paraguay Basin provenance regions and topography. A) Upper Paraguay River Basin (white outline) in South America. Red box denotes area shown in panel C. B) Pantanal Basin sediment generation (provenance) regions with major rivers (blue lines). Much of the areas covered at the surface by wetlands are designated as lowlands, in contrast with the fringing cratons and the plateau. C) GTOPO30 digital elevation model of South America (USGS, 1996), including a simplified topographic cross-section A-A' from Google Earth©. Modified from Lo et al. (*in review*).
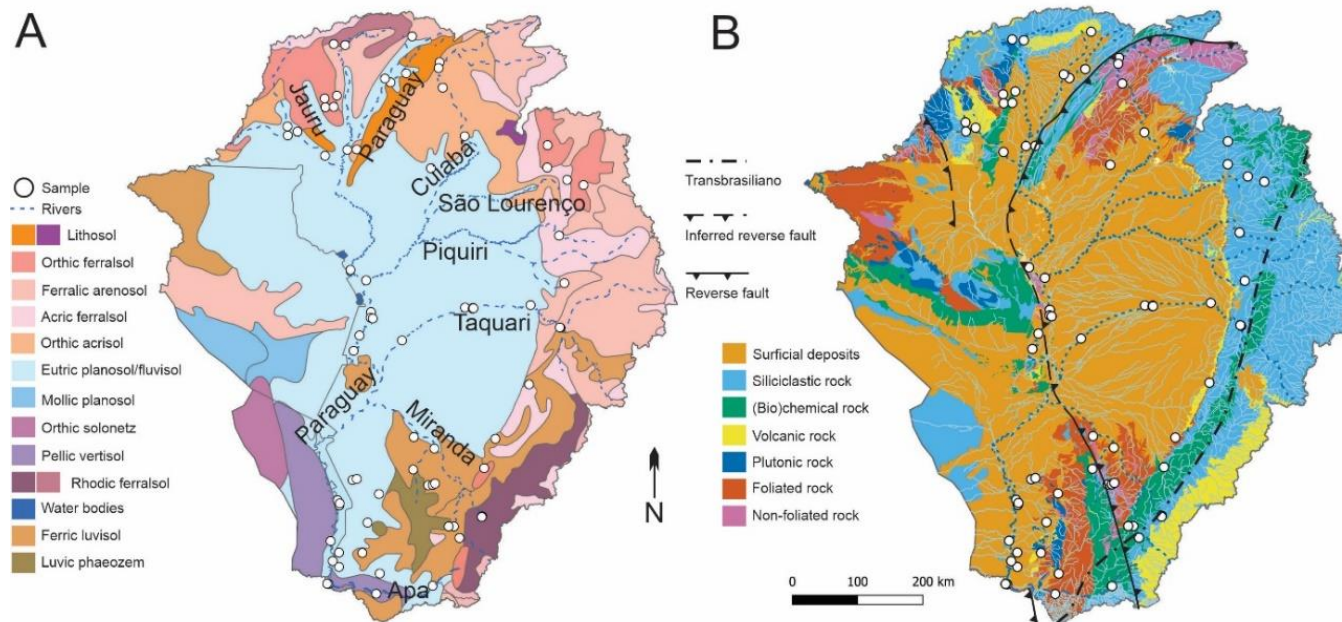
Figure 4.2 Pedology and lithology maps. A) Soil map for the Pantanal Basin (FAO, 1970). The most widespread soil classes are eutric planosol/fluvisol in the lowlands (Benedetti et al., 2011). B) Geology of the Pantanal Basin and drainage network, with major faults in the region. The plateau is dominated by siliciclastic sedimentary rock, whereas metamorphic rocks are restricted to the cratons and Paraguay Belt. Geologic information was obtained for Bolivia (Dirección de Ordenamiento Territorial, Gobierno Autónomo Departamental de Santa Cruz), Paraguay (Vice Ministerio de Minas y Energía), and Brazil (Serviço Geológico do Brasil, CPRM). Faults are based on published studies (Rizzotto & Hartmann, 2012; Warren et al., 2015; Faleiros et al., 2016; Barboza et al., 2018; Rivadeneyra-Vera et al., 2019; Cedraz et al., 2020). Modified from Lo et al. (*in review*).
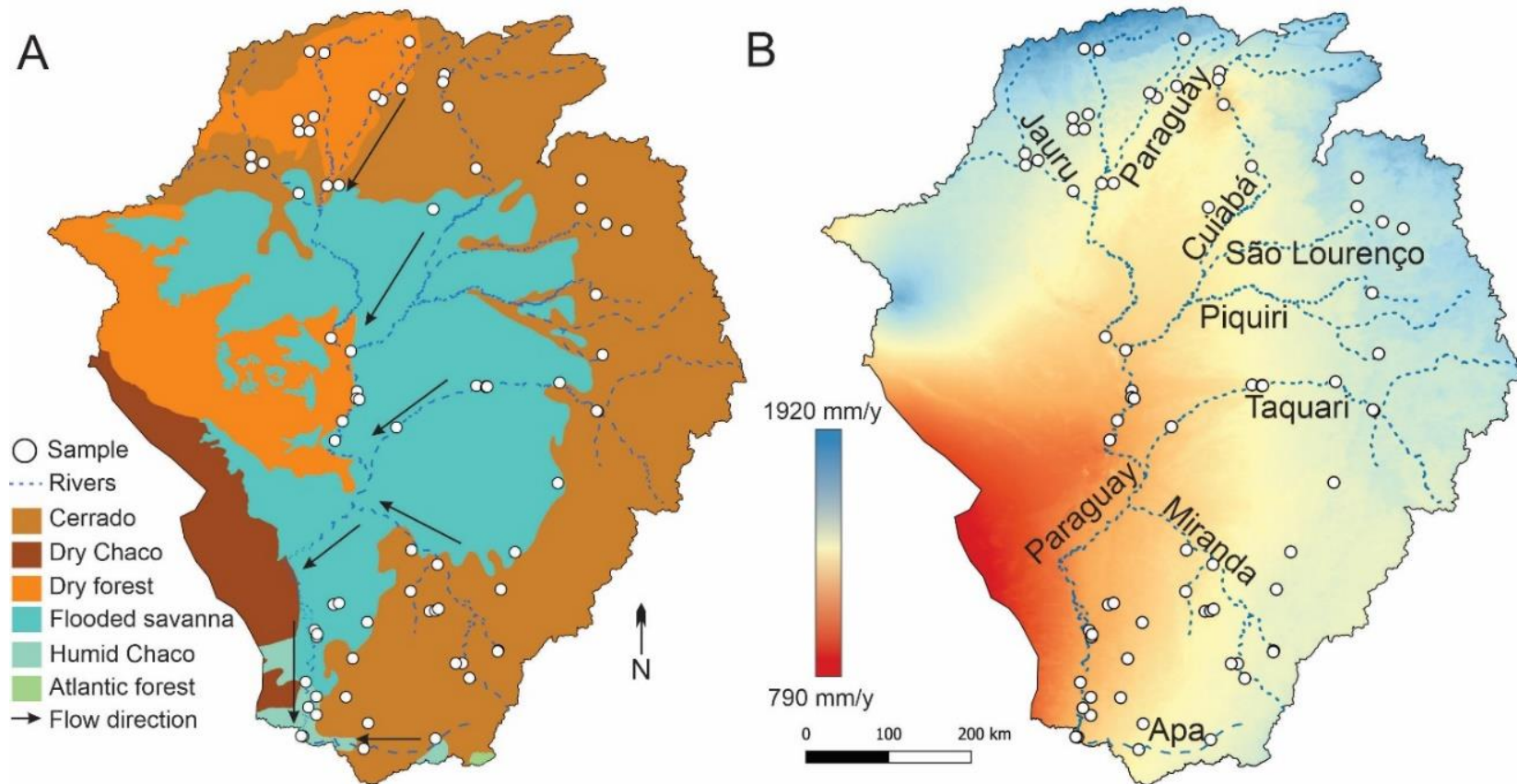
Figure 4.3 Vegetation and mean annual precipitation maps. A) Vegetation ecoregions regions of the Pantanal Basin (Olson et al., 2001). The primary vegetation of the Pantanal consists of flooded savanna and *cerrado* (tropical savanna). B) Mean annual precipitation (mm/y) from WorldClim database (Fick & Hijmans, 2017). In the Brazilian Pantanal, the precipitation is 970-1850 mm/y. Modified from Lo et al. (*in review*).
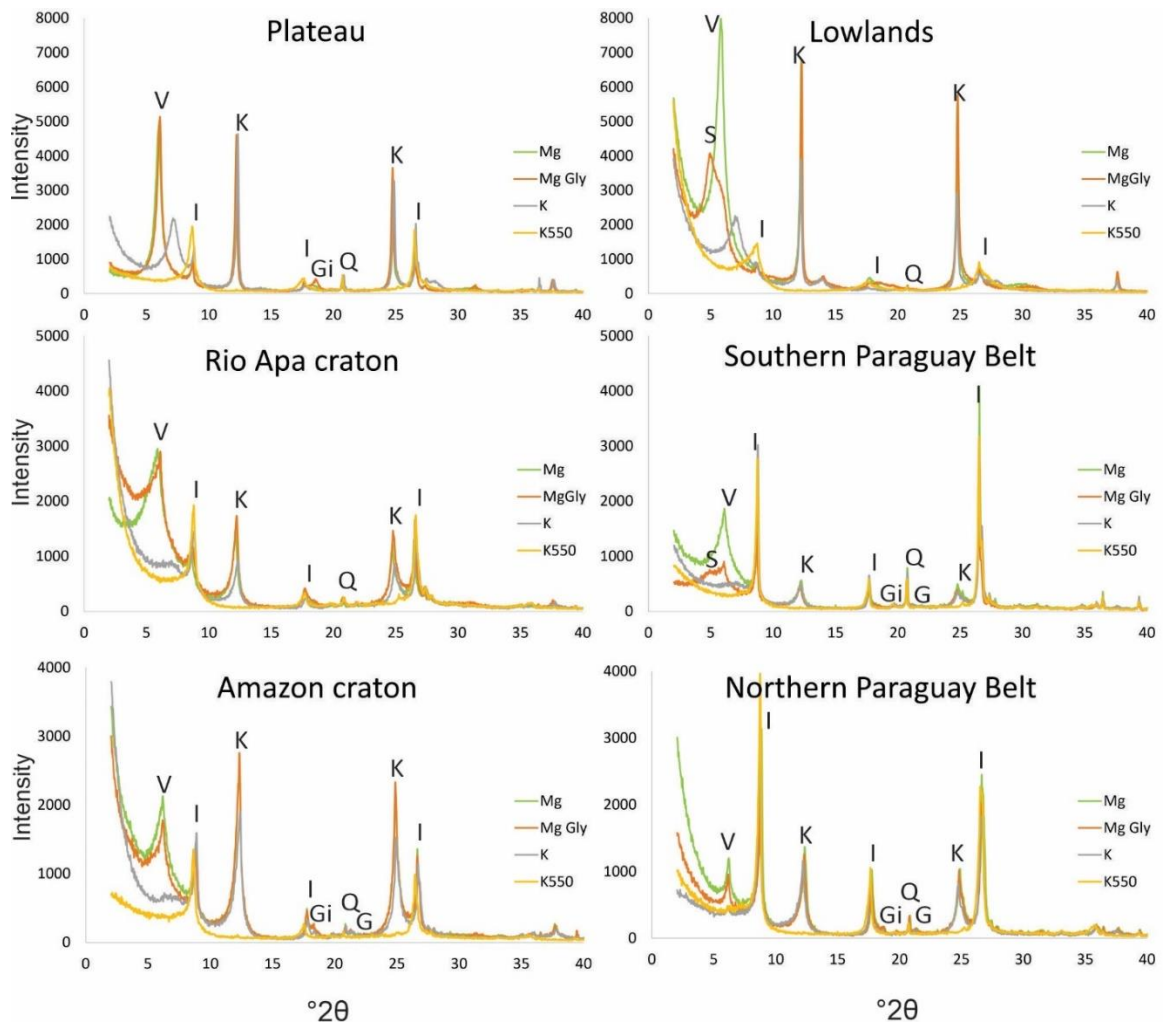
Figure 4.4 Representative X-ray diffractogram patterns from oriented clay mounts using diagnostic treatments of Mg-, Mg-glycerol, K-25°C, and K-550°C for the six provenance regions detailed in Figure 1B. The diagnostic peaks are labeled for quartz (Q), kaolinite (K), illite (I), smectite (S), vermiculite (V), goethite (G), and gibbsite (Gi).
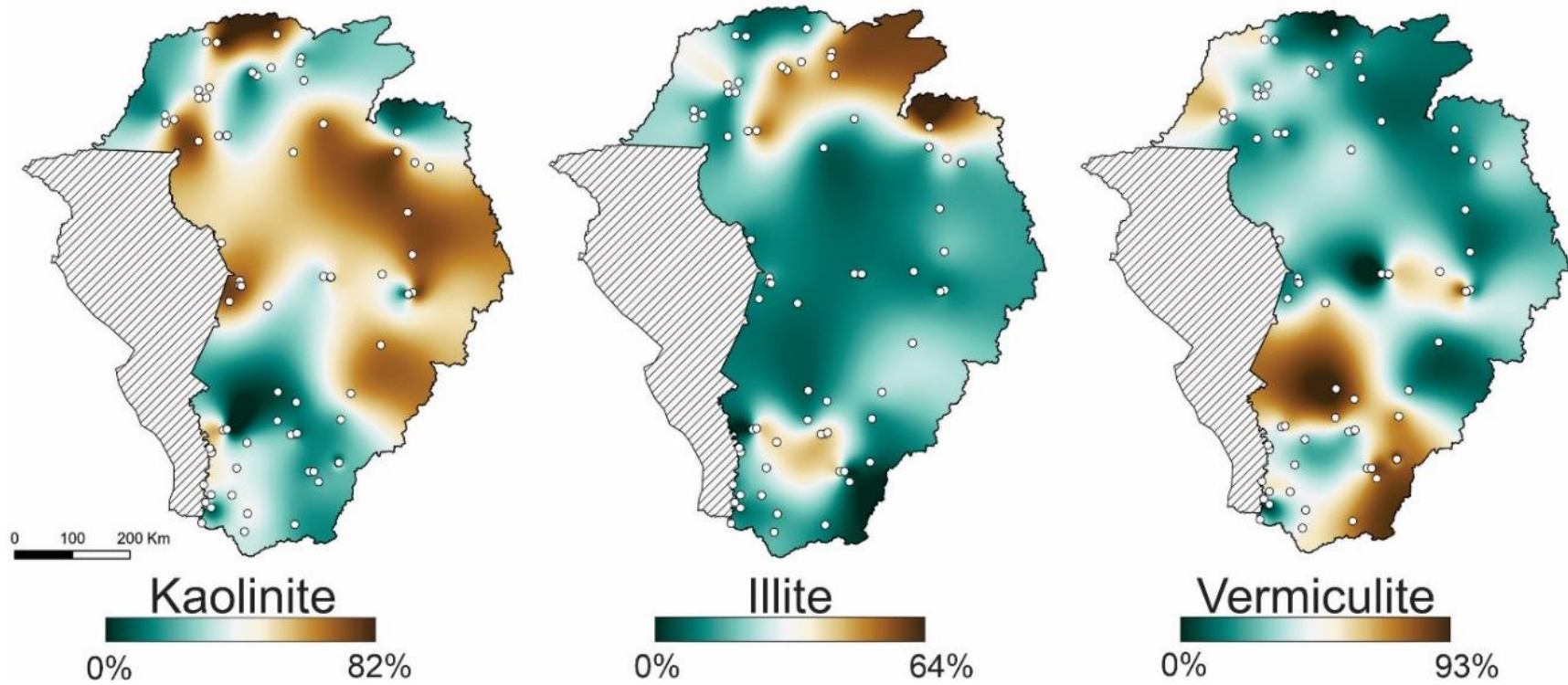
Figure 4.5 Spatial interpolation maps of the major clay mineral constituents at 71 sampling stations in the Pantanal. For each sampling station, the composition was normalized to 100 based on the kaolinite, illite, and vermiculite percent estimates. Interpretation was not extended to hashed areas.
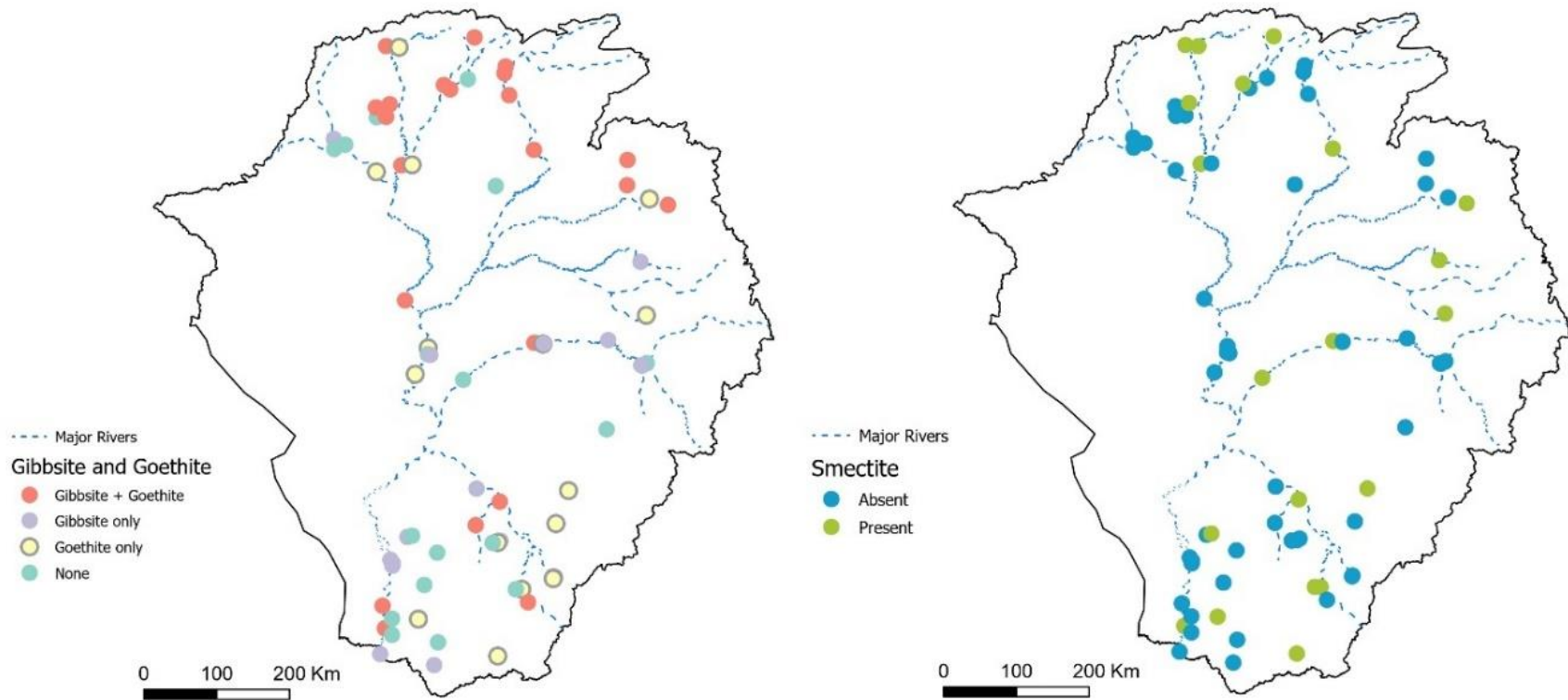
Figure 4.6 Presence of gibbsite, goethite, and smectite in the Pantanal. A) Basin-wide map of gibbsite and goethite among 71 stations. Red (gibbsite + goethite), purple (gibbsite), yellow (goethite), and green (neither). B) Map of smectite in the Pantanal marked as blue (no smectite) or green (smectite present). These maps did not account for the intensity or crystallinity of the mineral peaks.
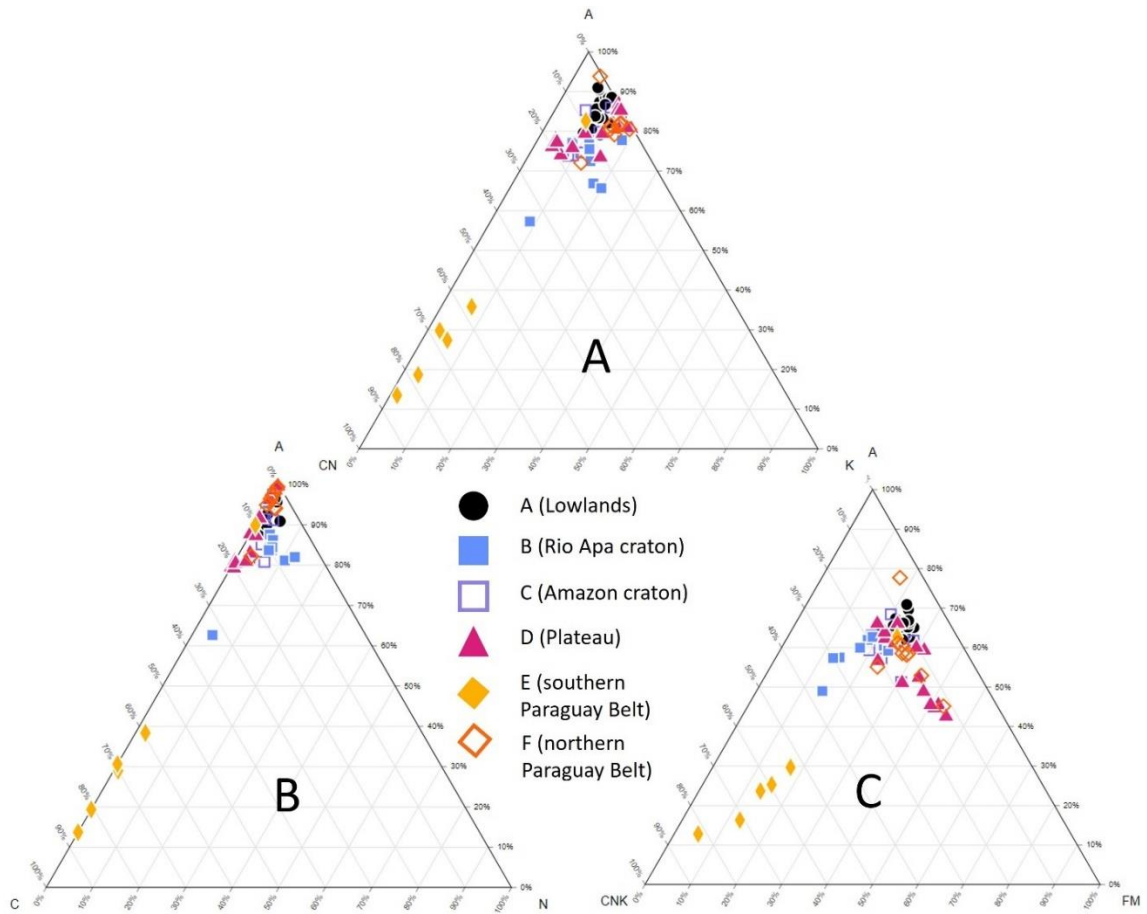
Figure 4.7 Major elemental compositions of fluvial sediments ($n = 66$) plotted as molar proportions on Al_2O_3-CaO-Na_2O (ACN), Al_2O_3-$(CaO + Na_2O + K_2O)$-$(Fe_2O_3 + MgO)$ (ACNKFM), and Al_2O_3-$(CaO + Na_2O)$-K_2O (ACNK). The ACN and ACNK plots form a linear array with southern Paraguay Belt samples closer to the C and the CN pole, respectively. Most mud samples rich in non-mobile Al plot closer to the A pole. The ACNKFM plot helps distinguish the Mg-rich samples.
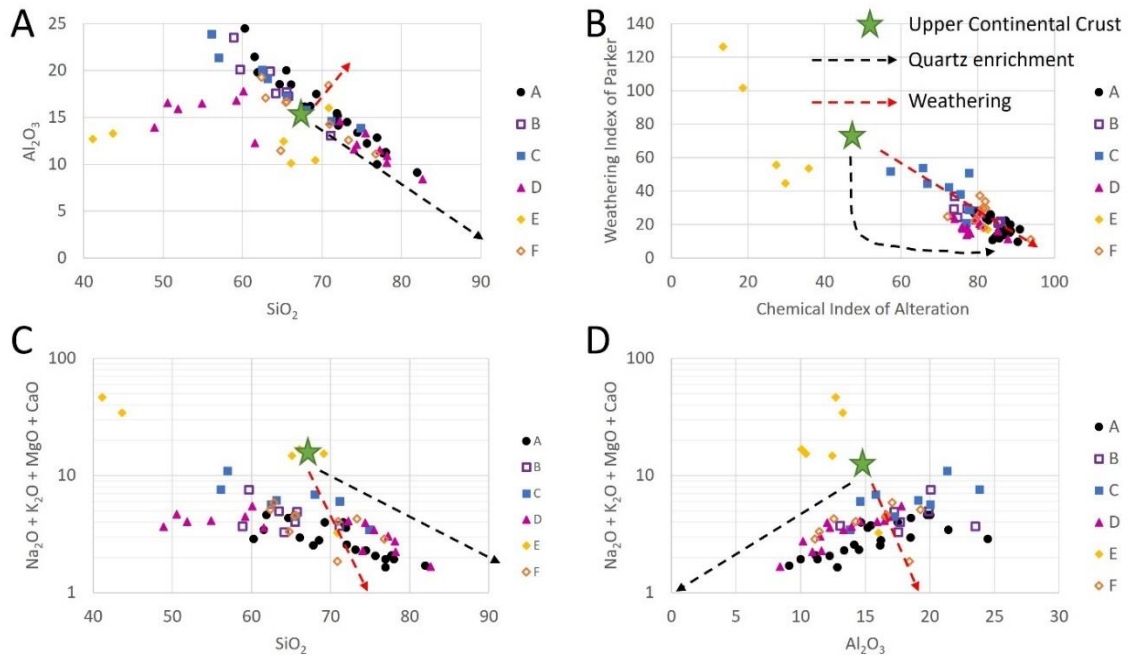
Figure 4.8 Geochemical discrimination plots are useful to separate effects of weathering and quartz recycling relative to the upper continental crust (UCC; green star) standard (S. R. Taylor & McLennan, 1995). Quartz addition is interpreted as the progressive addition of SiO_2, and chemical weathering is the progressive removal of mobile metals assuming Si and Al are immobile (Garzanti et al., 2010, 2011, 2012). The Al_2O_3/SiO_2 plot shows a quartz enrichment patterns for about half of the samples. The two lower plots suggest weathering control and only weak quartz enrichment. All regions here are consistent with the areas defined in Figure 1. The quartz enrichment and weathering trends are approximate in C and D due to the logarithmic scale on the y-axis.

Chemical Index of Alteration

- 13-68
- 69-80
- 81-82
- 83-94

Weathering Index of Parker

- 0-19
- 20-25
- 26-47
- 48-129
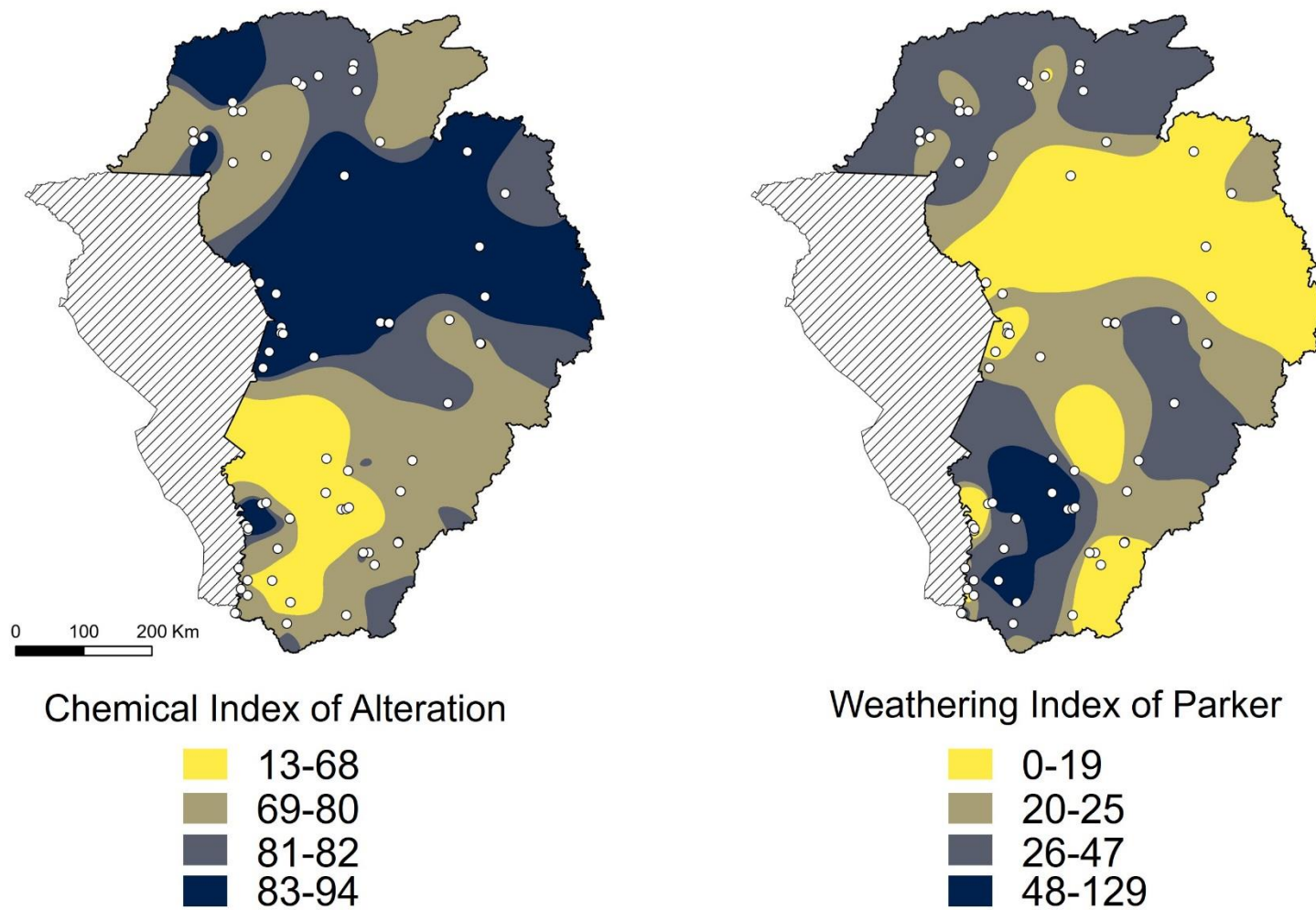
Figure 4.9 Spatial interpolation maps of chemical weathering indices based on the molar proportions of the major elemental data from 66 sampling stations.
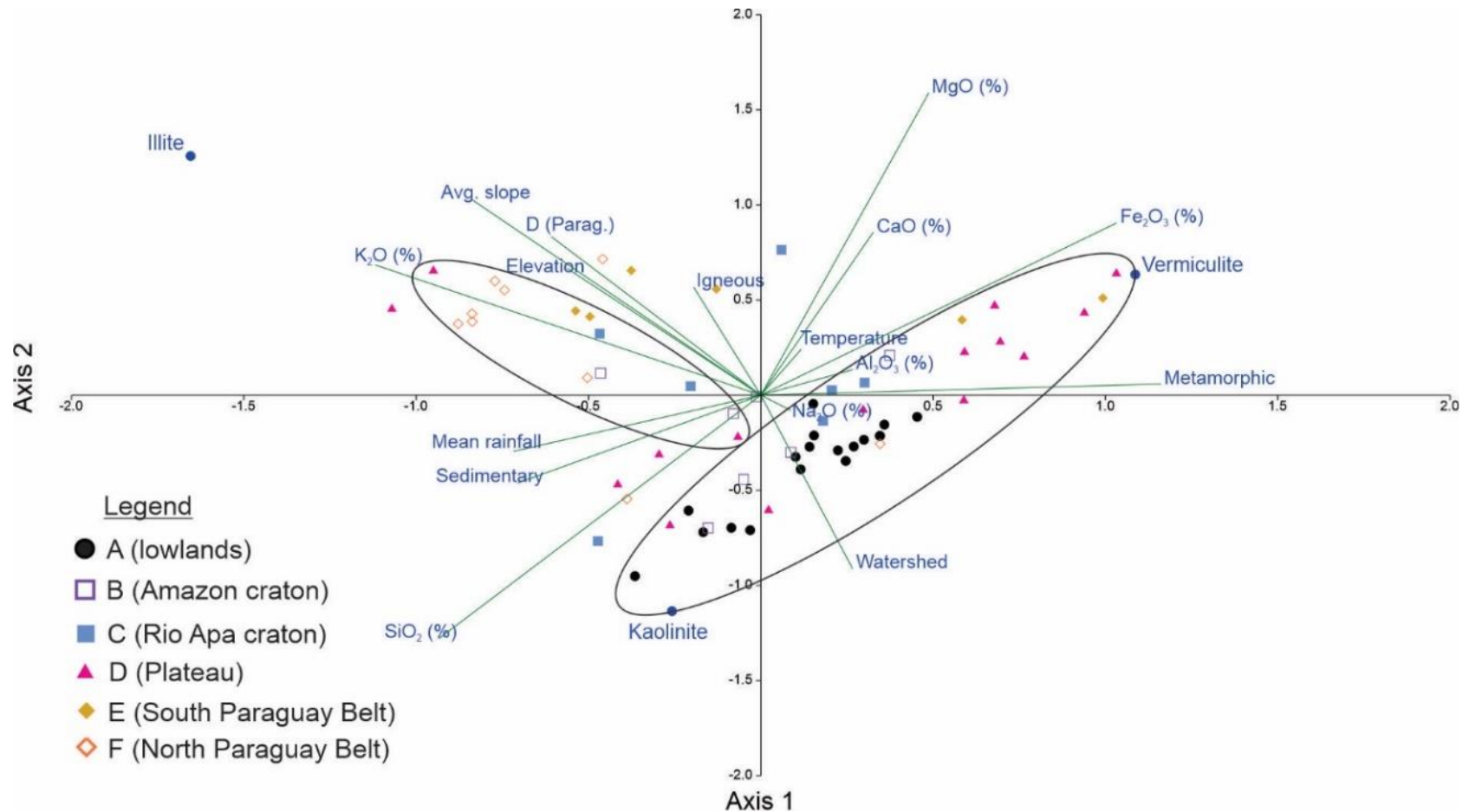
Figure 4.10 Canonical correspondence analysis shows that the southern and northern Paraguay Belt areas are enriched in K_2O, whereas the sampling stations in the Miranda River basin in the plateau region are enriched in Fe_2O_2 in the first axis. In the second axis, most of the Rio Apa craton and Paraguay Belt sampling stations show enriched MgO and CaO.

Figure 4.11 Uppermost hinterland of the Taquari River watershed consists of (A) deeply incised gullies facilitating sediment export to the lowlands. The surfaces are commonly characterized by friable iron-rich concretions (B, C, D). Photo credits: ELL on June 13, 2015.
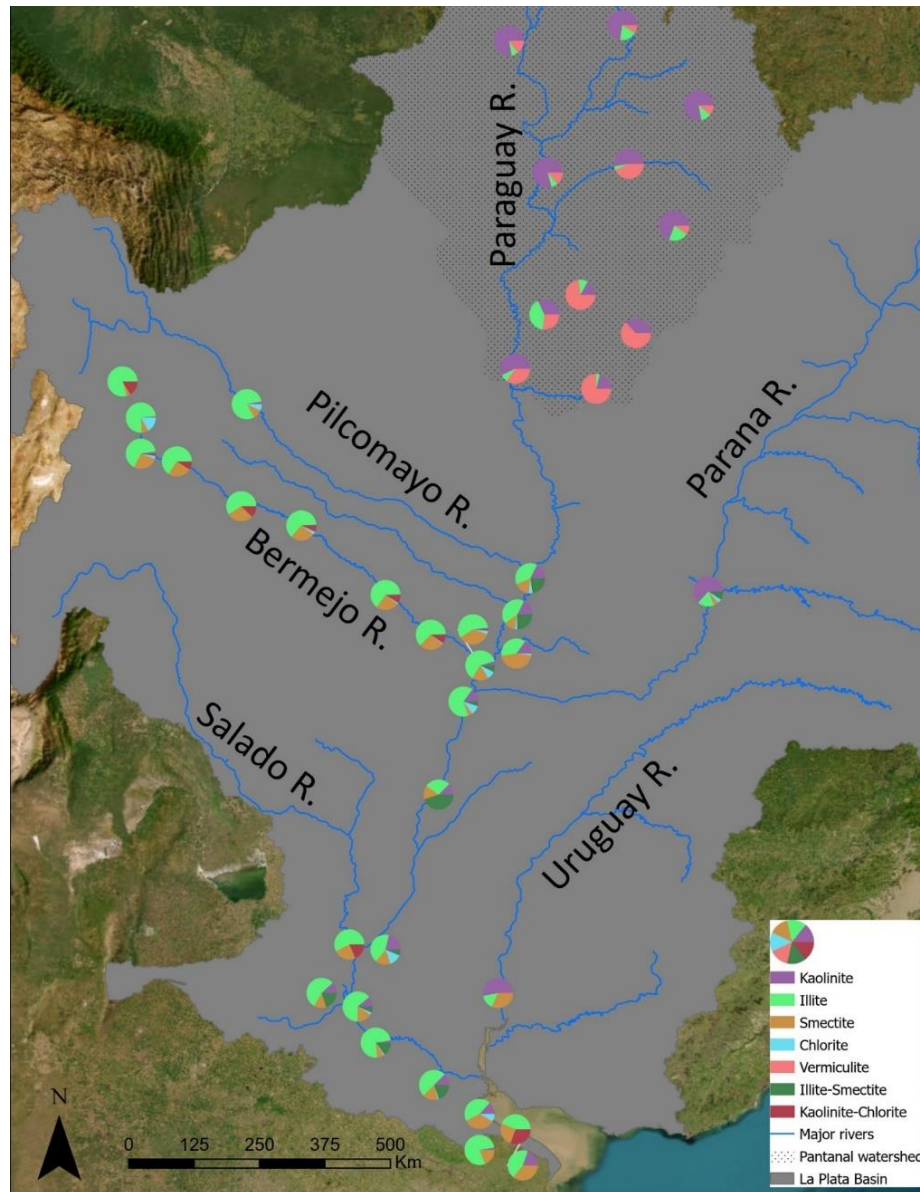
Figure 4.12 Summary of mud transport from the Paraguay River to the confluence with the Pilcomayo, Bermejo, Paraná, and Salado Rivers to the Plata River mouth. Data (*n = 84*) from past studies (Depetris & Griffin, 1968; Bertolino & Depetris, 1992; Ronco et al., 2001; Manassero et al., 2008; McGlue et al., 2016) (Table C.5). Pantanal samples in the hatched area are from this study. The Plata River watershed was downloaded from the Transboundary Freshwater Dispute Database (Oregon State University), and the rivers were obtained from the HydroSheds database (Lehner et al., 2008).

110

CHAPTER 5. CONCLUSIONS

This study demonstrated that ecosystem services are becoming rapidly reduced in lakes and rivers due to increased sedimentation. Chapter 2 showed that accelerated sedimentation was occurring throughout shallow tropical floodplain lakes. Although natural systems are highly complex, our multivariate statistics identified high slopes, tree loss, and population density as drivers for the most drastic changes to sedimentation rates in the past 50 years. The dataset suggests that complete infill of some tropical lakes will occur in as little as a few centuries, in contrast with other extratropical lakes. These conclusions carry important implications for water and sediment management in the low latitudes, many of which are located in developing nations.

Chapters 3 and 4 consisted of sediment mineralogical analyses to identify the main controls on sediment production in the tropics, focused on the Pantanal Basin. Most floodplain sands are quartzose non-orogenic detritus where the %Quartz\Feldspar\Lithic was 88\5\7 with more lithic grains from rivers draining the Paraguay Belt. K-feldspars >30% occurred downstream of foliated metamorphic Rio Apa lithotypes. Our set of sand petrography data showed key controls on the production of sands: parent rocks > mean annual precipitation. The watershed slope, temperature, and effects of dilution also provided supporting roles in the spatial distribution of dominant sands. In contrast, our clay mineralogy and fine-fraction geochemistry indicated the following controls: mean annual precipitation > soil > parent rocks. The abundance of clay minerals follows the rank order of kaolinite > vermiculite > illite > smectite. Sampling sites with the most quartzose sands in the medial Pantanal contained greater kaolinite abundance, thereby defining the Taquari River weathering hinge. Clays in the north-central Pantanal

contained more kaolinite abundance, whereas those in the southern Pantanal contained more vermiculite, downstream of dacitic parent rocks and rhodic ferralsols. Illite abundance was highest in rivers draining the Paraguay Belt, suggesting high rates of mechanical weathering and parent rock control.

The information provided by these fundamental studies sets the foundation for a more systematic, year-long sediment budget study that can provide critical estimates of the volumetric supply of suspended and bedload sediments in the Pantanal. The global tropics desperately require more long-term scientific attention to address climate change impacts to vulnerable communities.

APPENDICES

APPENDIX A SUPPLEMENTAL MATERIALS FOR CHAPTER 2

Table A.1

Lake	Latitude	Longitude	Rate (mm/yr)	Model	Wetzel lake	Lake area (km^2)	Depth (m)	Max/avg depth
Cashu	-11.882931	-71.409471	1.28	14C	Oxbow	0.625	2.2	Max
Totora	-11.882639	-71.391861	0.88	14C	Oxbow	0.625	2.2	Max
Tres Chim.	-12.788719	-69.33627	8.2	14C	Oxbow	0.5	2.8	Max
Tambopata	-12.805165	-69.28169	1.14	14C	Oxbow	0.04	1.5	Max
Amapa	-10.045417	-67.855056	0.95	14C	Oxbow	0.15	3.1	Avg
Lake 1	-18.402761	-54.979573	6.4	CRS	Oxbow	0.9	2	Avg
Lake 2	-18.361968	-54.993931	3.9	CIC	Oxbow	0.2	2	Avg
Lake 3	-18.367923	-55.005744	4.9	CIC	Oxbow	0.25	2	Avg
Marcio	0.128028	-51.079944	0.65	14C	Dish	0.105	2.5	Max
Jacadigo	-19.2061	-57.8167	2.46	CRS	Dish	24	2.6	Max
Chaplin	-14.466667	-61.066667	0.07	14C	Dish	12	2.5	Max
Bella Vista	-13.616667	-61.55	0.1	14C	Dish	24	2.5	Max
Tele, Congo	1.342898	17.155804	0.13	14C	Dish	23	2.5	Max
S. da Ponta	-18.98333333	-56.65972222	0.2	14C	Dish	0.19	2.5	Max
S. Babaçu	-18.928776	-56.55074	0.15	14C	Dish	0.14	2.5	Max
S. do Meio	-18.97472222	-56.64638889	5.9	CRS	Dish	0.1	3.5	Max
Nguengue	3.768944	18.12169	1.54	CIC	Dish	0.14	2.3	Max
Nhauhache	-21.980528	35.294066	0.98	14C	Dish	0.02	2.2	Avg
Caracaranã	3.844444	-59.780556	0.2	14C	Dish	0.7	5	Max
Santa Ninha	-2.12	-55.44	0.48	14C	Channel	154	5.5	Max
Caçó	-2.961204	-43.251279	0.15	14C	Channel	2.5	10	Max
Waigani	-9.372901	147.184063	1.2	14C	Channel	1.2	1.5	Avg
Quistococha	-3.830068	-73.320073	0.43	14C	Channel	1	3.2	Avg
Tembladera	-3.49125	-79.994444	3.46	CRS	Channel	1	8	Max
San José	-14.9495	-64.495	0.15	14C	Channel	14	1	Max
Sele, Benin	7.155358	2.440436	1.66	14C	Channel	1	1.5	Avg
Sinnda	-3.835556	12.804167	0.62	14C	Channel	1	4.7	Max
Tapajós	-2.775833	-55.082778	3.7	14C	Channel	2200	2.5	Avg
Daviambu	-7.60146	141.262021	0.02	14C	Channel	11.68	1.1	Avg
Bai	-7.367	141.183	0.06	14C	Channel	8.5	1.7	Avg
Yaguaru	-15.601893	-63.21001	0.46	?	Channel	2.5	4	Max
Xingu	-2.556209	-52.016087	1	OSL	Channel	1180	13	Max
Bera	3.12881	102.606518	6.4	CRS	Channel	0.54	3.5	Avg
Curuça	-0.766667	-47.85	0.07	14C	Channel	0.15	2	Avg
Mandioré	-18.18277	-57.524888	0.2	14C	Channel	148	3	Avg
Castelo	-18.533333	-57.566667	0.18	CRS	Channel	20	7.3	Max
Acarabixi	-0.345833	-64.498889	0.32	14C	Channel	0.4	2	Avg
Grande Curuai	-2.23	-55.32	13.4	CF:CS	Channel	1560	6.5	Max
Las Matas	18.039589	-94.510795	3.43	CF:CS	Channel	0.3	1	Avg
Negra	-19.08	-57.52833333	2.5	CRS	Channel	9	2.3	Max
Gaíva	-17.7575	-57.71916667	0.1	CRS	Channel	94	4.7	Max
Jacaretinga	-3.224968	-59.806838	4.9	?	Channel	0.05	5.5	Max
Caranã	-2.835556	-55.0425	0.24	CRS	Channel	0.2	3	Avg
Duas Bocas	1.540115	-50.820211	1.4	CF:CS	Channel	10.7	2.5	Avg
Kitina	-4.266202	11.996729	1	14C	Channel	3.4	4.5	Max
Gbali	4.818521	18.262776	5.07	CIC	Channel	0.02	2	Max
Doukoulou	4.252757	18.423595	2.16	CIC	Channel	0.36	2.35	Max
Canto Grande	-19.268474	-39.933275	0.12	14C	Channel	2.2	3	Avg
Pemerak	0.775413	112.035545	0.03	14C	Blocked valley	1	7	Avg
Calado	-3.266667	-60.583333	1.27	14C	Blocked valley	5	1.5	Avg
Nguène	-0.2	10.466667	0.9	14C	Blocked valley	2.7	5	Max
Lungue	-24.762212	33.63577	2.24	14C	Blocked valley	4.5	1.4	Max

Bosset	-7.226237	141.102591	0.09	14C	Blocked valley	16.8	2.4	Avg
Kai	-7.025751	141.033198	0.06	14C	Blocked valley	13.75	2.6	Avg
Tonle Sap	12.927639	104.053674	0.5	14C	Blocked valley	2500	7.5	Avg
Mitsinjo	-16.033333	45.85	1.36	14C	Blocked valley	12.5	2	Avg
Ossa	3.776721	10.016328	1.03	14C	Blocked valley	37	7	Avg
Maridor	-0.169583	9.357595	1	14C	Blocked valley	0.09	3	Max
Chini	3.421933	102.926198	4.2	CRS	Blocked valley	2	2.7	Max
Vellayani	8.432861	76.990961	0.43	14C	Blocked valley	3.975	5	Avg
Cristalino	-3.130076	-60.166539	5	?	Blocked valley	0.02	7.5	Avg
Macuco	-19.039082	-39.952385	0.25	14C	Blocked valley	1.4	3	Avg
Uberaba	-17.436	-57.748	2.8	CRS	Distal	258	3.5	Max
Melintang	-0.300575	116.351503	1.15	14C	Distal	77	5	Max
Cáceres	-18.961155	-57.77072	0.17	14C	Channel	31	3.2	Avg
Paca	-8.486266	-63.478636	1.7	CRS	Channel	0.11	10	Avg
Rogaguado	-12.988347	-65.989676	0.23	14C	Channel	315	2.5	Avg
Coari	-4.448901	-63.490981	3.89	14C	Channel	386	4.05	Max
Acara	-3.670903	-62.648194	3.5	14C	Channel	91	1.8	Avg
Brasileira	-8.49274	-63.489579	9	CRS	Oxbow	0.48	7.5	Avg
Tucunaré	-8.408496	-63.400219	6	CRS	Dish	0.05	7.5	Avg
Araçá	-8.469341	-63.506702	12.1	CRS	Channel	0.46	7.5	Avg
Nazaré	-8.157482	-63.326827	2.7	CRS	Channel	0.3	7.5	Avg
Santa Catarina	-8.257066	-63.200983	16.7	CRS	Blocked valley	2.44	10	Max
Conceição	-8.247439	-63.190879	8.6	CRS	Channel	0.45	7.5	Avg
Demarcação	-8.131592	-62.809991	5.4	CRS	Channel	1.66	7.5	Avg

Table A.2

Lake	Elevation (m amsl)	Distance from channel (km)	Avg. slope (degrees)	Annual Rainfall (mm)	Tree loss (value of 0-1)	Pop. Density	Infill time (yrs)	Reference
Cashu	329	1	9.1	2167	0.003	0.392	1719	(Räsänen et al., 1991)
Totora	332	1	9.1	2167	0.003	0.392	2500	(Räsänen et al., 1991)
Tres Chim.	195	1.5	13.4	2167	0.01	3.669	341	(Räsänen et al., 1991)
Tambopata	210	0.4	13.4	2167	0.01	3.669	1316	(Erwin, 1984; Räsänen et al., 1991)
Amapa	137	1.1	4.2	1998	0.072	6.58	3263	(Keppeler & Hardy, 2002; Rodríguez-Zorro et al., 2015)
Lake 1	185	0.4	4.5	1440	0.053	3.783	313	(Godoy et al., 2002)
Lake 2	183	0	4.5	1438	0.053	3.783	513	(Godoy et al., 2002)
Lake 3	184	0	4.5	1440	0.053	3.783	408	(Godoy et al., 2002)
Marcio	3	2	1.3	2550	0.01	637.421	3846	(Toledo & Bush, 2008)
Jacadigo	81	50	2.7	998	0.05	8.875	1057	(Bezerra, 1999; Bezerra & Mozeto, 2008)
Chaplin	170	15	2.5	1040	0.039	1.129	35714	(Burbridge et al., 2004)
Bella Vista	165	8	3.2	1040	0.074	2.568	25000	(Burbridge et al., 2004)
Tele, Congo	319	19	1.6	1590	0.003	7.578	19231	(Laraque et al., 1997, 1998; Master, 2010)
S. da Ponta	98	3.8	1.2	998	0.037	0.08	12500	(McGlue et al., 2017)
S. Babaçu	106	4.7	1.2	998	0.037	0.08	16667	(McGlue et al., 2017)
S. do Meio	101	3.5	1.2	998	0.037	0.08	593	(Fávaro et al., 2006; Mariot et al., 2007; Santos & Sant'anna, 2010)
Nguengue	386	13.2	3.3	1520	0.016	11.145	1494	(Aleman et al., 2013)
Nhauhache	12	0.5	1.1	780	0.03	49.758	2245	(Holmgren et al., 2012)
Caracaranã	104	15	1.3	1700	0.0005	0.535	25000	(Turcq et al., 2002)
Santa Ninha	1	8.7	1.5	1912	0.026	6.982	11458	(Moreira et al., 2009, 2012)
Caçó	120	3	1.5	2200	0.035	11.343	66667	(Ledru et al., 2001; Sifeddine et al., 2003; Mbengue, 2004; Nascimento et al., 2010)
Waigani	10	2.8	13.4	899	0.002	145.455	1250	(Osborne & Polunin, 1986; Osborne et al., 1993)
Quistococha	94	2	3.2	2980	0.024	10.134	7442	(Aniceto et al., 2014)
Tembladera	17	1.9	13.3	1273	0.016	41.693	2312	(López-Blanco et al., 2017, 2018)
San José	162	52	8.9	1914	0.056	22.079	6667	(Whitney et al., 2013; Lombardo & Veit, 2014)
Sele, Benin	9	1.6	2.3	1112	0.038	54.935	904	(Salzmann & Hoelzmann, 2005; Bremond et al., 2017)
Sinnda	128	11.3	6	1250	0.012	12.484	7581	(Vincens et al., 1998)
Tapajós	1	0	0.75	1854	0.09	2.423	676	(Irion et al., 2006)
Daviambu	5	5.6	5.6	2012	0.011	3.468	55000	(Chambers, 1987; Hettler et al., 1997)
Bai	8	2.6	5.8	6323	0.011	3.623	28333	(Hettler et al., 1997)
Yaguaru	188	3.5	3.2	1321	0.165	3.104	8696	(Taylor et al., 2010)
Xingu	2	0	0.8	2113	0.089	1.279	13000	(Sawakuchi et al., 2015; Bertassoli et al., 2017)
Bera	30	0.2	12	2052	0.13	34.669	547	(Furtado & Mori, 2012; Gharibreza et al., 2013; Gharibreza & Ashraf, 2014)
Curuça	35	1.5	1.9	2922	0.099	65.326	28571	(Behling, 2001)
Mandioré	90	14.5	2.6	1124	0.033	7.815	15000	(McGlue et al., 2011, 2012)
Castelo	87	6.5	2.6	998	0.032	7.536	40556	(Bezerra & Mozeto, 2008)
Acarabixi	33	4.4	0.5	3004	0.004	0.567	6250	(Cordeiro et al., 2008; Rodríguez-Zorro et al., 2018)
Grande Curuai	1	4	1.52	1912	0.026	6.982	485	(Moreira-Turcq et al., 2004; Alcântara et al., 2009; Zocatelli et al., 2013)
Las Matas	3	5	9.4	2492	0.058	33.532	292	(Ruiz-Fernández et al., 2012)
Negra	86	7	2.6	998	0.034	7.928	920	(Bezerra & Mozeto, 2008; Rasbold et al., 2019)
Gaíva	92	8	2.4	1271	0.033	3.894	47000	(McGlue et al., 2012)

Jacaretinga	12	0.3	1.2	2301	0.016	4.582	1122	(Rai & Hill, 1980; Tundisi et al., 1984; Devol et al., 1984)
Caranã	5	0.4	0.7	2119	0.092	2.577	12500	(Maezumi et al., 2018; Arienzo et al., 2019)
Duas Bocas	5	2.4	4.4	2550	0.034	4.52	1786	(Miserendino et al., 2018)
Kitina	6	9.5	6.7	1031	0.012	9.484	4500	(Elenga et al., 1996)
Gbali	390	11.6	2.9	1520	0.005	7.667	394	(Aleman et al., 2013)
Doukoulou	365	10.5	3.1	1520	0.008	10.908	1088	(Aleman et al., 2013)
Canto Grande	5	0	3	1226	0.097	2.171	25000	(Lorente et al., 2018)
Pemerak	24	1.2	4.1	3196	0.08	7.78	233333	(Anshari et al., 2004)
Calado	23	1.7	1.2	2012	0.016	4.553	1181	(Behling et al., 2001)
Nguène	20	1.4	7.9	1969	0.004	9.196	5556	(Ngomanda et al., 2007; Sebag et al., 2013)
Lungue	8	4.1	2.7	1000	0.003	45.165	625	(Sitoe et al., 2017)
Bosset	8	3.7	5.9	6323	0.011	3.678	26667	(Chambers, 1987; Hettler et al., 1997)
Kai	14	3.6	6.2	6323	0.011	3.823	43333	(Hettler et al., 1997)
Tonle Sap	4	120	4.8	1406	0.037	63.666	15000	(Penny et al., 2005; Darby et al., 2020)
Mitsinjo	9	3.9	5.6	1476	0.006	9.872	1471	(Matsumotot & Burneyt, 1994)
Ossa	8	3.3	5.4	3603	0.011	33.833	6796	(Wirrmann et al., 2001; Giresse et al., 2005)
Maridor	32	0.1	3.9	2842	0.001	42.782	3000	(Giresse et al., 2009)
Chini	15	5.1	11.7	2052	0.134	35.615	643	(Sharip et al., 2018; Briddon et al., 2020)
Vellayani	1	3.4	8.8	1640	0.006	1149.746	11628	(Veena et al., 2014)
Cristalino	32	0.2	0.7	2301	0.007	1.119	1500	(Rai & Hill, 1980; Tundisi et al., 1984; Devol et al., 1984)
Macuco	1	0	7.2	1207	0.038	24.22	12000	(Lorente et al., 2014)
Uberaba	93	20	2.4	1271	0.033	3.932	1250	(Lo et al., 2019)
Melintang	2	8	10.2	2102	0.058	6.016	4348	(Hope et al., 2005)
Cáceres	83	7.7	2.6	971	0.085	1.556	18824	(Rasbold et al., 2021)
Paca	53	0.2	4.1	2231	0.186	9.143	5882	(Forsberg et al., 1989; Vergotti, 2008; Vergotti et al., 2009; Bonotto & Vergotti, 2015)
Rogaguado	146	10.6	0.2	1544	0.015	0.579	10870	(Brugger et al., 2016; Giesche et al., 2021)
Coari	20	65	0.2	2262	0.001	0.126	1041	(Horbe et al., 2011)
Acara	18	21	2.3	2523	0.014	8.804	514	(Horbe et al., 2011)
Brasileira	57	0.4	4.1	2231	0.186	9.143	833	(Vergotti, 2008; Bonotto & Vergotti, 2015)
Tucunaré	63	3	2.2	2246	0.034	1.025	1250	(Vergotti, 2008; Bonotto & Vergotti, 2015)
Araçá	52	0.4	4.1	2225	0.186	9.143	620	(Vergotti, 2008; Bonotto & Vergotti, 2015)
Nazaré	50	0.7	1.9	2237	0.052	9.267	2778	(Vergotti, 2008; Bonotto & Vergotti, 2015)
Santa Catarina	50	3	1.6	2229	0.01	0.135	599	(Vergotti, 2008; Bonotto & Vergotti, 2015)
Conceição	48	2	2	2230	0.023	0.416	872	(Vergotti, 2008; Bonotto & Vergotti, 2015)
Demarcação	47	0.5	0.7	2202	0.124	9.767	1389	(Vergotti, 2008; Bonotto & Vergotti, 2015)

Table A.3 Parameters used in principal components analysis

Lake	Distance from channel (km)	Elevation (m amsl)	Lake area (km²)	Depth (m)	Infill time (yrs)	Annual Rainfall (mm)	Tree loss (value of 0-1)	Short-term LAR (mm/yr)	Avg. slope (degrees)	Pop. density
Lake 1	0.4	185	0.9	2	313	1440	0.053	11.9	4.5	3.783
Lake 2	0	183	0.2	2	513	1438	0.053	8.1	4.5	3.783
Lake 3	0	184	0.25	2	408	1440	0.053	4.9	4.5	3.783
Jacadigo	50	81	24	2.6	1057	998	0.05	4.2	2.7	8.875
Salina do Meio	3.5	101	0.1	3.5	593	998	0.037	8.8	1.2	0.08
Nguengue	13.2	386	0.14	2.3	1494	1520	0.016	5.3	3.3	11.145
Tembladera	1.9	17	1	8	2312	1273	0.016	4.4	13.3	41.693
Yaguaru	3.5	188	2.5	4	8696	1321	0.165	2.3	3.2	3.104
Bera	0.2	30	0.54	3.5	547	2052	0.13	18.8	12	34.669
Lago Castelo	6.5	87	20	7.3	40556	998	0.032	4.9	2.6	7.536
Las Matas	5	3	0.3	1	292	2492	0.058	3.4	9.4	33.352
Jacaretinga	0.3	12	0.05	5.5	1122	2301	0.016	4.9	1.2	4.582
Cristalino	0.4	5	0.2	3	12500	2119	0.007	5	0.7	1.119
Duas Bocas	2.4	5	10.7	2.5	1786	2550	0.034	2.7	4.4	4.52
Gbali	11.6	390	0.02	2	394	1520	0.005	10.3	2.9	7.667
Doukoulou	10.5	365	0.36	2.35	1088	1520	0.008	1.9	3.1	10.908
Chini	5.1	15	2	2.7	643	2052	0.134	6.3	11.7	35.615
Paca	0.2	56	0.1	10	5882	2231	0.186	5.7	4.1	9.143
Brasileira	0.4	57	0.48	7.5	833	2231	0.186	4.7	4.1	9.143
Tucunaré	3	63	0.05	7.5	1250	2246	0.034	18.7	2.2	1.025
Araçá	0.4	52	0.46	7.5	620	2225	0.186	10.5	4.1	9.143
Nazaré	0.7	50	0.3	7.5	2778	2237	0.052	6.4	1.9	9.267
Santa Catarina	3	50	2.44	10	599	2229	0.01	6.1	1.6	0.135
Conceição	2	48	0.45	7.5	872	2230	0.023	12.3	2	0.416
Demarcação	0.5	47	1.66	7.5	1389	2202	0.124	4.2	0.7	9.767
Negra	7	86	9	2.3	920	998	0.034	2.7	2.6	7.928
Uberaba	20	93	258	3.5	1250	1271	0.033	4.2	2.4	3.932
Gaiva	8	92	94	4.7	47000	1271	0.033	2.4	2.4	3.894
Carana	0.4	5	0.2	3	12500	2119	0.092	2.4	0.7	2.577

APPENDIX B SUPPLEMENTAL MATERIALS FOR CHAPTER 3

Table B.1 Watershed environmental characteristics

Sample	Latitude	Long.	River	Elevation (m.a.s.l)	Temp. (°C)	Mean rain (mm yr^{-1})	Avg. slope (°)	Distance from PR (km)
A1	-22.0843	-57.9877	Paraguay	74	24.5	1178	2.51	0
A2	-21.7705	-57.9095	Paraguay	71	24.7	1178	2.51	0
A3	-21.4907	-57.9382	Paraguay	72	25	1201	2.58	0
A4	-19.0002	-57.5954	Paraguay	83	26.1	1429	3.07	0
A5	-18.8531	-57.6172	Paraguay	87	26.2	1441	3.1	0
A6	-18.6412	-57.5345	Paraguay	87	26.1	1441	3.1	0
A7	-18.3156	-57.3763	Taquari	91	26.1	1444	3.1	0
A8	-18.3906	-57.3795	Paraguay	89	26.1	1444	3.1	0
A9	-17.73	-57.6632	Paraguay	98	26.2	1432	2.97	0
A10	-17.8111	-57.2407	Cuiabá	98	26.1	1477	3.25	35
A11	-17.1442	-57.3599	Paraguay	106	25.9	1477	3.07	0
A12	-16.9747	-57.3874	Paraguay	100	25.9	1486	3.2	0
A13	-16.8123	-57.6534	Paraguay	106	26	1533	3.45	0
A14	-16.8195	-57.6273	Paraguay	102	26	1533	3.45	0
A15	-16.8152	-57.6268	Paraguay	105	26	1533	3.45	0
A16	-16.5599	-57.835	Paraguay	112	26	1534	3.46	0
A17	-16.4718	-57.8001	Paraguay	111	26	1535	3.45	0
A18	-16.3141	-57.7734	Paraguay	115	25.8	1535	3.52	0
A19	-16.2225	-57.7591	Paraguay	114	25.7	1545	3.6	0
A20	-16.0746	-57.7025	Paraguay	118	25.5	1549	3.59	0
A21	-16.0225	-57.7008	Paraguay	118	25.4	1550	3.46	0
A22	-16.0615	-57.7056	Paraguay	116	25.5	1552	3.5	0
A23	-18.4027	-57.3517	Paraguai Mirim	93	4	1496	4.22	4
A24	-18.4932	-57.3359	Paraguai Mirim	92	26	1496	4.23	9
A25	-18.7093	-56.9459	Taquari	100	25.7	1505	4.34	104
A26	-18.2534	-56.0671	Taquari	139	25.2	1510	4.39	173
A27	-18.257	-55.9575	Taquari	140	25.2	1510	4.39	198
A28	-18.2646	-55.9618	Taquari	136	25.2	1510	4.39	254
A29	-18.2625	-55.9539	Taquari	139	25.2	1510	4.39	255
A30	-18.2185	-55.1583	Taquari	175	25	1513	4.47	377
A31	-15.9962	-57.7013	Paraguay	119	25.4	1551	3.46	0
A32	-15.933	-57.6616	Paraguay	128	25.3	1553	3.45	0
A33	-15.9247	-57.6494	Paraguay	124	25.3	1485	3.69	0
A34	-22.0869	-57.9657	Apa	71	24.5	1178	3.66	3
A35	-20.9269	-57.8414	Nabileque	78	25.3	1165	2.43	6
A36	-20.9702	-57.8177	Aquidabã	78	25.2	1203	4.13	1
A37	-20.9981	-57.8177	Branco	80	25.2	1229	4.33	1
A38	-20.6459	-57.6328	Nabileque	79	25.4	1153	2.09	73
A39	-21.5833	-57.9077	Tarumã	78	24.9	1163	1.45	1
Avg.				103	25	1430	3	38
St. Dev				23	3	142	1	89
B1	-16.1435	-58.0157	Jauru	125	26	1557	3.41	59
B2	-15.4731	-58.0129	Bugres	158	25.4	1513	3.93	141
B3	-15.7355	-58.539	Jauru	159	26.1	1624	3.8	194
B4	-15.4687	-57.8937	Cabaçal	145	25.4	1566	4.75	112
B5	-15.8615	-58.5339	Aguapeí	159	26.3	1527	3.93	185
B6	-15.8097	-58.3999	Córrego Pitas	147	26.1	1512	2.66	172
B7	-15.3103	-57.8521	Vermelho, C	153	25.4	1182	4.18	143
B8	-15.3491	-58.0207	Branco	155	25.4	1589	5.72	144
B9	-14.5951	-57.8949	Formoso, MT	264	24.9	1750	3.71	220
Avg.				163	26	1536	4	152
St. Dev				39	0	152	1	48
C1	-22.2229	-57.303	Apa	114	24.1	1384	3.4	127
C2	-20.6281	-57.5758	Naitaca	81	25.4	1183	2.82	81
C3	-21.9418	-57.2543	Perdido	153	24.1	1307	5.13	163
C4	-20.8398	-57.2639	Aquidabã	120	24.9	1239	4.67	115
C5	-21.2335	-57.4236	Branco, MS	126	24.8	1260	5.3	109
C6	-21.6523	-57.8246	Amonguijá	84	24.9	1232	3.97	15

			Córrego					
C7	-21.8504	-57.8246	Progresso	76	24.7	1220	2.5	29
C8	-21.6575	-57.4987	Amonguijá	124	24.6	1253	5.28	77
Avg.				110	25	1260	4	90
St. Dev				27	0	61	1	50
D1	-20.4784	-55.8027	Aquidauana	143	24.3	1428	3.81	484
D2	-18.5256	-54.7505	Taquari	201	24.8	1513	4.55	466
D3	-20.2086	-56.4943	Miranda	115	24.7	1363	4.03	294
D4	-18.5348	-54.7402	Coxim	207	24.8	1493	4.42	468
D5	-16.4796	-54.6475	Vermelho, SL	200	24.4	1609	6.01	608
D6	-18.5013	-54.6855	Taquari	207	24.8	1544	4.82	475
D7	-16.3114	-54.9237	São Lourenço	199	24.4	1595	5.16	592
D8	-16.4703	-54.4902	Vermelho, SL	217	24.2	1641	6.4	630
D9	-21.2879	-56.225	Miranda	206	23.9	1403	3.5	136
D10	-17.2516	-54.7613	Itiquira	441	23.6	1606	4.12	611
D11	-15.9977	-54.9218	São Lourenço	240	24.2	1617	6.13	642
D12	-22.1143	-56.5195	Apa	181	23.7	1433	4.16	298
D13	-19.3159	-55.1768	Negro	159	25	1438	4.78	418
D14	-21.4484	-56.1475	Miranda	223	23.7	1426	3.87	168
D15	-16.5529	-54.4207	Tadarimana	230	24.3	1601	6.41	643
D16	-20.0715	-55.6466	Taboco	150	24.6	1419	5.11	331
D17	-17.9144	-54.6892	Piquiri	199	24.7	1517	3.75	664
D18	-21.1472	-55.8336	Nioaque	192	24	1416	4.34	585
D19	-21.1596	-55.8368	Canindé	189	24	1416	4.21	587
D20	-15.8382	-54.3822	Poxoreó	336	23.5	1693	4.9	757
D21	-15.8334	-54.4029	Córrego Areia	344	23.5	1665	4.67	761
Avg.				218	24	1516	5	506
St. Dev				74	0	101	1	177
E1	-20.5013	-56.7901	Salobra	139	24.6	1286	9.67	393
E2	-21.1735	-56.4461	Formoso, MS	277	23.6	1340	4.91	650
E3	-20.6942	-56.4864	Rio do Peixe	168	24.2	1326	5.94	423
			Córrego					
E4	-21.2878	-56.2955	Mutum	221	23.7	1367	2.21	134
E5	-20.7138	-56.5208	Chapena	175	24.2	1319	5.47	434
E6	-20.0509	-56.7818	Terere	118	25	1240	5.19	222
E7	-20.718	-56.5806	Taquarussu	207	24.1	1317	6.79	440
Avg.				186	24	1314	6	385
St. Dev				54	0	41	2	167
F1	-15.8741	-56.0741	Cuiabá	143	25.1	1480	4.41	540
F2	-15.2021	-56.3781	Cuiabá	174	24	1516	4.52	652
F3	-14.9291	-56.4349	Cuiabá	186	24.2	1558	4.62	711
F4	-14.8475	-56.4236	Cuiabá	194	24.4	1562	4.65	730
F5	-14.608	-57.7349	Sepotuba	225	24.9	1745	2.91	220
F6	-16.3204	-56.5434	Bento Gomes	124	25.4	1339	2.13	215
F7	-14.4896	-56.8066	Santana	206	25	1724	3.01	28
F8	-16.0644	-57.8404	Padre Inácio	119	25.8	1414	1.93	37
F9	-15.1261	-57.1075	Jauquara	162	24.8	1370	6.9	6
F10	-15.0765	-57.1845	Paraguay	153	25	1531	3.97	0
F11	-15.0036	-56.8883	Parí	174	24.7	1434	5.99	23
F12	-16.0585	-57.5772	Piraputanga	164	25.2	1336	11.5	18
F13	-16.3894	-58.3364	Corixo Grande	120	26.8	1396	6.03	240
Avg.				165	25	1493	5	263
St. Dev				33	1	132	3	290

Note: Sampling locations and relevant environmental data. *Vermelho, C* is a tributary of the Cabaçal River, and *Vermelho, SL* is a tributary of the São Lourenço River. A, Lowlands. B, Amazon craton. C, Rio Apa craton. D, Plateau. E, southern Paraguay Belt. F, northern Paraguay Belt. PR = Paraguay River. Mean annual precipitation and temperature were derived from WorldClim data (Fick & Hijmans, 2017), and average slope was calculated from the SRTM digital elevation models.

Table B.2 Pour point analyses

Site	Area (km²)	Source	M.I.	Surface	S.C.	Biochem	Volcanic	Plutonic	Foliated	NFoliated	Other
A1	446863	Lowland	10	47.8	28	4.2	4.6	2	8.2	3	2.2
A2	445637	Lowland	7	47.2	28.4	4.5	4.6	2	8.4	3.1	1.8
A3	441437	Lowland	30	47.2	28.7	4.3	4.6	1.9	8.3	3.1	1.9
A4	250750	Lowland	491	46	24	6	3	2	11	4	4
A5	244190	Lowland	122	44	26	5	4	2	12	4	3
A6	243910	Lowland	492	44	26	5	3	2	12	4	4
A7	241900	Lowland	12	44	26	5	4	2	12	4	3
A8	241570	Lowland	98	44	26	5	3	2	12	4	4
A9	123800	Lowland	44	45	16	8	3	6	15	3	4
A10	106835	Lowland	7	38	44	1	2	0	7	7	1
A11	63320	Lowland	123	41	26	6	8	8	8	2	1
A12	60440	Lowland	123	38	27	6	9	8	8	2	2
A13	47640	Lowland	54	33	34	6	11	10	3	1	2
A14	47640	Lowland	30	33	34	6	11	10	3	1	2
A15	47640	Lowland	44	33	34	6	11	10	3	1	2
A16	47489	Lowland	30	33	34	6	11	9	3	1	3
A17	47170	Lowland	22	34	34	6	11	10	3	1	1
A18	35410	Lowland	48	40	38	5	7	5	3	1	1
A19	33250	Lowland	43	38	40	4	8	5	4	1	0
A20	32620	Lowland	20	37	41	4	8	5	4	1	0
A21	32550	Lowland	26	37	41	4	8	5	4	1	0
A22	32188	Lowland	60	38	40	3	8	5	4	1	1
A23	30898	Lowland	26	12	83	2	2	0	0	0	1
A24	30570	Lowland	37	12	85	0	2	0	0	0	1
A25	29620	Lowland	7	10	88	0	2	0	0	0	0
A26	29179	Lowland	4	8	88	0	2	0	0	0	2
A27	29158	Lowland	4	8	88	0	2	0	0	0	2
A28	29146	Lowland	7	8	88	0	2	0	0	0	2
A29	29120	Lowland	28	8	88	0	2	0	0	0	2
A30	28532	Lowland	7	6	90	0	2	0	0	0	2
A31	26960	Lowland	30	40	46	3	8	2	0	0	1
A32	26720	Lowland	53	40	46	3	8	2	0	0	1
A33	16380	Lowland	97	53	36	4	5	0	0	0	2
A34	15180	Lowland	3	6	32	11	6	2	42	1	0
A35	7011	Lowland	16	54	5	1	0	1	39	0	0
A36	3265	Lowland	6	37	1	3	0	9	45	5	0
A37	2337	Lowland	11	34	0	2	0	12	45	5	2
A38	1352	Lowland	15	44	14	0	0	0	42	0	0
A39	1052	Lowland	3	79	0	0	3	16	1	0	1
Avg.	93608		59	34	40	4	5	4	9	2	2
St.	126748		108								
Dev				16	27	3	4	4	14	2	1
B1	10564	Amazon	10	7	28	7	25	25	6	2	0
B2	9217	Amazon	7	7	0	4	19	21	47	0	2
B3	5247	Amazon	26	3	38	0	22	30	7	0	0
B4	3596	Amazon	31	7	0	4	19	21	47	0	2
B5	1770	Amazon	9	3	25	0	0	51	10	9	2
B6	1203	Amazon	15	4	0	0	74	19	3	0	0
B7	1182	Amazon	6	0	99	0	0	0	0	0	1
B8	1010	Amazon	22	0	7	0	0	15	45	33	0
B9	574	Amazon	69	0	81	0	1	17	0	0	1
Avg.	1318		22	3	31	2	18	22	18	5	1
St.	3761										
Dev			20	3	37	3	24	14	21	11	1
C1	10170	Apa	2	0	48	9	9	0	33	1	0
C2	3859	Apa	0	50	2	1	0	2	44	1	0
C3	2513	Apa	2	4	0	27	0	1	66	0	2
C4	1785	Apa	1	16	0	7	0	2	66	7	2
C5	1728	Apa	1	14	0	4	0	16	58	7	1
C6	964	Apa	2	30	0	0	3	37	30	0	0
C7	716	Apa	6	61	0	0	16	0	19	4	0
C8	453	Apa	1	0	0	0	0	69	30	0	1
Avg.	2774		2	22	6	6	4	16	43	3	1
St.	3183										
Dev			2	23	17	9	6	25	18	3	1

ID	Area	Region		Surface	S.C.	Biochem	Volcanic	Plutonic	Foliated	NFoliated	Other
D1	156858	Plateau	15	0	53	0	45	0	0	0	2
D2	27196	Plateau	17	4	93	0	2	0	0	0	1
D3	17508	Plateau	19	6	31	13	20	0	17	10	3
D4	15576	Plateau	19	7	90	0	3	0	0	0	0
D5	12295	Plateau	495	19	9	0	0	69	3	0	0
D6	10952	Plateau	16	0	98	0	1	0	0	0	1
D7	6973	Plateau	31	0	100	0	0	0	0	0	0
D8	6034	Plateau	163	0	100	0	0	0	0	0	0
D9	4672	Plateau	5	0	43	8	45	0	0	4	0
D10	3727	Plateau	96	1	87	0	11	0	0	0	1
D11	3182	Plateau	37	0	99	0	1	0	0	0	0
D12	2981	Plateau	23	0	68	0	32	0	0	0	0
D13	2866	Plateau	4	3	96	0	0	0	0	0	1
D14	2856	Plateau	8	0	26	0	74	0	0	0	0
D15	2702	Plateau	24	0	100	0	0	0	0	0	0
D16	2158	Plateau	27	0	92	0	0	3	5	0	0
D17	2136	Plateau	48	0	100	0	0	0	0	0	0
D18	1658	Plateau	15	0	17	0	83	0	0	0	0
D19	1270	Plateau	5	0	100	0	0	0	0	0	0
D20	1206	Plateau	N/A	0	99	0	1	0	0	0	0
D21	198	Plateau	124	0	97	0	3	0	0	0	0
Avg.	14240		60	2	76	1	15	3	1	1	0
St. Dev	33413		111	4	32	3	26	15	4	2	1
E1	861	SouthPB	0	1	9	85	0	1	0	3	1
E2	700	SouthPB	0	0	5	85	0	0	0	9	1
E3	334	SouthPB	1	0	11	38	0	0	7	44	0
E4	253	SouthPB	21	0	33	6	0	0	20	41	0
E5	215	SouthPB	3	3	25	28	0	0	0	42	2
E6	185	SouthPB	2	0	0	5	0	0	73	22	0
E7	142	SouthPB	2	0	14	54	0	0	0	32	0
Avg.	384		4	1	14	43	0	0	14	28	1
St. Dev	281		8	1	11	33	0	0	27	17	1
F1	24665	NorthPB	18	2	36	6	2	0	21	33	0
F2	19259	NorthPB	91	0	44	8	2	0	8	38	0
F3	15956	NorthPB	68	0	51	7	0	0	6	36	0
F4	15697	NorthPB	33	0	52	7	0	0	6	35	0
F5	3580	NorthPB	160	0	72	0	28	0	0	0	0
F6	2824	NorthPB	27	32	0	0	0	0	58	10	0
F7	1775	NorthPB	23	0	66	0	34	0	0	0	0
F8	1328	NorthPB	22	69	0	31	0	0	0	0	0
F9	1325	NorthPB	12	5	81	14	0	0	0	0	0
F10	1072	NorthPB	22	36	53	3	8	0	0	0	0
F11	1018	NorthPB	31	13	86	1	0	0	0	0	0
F12	107	NorthPB	13	0	46	54	0	0	0	0	0
F13	2	NorthPB	9	9	0	91	0	0	0	0	0
Avg.	6816		41	13	45	17	6	0	8	12	0
St. Dev	8689		43	21	30	27	12	0	16	17	0

Note: Pour points and compositions of watersheds in **percentage values (sample sum = 100%)** organized by region. Surface, unconsolidated alluvium. S.C., siliciclastic sedimentary rock. Biochem, (bio)chemical sedimentary rock. Volcanic, volcanic igneous rock. Plutonic, plutonic igneous rock. Foliated, foliated metamorphic rock. NFoliated, non-foliated metamorphic rock. Other, sum of remaining minor components of the watershed lithotypes. Watershed area was calculated from the SRTM digital elevation models.

Table B.3: Gazzi-Dickinson point counts

Sample	M.I.	Qm	Qp	Qpq	K	P	Acc	M	Cht	Ls	Lm	Lv	U	Qt	F	L	Lt
A1	10	439	9	7	33	2	2	4	2	11	0	0	0	448	35	11	18
A2	7	424	6	6	40	0	2	9	0	18	1	0	0	430	40	19	25
A3	30	480	2	2	11	0	0	0	0	4	0	1	2	482	11	5	7
A4	491	489	2	2	0	0	0	0	0	0	1	0	8	491	0	1	3
A5	122	483	3	2	4	0	0	0	1	0	0	0	10	486	4	0	2
A6	492	488	4	3	0	0	0	0	1	1	0	0	7	492	0	1	4
A7	12	445	9	8	26	0	1	0	1	13	0	0	6	454	26	13	21
A8	98	481	7	5	1	0	0	0	2	3	0	1	7	488	1	4	9
A9	44	477	3	3	8	0	1	0	0	0	3	0	8	480	8	3	6
A10	7	414	5	5	33	2	3	18	0	21	4	0	0	419	35	25	30
A11	123	486	5	4	2	0	1	0	1	2	0	0	4	491	2	2	6
A12	123	490	1	1	3	0	0	0	0	1	0	0	5	491	3	1	2
A13	54	483	3	3	7	0	0	0	0	3	1	0	3	486	7	4	7
A14	30	466	6	5	10	1	0	1	1	5	0	0	11	472	11	5	10
A15	44	481	5	5	7	0	0	0	0	1	1	0	5	486	7	2	7
A16	30	475	4	3	11	1	2	0	1	4	0	0	3	479	12	4	7
A17	22	470	3	3	17	1	0	0	0	3	1	0	5	473	18	4	7
A18	48	474	9	7	7	0	1	0	2	2	1	0	6	483	7	3	10
A19	43	467	6	6	8	0	2	0	0	2	0	1	14	473	8	3	9
A20	20	459	8	8	16	1	2	0	0	3	1	2	8	467	17	6	14
A21	26	465	10	10	9	2	1	1	0	5	2	0	5	475	11	7	17
A22	60	469	11	11	7	0	0	0	0	1	0	0	12	480	7	1	12
A23	26	459	12	10	13	0	2	2	2	4	1	0	7	471	13	5	15
A24	37	470	6	4	13	0	1	0	2	0	0	0	10	476	13	0	4
A25	7	427	4	4	34	0	2	0	0	27	3	0	3	431	34	30	34
A26	4	403	5	3	64	0	1	0	2	26	1	0	0	408	64	27	30
A27	4	376	11	9	84	0	1	1	2	21	0	0	6	387	84	21	30
A28	7	426	6	5	43	0	1	2	1	17	2	0	3	432	43	19	24
A29	28	470	7	5	10	0	0	0	2	6	1	0	6	477	10	7	12
A30	7	412	16	13	40	0	2	0	3	25	0	0	5	428	40	25	38
A31	30	455	17	16	13	1	0	0	1	1	1	0	12	472	14	2	18
A32	53	471	9	6	4	0	1	0	3	3	2	0	10	480	4	5	11
A33	97	479	6	5	0	0	0	0	0	1	5	0	10	485	0	5	10
A34	3	332	38	37	76	40	1	1	1	7	4	0	1	370	116	11	48
A35	16	459	6	4	16	2	5	1	2	7	4	0	0	465	18	11	15
A36	6	401	26	25	50	5	1	3	1	11	3	0	0	427	55	14	39
A37	11	451	5	5	36	3	1	0	0	2	0	0	2	456	39	2	7
A38	15	461	7	7	29	1	0	0	0	1	0	0	1	468	30	1	8
A39	3	359	24	24	90	23	0	0	0	3	1	0	0	383	113	4	28
Avg.	59	451.7	8.4	7.5	22.4	2.2	0.9	1.1	0.9	6.9	1	0.1	5.3	460.1	24.6	8	15.5
St. Dev	108	37.6	7.3	7.1	23.7	7.3	1.1	3.2	0.9	8	1.3	0.4	4	32.5	28.5	8.3	11.6
B1	107	413	27	26	38	1	4	1	1	2	0	1	13	440	39	3	29
B2	19	248	178	178	45	0	1	2	0	15	0	0	11	426	45	15	193
B3	26	429	9	9	14	3	15	12	0	0	0	0	18	438	17	0	9
B4	31	453	10	9	3	1	9	0	1	8	1	2	13	463	4	11	20
B5	9	406	26	26	32	13	0	3	0	4	0	0	16	432	45	4	30
B6	15	402	51	49	17	3	0	3	2	9	1	0	14	453	20	10	59
B7	6	382	12	3	9	0	35	0	9	61	1	0	0	394	9	62	65
B8	22	456	8	8	10	1	13	0	0	10	0	0	2	464	11	10	18
B9	69	468	14	12	3	1	1	0	2	3	0	0	10	482	4	3	15
Avg.	22	406.3	37.2	35.6	19	2.6	8.7	2.3	1.7	12.4	0.3	0.3	10.8	443.6	21.6	13.1	48.7
St. Dev	20	65.8	54.5	55.3	15.5	4.1	11.4	3.8	2.9	18.8	0.5	0.7	6.1	25.7	17	19	57.5
C1	20	321	6	5	106	17	10	7	1	30	1	0	2	327	123	31	36
C2		83	6	5	23	0	4	49	1	6	328	0	1	89	23	4	9
C3	2	294	18	17	112	33	4	9	1	21	7	0	2	312	145	28	45
C4	1	215	3	3	193	4	1	11	0	61	1	0	11	218	197	62	65
C5	1	261	3	3	195	2	1	7	0	24	1	0	6	264	197	25	28
C6	2	319	1	1	157	10	0	1	0	8	0	0	4	320	167	8	9
C7	61	407	15	15	53	15	2	1	0	7	0	0	0	422	68	7	22
C8		218	45	44	148	17	0	0	1	8	12	50	2	263	165	70	114
Avg.	2	264.8	12.1	11.6	123	12	2.8	11	0.5	20.6	44	6	3.5	277	136	71	82
St. Dev	2	96.3	14.6	14.3	62	11	3.3	16	0.5	18.7	115	18	3.5	97	62	109	109
D1	15	428	24	16	16	0	3	1	8	5	9	1	13	452	16	15	31
D2	17	442	25	15	13	1	1	1	10	9	5	0	3	467	14	14	29
D3	19	446	19	18	5	0	3	0	1	9	9	1	8	465	5	19	37
D4	19	445	23	16	15	1	0	0	7	7	2	0	7	468	16	9	25
D5	495	458	37	36	0	1	4	0	1	0	0	0	0	495	1	0	36

123

Sample																	
D6	16	432	26	15	11	3	5	0	11	13	0	1	9	458	14	14	29
D7	31	453	14	2	2	0	18	0	12	7	6	0	0	467	2	13	15
D8	163	468	20	18	0	2	7	2	2	1	0	0	0	488	2	1	19
D9	5	376	10	7	9	3	27	0	3	60	6	5	4	386	12	71	78
D10	96	464	14	7	5	0	1	1	7	0	0	0	15	478	5	0	7
D11	37	443	33	31	9	0	2	0	2	4	0	0	9	476	9	4	35
D12	23	422	30	29	11	1	21	1	1	2	5	1	6	452	12	8	37
D13	4	390	4	3	31	0	1	2	1	69	2	0	1	394	31	71	74
D14	8	390	22	13	5	4	35	0	9	35	2	4	3	412	9	41	54
D15	24	421	58	57	9	5	1	0	1	6	0	0	0	479	14	6	63
D16	27	475	4	4	15	0	0	0	0	3	0	0	3	479	15	3	7
D17	48	455	29	29	5	0	0	0	0	3	2	0	6	484	5	5	34
D18	15	377	22	18	4	2	64	0	4	9	3	8	11	399	6	20	38
D19	5	376	3	3	35	3	25	24	0	31	0	3	0	379	38	34	37
D20	N/A	480	17	17	0	0	3	0	0	0	0	0	0	497	0	0	17
D21	124	481	14	14	0	0	1	0	0	4	0	0	0	495	0	4	18
Avg.	60	434.4	21.3	17.5	9.5	1.2	10.6	1.5	3.8	13.2	2.4	1.1	4.7	456	10.8	16.8	34.3
St. Dev	1110	34.7	12.6	13.2	9.4	1.5	16.2	5.2	4.1	19.4	3	2.1	4.7	38	9.7	21.3	19.4
E1	0	100	13	12	48	1	0	0	1	331	5	0	2	113	49	6.49	8.49
E2	1	9	0	0	0	0	0	0	0	491	0	0	0	9	0	1.24	1.28
E3		196	42	42	10	2	1	5	0	166	75	1	2	238	12	2	4
E4	21	427	39	39	2	0	2	0	0	5	15	0	10	466	2	20.12	59.20
E5	2	262	83	82	13	2	7	6	1	100	19	3	5	345	15	2.17	4.18
E6	2	297	30	14	0	0	0	0	16	160	10	0	3	327	0	0.15	4.19
E7		262	47	47	20	7	7	4	0	84	67	0	2	309	27	1.21	8.25
Avg.	4	221.9	36.3	33.7	13.3	1.7	2.4	2.1	2.6	191	27	0.6	3.4	258	15	9.15	3.13
St. Dev	8	136.5	26.6	27.7	17	2.5	3.2	2.7	5.9	166	31	1.1	3.3	154	18	5	8
F1	18	417	42	38	11	0	3	1	4	6	9	0	11	459	11	15	53
F2	91	408	47	28	2	0	27	6	19	3	0	0	7	455	2	3	31
F3	68	465	11	11	0	1	2	0	0	6	0	0	15	476	1	6	17
F4	33	440	21	19	6	1	16	0	2	7	0	0	9	461	7	7	26
F5	160	462	19	15	3	0	3	0	4	0	0	0	13	481	3	0	15
F6	27	447	13	13	0	0	5	0	0	16	1	0	18	460	0	17	30
F7	23	439	12	6	2	0	13	1	6	18	0	0	15	451	2	18	24
F8	22	448	8	7	2	0	6	2	1	19	0	0	15	456	2	19	26
F9	12	403	44	41	0	0	7	0	3	37	0	1	8	447	0	38	79
F10	22	450	13	11	0	0	1	0	2	14	7	0	15	463	0	21	32
F11	31	434	37	32	2	0	0	0	5	6	6	1	14	471	2	13	45
F12	13	405	41	40	3	0	12	0	1	31	0	0	8	446	3	31	71
F13	9	347	34	21	3	0	60	2	13	41	0	0	13	381	3	41	62
Avg.	41	428.1	26.3	21.7	2.6	0.2	11.9	0.9	4.6	15.7	1.8	0.2	12.4	454	2.8	17.6	39
St. Dev	43	32	14.7	12.7	3	0.4	16.3	1.7	5.5	13.3	3.2	0.4	3.5	24	3.1	12.8	21

Note: Raw point counts (sample size = 500). See Table 3.1 for abbreviations. M.I., Maturity Index.

APPENDIX C SUPPLEMENTAL MATERIALS FOR CHAPTER 4

Table C.1 Watershed environmental characteristics

Sample	Latitude	Long.	River	Elevation (m.a.s.l)	Temp. (°C)	Mean rain (mm yr^{-1})	Avg. slope (°)	Distance from PR (km)
A1	-22.0843	-57.9877	Paraguay	74	24.5	1178	2.51	0
A2	-21.7705	-57.9095	Paraguay	71	24.7	1178	2.51	0
A3	-21.4907	-57.9382	Paraguay	72	25	1201	2.58	0
A5	-18.8531	-57.6172	Paraguay	87	26.2	1441	3.1	0
A6	-18.6412	-57.5345	Paraguay	87	26.1	1441	3.1	0
A7	-18.3156	-57.3763	Taquari	91	26.1	1444	3.1	0
A8	-18.3906	-57.3795	Paraguay	89	26.1	1444	3.1	0
A9	-17.73	-57.6632	Paraguay	98	26.2	1432	2.97	0
A10	-17.8111	-57.2407	Cuiabá	98	26.1	1477	3.25	35
A22	-16.0615	-57.7056	Paraguay Paraguai	116	25.5	1552	3.5	0
A23	-18.4027	-57.3517	Mirim	93	4	1496	4.22	4
A25	-18.7093	-56.9459	Taquari	100	25.7	1505	4.34	104
A26	-18.2534	-56.0671	Taquari	139	25.2	1510	4.39	173
A27	-18.257	-55.9575	Taquari	140	25.2	1510	4.39	198
A28	-18.2646	-55.9618	Taquari	136	25.2	1510	4.39	254
A29	-18.2625	-55.9539	Taquari	139	25.2	1510	4.39	255
A30	-18.2185	-55.1583	Taquari	175	25	1513	4.47	377
A34	-22.0869	-57.9657	Apa	71	24.5	1178	3.66	3
A35	-20.9269	-57.8414	Nabileque	78	25.3	1165	2.43	6
A36	-20.9702	-57.8177	Aquidabã	78	25.2	1203	4.13	1
A37	-20.9981	-57.8177	Branco	80	25.2	1229	4.33	1
A38	-20.6459	-57.6328	Nabileque	79	25.4	1153	2.09	73
Avg.				100	24	1376	3.5	67
St. Dev				29	5	151	1	111
B1	-16.1435	-58.0157	Jauru	125	26	1557	3.41	59
B2	-15.4731	-58.0129	Bugres	158	25.4	1513	3.93	141
B3	-15.7355	-58.539	Jauru	159	26.1	1624	3.8	194
B4	-15.4687	-57.8937	Cabaçal	145	25.4	1566	4.75	112
B5	-15.8615	-58.5339	Aguapeí	159	26.3	1527	3.93	185
B6	-15.8097	-58.3999	Córrego Pitas	147	26.1	1512	2.66	172
B7	-15.3103	-57.8521	Vermelho, C	153	25.4	1182	4.18	143
B8	-15.3491	-58.0207	Branco	155	25.4	1589	5.72	144
B9	-14.5951	-57.8949	Formoso, MT	264	24.9	1750	3.71	220
Avg.				163	26	1536	4	152
St. Dev				39	0	152	1	48
C1	-22.2229	-57.303	Apa	114	24.1	1384	3.4	127
C2	-20.6281	-57.5758	Naitaca	81	25.4	1183	2.82	81
C3	-21.9418	-57.2543	Perdido	153	24.1	1307	5.13	163
C4	-20.8398	-57.2639	Aquidabã	120	24.9	1239	4.67	115
C5	-21.2335	-57.4236	Branco, MS	126	24.8	1260	5.3	109
C6	-21.6523	-57.8246	Amonguijá Córrego	84	24.9	1232	3.97	15
C7	-21.8504	-57.8246	Progresso	76	24.7	1220	2.5	29
C8	-21.6575	-57.4987	Amonguijá	124	24.6	1253	5.28	77
Avg.				110	25	1260	4	90
St. Dev				27	0	61	1	50
D1	-20.4784	-55.8027	Aquidauana	143	24.3	1428	3.81	484
D2	-18.5256	-54.7505	Taquari	201	24.8	1513	4.55	466
D3	-20.2086	-56.4943	Miranda	115	24.7	1363	4.03	294
D4	-18.5348	-54.7402	Coxim	207	24.8	1493	4.42	468
D5	-16.4796	-54.6475	Vermelho, SL	200	24.4	1609	6.01	608
D6	-18.5013	-54.6855	Taquari	207	24.8	1544	4.82	475
D7	-16.3114	-54.9237	São Lourenço	199	24.4	1595	5.16	592
D9	-21.2879	-56.225	Miranda	206	23.9	1403	3.5	136
D10	-17.2516	-54.7613	Itiquira	441	23.6	1606	4.12	611
D11	-15.9977	-54.9218	São Lourenço	240	24.2	1617	6.13	642
D12	-22.1143	-56.5195	Apa	181	23.7	1433	4.16	298
D13	-19.3159	-55.1768	Negro	159	25	1438	4.78	418
D14	-21.4484	-56.1475	Miranda	223	23.7	1426	3.87	168
D15	-16.5529	-54.4207	Tadarimana	230	24.3	1601	6.41	643
D16	-20.0715	-55.6466	Taboco	150	24.6	1419	5.11	331
D17	-17.9144	-54.6892	Piquiri	199	24.7	1517	3.75	664

D18	-21.1472	-55.8336	Nioaque	192	24	1416	4.34	585
D19	-21.1596	-55.8368	Canindé	189	24	1416	4.21	587
Avg.				205	24	1491	5	471
St. Dev				67	0	86	1	165
E1	-20.5013	-56.7901	Salobra	139	24.6	1286	9.67	393
E3	-20.6942	-56.4864	Rio do Peixe Córrego	168	24.2	1326	5.94	423
E4	-21.2878	-56.2955	Mutum	221	23.7	1367	2.21	134
E5	-20.7138	-56.5208	Chapena	175	24.2	1319	5.47	434
E6	-20.0509	-56.7818	Terere	118	25	1240	5.19	222
E7	-20.718	-56.5806	Taquarussu	207	24.1	1317	6.79	440
Avg.				186	24	1314	6	385
St. Dev				54	0	41	2	167
F1	-15.8741	-56.0741	Cuiabá	143	25.1	1480	4.41	540
F2	-15.2021	-56.3781	Cuiabá	174	24	1516	4.52	652
F3	-14.9291	-56.4349	Cuiabá	186	24.2	1558	4.62	711
F4	-14.8475	-56.4236	Cuiabá	194	24.4	1562	4.65	730
F5	-14.608	-57.7349	Sepotuba	225	24.9	1745	2.91	220
F6	-16.3204	-56.5434	Bento Gomes	124	25.4	1339	2.13	215
F7	-14.4896	-56.8066	Santana	206	25	1724	3.01	28
F9	-15.1261	-57.1075	Jauquara	162	24.8	1370	6.9	6
F10	-15.0765	-57.1845	Paraguay	153	25	1531	3.97	0
F11	-15.0036	-56.8883	Parí	174	24.7	1434	5.99	23
F12	-16.0585	-57.5772	Piraputanga	164	25.2	1336	11.5	18
Avg.				173	25	1509	5	286
St. Dev				29	1	139	3	309

Note: Sampling locations and relevant environmental data. *Vermelho, C* is a tributary of the Cabaçal River, and *Vermelho, SL* is a tributary of the São Lourenço River. A, Lowlands. B, Amazon craton. C, Rio Apa craton. D, Plateau. E, southern Paraguay Belt. F, northern Paraguay Belt. PR = Paraguay River. Mean annual precipitation and temperature were derived from WorldClim data (Fick & Hijmans, 2017), and average slope was calculated from the SRTM digital elevation models.

Table C.2 Lithologies by watershed

Site	Area (km²)	Source	M.I.	Surface	S.C.	Biochem	Volcanic	Plutonic	Foliated	NFoliated	Other
A1	446863	Lowland	10	47.8	28	4.2	4.6	2	8.2	3	2.2
A2	445637	Lowland	7	47.2	28.4	4.5	4.6	2	8.4	3.1	1.8
A3	441437	Lowland	30	47.2	28.7	4.3	4.6	1.9	8.3	3.1	1.9
A5	244190	Lowland	122	44	26	5	4	2	12	4	3
A6	243910	Lowland	492	44	26	5	3	2	12	4	4
A7	241900	Lowland	12	44	26	5	4	2	12	4	3
A8	241570	Lowland	98	44	26	5	3	2	12	4	4
A9	123800	Lowland	44	45	16	8	3	6	15	3	4
A10	106835	Lowland	7	38	44	1	2	0	7	7	1
A22	32188	Lowland	60	38	40	3	8	5	4	1	1
A23	30898	Lowland	26	12	83	2	2	0	0	0	1
A25	29620	Lowland	7	10	88	0	2	0	0	0	0
A26	29179	Lowland	4	8	88	0	2	0	0	0	2
A27	29158	Lowland	4	8	88	0	2	0	0	0	2
A28	29146	Lowland	7	8	88	0	2	0	0	0	2
A29	29120	Lowland	28	8	88	0	2	0	0	0	2
A30	28532	Lowland	7	6	90	0	2	0	0	0	2
A34	15180	Lowland	3	6	32	11	6	2	42	1	0
A35	7011	Lowland	16	54	5	1	0	1	39	0	0
A36	3265	Lowland	6	37	1	3	0	9	45	5	0
A37	2337	Lowland	11	34	0	2	0	12	45	5	2
A38	1352	Lowland	15	44	14	0	0	0	42	0	0
Avg.	127415		46	31	43	3	3	2	14	2	2
St. Dev	155241		104	18	33	3	2	3	17	2	1
B1	10564	Amazon	10	7	28	7	25	25	6	2	0
B2	9217	Amazon	7	7	0	4	19	21	47	0	2
B3	5247	Amazon	26	3	38	0	22	30	7	0	0
B4	3596	Amazon	31	7	0	4	19	21	47	0	2
B5	1770	Amazon	9	3	25	0	0	51	10	9	2
B6	1203	Amazon	15	4	0	0	74	19	3	0	0
B7	1182	Amazon	6	0	99	0	0	0	0	0	1
B8	1010	Amazon	22	0	7	0	0	15	45	33	0
B9	574	Amazon	69	0	81	0	1	17	0	0	1
Avg.	3818		22	3	31	2	18	22	18	5	1
St. Dev	3761		20	3	37	3	24	14	21	11	1
C1	10170	Apa	2	0	48	9	9	0	33	1	0
C2	3859	Apa	0	50	2	1	0	2	44	1	0
C3	2513	Apa	2	4	0	27	0	1	66	0	2
C4	1785	Apa	1	16	0	7	0	2	66	7	2
C5	1728	Apa	1	14	0	4	0	16	58	7	1
C6	964	Apa	2	30	0	0	3	37	30	0	0
C7	716	Apa	6	61	0	0	16	0	19	4	0
C8	453	Apa	1	0	0	0	0	69	30	0	1
Avg.	2774		2	22	6	6	4	16	43	3	1
St. Dev	3183		2	23	17	9	6	25	18	3	1
D1	156858	Plateau	15	0	53	0	45	0	0	0	2
D2	27196	Plateau	17	4	93	0	2	0	0	0	1
D3	17508	Plateau	19	6	31	13	20	0	17	10	3
D4	15576	Plateau	19	7	90	0	3	0	0	0	0
D5	12295	Plateau	495	19	9	0	0	69	3	0	0
D6	10952	Plateau	16	0	98	0	1	0	0	0	1
D7	6973	Plateau	31	0	100	0	0	0	0	0	0
D9	4672	Plateau	5	0	43	8	45	0	0	4	0
D10	3727	Plateau	96	1	87	0	11	0	0	0	1
D11	3182	Plateau	37	0	99	0	1	0	0	0	0
D12	2981	Plateau	23	0	68	0	32	0	0	0	0
D13	2866	Plateau	4	3	96	0	0	0	0	0	1
D14	2856	Plateau	8	0	26	0	74	0	0	0	0
D15	2702	Plateau	24	0	100	0	0	0	0	0	0
D16	2158	Plateau	27	0	92	0	0	3	5	0	0
D17	2136	Plateau	48	0	100	0	0	0	0	0	0
D18	1658	Plateau	15	0	17	0	83	0	0	0	0
D19	1270	Plateau	5	0	100	0	0	0	0	0	0

ID	Area	Region									
Avg.	15420		50	2	72	1	18	4	1	1	1
St. Dev	35994		113	5	33	4	27	16	4	2	1
E1	861	SouthPB	0	1	9	85	0	1	0	3	1
E3	334	SouthPB	1	0	11	38	0	0	7	44	0
E4	253	SouthPB	21	0	33	6	0	0	20	41	0
E5	215	SouthPB	3	3	25	28	0	0	0	42	2
E6	185	SouthPB	2	0	0	5	0	0	73	22	0
E7	142	SouthPB	2	0	14	54	0	0	0	32	0
Avg.	332		5	1	15	36	0	0	17	31	1
St. Dev	267		8	1	12	31	0	0	29	16	1
F1	24665	NorthPB	18	2	36	6	2	0	21	33	0
F2	19259	NorthPB	91	0	44	8	2	0	8	38	0
F3	15956	NorthPB	68	0	51	7	0	0	6	36	0
F4	15697	NorthPB	33	0	52	7	0	0	6	35	0
F5	3580	NorthPB	160	0	72	0	28	0	0	0	0
F6	2824	NorthPB	27	32	0	0	0	0	58	10	0
F7	1775	NorthPB	23	0	66	0	34	0	0	0	0
F9	1325	NorthPB	12	5	81	14	0	0	0	0	0
F10	1072	NorthPB	22	36	53	3	8	0	0	0	0
F11	1018	NorthPB	31	13	86	1	0	0	0	0	0
F12	107	NorthPB	13	0	46	54	0	0	0	0	0
Avg.	7934		45	8	53	9	7	0	9	14	0
St. Dev	9031		45	13	24	16	12	0	17	17	0

Note: Pour points and compositions of watersheds in **percentage values (sample sum = 100%)** organized by region. Surface, unconsolidated alluvium. S.C., siliciclastic sedimentary rock. Biochem, (bio)chemical sedimentary rock. Volcanic, volcanic igneous rock. Plutonic, plutonic igneous rock. Foliated, foliated metamorphic rock. NFoliated, non-foliated metamorphic rock. Other, sum of remaining minor components of the watershed lithotypes. Watershed area was calculated from the SRTM digital elevation models.

Table C.3 Semi-quantitative clay mineral estimates

Site	Kaolinite	Illite	Vermiculite	Smectite	Goethite + Gibbsite presence	Illite I(001)/I(002)
A2	57	8	35	0	Both	1.7
A3	51	4	46	0	Both	1.3
A6	77	5	18	0	Goethite	1.1
A7	74	11	15	0	Goethite	1.8
A8	77	3	20	0	None	0.9
A9	57	3	41	0	Both	0.6
A23	79	7	14	0	Gibbsite	1.8
A25	43	2	55	0	None	0.8
A26	36	3	0	61	Both	1.9
A27	52	4	43	0	Gibbsite	2.1
A28	54	5	41	0	Goethite	1.5
A29	46	4	50	0	Gibbsite	1.3
A30	49	3	48	0	Gibbsite	1.8
A34	43	13	44	0	Gibbsite	1.6
A35	60	6	34	0	Gibbsite	1.5
A36	54	8	38	0	Gibbsite	1.8
A37	51	9	40	0	Gibbsite	1.8
A38	49	3	48	0	Gibbsite	0.9
Avg.	**56**	**5.6**	**35**			**1.5**
St. Dev.	**12.7**	**3.1**	**15.2**			**0.4**
B1	77	7	15	0	Goethite	3.1
B2	56	9	35	0	None	5.4
B3	28	12	59	0	Gibbsite	4.3
B4	48	19	33	0	Both	2.3
B5	43	19	38	0	None	2.6
B6	65	10	26	0	None	2.7
B8	42	36	22	0	Both	2.2
Avg.	**51.3**	**16**	**32.6**			**3.2**
St. Dev.	**16.2**	**10**	**14.1**			**1.2**
C1	39	13	48	0	Gibbsite	2.1
C2	5	35	60	0	None	4.1
C3	47	10	43	0	None	2.8
C4	32	41	27	0	None	2.7
C5	42	26	31	0	None	2.5
C6	36	11	53	0	None	1.7
C7	11	2	0	87	None	0.6
C8	39	13	48	0	Goethite	2.4
Avg.	**37.4**	**18.9**	**38.8**			**2.4**
St. Dev.	**15.1**	**13.6**	**19.1**			**1.0**
D1	25	6	70	0	Goethite	3.0
D3	12	9	79	0	Both	1.5
D4	43	8	50	0	Gibbsite	2.6
D6	71	4	25	0	None	2.5
D9	0	2	98	0	Goethite	1.2
D10	78	11	11	0	Gibbsite	2.4
D11	21	64	15	0	Both	2.6
D12	21	4	75	0	Goethite	1.8
D13	70	21	10	0	None	3.0
D14	24	0	76	0	Both	-
D15	54	16	31	0	Both	2.4
D16	61	21	19	0	Goethite	2.5
D17	32	63	5	0	Goethite	2.6
D18	11	0	89	0	Goethite	-
D19	37	0	63	0	Goethite	-
Avg.	**37.3**	**15.3**	**47.7**			**2.4**
St. Dev.	**24.4**	**20.8**	**32.5**			**0.6**
E1	17	10	73	0	Both	1.1
E3	15	46	39	0	Gibbsite	-
E4	17	36	47	0	None	3.0
E5	28	44	28	0	Goethite	1.9
E6	7	0	93	0	Gibbsite	-
E7	27	46	27	0	None	1.8
Avg.	**18.5**	**30.3**	**51.2**			**2.0**
St. Dev.	**7.9**	**20.2**	**26.5**			**0.8**
F01	73	18	9	0	Both	2.3
F02	34	55	11	0	Both	2.6
F03	31	55	14	0	Both	2.4

F04	22	57	21	0	Both	2.7
F06	51	2	47	0	None	-
F09	24	55	21	0	Both	2.9
F10	13	50	37	0	Both	2.7
F11	44	37	20	0	None	3.2
F12	33	54	13	0	Goethite	2.8
Avg.	**36.1**	**42.6**	**21.4**			**2.7**
St. Dev.	**17.9**	**19.8**	**12.7**			**0.3**
A22	42	34	24	0	Both	3.1
B7	53	13	34	0	Both	2.2
B9	43	10	48	0	Both	1.9
D2	19	3	78	0	Gibbsite	1.0
D5	54	30	16	0	Goethite	2.9
D7	74	15	11	0	Both	2.0
F5	82	1	17	0	Goethite	-
F7	79	8	0	13	Both	2.1

Note: Semi-quantitative clay mineral estimates based on known diagnostic peaks (Biscaye, 1965; Moore & Reynolds, 1989). The last eight rows did not have accompanying XRF geochemical data, so although they were used in the spatial distribution maps, they were not calculated in the regional averages.

Table C.4 major elemental geochemistry and weathering indices

Site	SiO$_2$ wt%	Al$_2$O$_3$ wt%	Fe$_2$O$_3$ wt%	K$_2$O wt%	Na$_2$O wt%	CaO wt%	MgO wt%	CIA	WIP
A2	72.1	14.1	6.9	1.5	0.1	0.4	0.6	85.6	15.9
A3	77.7	11.2	5.2	1.3	0.1	0.3	0.5	84.9	13.3
A6	67.8	16.2	7.4	1.6	0.0	0.2	0.8	88.6	16.1
A7	74.5	13.4	5.7	1.5	0.0	0.2	0.6	87.1	14.9
A8	73.2	14.5	5.9	1.5	0.0	0.1	0.7	88.4	15.2
A9	76.9	12.8	4.6	0.9	0.0	0.2	0.5	90.5	9.7
A23	60.3	24.5	8.5	1.6	0.0	0.4	0.9	91.0	17.2
A25	64.6	18.5	6.5	2.3	0.0	0.7	1.4	83.3	24.8
A26	71.9	15.2	4.5	2.2	0.0	0.4	0.9	82.8	22.6
A27	71.9	15.4	4.7	2.3	0.0	0.5	1.0	82.1	23.5
A28	69.3	17.5	5.2	2.3	0.0	0.6	1.1	83.1	23.8
A29	65.5	20.0	5.2	2.3	0.0	0.8	1.5	83.4	25.9
A30	71.6	14.7	4.5	2.2	0.5	0.4	0.9	79.1	26.7
A34	61.9	19.8	7.9	2.1	0.4	1.2	0.9	79.6	27.1
A35	78.0	11.3	3.8	1.1	0.0	0.4	0.4	85.6	11.6
A36	75.7	12.2	5.0	1.3	0.1	0.2	0.5	86.7	13.8
A37	76.9	10.0	6.1	1.1	0.0	0.3	0.5	84.3	11.8
A38	82.0	9.1	3.4	1.0	0.1	0.3	0.3	83.8	10.6
Avg.	71.8	15.0	5.6	1.7	0.1	0.4	0.8	85.0	18.0
S.D.	5.9	3.9	1.4	0.5	0.1	0.3	0.3	3.3	6.0
B1	63.5	19.9	6.0	2.2	0.5	1.4	0.8	77.2	29.5
B2	65.8	17.3	6.2	1.9	0.8	1.5	0.7	73.8	29.3
B3	59.7	20.1	8.4	2.4	0.4	2.1	2.6	73.9	36.8
B4	71.1	13.1	6.3	1.8	0.6	0.8	0.5	74.7	24.2
B5	65.5	17.7	7.6	2.5	0.4	0.6	0.5	79.9	27.9
B6	58.9	23.5	7.7	1.7	0.2	1.0	0.7	85.3	21.1
B8	64.2	17.6	9.4	2.2	0.0	0.2	0.8	86.0	21.8
Avg.	64.1	18.4	7.4	2.1	0.4	1.1	0.9	78.7	27.2
S.D.	4.1	3.2	1.3	0.3	0.3	0.6	0.7	5.2	5.5
C1	65.6	17.2	6.8	2.3	0.5	0.9	0.8	77.8	28.6
C2	56.1	23.9	8.1	5.2	0.0	0.6	1.7	77.8	50.7
C3	57.0	21.3	6.3	3.0	0.9	6.2	0.9	57.3	51.7
C4	62.5	20.1	6.2	3.1	0.8	1.0	0.7	75.5	37.9
C5	63.2	19.1	6.1	3.5	0.9	1.1	0.6	72.5	42.1
C6	71.2	14.6	3.6	3.6	1.2	0.8	0.5	66.9	44.4
C7	74.9	13.8	4.1	1.3	0.6	0.9	0.6	77.1	20.7
C8	68.0	15.8	3.9	4.4	1.5	0.6	0.4	65.7	53.7
Avg.	64.8	18.2	5.7	3.3	0.8	1.5	0.8	71.3	41.2
S.D.	6.5	3.5	1.6	1.2	0.4	1.9	0.4	7.4	11.7
D1	59.2	16.8	11.9	1.9	0.0	1.3	1.3	79.4	22.7
D3	60.1	17.8	11.3	1.5	0.0	2.5	1.4	74.0	23.5
D4	72.3	14.6	3.6	2.3	0.0	0.7	1.1	79.4	24.1
D6	77.3	11.5	3.4	2.2	0.0	0.2	0.6	80.5	20.7
D9	51.9	15.9	17.7	0.7	0.0	2.0	1.3	78.1	14.8
D10	82.7	8.4	4.8	1.2	0.0	-0.1	0.6	87.9	11.4
D11	74.1	11.6	7.1	1.7	0.0	0.1	0.5	85.2	16.2
D12	61.6	12.3	13.4	1.3	0.2	1.2	0.9	75.8	18.3
D13	75.5	13.3	3.6	2.9	0.0	0.0	0.5	80.9	26.4
D14	48.9	13.9	18.6	0.7	0.1	1.8	1.1	77.2	13.9
D15	78.1	10.2	4.1	2.1	0.0	0.1	0.6	80.8	19.6
D16	74.4	12.1	5.4	2.4	0.1	0.9	0.6	73.4	25.3
D17	78.2	10.9	3.8	1.7	0.0	0.0	0.5	85.2	16.0
D18	50.6	16.5	18.1	0.8	0.1	2.3	1.5	76.1	17.6
D19	54.9	16.5	15.2	0.9	0.3	1.9	1.1	77.3	18.1
Avg.	66.6	13.5	9.5	1.6	0.1	1.0	0.9	79.4	19.2
S.D.	11.7	2.8	5.9	0.7	0.1	0.9	0.4	4.2	4.5
E1	41.1	12.7	3.9	1.3	0.0	44.0	1.1	13.5	126.3
E3	65.2	12.5	5.0	2.1	0.4	10.6	1.6	35.8	53.5
E4	70.9	16.0	6.4	1.5	0.0	1.0	0.8	82.6	17.1
E5	66.1	10.1	4.1	1.9	0.2	13.4	1.2	27.4	55.5
E6	69.1	10.4	3.8	0.9	0.0	13.0	1.5	29.8	44.6
E7	43.7	13.3	9.9	2.3	0.0	30.4	1.6	18.7	101.6
Avg.	59.3	12.5	5.5	1.7	0.1	18.7	1.3	34.6	66.4
S.D.	13.3	2.2	2.4	0.6	0.2	15.6	0.3	24.8	40.1
F1	64.8	11.5	14.0	2.1	0.1	0.3	0.8	79.2	22.3

F2	62.4	19.3	7.5	3.4	0.0	0.3	1.4	82.0	33.7
F3	65.5	16.6	7.7	3.0	0.0	0.2	1.3	82.0	29.7
F4	65.6	16.7	7.8	3.0	0.0	0.3	1.3	81.3	29.8
F6	70.9	18.4	3.3	1.0	0.0	0.1	0.8	93.8	10.9
F9	71.0	14.3	5.8	2.4	0.2	0.3	1.2	80.5	26.0
F10	62.9	17.1	8.9	3.7	0.0	0.1	2.1	80.5	37.2
F11	76.8	11.1	4.1	1.8	0.0	0.3	0.8	81.5	18.1
F12	73.3	12.6	5.4	2.0	0.3	1.2	0.8	72.1	24.7
Avg.	68.1	15.3	7.2	2.5	0.1	0.3	1.1	81.4	25.8
S.D.	5.0	3.0	3.2	0.9	0.1	0.4	0.5	5.6	8.0
A1	61.5	21.4	8.4	2.0	0.2	0.3	0.9	86.5	17.5
A5	66.1	18.5	7.5	2.1	0.0	0.1	0.8	87.3	22.4
A10	68.5	16.2	7.4	1.6	0.1	0.3	0.7	88.5	20.1

Note: Following calibration with laboratory standards, major elemental geochemistry was used as weight percent (wt%) to plot the discrimination plots in Fig. 6. The weight percent values were converted to molar proportions by dividing each value by the elemental atomic weight and used to calculate the weathering indices. The last three rows did not have accompanying XRD data, so although they were used in the spatial distribution maps, they were not calculated in the regional averages.

Table C.5 Plata River literature review

Site	Latitude	Longitude	Smectite	Illite	Kaolinite	Chlorite	Ill/Smec	Kao/Chl	Source
Pilcomayo mouth	-25.3536	-57.6681	15.0	43.3	16.7	1.7	23.3	0.0	Manassero
Paraguay	-25.3647	-57.6511	18.3	35.0	18.3	6.7	21.7	0.0	Manassero
Arroyo Monte Lindo	-25.8786	-57.875	5.0	65.0	15.0	5.0	10.0	0.0	Manassero
Riacho Pilaga	-26.0811	-57.9872	20.0	20.0	20.0	0.0	40.0	0.0	Manassero
Rio Bermejo	-26.8703	-58.3844	10.0	60.0	5.0	10.0	15.0	0.0	Manassero
Rio Iguazu	-25.5931	-54.5803	6.5	8.5	75.0	2.5	7.5	0.0	Manassero
Rio Parana	-25.5908	-54.5931	5.0	12.5	62.5	10.0	10.0	0.0	Manassero
Rio Negro	-27.4019	-58.7981	5.0	65.0	15.0	10.0	5.0	0.0	Manassero
Rio Uruguay	-25.8758	-54.5583	5.0	32.5	52.5	0.0	10.0	0.0	Manassero
Arroyo San Lorenzo	-32.7197	-60.7275	15.0	55.0	5.0	0.0	25.0	0.0	Manassero
Rio Santa Lucia	-29.0761	-59.2256	10.0	30.0	10.0	0.0	50.0	0.0	Manassero
Rio Corrientes	-30.0167	-59.5367	20.0	20.0	10.0	0.0	50.0	0.0	Manassero
Rio Guayquiraro	-30.3419	-59.5136	20.0	20.0	10.0	0.0	50.0	0.0	Manassero
Rio Feliciano	-31.1069	-59.8789	10.0	40.0	20.0	0.0	30.0	0.0	Manassero
Rio Salado	-31.6556	-60.7442	10.0	55.0	5.0	5.0	25.0	0.0	Manassero
Rio Coronda	-32.4778	-60.7978	20.0	40.0	15.0	0.0	25.0	0.0	Manassero
Rio Carcarana	-32.4436	-60.8056	5.0	70.0	15.0	0.0	10.0	0.0	Manassero
Arroyo Luduena	-32.9069	-60.6769	5.0	70.0	15.0	0.0	10.0	0.0	Manassero
Rio Saladillo	-32.9994	-60.6144	7.5	77.5	5.0	0.0	10.0	0.0	Manassero
Arroyo Pavon	-33.2417	-60.4406	5.0	85.0	0.0	0.0	10.0	0.0	Manassero
Arroyo del Medio	-33.3306	-60.3039	10.0	62.5	5.0	2.5	20.0	0.0	Manassero
Rio Arrecifes	-33.8172	-59.5922	12.5	40.0	10.0	2.5	35.0	0.0	Manassero
Rio Areco	-34.0561	-59.3019	20.0	60.0	15.0	0.0	5.0	0.0	Manassero
1C	-34.8567	-57.9572	16.4	16.9	7.6	0.0	0.0	0.0	Ronco
2B	-34.9686	-57.7798	23.0	23.0	10.1	0.0	0.0	0.0	Ronco
3B	-34.8732	-58.0901	2.9	29.1	0.0	0.0	0.0	0.0	Ronco
4A	-34.9226	-58.0829	12.8	30.0	2.7	0.0	0.0	0.0	Ronco
4B	-34.8783	-58.07	3.7	20.7	0.0	0.0	0.0	0.0	Ronco
5C	-34.8568	-58.0617	21.1	31.3	15.6	0.0	0.0	0.0	Ronco
5D	-34.8095	-58.0417	24.7	34.9	13.1	0.0	0.0	0.0	Ronco
ParanaSF	-31.735	-60.6522	16.0	36.0	32.0	16.0	0.0	0.0	DePetris
Coronda	-31.6802	-60.7362	22.0	42.0	22.0	14.0	0.0	0.0	DePetris
Colastine	-31.6853	-60.6503	17.5	38.5	26.5	17.5	0.0	0.0	DePetris
Salado	-31.6458	-60.7578	23.8	56.0		0.0	0.0	18.0	DePetris
ParanaR	-32.8823	-60.6815	36.0	44.0	13.0	7.0	0.0	0.0	DePetris
Uruguay	-32.4805	-58.2045	32.0	15.0	53.0	0.0	0.0	0.0	DePetris
Buenos Aires	-34.5532	-58.3894	34.0	44.0	13.0	8.0	0.0	0.0	DePetris
La Plata	-34.8175	-57.9034	26.0	44.0		0.0	0.0	31.0	DePetris
1	-22.7615	-64.3382	10.0	73.0	3.0	13.0	0.0	0.0	Bertolino
2	-22.6977	-64.5648	5.0	75.0		20.0	0.0	0.0	Bertolino
3	-23.2275	-64.2064	35.0	56.0	6.0	3.0	0.0	0.0	Bertolino
4	-23.3574	-64.1843	24.0	68.0	1.0	7.0	0.0	0.0	Bertolino
7	-24.2159	-61.9426	26.0	61.0	3.0	9.0	0.0	0.0	Bertolino
8	-25.6508	-60.1357	27.0	63.0	3.0	5.0	0.0	0.0	Bertolino
9	-26.1312	-59.5794	35.0	59.0	2.0	4.0	0.0	0.0	Bertolino
10	-26.6604	-58.634	33.0	57.0	3.0	7.0	0.0	0.0	Bertolino
11	-26.8623	-58.3798	41.0	54.0	2.0	3.0	0.0	0.0	Bertolino
12	-22.3783	-62.5185	10.0	81.0	3.0	7.0	0.0	0.0	Bertolino
13	-26.1818	-58.1594	55.0	30.0	15.0	0.0	0.0	0.0	Bertolino
14	-26.6548	-58.2046	37.0	46.0	15.0	4.0	0.0	0.0	Bertolino
17	-27.0617	-58.5093	27.0	64.0	4.0	7.0	0.0	0.0	Bertolino
B1	-22.1907	-64.6525	5.6	80.1	0.0	0.0	0.0	14.3	McGlue
B17	-22.2477	-64.5878	2.4	79.1	0.0	0.0	0.0	18.5	McGlue
B4	-23.7259	-63.1559	12.7	68.1	0.0	0.0	0.0	19.2	McGlue
B5	-25.3882	-60.3053	25.1	63.1	0.0	0.0	0.0	11.7	McGlue

B6	-23.3594	-63.7195	39.2	55.1	0.0	0.0	0.0	5.6	McGlue
B7	-24.1284	-62.6143	40.3	54.0	0.0	0.0	0.0	5.7	McGlue
B8	-24.0801	-62.3331	32.8	55.3	0.0	0.0	0.0	12.0	McGlue
B9	-26.1149	-59.6022	29.8	57.6	0.0	0.0	0.0	12.5	McGlue
B12	-24.2553	-61.9257	29.7	60.0	0.0	0.0	0.0	10.3	McGlue
B13	-24.4583	-61.5824	23.5	66.0	0.0	0.0	0.0	10.5	McGlue
B14	-25.6551	-60.1295	22.9	64.6	0.0	0.0	0.0	12.5	McGlue
B15	-26.3342	-59.361	19.4	63.3	0.0	0.0	0.0	17.4	McGlue
B16	-26.3326	-59.3599	23.8	67.8	0.0	0.0	0.0	8.3	McGlue
B18	-23.1485	-64.2071	21.3	71.7	0.0	0.0	0.0	7.0	McGlue
B19	-23.3856	-63.6699	17.2	72.1	0.0	0.0	0.0	10.7	McGlue
B20	-23.3856	-63.6698	19.6	69.4	0.0	0.0	0.0	11.0	McGlue
B21	-25.1668	-60.5401	23.5	64.9	0.0	0.0	0.0	11.6	McGlue
B22	-26.5231	-58.8279	33.9	61.0	0.0	0.0	0.0	5.0	McGlue

Note: All available data considered for the n = 84 sampling stations. Average values were reported if duplicate samples were available from the same study. All values were normalized to 100. In the Source column, data were from Manassero, Ronco, DePetris, Bertolino, and McGlue (Depetris & Griffin, 1968; Bertolino & Depetris, 1992; Ronco et al., 2001; Manassero et al., 2008; McGlue et al., 2016).

REFERENCES

Abel, C., Horion, S., Tagesson, T., De Keersmaecker, W., Seddon, A. W. R., Abdi, A. M., & Fensholt, R. (2021). The human–environment nexus and vegetation–rainfall sensitivity in tropical drylands. *Nature Sustainability*, *4*(1), Article 1. https://doi.org/10.1038/s41893-020-00597-z

Adams, E. A., Stoler, J., & Adams, Y. (2020). Water insecurity and urban poverty in the Global South: Implications for health and human biology. *American Journal of Human Biology*, *32*(1), e23368. https://doi.org/10.1002/ajhb.23368

Alavez-Vargas, M., Birkel, C., Corona, A., & Breña-Naranjo, J. A. (2021). Land cover change induced sediment transport behaviour in a large tropical Mexican catchment. *Hydrological Sciences Journal*, *66*(6), 1069–1082. https://doi.org/10.1080/02626667.2021.1903472

Alcântara, E., Barbosa, C., Stech, J., Novo, E., & Shimabukuro, Y. (2009). Improving the spectral unmixing algorithm to map water turbidity Distributions. *Environmental Modelling & Software*, *24*(9), 1051–1061. https://doi.org/10.1016/j.envsoft.2009.02.013

Aleman, J. C., Blarquez, O., Bentaleb, I., Bonté, P., Brossier, B., Carcaillet, C., Gond, V., Gourlet-Fleury, S., Kpolita, A., Lefèvre, I., Oslisly, R., Power, M. J., Yongo, O., Bremond, L., & Favier, C. (2013). Tracking land-cover changes with sedimentary charcoal in the Afrotropics. *The Holocene*, *23*(12), 1853–1862. https://doi.org/10.1177/0959683613508159

Allen, P. A., & Allen, J. R. (2013). *Basin Analysis: Principles and Applications*. John Wiley & Sons.

Almeida, F. F. M. de, Hasui, Y., & Neves, B. B. de B. (1976). The Upper Precambrian of South America. *Boletim IG*, *7*, 45–80. https://doi.org/10.11606/issn.2316-8978.v7i0p45-80

Alvarenga, C. J. S., Boggiani, P. C., Babinski, M., Dardenne, M. A., Figueiredo, M. F., Dantas, E. L., Uhlein, A., Santos, R. V., Sial, A. N., & Trompette, R. (2011). Chapter 45 Glacially influenced sedimentation of the Puga Formation, Cuiabá Group and Jacadigo Group, and associated carbonates of the Araras and Corumbá groups, Paraguay Belt, Brazil. *Geological Society, London, Memoirs*, *36*(1), 487–497. https://doi.org/10.1144/M36.45

Ambrosi, J. P., Nahon, D., & Herbillon, A. J. (1986). The epigenetic replacement of kaolinite by hematite in laterite — petrographic evidence and the mechanisms involved. *Geoderma*, *37*(4), 283–294. https://doi.org/10.1016/0016-7061(86)90030-3

Ang, W. J., Park, E., & Alcantara, E. (2021). Mapping floodplain bathymetry in the middle-lower Amazon River using inundation frequency and field control. *Geomorphology*, *392*, 107937. https://doi.org/10.1016/j.geomorph.2021.107937

Aniceto, K., Moreira-Turcq, P., Cordeiro, R. C., Fraizy, P., Quintana, I., & Turcq, B. (2014). Holocene paleohydrology of Quistococha Lake (Peru) in the upper Amazon Basin: Influence on carbon accumulation. *Palaeogeography, Palaeoclimatology, Palaeoecology*, *415*, 165–174. https://doi.org/10.1016/j.palaeo.2014.08.018

Anshari, G., Peter Kershaw, A., Van Der Kaars, S., & Jacobsen, G. (2004). Environmental change and peatland forest dynamics in the Lake Sentarum area, West Kalimantan, Indonesia. *Journal of Quaternary Science*, *19*(7), 637–655. https://doi.org/10.1002/jqs.879

Aparicio, P., Galán, E., & Ferrell, R. E. (2006). A new kaolinite order index based on XRD profile fitting. *Clay Minerals*, *41*(4), 811–817. https://doi.org/10.1180/0009855064140220

Apitz, S. E. (2011). Sustainable sediment management? *Integrated Environmental Assessment and Management*, *7*(4), 691–693. https://doi.org/10.1002/ieam.264

Appleby, P. G., & Oldfield, F. (1978). The calculation of lead-210 dates assuming a constant rate of supply of unsupported 210Pb to the sediment. *CATENA*, *5*(1), 1–8. https://doi.org/10.1016/S0341-8162(78)80002-2

Appleby, P. G., & Oldfield, F. (1992). *Applications of lead-210 to sedimentation studies*. Clarendon Press.

Archer, C., Penny, A., Templeman, S., McKenzie, M., Hunt, E., Tello Toral, D., Diakhite, M., Nhlapo, T., Mawoko, D., Vergnani, Li., Chamdimba, C., Diop, H., Kalanzi, B., Touitha, Y., Jackson, A., Mchugh, J., Chang, O., Mohamad, Ar., Hunter, E., & Rojas Lopez, M. C. (2020). *State of the Tropics 2020 Report*.

Arienzo, M. M., Maezumi, S. Y., Chellman, N. J., & Iriarte, J. (2019). Pre-Columbian Fire Management Linked to Refractory Black Carbon Emissions in the Amazon. *Fire*, *2*(2), Article 2. https://doi.org/10.3390/fire2020031

Aristizábal, E., Roser, B., & Yokota, S. (2005). Tropical chemical weathering of hillslope deposits and bedrock source in the Aburrá Valley, northern Colombian Andes. *Engineering Geology*, *81*(4), 389–406. https://doi.org/10.1016/j.enggeo.2005.08.001

Armitage, J. J., Duller, R. A., Whittaker, A. C., & Allen, P. A. (2011). Transformation of tectonic and climatic signals from source to sedimentary archive. *Nature Geoscience*, *4*(4), Article 4. https://doi.org/10.1038/ngeo1087

Arribas, M. E., & Arribas, J. (2007). Interpreting carbonate particles in modern continental sands: An example from fluvial sands (Iberian Range, Spain). In J. Arribas, M. J. Johnsson, & S. Critelli (Eds.), *Sedimentary Provenance and Petrogenesis: Perspectives from Petrography and Geochemistry* (Vol. 420, p. 0). Geological Society of America. https://doi.org/10.1130/2006.2420(11)

Assine, M. L. (2005). River avulsions on the Taquari megafan, Pantanal wetland, Brazil. *Geomorphology*, *70*(3), 357–371. https://doi.org/10.1016/j.geomorph.2005.02.013

Assine, M. L., Macedo, H. A., Stevaux, J. C., Bergier, I., Padovani, C. R., & Silva, A. (2015). Avulsive Rivers in the Hydrology of the Pantanal Wetland. In I. Bergier & M. L. Assine (Eds.), *Dynamics of the Pantanal Wetland in South America* (pp. 83–110). Springer International Publishing. https://doi.org/10.1007/698_2015_351

Assine, M. L., Merino, E. R., Pupim, F. do N., Macedo, H. de A., & Santos, M. G. M. dos. (2015). The Quaternary alluvial systems tract of the Pantanal Basin, Brazil. *Brazilian Journal of Geology*, *45*, 475–489. https://doi.org/10.1590/2317-4889201520150014

Assine, M. L., Merino, E. R., Pupim, F. N., Warren, L. V., Guerreiro, R. L., & McGlue, M. M. (2016). Geology and Geomorphology of the Pantanal Basin. In I. Bergier & M. L. Assine (Eds.), *Dynamics of the Pantanal Wetland in South America* (pp. 23–50). Springer International Publishing. https://doi.org/10.1007/698_2015_349

Assine, M. L., & Silva, A. (2009). Contrasting fluvial styles of the Paraguay River in the northwestern border of the Pantanal wetland, Brazil. *Geomorphology*, *113*(3), 189–199. https://doi.org/10.1016/j.geomorph.2009.03.012

Avnimelech, Y., Ritvo, G., Meijer, L. E., & Kochba, M. (2001). Water content, organic carbon and dry bulk density in flooded sediments. *Aquacultural Engineering*, *25*(1), 25–33. https://doi.org/10.1016/S0144-8609(01)00068-1

Balan, E., Fritsch, E., Allard, T., & Calas, G. (2007). Inheritance vs. neoformation of kaolinite during lateritic soil formation: a case study in the middle Amazon Basin. *Clays and Clay Minerals*, *55*(3), 253–259. https://doi.org/10.1346/CCMN.2007.0550303

Balbino, L. C., Bruand, A., Brossard, M., Grimaldi, M., Hajnos, M., & Guimarães, M. F. (2002). Changes in porosity and microaggregation in clayey Ferralsols of the Brazilian Cerrado on clearing for pasture. *European Journal of Soil Science*, *53*(2), 219–230. https://doi.org/10.1046/j.1365-2389.2002.00446.x

Barboza, E., Santos, A., Fernandes, C., & Geraldes, M. (2018). Paraguay Belt lithostratigraphic and tectonic characterization: implications in the evolution of the orogen (Mato Grosso-Brazil). *Journal of Sedimentary Environments*, *3*, 54–73. https://doi.org/10.12957/jse.2018.34219

Barichivich, J., Gloor, E., Peylin, P., Brienen, R. J. W., Schöngart, J., Espinoza, J. C., & Pattnayak, K. C. (2018). Recent intensification of Amazon flooding extremes driven by strengthened Walker circulation. *Science Advances*, *4*(9), eaat8785. https://doi.org/10.1126/sciadv.aat8785

Barlow, J., França, F., Gardner, T. A., Hicks, C. C., Lennox, G. D., Berenguer, E., Castello, L., Economo, E. P., Ferreira, J., Guénard, B., Gontijo Leal, C., Isaac, V., Lees, A. C., Parr, C. L., Wilson, S. K., Young, P. J., & Graham, N. A. J. (2018). The future of hyperdiverse tropical ecosystems. *Nature*, *559*(7715), Article 7715. https://doi.org/10.1038/s41586-018-0301-1

Barshep, D. V., & Worden, R. H. (2023). Hinterland environments of the Late Jurassic northern Weald Basin, England. *Geological Journal*, *n/a*(n/a), 1–23. https://doi.org/10.1002/gj.4720

Bartczak, A., Słowińska, S., Tyszkowski, S., Kramkowski, M., Kaczmarek, H., Kordowski, J., & Słowiński, M. (2019). Ecohydrological Changes and Resilience of a Shallow Lake Ecosystem under Intense Human Pressure and Recent Climate Change. *Water*, *11*(1), Article 1. https://doi.org/10.3390/w11010032

Baud, A., Jenny, J.-P., Francus, P., & Gregory-Eaves, I. (2021). Global acceleration of lake sediment accumulation rates associated with recent human population growth and land-use changes. *Journal of Paleolimnology*, *66*(4), 453–467. https://doi.org/10.1007/s10933-021-00217-6

Bauluz, B., Mayayo, M. J., Yuste, A., & López, J. M. G. (2008). Genesis of kaolinite from Albian sedimentary deposits of the Iberian Range (NE Spain): analysis by XRD, SEM and TEM. *Clay Minerals*, *43*(3), 459–475. https://doi.org/10.1180/claymin.2008.043.3.10

Beck, H. E., Zimmermann, N. E., McVicar, T. R., Vergopolan, N., Berg, A., & Wood, E. F. (2018). Present and future Köppen-Geiger climate classification maps at 1-km resolution. *Scientific Data*, *5*(1), Article 1. https://doi.org/10.1038/sdata.2018.214

Behling, H. (2001). Late Quaternary environmental changes in the Lagoa da Curuça region (eastern Amazonia, Brazil) and evidence of Podocarpus in the Amazon lowland. *Vegetation History and Archaeobotany*, *10*(3), 175–183.

Behling, H., Keim, G., Irion, G., Junk, W., & Nunes de Mello, J. (2001). Holocene environmental changes in the Central Amazon Basin inferred from Lago Calado (Brazil). *Palaeogeography, Palaeoclimatology, Palaeoecology*, *173*(1), 87–101. https://doi.org/10.1016/S0031-0182(01)00321-2

Benedetti, M. M., Curi, N., Sparovek, G., Carvalho Filho, A. de, & Silva, S. H. G. (2011). Updated Brazilian's Georeferenced Soil Database – an Improvement for International Scientific Information Exchanging. In *Principles, Application, and Assessment in Soil Science* (p. 408).

Bennett, K., & Buck, C. E. (2016). Interpretation of lake sediment accumulation rates. *The Holocene*, *26*(7), 1092–1102. https://doi.org/10.1177/0959683616632880

Bergier, I., Assine, M. L., McGlue, M. M., Alho, C. J. R., Silva, A., Guerreiro, R. L., & Carvalho, J. C. (2018). Amazon rainforest modulation of water security in the Pantanal wetland. *Science of The Total Environment*, *619–620*, 1116–1125. https://doi.org/10.1016/j.scitotenv.2017.11.163

Berner, R. A., & Holdren, G. R. (1979). Mechanism of feldspar weathering—II. Observations of feldspars from soils. *Geochimica et Cosmochimica Acta*, *43*(8), 1173–1186. https://doi.org/10.1016/0016-7037(79)90110-8

Bertassoli, D. J., Sawakuchi, A. O., Sawakuchi, H. O., Pupim, F. N., Hartmann, G. A., McGlue, M. M., Chiessi, C. M., Zabel, M., Schefuß, E., Pereira, T. S., Santos, R. A., Faustino, S. B., Oliveira, P. E., & Bicudo, D. C. (2017). The Fate of Carbon in Sediments of the Xingu and Tapajós Clearwater Rivers, Eastern Amazon.

Frontiers in Marine Science, *4*.
https://www.frontiersin.org/articles/10.3389/fmars.2017.00044

Bertolini, G., Marques, J. C., Hartley, A. J., Basei, M. A. S., Frantz, J. C., & Santos, P. R. (2021). Determining sediment provenance history in a Gondwanan erg: Botucatu formation, Northern Paraná Basin, Brazil. *Sedimentary Geology*, *417*, 105883. https://doi.org/10.1016/j.sedgeo.2021.105883

Bertolino, S., & Depetris, P. (1992). *Mineralogy of the Clay-Sized Suspended Load from Headwater Tributaries on the Paraná River: Bermejo, Pilcomayo, and Paraguay Rivers* (Vol. 52, pp. 19–31).

Bezerra, M. A. de O. (1999). *O uso de multi-traçadores na reconstrução do Holoceno no Pantanal Mato-grossense* [Dissertation]. Universidade Federal de São Carlos.

Bezerra, M. A. de O., & Mozeto, A. A. (2008). Deposição de carbono orgânico na planície de inundação do rio Paraguai durante o holoceno médio. *Oecologia Brasiliensis*, *12*(1), 14.

Bhattacharyya, T., PAL, D. K., & SRIVASTAVA, P. (2000). Formation of gibbsite in the presence of 2:1 minerals: an example from Ultisols of northeast India. *Clay Minerals*, *35*(5), 827–840.

Binford, M. W., Kahl, J. S., & Norton, S. A. (1993). Interpretation of ^{210}Pb profiles and verification of the CRS dating model in PIRLA project lake sediment cores. *Journal of Paleolimnology*, *9*(3), 275–296. https://doi.org/10.1007/BF00677218

Biscaye, P. E. (1965). Mineralogy and Sedimentation of Recent Deep-Sea Clay in the Atlantic Ocean and Adjacent Seas and Oceans. *GSA Bulletin*, *76*(7), 803–832. https://doi.org/10.1130/0016-7606(1965)76[803:MASORD]2.0.CO;2

Biswas, M., & Dhara, P. (2019). Evolutionary characteristics of meander cut-off— A hydro-morphological study of the Jalangi River, West Bengal, India. *Arabian Journal of Geosciences*, *12*(21), 667. https://doi.org/10.1007/s12517-019-4711-7

Blaauw, M., & Christen, J. A. (2005). Radiocarbon Peat Chronologies and Environmental Change. *Journal of the Royal Statistical Society Series C: Applied Statistics*, *54*(4), 805–816. https://doi.org/10.1111/j.1467-9876.2005.00516.x

Blatt, H. (1985). Provenance studies and mudrocks. *Journal of Sedimentary Research*, *55*(1), 69–75. https://doi.org/10.1306/212F8611-2B24-11D7-8648000102C1865D

Boggiani, P. C., Coimbra, A. M., & Coutinho, J. M. V. (1995). Quaternary limestones of the Pantanal area, Brazil. *Anais Da Academia Brasileira de Ciências*, *67*(3), 343–349.

Bonotto, D. M., & Vergotti, M. (2015). 210Pb and compositional data of sediments from Rondonian lakes, Madeira River basin, Brazil. *Applied Radiation and Isotopes*, *99*, 5–19. https://doi.org/10.1016/j.apradiso.2015.02.002

Braga, L. G., Pierosan, R., & Geraldes, M. C. (2019). Paleoproterozoic (2.0 Ga) volcano-plutonism in the southeastern region of the Amazon Craton: Petrological aspects and geotectonic implications. *Geological Journal*, *55*(6), 4352–4374. https://doi.org/10.1002/gj.3686

Bravo, J. M., Allasia, D., Paz, A. R., Collischonn, W., & Tucci, C. E. M. (2012). Coupled Hydrologic-Hydraulic Modeling of the Upper Paraguay River Basin. *Journal of Hydrologic Engineering*, *17*(5), 635–646. https://doi.org/10.1061/(ASCE)HE.1943-5584.0000494

Bremond, L., Favier, C., Ficetola, G. F., Tossou, M. G., Akouégninou, A., Gielly, L., Giguet-Covex, C., Oslisly, R., & Salzmann, U. (2017). Five thousand years of tropical lake sediment DNA records from Benin. *Quaternary Science Reviews*, *170*, 203–211. https://doi.org/10.1016/j.quascirev.2017.06.025

Brewer, C. J., Hampson, G. J., Whittaker, A. C., Roberts, G. G., & Watkins, S. E. (2020). Comparison of methods to estimate sediment flux in ancient sediment routing systems. *Earth-Science Reviews*, *207*, 103217. https://doi.org/10.1016/j.earscirev.2020.103217

Briddon, C. L., McGowan, S., Metcalfe, S. E., Panizzo, V., Lacey, J., Engels, S., Leng, M., Mills, K., Shafiq, M., & Idris, M. (2020). Diatoms in a sediment core from a flood pulse wetland in Malaysia record strong responses to human impacts and hydro-climate over the past 150 years. *Geo: Geography and Environment*, *7*(1), e00090. https://doi.org/10.1002/geo2.90

Brosens, L., Campforts, B., Robinet, J., Vanacker, V., Opfergelt, S., Ameijeiras-Mariño, Y., Minella, J. P. G., & Govers, G. (2020). Slope Gradient Controls Soil Thickness and Chemical Weathering in Subtropical Brazil: Understanding Rates and Timescales of Regional Soilscape Evolution Through a Combination of Field Data and Modeling. *Journal of Geophysical Research: Earth Surface*, *125*(6), e2019JF005321. https://doi.org/10.1029/2019JF005321

Brown, G., & Brindley, G. W. (1980). X-ray Diffraction Procedures for Clay Mineral Identification. In G. W. Brindley & G. Brown (Eds.), *Crystal Structures of Clay Minerals and their X-Ray Identification* (Vol. 5, p. 0). Mineralogical Society of Great Britain and Ireland. https://doi.org/10.1180/mono-5.5

Brugger, S. O., Gobet, E., van Leeuwen, J. F. N., Ledru, M.-P., Colombaroli, D., van der Knaap, W. O., Lombardo, U., Escobar-Torrez, K., Finsinger, W., Rodrigues, L., Giesche, A., Zarate, M., Veit, H., & Tinner, W. (2016). Long-term man–environment interactions in the Bolivian Amazon: 8000 years of vegetation dynamics. *Quaternary Science Reviews*, *132*, 114–128. https://doi.org/10.1016/j.quascirev.2015.11.001

Buehler, H. A., Weissmann, G. S., Scuderi, L. A., & Hartley, A. J. (2011). Spatial and Temporal Evolution of an Avulsion on the Taquari River Distributive Fluvial System from Satellite Image Analysis. *Journal of Sedimentary Research*, *81*(8), 630–640. https://doi.org/10.2110/jsr.2011.040

Burbridge, R. E., Mayle, F. E., & Killeen, T. J. (2004). Fifty-thousand-year vegetation and climate history of Noel Kempff Mercado National Park, Bolivian Amazon. *Quaternary Research*, *61*(2), 215–230. https://doi.org/10.1016/j.yqres.2003.12.004

Busker, T., de Roo, A., Gelati, E., Schwatke, C., Adamovic, M., Bisselink, B., Pekel, J.-F., & Cottam, A. (2019). A global lake and reservoir volume analysis using a

surface water dataset and satellite altimetry. *Hydrology and Earth System Sciences*, *23*(2), 669–690. https://doi.org/10.5194/hess-23-669-2019

Camargo, M. N., & Bennema, J. (1966). Delineamento esquemático dos solos do Brasil. *Pesquisa Agropecuária Brasileira*, *1*(1), Article 1.

Campodonico, V. A., García, M. G., & Pasquini, A. I. (2016). The geochemical signature of suspended sediments in the Parana River basin: Implications for provenance, weathering and sedimentary recycling. *CATENA*, *143*, 201–214. https://doi.org/10.1016/j.catena.2016.04.008

Capaldi, T. N., George, S. W. M., Hirtz, J. A., Horton, B. K., & Stockli, D. F. (2019). Fluvial and Eolian Sediment Mixing During Changing Climate Conditions Recorded in Holocene Andean Foreland Deposits From Argentina (31–33°S). *Frontiers in Earth Science*, *7*. https://www.frontiersin.org/articles/10.3389/feart.2019.00298

Carabajal, C. C., & Boy, J.-P. (2021). Lake and reservoir volume variations in South America from radar altimetry, ICESat laser altimetry, and GRACE time-variable gravity. *Advances in Space Research*, *68*(2), 652–671. https://doi.org/10.1016/j.asr.2020.04.022

Caracciolo, L. (2020). Sediment generation and sediment routing systems from a quantitative provenance analysis perspective: Review, application and future development. *Earth-Science Reviews*, *209*, 103226. https://doi.org/10.1016/j.earscirev.2020.103226

Carlson, K. M., Curran, L. M., Ponette-González, A. G., Ratnasari, D., Ruspita, Lisnawati, N., Purwanto, Y., Brauman, K. A., & Raymond, P. A. (2014). Influence of watershed-climate interactions on stream temperature, sediment yield, and metabolism along a land use intensity gradient in Indonesian Borneo. *Journal of Geophysical Research: Biogeosciences*, *119*(6), 1110–1128. https://doi.org/10.1002/2013JG002516

Carrapa, B., Trimble, J. D., & Stockli, D. F. (2011). Patterns and timing of exhumation and deformation in the Eastern Cordillera of NW Argentina revealed by (U-Th)/He thermochronology. *Tectonics*, *30*(3). https://doi.org/10.1029/2010TC002707

Cedraz, V., Julià, J., & Assumpção, M. (2020). Joint Inversion of Receiver Functions and Surface-Wave Dispersion in the Pantanal Wetlands: Implications for Basin Formation. *Journal of Geophysical Research: Solid Earth*, *125*(2), e2019JB018337. https://doi.org/10.1029/2019JB018337

Center for International Earth Science Information Network - CIESIN - Columbia University. (2018). *Gridded Population of the World, Version 4 (GPWv4): Population Density, Revision 11* [Data set]. NASA Socioeconomic Data and Applications Center (SEDAC). https://doi.org/10.7927/H49C6VHW

Certini, G., Wilson, M. J., Hillier, S. J., Fraser, A. R., & Delbos, E. (2006). Mineral weathering in trachydacitic-derived soils and saprolites involving formation of

embryonic halloysite and gibbsite at Mt. Amiata, Central Italy. *Geoderma*, *133*(3), 173–190. https://doi.org/10.1016/j.geoderma.2005.07.005

Chambers, M. R. (1987). The freshwater lakes of Papua New Guinea: an inventory and limnological review. *Journal of Tropical Ecology*, *3*(1), 1–23. https://doi.org/10.1017/S0266467400001073

Chambers, P. A., Lacoul, P., Murphy, K. J., & Thomaz, S. M. (2008). Global diversity of aquatic macrophytes in freshwater. In E. V. Balian, C. Lévêque, H. Segers, & K. Martens (Eds.), *Freshwater Animal Diversity Assessment* (pp. 9–26). Springer Netherlands. https://doi.org/10.1007/978-1-4020-8259-7_2

Chamley, H. (1989). *Clay Sedimentology*. Springer. https://doi.org/10.1007/978-3-642-85916-8

Chant, S. H., & McIlwaine, C. (2009). *Geographies of Development in the 21st Century: An Introduction to the Global South*. Edward Elgar Publishing.

Chase, C. G., Sussman, A. J., & Coblentz, D. D. (2009). Curved Andes: Geoid, forebulge, and flexure. *Lithosphere*, *1*(6), 358–363. https://doi.org/10.1130/L67.1

Chiang, J. C. H., & Friedman, A. R. (2012). Extratropical Cooling, Interhemispheric Thermal Gradients, and Tropical Climate Change. *Annual Review of Earth and Planetary Sciences*, *40*(1), 383–412. https://doi.org/10.1146/annurev-earth-042711-105545

Cleaves, E. T., Godfrey, A. E., & Bricker, O. P. (1970). Geochemical Balance of a Small Watershed and Its Geomorphic Implications. *GSA Bulletin*, *81*(10), 3015–3032. https://doi.org/10.1130/0016-7606(1970)81[3015:GBOASW]2.0.CO;2

Clemens, S. C., Prell, W. L., & Howard, W. R. (1987). Retrospective dry bulk density estimates from southeast Indian Ocean sediments — Comparison of water loss and chloride-ion methods. *Marine Geology*, *76*, 57–69. https://doi.org/10.1016/0025-3227(87)90017-X

Cohen, A., McGlue, M., Ellis, G., Zani, H., Swarzenski, P., Assine, M., & Silva, A. (2015). Lake formation, characteristics, and evolution in retroarc deposystems: A synthesis of the modern Andean orogen and its associated basins. *Memoir of the Geological Society of America*, *212*, 309–335. https://doi.org/10.1130/2015.1212(16)

Cole, M. M. (1960). Cerrado, Caatinga and Pantanal: The Distribution and Origin of the Savanna Vegetation of Brazil. *The Geographical Journal*, *126*(2), 168–179. https://doi.org/10.2307/1793957

Colloff, M. J., & Baldwin, D. S. (2010). Resilience of floodplain ecosystems in a semi-arid environment. *The Rangeland Journal*, *32*(3), 305–314. https://doi.org/10.1071/RJ10015

Conrad, O., Bechtel, B., Bock, M., Dietrich, H., Fischer, E., Gerlitz, L., Wehberg, J., Wichmann, V., & Böhner, J. (2015). System for Automated Geoscientific Analyses (SAGA) v. 2.1.4. *Geoscientific Model Development*, *8*(7), 1991–2007. https://doi.org/10.5194/gmd-8-1991-2015

Cordani, U. G., Teixeira, W., Tassinari, C. C. G., Coutinho, J. M. V., & Ruiz, A. S. (2010). The Rio Apa Craton in Mato Grosso do Sul (Brazil) and northern Paraguay: Geochronological evolution, correlations and tectonic implications for Rodinia and Gondwana. *American Journal of Science*, *310*(9), 981–1023. https://doi.org/10.2475/09.2010.09

Cordeiro, R. C., Turcq, P. F. M., Turcq, B. J., Moreira, L. S., Rodrigues, R. de C., Costa, R. L. da, Sifeddine, A., & Filho, F. F. L. S. (2008). Acumulação de carbono em lagos amazônicos como indicador de eventos paleoclimáticos e antrópicos. *Oecologia Brasiliensis*, *12*(1), 13.

Coringa, E. de A. O., Couto, E. G., Otero Perez, X. L., & Torrado, P. V. (2012). Atributos de solos hidromórficos no Pantanal Norte Matogrossense. *Acta Amazonica*, *42*, 19–28. https://doi.org/10.1590/S0044-59672012000100003

Correa, J. C., Cavallaro, F. A., Garcia, R. H. L., Santos, R. S., Amade, R. A., Bernardes, T. L. da S., Velo, A. F., Mesquita, C. H., & Hamada, M. M. (2021). Chemical and physical analysis of sandstone rock from Botucatu Formation. *Brazilian Journal of Radiation Sciences*, *9*(1A), Article 1A. https://doi.org/10.15392/bjrs.v9i1A.1479

Costa, M. P. F., & Telmer, K. H. (2006). Utilizing SAR imagery and aquatic vegetation to map fresh and brackish lakes in the Brazilian Pantanal wetland. *Remote Sensing of Environment*, *105*(3), 204–213. https://doi.org/10.1016/j.rse.2006.06.014

Coutinho, B. A., Pott, V. J., Arrua, B. A., Aoki, C., & Pott, A. (2018). Ecological succession of aquatic macrophytes on floating meadows in the Pantanal wetland. *Brazilian Journal of Botany*, *41*(1), 65–75. https://doi.org/10.1007/s40415-017-0425-9

Covault, J. A., Romans, B. W., Fildani, A., McGann, M., & Graham, S. A. (2010). Rapid Climatic Signal Propagation from Source to Sink in a Southern California Sediment-Routing System. *The Journal of Geology*, *118*(3), 247–259. https://doi.org/10.1086/651539

Crawley, M. J. (2012). *The R Book*. John Wiley & Sons.

Crisman, T. L., Mitraki, C., & Zalidis, G. (2005). Integrating vertical and horizontal approaches for management of shallow lakes and wetlands. *Ecological Engineering*, *24*(4), 379–389. https://doi.org/10.1016/j.ecoleng.2005.01.006

Cross, B. K., & Moore, B. C. (2014). Lake and reservoir volume: Hydroacoustic survey resolution and accuracy. *Lake and Reservoir Management*, *30*(4), 405–411. https://doi.org/10.1080/10402381.2014.960115

Cruz, A. T., Dinis, P. A., Lucic, M., & Gomes, A. (2022). Spatial variations in sediment production and surface transformations in subtropical fluvial basins (Caculuvar River, south-west Angola): Implications for the composition of sedimentary deposits. *The Depositional Record*, *9*(1), 83–98. https://doi.org/10.1002/dep2.208

Darby, S. E., Langdon, P. G., Best, J. L., Leyland, J., Hackney, C. R., Marti, M., Morgan, P. R., Ben, S., Aalto, R., Parsons, D. R., Nicholas, A. P., & Leng, M. J. (2020).

Drainage and erosion of Cambodia's great lake in the middle-late Holocene: The combined role of climatic drying, base-level fall and river capture. *Quaternary Science Reviews*, *236*, 106265. https://doi.org/10.1016/j.quascirev.2020.106265

Davaud, E., & Girardclos, S. (2001). Recent Freshwater Ooids and Oncoids from Western Lake Geneva (Switzerland): Indications of a Common Organically Mediated Origin. *Journal of Sedimentary Research*, *71*(3), 423–429. https://doi.org/10.1306/2DC40950-0E47-11D7-8643000102C1865D

Dearing, J. A., & Jones, R. T. (2003). Coupling temporal and spatial dimensions of global sediment flux through lake and marine sediment records. *Global and Planetary Change*, *39*(1), 147–168. https://doi.org/10.1016/S0921-8181(03)00022-5

Debret, M., Bentaleb, I., Sebag, D., Favier, C., Nguetsop, V., Fontugne, M., Oslisly, R., & Ngomanda, A. (2014). Influence of inherited paleotopography and water level rise on the sedimentary infill of Lake Ossa (S Cameroon) inferred by continuous color and bulk organic matter analyses. *Palaeogeography, Palaeoclimatology, Palaeoecology*, *411*, 110–121. https://doi.org/10.1016/j.palaeo.2014.06.021

DeCelles, P. G., & Giles, K. A. (1996). Foreland basin systems. *Basin Research*, *8*(2), 105–123. https://doi.org/10.1046/j.1365-2117.1996.01491.x

Decelles, P. G., & Hertel, F. (1989). Petrology of fluvial sands from the Amazonian foreland basin, Peru and Bolivia. *GSA Bulletin*, *101*(12), 1552–1562. https://doi.org/10.1130/0016-7606(1989)101<1552:POFSFT>2.3.CO;2

Deckers, J., Nachtergaele, F., & Spaargaren, O. (2003). Tropical soils in the classification systems of USDA, FAO and WRB. *Evolution of Tropical Soil Science: Past and Future: Workshop Brussels, 6 March 2002*, 79–94.

Deconinck, J. F., Strasser, A., & Debrabant, P. (1988). Formation of illitic minerals at surface temperatures in Purbeckian sediments (Lower Berriasian, Swiss and French Jura). *Clay Minerals*, *23*(1), 91–103. https://doi.org/10.1180/claymin.1988.023.1.09

Delarmelinda, E. A., Souza Júnior, V. S. de, Wadt, P. G. S., Deng, Y., Campos, M. C. C., & Câmara, E. R. G. (2017). Soil-landscape relationship in a chronosequence of the middle Madeira River in southwestern Amazon, Brazil. *CATENA*, *149*, 199–208. https://doi.org/10.1016/j.catena.2016.09.021

Depetris, P. J., & Griffin, J. J. (1968). Suspended Load in the Río De La Plata Drainage Basin. *Sedimentology*, *11*(1–2), 53–60. https://doi.org/10.1111/j.1365-3091.1968.tb00840.x

Depetris, P., & Probst, J.-L. (1998). Variability of the Chemical Index of Alteration (CIA) in the Paraná River Suspended Load. *Mineralogical Magazine*, *62A*. https://doi.org/10.1180/minmag.1998.62A.1.193

Devol, A. H., Zaret, T. M., & Forsberg, B. R. (1984). Sedimentary organic matter diagenesis and its relation to the carbon budget of tropical Amazon floodplain lakes. *SIL Proceedings, 1922-2010*, *22*(2), 1299–1304. https://doi.org/10.1080/03680770.1983.11897489

Dias, F. L., Assumpção, M., Facincani, E. M., França, G. S., Assine, M. L., Paranhos Filho, A. C., & Gamarra, R. M. (2016). The 2009 earthquake, magnitude m_b 4.8, in the Pantanal Wetlands, west-central Brazil. *Anais Da Academia Brasileira de Ciências*, *88*, 1253–1264. https://doi.org/10.1590/201620140507

Dickinson, W. R. (1985). Interpreting Provenance Relations from Detrital Modes of Sandstones. In G. G. Zuffa (Ed.), *Provenance of Arenites* (pp. 333–361). Springer Netherlands. https://doi.org/10.1007/978-94-017-2809-6_15

Dickinson, W. R., Beard, L. S., Brakenridge, G. R., ERJAVEC, J. L., Ferguson, R. C., Inman, K. F., Knepp, R. A., Lindberg, F. A., & Ryberg, P. T. (1983). Provenance of North American Phanerozoic sandstones in relation to tectonic setting. *GSA Bulletin*, *94*(2), 222–235. https://doi.org/10.1130/0016-7606(1983)94<222:PONAPS>2.0.CO;2

dos Santos Vila da Silva, J., Pott, A., & Chaves, J. V. B. (2021). Classification and Mapping of the Vegetation of the Brazilian Pantanal. In G. A. Damasceno-Junior & A. Pott (Eds.), *Flora and Vegetation of the Pantanal Wetland* (pp. 11–38). Springer International Publishing. https://doi.org/10.1007/978-3-030-83375-6_2

Drever, J. I. (1973). The preparation of oriented clay mineral specimens for X-ray diffraction analysis by a filter-membrane peel technique. *American Mineralogist*, *58*(5–6), 553–554.

Eberl, D. D., Farmer, V. C., Barrer, R. M., Fowden, L., Barrer, R. M., & Tinker, P. B. (1997). Clay mineral formation and transformation in rocks and soils. *Philosophical Transactions of the Royal Society of London. Series A, Mathematical and Physical Sciences*, *311*(1517), 241–257. https://doi.org/10.1098/rsta.1984.0026

Elenga, H., Schwartz, D., Vincens, A., Bertaux, J., Namur, C. de, Martin, L., Wirrmann, D., & Servant, M. (1996). Diagramme pollinique holocène du Lac Kitina (Congo): mise en évidence de changements paléobotaniques et paléoclimatiques dans le massif forestier du Mayombe. *Comptes Rendus de l'Académie des Sciences, Paris, série 2a*, *323*, 403–410.

Erenstein, O. (2006). Intensification or extensification? Factors affecting technology use in peri-urban lowlands along an agro-ecological gradient in West Africa. *Agricultural Systems*, *90*(1), 132–158. https://doi.org/10.1016/j.agsy.2005.12.005

Erwin, T. L. (1984). Tambopata Reserved Zone, Madre de Dios, Peru: history and description of the reserve. *Revista Peruana de Entomología*, *27*, 1–8.

Evenson, R. E., & Gollin, D. (2003). Assessing the Impact of the Green Revolution, 1960 to 2000. *Science*, *300*(5620), 758–762. https://doi.org/10.1126/science.1078710

Fagundes, J. R. T., & Zuquette, L. V. (2011). Sorption behavior of the sandy residual unconsolidated materials from the sandstones of the Botucatu Formation, the main aquifer of Brazil. *Environmental Earth Sciences*, *62*(4), 831–845. https://doi.org/10.1007/s12665-010-0570-y

Faleiros, F. M., Pavan, M., Remédio, M. J., Rodrigues, J. B., Almeida, V. V., Caltabeloti, F. P., Pinto, L. G. R., Oliveira, A. A., Pinto de Azevedo, E. J., & Costa, V. S.

(2016). Zircon U–Pb ages of rocks from the Rio Apa Cratonic Terrane (Mato Grosso do Sul, Brazil): New insights for its connection with the Amazonian Craton in pre-Gondwana times. *Gondwana Research*, *34*, 187–204. https://doi.org/10.1016/j.gr.2015.02.018

Fantin-Cruz, I., de Oliveira, M. D., Campos, J. A., de Campos, M. M., de Souza Ribeiro, L., Mingoti, R., de Souza, M. L., Pedrollo, O., & Hamilton, S. K. (2020). Further Development of Small Hydropower Facilities Will Significantly Reduce Sediment Transport to the Pantanal Wetland of Brazil. *Frontiers in Environmental Science*, *8*. https://www.frontiersin.org/articles/10.3389/fenvs.2020.577748

FAO. (1970). *Soil map of the world IV*. FAO.

Fávaro, D. I. T., Damatto, S. R., Silva, P. S. C., Riga, A. A., Sakamoto, A. Y., & Mazzilli, B. P. (2006). Chemical characterization and 210Pb dating in wetland sediments from the Nhecolândia Pantanal Pond, Brazil. *Journal of Radioanalytical and Nuclear Chemistry*, *269*(3), 719–726. https://doi.org/10.1007/s10967-006-0292-5

Fedo, C. M., Wayne Nesbitt, H., & Young, G. M. (1995). Unraveling the effects of potassium metasomatism in sedimentary rocks and paleosols, with implications for paleoweathering conditions and provenance. *Geology*, *23*(10), 921–924. https://doi.org/10.1130/0091-7613(1995)023<0921:UTEOPM>2.3.CO;2

Fernandes, L. A., & Magalhães Ribeiro, C. M. (2015). Evolution and palaeoenvironment of the Bauru Basin (Upper Cretaceous, Brazil). *Journal of South American Earth Sciences*, *61*, 71–90. https://doi.org/10.1016/j.jsames.2014.11.007

Fick, S. E., & Hijmans, R. J. (2017). WorldClim 2: new 1-km spatial resolution climate surfaces for global land areas. *International Journal of Climatology*, *37*(12), 4302–4315. https://doi.org/10.1002/joc.5086

Forsberg, B., Godoy, J. M., Victoria, R., & Martinelli, L. A. (1989). Development and erosion in the Brazilian Amazon: A geochronological case study. *GeoJournal*, *19*(4), 399–405. https://doi.org/10.1007/BF00176909

França, A. B., Arajo, L. M., Maynard, J. B., & Potter, P. E. (2003). Secondary porosity formed by deep meteoric leaching: Botucatu eolianite, southern South America. *AAPG Bulletin*, *87*(7), 1073–1082.

Furian, S., Barbiéro, L., Boulet, R., Curmi, P., Grimaldi, M., & Grimaldi, C. (2002). Distribution and dynamics of gibbsite and kaolinite in an oxisol of Serra do Mar, southeastern Brazil. *Geoderma*, *106*(1), 83–100. https://doi.org/10.1016/S0016-7061(01)00117-3

Furian, S., Martins, E. R. C., Parizotto, T. M., Rezende-Filho, A. T., Victoria, R. L., & Barbiero, L. (2013). Chemical diversity and spatial variability in myriad lakes in Nhecolândia in the Pantanal wetlands of Brazil. *Limnology and Oceanography*, *58*(6), 2249–2261. https://doi.org/10.4319/lo.2013.58.6.2249

Furquim, S. A. C., Barbiéro, L., Graham, R. C., de Queiroz Neto, J. P., Ferreira, R. P. D., & Furian, S. (2010). Neoformation of micas in soils surrounding an alkaline-

saline lake of Pantanal wetland, Brazil. *Geoderma*, *158*(3), 331–342. https://doi.org/10.1016/j.geoderma.2010.05.015

Furtado, J. I., & Mori, S. (2012). *Tasek Bera: The Ecology of a Freshwater Swamp*. Springer Science & Business Media.

Garreaud, R. D., Vuille, M., Compagnucci, R., & Marengo, J. (2009). Present-day South American climate. *Palaeogeography, Palaeoclimatology, Palaeoecology*, *281*(3), 180–195. https://doi.org/10.1016/j.palaeo.2007.10.032

Garzanti, E., Andó, S., France-Lanord, C., Censi, P., Vignola, P., Galy, V., & Lupker, M. (2011). Mineralogical and chemical variability of fluvial sediments 2. Suspended-load silt (Ganga–Brahmaputra, Bangladesh). *Earth and Planetary Science Letters*, *302*(1), 107–120. https://doi.org/10.1016/j.epsl.2010.11.043

Garzanti, E., Andò, S., France-Lanord, C., Vezzoli, G., Censi, P., Galy, V., & Najman, Y. (2010). Mineralogical and chemical variability of fluvial sediments: 1. Bedload sand (Ganga–Brahmaputra, Bangladesh). *Earth and Planetary Science Letters*, *299*(3), 368–381. https://doi.org/10.1016/j.epsl.2010.09.017

Garzanti, E., Andò, S., & Vezzoli, G. (2008). Settling equivalence of detrital minerals and grain-size dependence of sediment composition. *Earth and Planetary Science Letters*, *273*(1), 138–151. https://doi.org/10.1016/j.epsl.2008.06.020

Garzanti, E., Andò, S., & Vezzoli, G. (2009). Grain-size dependence of sediment composition and environmental bias in provenance studies. *Earth and Planetary Science Letters*, *277*(3), 422–432. https://doi.org/10.1016/j.epsl.2008.11.007

Garzanti, E., Capaldi, T., Vezzoli, G., Limonta, M., & Sosa, N. (2021). Transcontinental retroarc sediment routing controlled by subduction geometry and climate change (Central and Southern Andes, Argentina). *Basin Research*, *33*(6), 3406–3437. https://doi.org/10.1111/bre.12607

Garzanti, E., He, J., Barbarano, M., Resentini, A., Li, C., Yang, L., Yang, S., & Wang, H. (2021). Provenance versus weathering control on sediment composition in tropical monsoonal climate (South China) - 2. Sand petrology and heavy minerals. *Chemical Geology*, *564*, 119997. https://doi.org/10.1016/j.chemgeo.2020.119997

Garzanti, E., Limonta, M., Vezzoli, G., & Sosa, N. (2021). From Patagonia to Río de la Plata: Multistep long-distance littoral transport of Andean volcaniclastic sand along the Argentine passive margin. *Sedimentology*, *68*(7), 3357–3384. https://doi.org/10.1111/sed.12902

Garzanti, E., Padoan, M., Andò, S., Resentini, A., Vezzoli, G., & Lustrino, M. (2013). Weathering and Relative Durability of Detrital Minerals in Equatorial Climate: Sand Petrology and Geochemistry in the East African Rift. *The Journal of Geology*, *121*(6), 547–580. https://doi.org/10.1086/673259

Garzanti, E., Padoan, M., Setti, M., López-Galindo, A., & Villa, I. M. (2014). Provenance versus weathering control on the composition of tropical river mud (southern Africa). *Chemical Geology*, *366*, 61–74. https://doi.org/10.1016/j.chemgeo.2013.12.016

Garzanti, E., Pastore, G., Resentini, A., Vezzoli, G., Vermeesch, P., Ncube, L., Niekerk, H. J. V., Jouet, G., & Dall'Asta, M. (2021). The Segmented Zambezi Sedimentary System from Source to Sink: 1. Sand Petrology and Heavy Minerals. *The Journal of Geology*, *129*(4), 343–369. https://doi.org/10.1086/715792

Garzanti, E., Resentini, A., Vezzoli, G., Andò, S., Malusà, M., & Padoan, M. (2012). Forward compositional modelling of Alpine orogenic sediments. *Sedimentary Geology*, *280*, 149–164. https://doi.org/10.1016/j.sedgeo.2012.03.012

Garzanti, E., Vermeesch, P., Vezzoli, G., Andò, S., Botti, E., Limonta, M., Dinis, P., Hahn, A., Baudet, D., De Grave, J., & Yaya, N. K. (2019). Congo River sand and the equatorial quartz factory. *Earth-Science Reviews*, *197*, 102918. https://doi.org/10.1016/j.earscirev.2019.102918

Geno, K. R., & Chafetz, H. S. (1982). Petrology of Quaternary fluvial low-magnesian calcite coated grains from central Texas. *Journal of Sedimentary Research*, *52*(3), 833–842. https://doi.org/10.1306/212F8067-2B24-11D7-8648000102C1865D

Gharibreza, M., & Ashraf, M. A. (2014). Sedimentation Rate in Bera Lake. In M. Gharibreza & M. A. Ashraf (Eds.), *Applied Limnology: Comprehensive View from Watershed to Lake* (pp. 63–105). Springer Japan. https://doi.org/10.1007/978-4-431-54980-2_3

Gharibreza, M., Raj, J. K., Yusoff, I., Othman, Z., Tahir, W. Z. W. M., & Ashraf, M. A. (2013). Sedimentation rates in Bera Lake (Peninsular Malaysia) using 210Pb and 137Cs radioisotopes. *Geosciences Journal*, *17*(2), 211–220. https://doi.org/10.1007/s12303-013-0013-3

Gibbs, H. K., Ruesch, A. S., Achard, F., Clayton, M. K., Holmgren, P., Ramankutty, N., & Foley, J. A. (2010). Tropical forests were the primary sources of new agricultural land in the 1980s and 1990s. *Proceedings of the National Academy of Sciences*, *107*(38), 16732–16737. https://doi.org/10.1073/pnas.0910275107

Giesche, A., Lombardo, U., Finsinger, W., & Veit, H. (2021). Reconstructing Holocene landscape and environmental changes at Lago Rogaguado, Bolivian Amazon. *Journal of Paleolimnology*, *65*(2), 235–253. https://doi.org/10.1007/s10933-020-00164-8

Giresse, P., Makaya Mvoubou, Maley, J., & Ngomanda, A. (2009). Late-Holocene equatorial environments inferred from deposition processes, carbon isotopes of organic matter, and pollen in three shallow lakes of Gabon, west-central Africa. *Journal of Paleolimnology*, *41*(2), 369–392. https://doi.org/10.1007/s10933-008-9231-5

Giresse, P., Maley, J., & Kossoni, A. (2005). Sedimentary environmental changes and millennial climatic variability in a tropical shallow lake (Lake Ossa, Cameroon) during the Holocene. *Palaeogeography, Palaeoclimatology, Palaeoecology*, *218*(3), 257–285. https://doi.org/10.1016/j.palaeo.2004.12.018

Gleyzer, A., Denisyuk, M., Rimmer, A., & Salingar, Y. (2004). A Fast Recursive Gis Algorithm for Computing Strahler Stream Order in Braided and Nonbraided

Networks1. *JAWRA Journal of the American Water Resources Association*, *40*(4), 937–946. https://doi.org/10.1111/j.1752-1688.2004.tb01057.x

Godoy, J. M., Padovani, C. R., Guimarães, J. R. D., Pereira, J. C. A., Vieira, L. M., Carvalho, Z. L., & Galdino, S. (2002). Evaluation of the Siltation of River Taquari, Pantanal, Brazil, through 210Pb Geochronology of Floodplain Lake Sediments. *Journal of the Brazilian Chemical Society*, *13*, 71–77. https://doi.org/10.1590/S0103-50532002000100011

Goldewijk, K. K., Beusen, A., van Drecht, G., & de Vos, M. (2011). The HYDE 3.1 spatially explicit database of human-induced global land-use change over the past 12,000 years. *Global Ecology and Biogeography*, *20*(1), 73–86. https://doi.org/10.1111/j.1466-8238.2010.00587.x

Goldich, S. S. (1938). A Study in Rock-Weathering. *The Journal of Geology*, *46*(1), 17–58. https://doi.org/10.1086/624619

Gomes, L., Simões, S. J. C., Dalla Nora, E. L., de Sousa-Neto, E. R., Forti, M. C., & Ometto, J. P. H. B. (2019). Agricultural Expansion in the Brazilian Cerrado: Increased Soil and Nutrient Losses and Decreased Agricultural Productivity. *Land*, *8*(1), Article 1. https://doi.org/10.3390/land8010012

Grossman, R. B. (1983). Chapter 2 Entisols. In L. P. Wilding, N. E. Smeck, & G. F. Hall (Eds.), *Developments in Soil Science* (Vol. 11, pp. 55–90). Elsevier. https://doi.org/10.1016/S0166-2481(08)70613-5

Guerreiro, R. L., Bergier, I., McGlue, M. M., Warren, L. V., Abreu, U. G. P. de, Abrahão, J., & Assine, M. L. (2019). The soda lakes of Nhecolândia: A conservation opportunity for the Pantanal wetlands. *Perspectives in Ecology and Conservation*, *17*(1), 9–18. https://doi.org/10.1016/j.pecon.2018.11.002

Guinoiseau, D., Fekiacova, Z., Allard, T., Druhan, J. L., Balan, E., & Bouchez, J. (2021). Tropical Weathering History Recorded in the Silicon Isotopes of Lateritic Weathering Profiles. *Geophysical Research Letters*, *48*(19), e2021GL092957. https://doi.org/10.1029/2021GL092957

Guyot, J. L., Jouanneau, J. M., Soares, L., Boaventura, G. R., Maillet, N., & Lagane, C. (2007). Clay mineral composition of river sediments in the Amazon Basin. *CATENA*, *71*(2), 340–356. https://doi.org/10.1016/j.catena.2007.02.002

Hamilton, D. P., & Mitchell, S. F. (1996). An empirical model for sediment resuspension in shallow lakes. *Hydrobiologia*, *317*(3), 209–220. https://doi.org/10.1007/BF00036471

Hammer, Ø., Harper, D. A. T., & Ryan, P. D. (2001). *PAST: Paleontological statistics software package for education and data analysis version 2.09 – ScienceOpen*. https://www.scienceopen.com/document?vid=f7c81409-9131-4ded-a3d6-e1509342d3df

Han, W., Hong, H. L., Yin, K., Churchman, G. J., Li, Z. H., & Chen, T. (2014). Pedogenic alteration of illite in subtropical China. *Clay Minerals*, *49*(3), 379–390. https://doi.org/10.1180/claymin.2014.049.3.03

Hansen, M. C., Potapov, P. V., Moore, R., Hancher, M., Turubanova, S. A., Tyukavina, A., Thau, D., Stehman, S. V., Goetz, S. J., Loveland, T. R., Kommareddy, A., Egorov, A., Chini, L., Justice, C. O., & Townshend, J. R. G. (2013). High-Resolution Global Maps of 21st-Century Forest Cover Change. *Science*, *342*(6160), 850–853. https://doi.org/10.1126/science.1244693

Hartley, A. J., Weissmann, G. S., Bhattacharayya, P., Nichols, G. J., Scuderi, L. A., Davidson, S. K., Leleu*, S., Chakraborty, T., Ghosh*, P., & Mather, A. E. (2013). Soil Development on Modern Distributive Fluvial Systems: Preliminary Observations with Implications for Interpretation of Paleosols in the Rock Record. In S. G. Driese & L. C. Nordt (Eds.), *New Frontiers in Paleopedology and Terrestrial Paleoclimatology: Paleosols and Soil Surface Analog Systems* (Vol. 104, p. 0). SEPM Society for Sedimentary Geology.

Hartley, A. J., Weissmann, G. S., Nichols, G. J., & Warwick, G. L. (2010). Large Distributive Fluvial Systems: Characteristics, Distribution, and Controls on Development. *Journal of Sedimentary Research*, *80*(2), 167–183. https://doi.org/10.2110/jsr.2010.016

Harvey, R. D., & Beck, C. W. (1962). HYDROTHERMAL REGULARLY INTERSTRATIFIED CHLORITE-VERMICULITE AND TOBERMORITE IN ALTERATION ZONES AT GOLDFIELD, NEVADA. In E. Ingerson (Ed.), *Clays and Clay Minerals* (pp. 343–354). Pergamon. https://doi.org/10.1016/B978-1-4831-9842-2.50024-9

Hatzenbühler, D., Caracciolo, L., Weltje, G. J., Piraquive, A., & Regelous, M. (2022). Lithologic, geomorphic, and climatic controls on sand generation from volcanic rocks in the Sierra Nevada de Santa Marta massif (NE Colombia). *Sedimentary Geology*, *429*, 106076. https://doi.org/10.1016/j.sedgeo.2021.106076

Havens, K., Paerl, H., Phlips, E., Zhu, M., Beaver, J., & Srifa, A. (2016). Extreme Weather Events and Climate Variability Provide a Lens to How Shallow Lakes May Respond to Climate Change. *Water*, *8*(6), Article 6. https://doi.org/10.3390/w8060229

Hayashi, M., & van der Kamp, G. (2000). Simple equations to represent the volume–area–depth relations of shallow wetlands in small topographic depressions. *Journal of Hydrology*, *237*(1), 74–85. https://doi.org/10.1016/S0022-1694(00)00300-0

He, J., Garzanti, E., Dinis, P., Yang, S., & Wang, H. (2020). Provenance versus weathering control on sediment composition in tropical monsoonal climate (South China) - 1. Geochemistry and clay mineralogy. *Chemical Geology*, *558*, 119860. https://doi.org/10.1016/j.chemgeo.2020.119860

Heins, W. A. (1993). Source rock texture versus climate and topography as controls on the composition of modern, plutoniclastic sand. In M. J. Johnsson & A. Basu (Eds.), *Processes Controlling the Composition of Clastic Sediments* (Vol. 284, p. 0). Geological Society of America. https://doi.org/10.1130/SPE284-p135

Heins, W., & Kairo, S. (2007). Predicting sand character with integrated genetic analysis. In *Special Paper of the Geological Society of America* (Vol. 420, pp. 345–379). https://doi.org/10.1130/2006.2420(20)

Heiri, O., Lotter, A. F., & Lemcke, G. (2001). Loss on ignition as a method for estimating organic and carbonate content in sediments: reproducibility and comparability of results. *Journal of Paleolimnology*, *25*(1), 101–110. https://doi.org/10.1023/A:1008119611481

Hettler, J., Irion, G., & Lehmann, B. (1997). Environmental impact of mining waste disposal on a tropical lowland river system: a case study on the Ok Tedi Mine, Papua New Guinea. *Mineralium Deposita*, *32*(3), 280–291. https://doi.org/10.1007/s001260050093

Hillier, S. (1995). Erosion, Sedimentation and Sedimentary Origin of Clays. In B. Velde (Ed.), *Origin and Mineralogy of Clays: Clays and the Environment* (pp. 162–219). Springer. https://doi.org/10.1007/978-3-662-12648-6_4

Hirata, R., Gesicki, A., Sracek, O., Bertolo, R., Giannini, P. C., & Aravena, R. (2011). Relation between sedimentary framework and hydrogeology in the Guarani Aquifer System in São Paulo state, Brazil. *Journal of South American Earth Sciences*, *31*(4), 444–456. https://doi.org/10.1016/j.jsames.2011.03.006

Hogg, A. G., Hua, Q., Blackwell, P. G., Niu, M., Buck, C. E., Guilderson, T. P., Heaton, T. J., Palmer, J. G., Reimer, P. J., Reimer, R. W., Turney, C. S. M., & Zimmerman, S. R. H. (2013). SHCal13 Southern Hemisphere Calibration, 0–50,000 Years cal BP. *Radiocarbon*, *55*(4), 1889–1903. https://doi.org/10.2458/azu_js_rc.55.16783

Holmgren, K., Risberg, J., Freudendahl, J., Achimo, M., Ekblom, A., Mugabe, J., Norström, E., & Sitoe, S. (2012). Water-level variations in Lake Nhauhache, Mozambique, during the last 2,300 years. *Journal of Paleolimnology*, *48*(2), 311–322. https://doi.org/10.1007/s10933-012-9596-3

Holz, M. (2015). Mesozoic paleogeography and paleoclimates – A discussion of the diverse greenhouse and hothouse conditions of an alien world. *Journal of South American Earth Sciences*, *61*, 91–107. https://doi.org/10.1016/j.jsames.2015.01.001

Hope, G., Chokkalingam, U., & Anwar, S. (2005). The Stratigraphy and Fire History of the Kutai Peatlands, Kalimantan, Indonesia. *Quaternary Research*, *64*(3), 407–417. https://doi.org/10.1016/j.yqres.2005.08.009

Horbe, A. M. C., Behling, H., Nogueira, A. C. R., & Mapes, R. (2011). Environmental changes in the western Amazônia: morphological framework, geochemistry, palynology and radiocarbon dating data. *Anais Da Academia Brasileira de Ciências*, *83*, 863–874. https://doi.org/10.1590/S0001-37652011005000030

Horbe, A. M. C., Motta, M. B., de Almeida, C. M., Dantas, E. L., & Vieira, L. C. (2013). Provenance of Pliocene and recent sedimentary deposits in western Amazônia, Brazil: Consequences for the paleodrainage of the Solimões-Amazonas River. *Sedimentary Geology*, *296*, 9–20. https://doi.org/10.1016/j.sedgeo.2013.07.007

Horton, B. K. (2022). Unconformity development in retroarc foreland basins: implications for the geodynamics of Andean-type margins. *Journal of the Geological Society*, *179*(3), jgs2020-263. https://doi.org/10.1144/jgs2020-263

Horton, B. K., & DeCelles, P. G. (1997). The modern foreland basin system adjacent to the Central Andes. *Geology*, *25*(10), 895–898. https://doi.org/10.1130/0091-7613(1997)025<0895:TMFBSA>2.3.CO;2

Huong, H. L., & Son, N. T. (2020). Response of Streamflow and Soil Erosion to Climate Change and Human Activities in Nam Rom River Basin, Northwest of Vietnam: DOI: 10.32526/ennrj.18.4.2020.39. *Environment and Natural Resources Journal*, *18*(4), Article 4.

IBGE. (2002). *Mapa de Clima do Brasil*. Instituto Brasileiro de Geografia e Estatística. https://www.ibge.gov.br/geociencias/informacoes-ambientais/climatologia/15817-clima.html

Ingersoll, R. V., Bullard, T. F., Ford, R. L., Grimm, J. P., Pickle, J. D., & Sares, S. W. (1984). The Effect of Grain Size on Detrital Modes: A Test of the Gazzi-Dickinson Point-Counting Method. *Journal of Sedimentary Research*, *54*(1). http://archives.datapages.com/data/sepm/journals/v51-54/data/054/054001/0103.htm

Irion, G., Bush, M. B., Nunes de Mello, J. A., Stüben, D., Neumann, T., Müller, G., Morais de, J. O., & Junk, J. W. (2006). A multiproxy palaeoecological record of Holocene lake sediments from the Rio Tapajós, eastern Amazonia. *Palaeogeography, Palaeoclimatology, Palaeoecology*, *240*(3), 523–535. https://doi.org/10.1016/j.palaeo.2006.03.005

Islam, Md. R., Stuart, R., Risto, A., & Vesa, P. (2002). Mineralogical changes during intense chemical weathering of sedimentary rocks in Bangladesh. *Journal of Asian Earth Sciences*, *20*(8), 889–901. https://doi.org/10.1016/S1367-9120(01)00078-5

Ito, A., & Wagai, R. (2017). Global distribution of clay-size minerals on land surface for biogeochemical and climatological studies. *Scientific Data*, *4*(1), Article 1. https://doi.org/10.1038/sdata.2017.103

Ivory, S. J., McGlue, M. M., Ellis, G. S., Boehlke, A., Lézine, A.-M., Vincens, A., & Cohen, A. S. (2017). East African weathering dynamics controlled by vegetation-climate feedbacks. *Geology*, *45*(9), 823–826. https://doi.org/10.1130/G38938.1

Ivory, S. J., McGlue, M. M., Peterman, C., Baldwin, P., Lucas, J., Cohen, A., Russell, J., Saroni, J., Msaky, E., Kimirei, I., & Soreghan, M. (2021). Climate, vegetation, and weathering across space and time in Lake Tanganyika (tropical eastern Africa). *Quaternary Science Advances*, *3*, 100023. https://doi.org/10.1016/j.qsa.2021.100023

Ivory, S. J., McGlue, M. M., Spera, S., Silva, A., & Bergier, I. (2019). *Vegetation, rainfall, and pulsing hydrology in the Pantanal, the world's largest tropical wetland - IOPscience*. https://iopscience.iop.org/article/10.1088/1748-9326/ab4ffe/meta

Jackson, M. L. (1969). Soil Chemical Analysis - Advanced Course. *Soil Chemical Analysis - Advanced Course.*, *Edition 2*. https://www.cabdirect.org/cabdirect/abstract/19791945527

Jankowski, K. J., Deegan, L. A., Neill, C., Sullivan, H. L., Ilha, P., Maracahipes-Santos, L., Marques, N., & Macedo, M. N. (2021). Land Use Change Influences Ecosystem Function in Headwater Streams of the Lowland Amazon Basin. *Water*, *13*(12), Article 12. https://doi.org/10.3390/w13121667

Janse, J. H., van Dam, A. A., Hes, E. M. A., de Klein, J. J. M., Finlayson, C. M., Janssen, A. B. G., van Wijk, D., Mooij, W. M., & Verhoeven, J. T. A. (2019). Towards a global model for wetlands ecosystem services. *Current Opinion in Environmental Sustainability*, *36*, 11–19. https://doi.org/10.1016/j.cosust.2018.09.002

Johnson, J. I., Sharman, G. R., Szymanski, E., & Huang, X. (2022). Machine Learning Applied to a Modern-Pleistocene Petrographic Data Set: The Global Prediction of Sand Modal Composition (GloPrSM) Model. *Journal of Geophysical Research: Earth Surface*, *127*(7), e2022JF006595. https://doi.org/10.1029/2022JF006595

Johnsson, M. J. (1990). Tectonic versus chemical-weathering controls on the composition of fluvial sands in tropical environments. *Sedimentology*, *37*(4), 713–726. https://doi.org/10.1111/j.1365-3091.1990.tb00630.x

Johnsson, M. J. (1993). The system controlling the composition of clastic sediments. In M. J. Johnsson & A. Basu (Eds.), *Processes Controlling the Composition of Clastic Sediments* (Vol. 284, p. 0). Geological Society of America. https://doi.org/10.1130/SPE284-p1

Johnsson, M. J., & Meade, R. H. (1990). Chemical weathering of fluvial sediments during alluvial storage; the Macuapanim Island point bar, Solimoes River, Brazil. *Journal of Sedimentary Research*, *60*(6), 827–842. https://doi.org/10.1306/212F9296-2B24-11D7-8648000102C1865D

Johnsson, M. J., Stallard, R. F., & Lundberg, N. (1991). Controls on the composition of fluvial sands from a tropical weathering environment: Sands of the Orinoco River drainage basin, Venezuela and Colombia. *GSA Bulletin*, *103*(12), 1622–1647. https://doi.org/10.1130/0016-7606(1991)103<1622:COTCOF>2.3.CO;2

Jonell, T. N., Clift, P. D., Hoang, L. V., Hoang, T., Carter, A., Wittmann, H., Böning, P., Pahnke, K., & Rittenour, T. (2017). Controls on erosion patterns and sediment transport in a monsoonal, tectonically quiescent drainage, Song Gianh, central Vietnam. *Basin Research*, *29*(S1), 659–683. https://doi.org/10.1111/bre.12199

Junk, W. J., da Cunha, C. N., Wantzen, K. M., Petermann, P., Strüssmann, C., Marques, M. I., & Adis, J. (2006). Biodiversity and its conservation in the Pantanal of Mato Grosso, Brazil. *Aquatic Sciences*, *68*(3), 278–309. https://doi.org/10.1007/s00027-006-0851-4

Keller, W. D., & Frederickson, A. F. (1952). Role of plants and colloidal acids in the mechanism of weathering. *American Journal of Science*, *250*(8), 594–608. https://doi.org/10.2475/ajs.250.8.594

Keppeler, E. C. [UNESP, & Hardy, E. R. (2002). Estimativa do tamanho das fêmeas com ovos de Moina minuta Hansen, 1899 (Cladocera, Crustacea) no lago Amapá, Rio Branco, Estado do Acre Brasil. *Acta Scientiarum: Biological and Health Sciences*, 321. https://doi.org/10.4025/actascibiolsci.v24i0.2278

Khazaei, B., Read, L. K., Casali, M., Sampson, K. M., & Yates, D. N. (2022). GLOBathy, the global lakes bathymetry dataset. *Scientific Data*, *9*(1), Article 1. https://doi.org/10.1038/s41597-022-01132-9

Komar, P. D. (1987). Selective grain entrainment by a current from a bed of mixed sizes; a reanalysis. *Journal of Sedimentary Research*, *57*(2), 203–211. https://doi.org/10.1306/212F8AE4-2B24-11D7-8648000102C1865D

Kossoni, A., & Giresse, P. (2010). Interaction of Holocene infilling processes between a tropical shallow lake system (Lake Ossa) and a nearby river system (Sanaga River) (South Cameroon). *Journal of African Earth Sciences*, *56*(1), 1–14. https://doi.org/10.1016/j.jafrearsci.2009.05.012

Krishnaswamy, J., Halpin, P. N., & Richter, D. D. (2001). Dynamics of sediment discharge in relation to land-use and hydro-climatology in a humid tropical watershed in Costa Rica. *Journal of Hydrology*, *253*(1), 91–109. https://doi.org/10.1016/S0022-1694(01)00474-7

Kroonenberg, S. (1992). Effects of provenance, sorting and weathering on the geochemistry of fluvial sands from different tectonic and climatic environments. In *Proceedings of the 29th International Geological Congress Part A* (pp. 69–81).

Kuerten, S., & Stevaux, J. C. (2021). Megaleques das bacias sedimentares do Chaco e Pantanal: uma revisão comparada. *Revista Brasileira de Geomorfologia*, *22*(3), Article 3. https://doi.org/10.20502/rbg.v22i3.1886

Lacerda Filho, J. V. de, Abreu Filho, W., Valente, C. R., Oliveira, C. C. de, & Albuquerque, M. C. de. (2004). *Geologia e recursos minerais do estado de Mato Grosso* [Technical Report]. CPRM; Secretaria de Estado de Indústria, Comércio, Minas e Energia do Estado de Mato Grosso (SICME-MT). http://rigeo.cprm.gov.br/jspui/handle/doc/4871

Lacerda Filho, J. V. de, Brito, R. S. C. de, Silva, M. da G. da, Oliveira, C. C. de, Moreton, L. C., Martins, E. G., Lopes, R. da C., Lima, T. M., Larizzatt, J. H., & Valente, C. R. (2006). *Geologia e recursos minerais do estado de Mato Grosso do Sul* [Technical Report]. CPRM; SEPROTUR/MS; EGRHP/MS. http://rigeo.cprm.gov.br/jspui/handle/doc/10217

Laraque, A., Pouyaud, B., Chaffaut, I., Moutsambote, J.-M., Maziezoula, B., Censier, C., Albouy, Y., Elenga, H., Etcheber, H., Delaune, M., Sondag, F., & Gasse, F. (1997). Reconnaissance scientifique du lac Télé (Nord-Congo) —Premiers résultats et interprétations. *Comptes Rendus de l'Académie des Sciences - Series IIA - Earth and Planetary Science*, *325*(1), 49–56. https://doi.org/10.1016/S1251-8050(97)83272-7

Laraque, A., Pouyaud, B., Rocchia, R., Robin, E., Chaffaut, I., Moutsambote, J. M., Maziezoula, B., Censier, C., Albouy, Y., Elenga, H., Etcheber, H., Delaune, M.,

Sondag, F., & Gasse, F. (1998). Origin and function of a closed depression in equatorial humid zones: The Lake Télé in North Congo. *Journal of Hydrology*, *207*(3), 236–253. https://doi.org/10.1016/S0022-1694(98)00137-1

Latrubesse, E. M., Stevaux, J. C., Cremon, E. H., May, J.-H., Tatumi, S. H., Hurtado, M. A., Bezada, M., & Argollo, J. B. (2012). Late Quaternary megafans, fans and fluvio-aeolian interactions in the Bolivian Chaco, Tropical South America. *Palaeogeography, Palaeoclimatology, Palaeoecology*, *356–357*, 75–88. https://doi.org/10.1016/j.palaeo.2012.04.003

Laurance, W. F., Sayer, J., & Cassman, K. G. (2014). Agricultural expansion and its impacts on tropical nature. *Trends in Ecology & Evolution*, *29*(2), 107–116. https://doi.org/10.1016/j.tree.2013.12.001

Ledru, M.-P., Cordeiro, R. C., Dominguez, J. M. L., Martin, L., Mourguiart, P., Sifeddine, A., & Turcq, B. (2001). Late-Glacial Cooling in Amazonia Inferred from Pollen at Lagoa do Caçó, Northern Brazil. *Quaternary Research*, *55*(1), 47–56. https://doi.org/10.1006/qres.2000.2187

Lehner, B., Verdin, K., & Jarvis, A. (2008). New Global Hydrography Derived From Spaceborne Elevation Data. *Eos, Transactions American Geophysical Union*, *89*(10), 93–94. https://doi.org/10.1029/2008EO100001

Leite, C. C., Costa, M. H., Soares-Filho, B. S., & de Barros Viana Hissa, L. (2012). Historical land use change and associated carbon emissions in Brazil from 1940 to 1995. *Global Biogeochemical Cycles*, *26*(2). https://doi.org/10.1029/2011GB004133

Lewis, W. M. (1996). *Tropical lakes: how latitude makes a difference*.

Li, C., Shi, X., Kao, S., Chen, M., Liu, Y., Fang, X., Lü, H., Zou, J., Liu, S., & Qiao, S. (2012). Clay mineral composition and their sources for the fluvial sediments of Taiwanese rivers. *Chinese Science Bulletin*, *57*(6), 673–681. https://doi.org/10.1007/s11434-011-4824-1

Liptzin, D., & Silver, W. L. (2009). Effects of carbon additions on iron reduction and phosphorus availability in a humid tropical forest soil. *Soil Biology and Biochemistry*, *41*(8), 1696–1702. https://doi.org/10.1016/j.soilbio.2009.05.013

Liu, K., & Song, C. (2022). Modeling lake bathymetry and water storage from DEM data constrained by limited underwater surveys. *Journal of Hydrology*, *604*, 127260. https://doi.org/10.1016/j.jhydrol.2021.127260

Liu, Z., Wang, H., Hantoro, W. S., Sathiamurthy, E., Colin, C., Zhao, Y., & Li, J. (2012). Climatic and tectonic controls on chemical weathering in tropical Southeast Asia (Malay Peninsula, Borneo, and Sumatra). *Chemical Geology*, *291*, 1–12. https://doi.org/10.1016/j.chemgeo.2011.11.015

Lo, E. L., McGlue, M. M., Silva, A., Bergier, I., Yeager, K. M., de Azevedo Macedo, H., Swallom, M., & Assine, M. L. (2019). Fluvio-lacustrine sedimentary processes and landforms on the distal Paraguay fluvial megafan (Brazil). *Geomorphology*, *342*, 163–175. https://doi.org/10.1016/j.geomorph.2019.06.001

Lo, E. L., Silva, A., Bergier, I., Mcglue, M. M., Silva, B. L. de P., Silva, A. P. S., Pereira, L. E., Macedo, H. de A., Assine, M. L., & Silva, E. R. dos S. da. (2017). SPATIOTEMPORAL EVOLUTION OF THE MARGINS OF LAKE UBERABA, PANTANAL FLOODPLAIN (BRAZIL). *GEOGRAFIA*, *42*(3), Article 3. https://doi.org/10.5016/geografia.v42i3.13096

Lombardo, U., & Veit, H. (2014). The origin of oriented lakes: Evidence from the Bolivian Amazon. *Geomorphology*, *204*, 502–509. https://doi.org/10.1016/j.geomorph.2013.08.029

Long, K. E., Schneider, L., Connor, S. E., Shulmeister, N., Finn, J., Roberts, G. L., Zawadzki, A., Enge, T. G., Smol, J. P., Ballard, C., & Haberle, S. G. (2021). Human impacts and Anthropocene environmental change at Lake Kutubu, a Ramsar wetland in Papua New Guinea. *Proceedings of the National Academy of Sciences*, *118*(40), e2022216118. https://doi.org/10.1073/pnas.2022216118

López-Blanco, C., Kenney, W. F., & Varas, A. (2017). Recent flood management efforts obscure the climate signal in a sediment record from a tropical lake. *Journal of Paleolimnology*, *58*(4), 467–478. https://doi.org/10.1007/s10933-017-0004-x

López-Blanco, C., Kenney, W. F., & Varas, A. (2018). Multiple stressors trigger ecological changes in tropical Lake La Tembladera (Ecuador). *Aquatic Ecology*, *52*(2), 211–224. https://doi.org/10.1007/s10452-018-9656-5

Lorente, F. L., Pessenda, L. C. R., Oboh-Ikuenobe, F., Buso Jr., A. A., Cohen, M. C. L., Meyer, K. E. B., Giannini, P. C. F., de Oliveira, P. E., Rossetti, D. de F., Borotti Filho, M. A., França, M. C., de Castro, D. F., Bendassolli, J. A., & Macario, K. (2014). Palynofacies and stable C and N isotopes of Holocene sediments from Lake Macuco (Linhares, Espírito Santo, southeastern Brazil): Depositional settings and palaeoenvironmental evolution. *Palaeogeography, Palaeoclimatology, Palaeoecology*, *415*, 69–82. https://doi.org/10.1016/j.palaeo.2013.12.004

Lorente, F. L., Pessenda, L. C. R., Oboh-Ikuenobe, F., Buso Junior, A. A., Rossetti, D. de F., Giannini, P. C. F., Cohen, M. C. L., de Oliveira, P. E., Mayle, F. E., Francisquini, M. I., França, M. C., Bendassolli, J. A., & Macario, K. (2018). An 11,000-year record of depositional environmental change based upon particulate organic matter and stable isotopes (C and N) in a lake sediment in southeastern Brazil. *Journal of South American Earth Sciences*, *84*, 373–384. https://doi.org/10.1016/j.jsames.2018.04.006

Louzada, R. O., Bergier, I., & Assine, M. L. (2020). Landscape changes in avulsive river systems: Case study of Taquari River on Brazilian Pantanal wetlands. *Science of The Total Environment*, *723*, 138067. https://doi.org/10.1016/j.scitotenv.2020.138067

Louzada, R. O., Bergier, I., Roque, F. O., McGlue, M. M., Silva, A., & Assine, M. L. (2021). Avulsions drive ecosystem services and economic changes in the Brazilian Pantanal wetlands. *Current Research in Environmental Sustainability*, *3*, 100057. https://doi.org/10.1016/j.crsust.2021.100057

Macquaker, J. H. S., Taylor, K. G., & Gawthorpe, R. L. (2007). High-Resolution Facies Analyses of Mudstones: Implications for Paleoenvironmental and Sequence Stratigraphic Interpretations of Offshore Ancient Mud-Dominated Successions. *Journal of Sedimentary Research*, *77*(4), 324–339. https://doi.org/10.2110/jsr.2007.029

Madeira, J., Bedidi, A., Cervelle, B., Pouget, M., & Flay, N. (1997). Visible spectrometric indices of hematite (Hm) and goethite (Gt) content in lateritic soils: The application of a Thematic Mapper (TM) image for soil-mapping in Brasilia, Brazil. *International Journal of Remote Sensing*, *18*(13), 2835–2852. https://doi.org/10.1080/014311697217369

Maezumi, S. Y., Robinson, M., de Souza, J., Urrego, D. H., Schaan, D., Alves, D., & Iriarte, J. (2018). New Insights From Pre-Columbian Land Use and Fire Management in Amazonian Dark Earth Forests. *Frontiers in Ecology and Evolution*, *6*. https://www.frontiersin.org/articles/10.3389/fevo.2018.00111

Makwinja, R., Mengistou, S., Kaunda, E., & Alamirew, T. (2022). Economic value of tropical inland freshwater shallow lakes: Lesson from Lake Malombe, Malawi. *African Journal of Ecology*, *60*(3), 566–580. https://doi.org/10.1111/aje.12935

Manassero, M., Camilión, C., Poiré, D., Da Silva, M., & Ronco, A. (2008). Grain Size Analysis and Clay Mineral Associations in Bottom Sediments From Paraná River Basin. *Latin American Journal of Sedimentology and Basin Analysis*, *15*(2), 125–137.

Marengo, J. A., Cunha, A. P. M. A., Nobre, C. A., Ribeiro Neto, G. G., Magalhaes, A. R., Torres, R. R., Sampaio, G., Alexandre, F., Alves, L. M., Cuartas, L. A., Deusdará, K. R. L., & Álvala, R. C. S. (2020). Assessing drought in the drylands of northeast Brazil under regional warming exceeding 4 °C. *Natural Hazards*, *103*(2), 2589–2611. https://doi.org/10.1007/s11069-020-04097-3

Mariot, M., Dudal, Y., Furian, S., Sakamoto, A., Vallès, V., Fort, M., & Barbiero, L. (2007). Dissolved organic matter fluorescence as a water-flow tracer in the tropical wetland of Pantanal of Nhecolândia, Brazil. *Science of The Total Environment*, *388*(1), 184–193. https://doi.org/10.1016/j.scitotenv.2007.08.003

Master, S. (2010). Lac Télé structure, Republic of Congo: Geological setting of a cryptozoological and biodiversity hotspot, and evidence against an impact origin. *Journal of African Earth Sciences*, *58*(4), 667–679. https://doi.org/10.1016/j.jafrearsci.2009.07.017

Mathian, M., Bueno, G. T., Balan, E., Fritsch, E., Do Nascimento, N. R., Selo, M., & Allard, T. (2020). Kaolinite dating from Acrisol and Ferralsol: A new key to understanding the landscape evolution in NW Amazonia (Brazil). *Geoderma*, *370*, 114354. https://doi.org/10.1016/j.geoderma.2020.114354

Matsumotot, K., & Burneyt, D. A. (1994). Late Holocene environments at Lake Mitsinjo, northwestern Madagascar. *The Holocene*, *4*(1), 16–24. https://doi.org/10.1177/095968369400400103

Mbengue, A. (2004). *Distribuição mineralógica dos sedimentos superficiais da lagoa do Caçó (MA)*. http://app.uff.br/riuff/handle/1/3995

McGlue, M. M., Guerreiro, R. L., Bergier, I., Silva, A., Pupim, F. N., Oberc, V., & Assine, M. L. (2017). Holocene stratigraphic evolution of saline lakes in Nhecolândia, southern Pantanal wetlands (Brazil). *Quaternary Research*, *88*(3), 472–490. https://doi.org/10.1017/qua.2017.57

McGlue, M. M., Silva, A., Assine, M. L., Stevaux, J. C., & Pupim, F. do N. (2015). Paleolimnology in the Pantanal: Using Lake Sediments to Track Quaternary Environmental Change in the World's Largest Tropical Wetland. In I. Bergier & M. L. Assine (Eds.), *Dynamics of the Pantanal Wetland in South America* (pp. 51–81). Springer International Publishing. https://doi.org/10.1007/698_2015_350

McGlue, M. M., Silva, A., Corradini, F. A., Zani, H., Trees, M. A., Ellis, G. S., Parolin, M., Swarzenski, P. W., Cohen, A. S., & Assine, M. L. (2011). Limnogeology in Brazil's "forgotten wilderness": a synthesis from the large floodplain lakes of the Pantanal. *Journal of Paleolimnology*, *46*(2), 273–289. https://doi.org/10.1007/s10933-011-9538-5

McGlue, M. M., Silva, A., Zani, H., Corradini, F. A., Parolin, M., Abel, E. J., Cohen, A. S., Assine, M. L., Ellis, G. S., Trees, M. A., Kuerten, S., Gradella, F. dos S., & Rasbold, G. G. (2012). Lacustrine records of Holocene flood pulse dynamics in the Upper Paraguay River watershed (Pantanal wetlands, Brazil). *Quaternary Research*, *78*(2), 285–294. https://doi.org/10.1016/j.yqres.2012.05.015

McGlue, M. M., Smith, P. H., Zani, H., Silva, A., Carrapa, B., Cohen, A. S., & Pepper, M. B. (2016). An Integrated Sedimentary Systems Analysis of the RíO Bermejo (Argentina): Megafan Character in the Overfilled Southern Chaco Foreland BasinM.M. McGlue et al.Modern Sedimentary Systems Analysis of the RíO Bermejo Megafan, Argentina. *Journal of Sedimentary Research*, *86*(12), 1359–1377. https://doi.org/10.2110/jsr.2016.82

Merino, E. R., & Assine, M. L. (2020). Hidden in plain sight: How finding a lake in the Brazilian Pantanal improves understanding of wetland hydrogeomorphology. *Earth Surface Processes and Landforms*, *45*(2), 440–458. https://doi.org/10.1002/esp.4745

Messager, M. L., Lehner, B., Grill, G., Nedeva, I., & Schmitt, O. (2016). Estimating the volume and age of water stored in global lakes using a geo-statistical approach. *Nature Communications*, *7*(1), Article 1. https://doi.org/10.1038/ncomms13603

Miller, K. L., Szabó, T., Jerolmack, D. J., & Domokos, G. (2014). Quantifying the significance of abrasion and selective transport for downstream fluvial grain size evolution. *Journal of Geophysical Research: Earth Surface*, *119*(11), 2412–2429. https://doi.org/10.1002/2014JF003156

Miserendino, R. A., Guimarães, J. R. D., Schudel, G., Ghosh, S., Godoy, J. M., Silbergeld, E. K., Lees, P. S. J., & Bergquist, B. A. (2018). Mercury Pollution in Amapá, Brazil: Mercury Amalgamation in Artisanal and Small-Scale Gold Mining or Land-Cover and Land-Use Changes? *ACS Earth and Space Chemistry*, *2*(5), 441–450. https://doi.org/10.1021/acsearthspacechem.7b00089

Moore, D. M., & Reynolds, R. C. (1989). X-ray diffraction and the identification and analysis of clay minerals. *X-Ray Diffraction and the Identification and Analysis of Clay Minerals.* https://www.cabdirect.org/cabdirect/abstract/19901943215?freeview=true

Moreira, L. S., Moreira-Turcq, P. F., Cordeiro, R. C., & Turcq, B. J. (2009). Reconstituição paleoambiental do Lago Santa Ninha, Várzea do Lago Grande de Curuai, Pará, Brasil. *Acta Amazonica*, *39*, 609–616. https://doi.org/10.1590/S0044-59672009000300016

Moreira, L. S., Moreira-Turcq, P., Turcq, B., Caquineau, S., & Cordeiro, R. C. (2012). Paleohydrological changes in an Amazonian floodplain lake: Santa Ninha Lake. *Journal of Paleolimnology*, *48*(2), 339–350. https://doi.org/10.1007/s10933-012-9601-x

Moreira-Turcq, P., Jouanneau, J. M., Turcq, B., Seyler, P., Weber, O., & Guyot, J. L. (2004). Carbon sedimentation at Lago Grande de Curuai, a floodplain lake in the low Amazon region: insights into sedimentation rates. *Palaeogeography, Palaeoclimatology, Palaeoecology*, *214*(1), 27–40. https://doi.org/10.1016/j.palaeo.2004.06.013

Mosquera, P. V., Hampel, H., Vázquez, R. F., Alonso, M., & Catalan, J. (2017). Abundance and morphometry changes across the high-mountain lake-size gradient in the tropical Andes of Southern Ecuador. *Water Resources Research*, *53*(8), 7269–7280. https://doi.org/10.1002/2017WR020902

Nascimento, A. F., Furquim, S. A. C., Graham, R. C., Beirigo, R. M., Oliveira Junior, J. C., Couto, E. G., & Vidal-Torrado, P. (2015). Pedogenesis in a Pleistocene fluvial system of the Northern Pantanal — Brazil. *Geoderma*, *255–256*, 58–72. https://doi.org/10.1016/j.geoderma.2015.04.025

Nascimento, L. R. do, Sifeddine, A., Torgan, L. C., & Albuquerque, A. L. S. (2010). Diatom assemblage in a tropical lake of northeastern Brazil. *Brazilian Archives of Biology and Technology*, *53*, 241–248. https://doi.org/10.1590/S1516-89132010000100030

Ndehedehe, C. E., Onojeghuo, A. O., Stewart-Koster, B., Bunn, S. E., & Ferreira, V. G. (2021). Upstream flows drive the productivity of floodplain ecosystems in tropical Queensland. *Ecological Indicators*, *125*, 107546. https://doi.org/10.1016/j.ecolind.2021.107546

Nesbitt, H. W., & Wilson, R. E. (1992). Recent chemical weathering of basalts. *American Journal of Science*, *292*(10), 740–777. https://doi.org/10.2475/ajs.292.10.740

Nesbitt, H. W., & Young, G. M. (1982). Early Proterozoic climates and plate motions inferred from major element chemistry of lutites. *Nature*, *299*(5885), Article 5885. https://doi.org/10.1038/299715a0

Nesbitt, H. W., & Young, G. M. (1984). Prediction of some weathering trends of plutonic and volcanic rocks based on thermodynamic and kinetic considerations. *Geochimica et Cosmochimica Acta*, *48*(7), 1523–1534. https://doi.org/10.1016/0016-7037(84)90408-3

Ngomanda, A., Jolly, D., Bentaleb, I., Chepstow-Lusty, A., Makaya, M., Maley, J., Fontugne, M., Oslisly, R., & Rabenkogo, N. (2007). Lowland rainforest response to hydrological changes during the last 1500 years in Gabon, Western Equatorial Africa. *Quaternary Research*, *67*(3), 411–425. https://doi.org/10.1016/j.yqres.2007.01.006

Nobre, R. L. G., Caliman, A., Cabral, C. R., Araújo, F. de C., Guérin, J., Dantas, F. da C. C., Quesado, L. B., Venticinque, E. M., Guariento, R. D., Amado, A. M., Kelly, P., Vanni, M. J., & Carneiro, L. S. (2020). Precipitation, landscape properties and land use interactively affect water quality of tropical freshwaters. *Science of The Total Environment*, *716*, 137044. https://doi.org/10.1016/j.scitotenv.2020.137044

Nõges, T. (2009). Relationships between morphometry, geographic location and water quality parameters of European lakes. *Hydrobiologia*, *633*(1), 33–43. https://doi.org/10.1007/s10750-009-9874-x

Novello, V. F., Cruz, F. W., Vuille, M., Stríkis, N. M., Edwards, R. L., Cheng, H., Emerick, S., de Paula, M. S., Li, X., Barreto, E. de S., Karmann, I., & Santos, R. V. (2017). A high-resolution history of the South American Monsoon from Last Glacial Maximum to the Holocene. *Scientific Reports*, *7*(1), Article 1. https://doi.org/10.1038/srep44267

O'Callaghan, J. F., & Mark, D. M. (1984). The extraction of drainage networks from digital elevation data. *Computer Vision, Graphics, and Image Processing*, *28*(3), 323–344. https://doi.org/10.1016/S0734-189X(84)80011-0

Odom, I. E. (1975). Feldspar-grain size relations in Cambrian arenites, upper Mississippi Valley. *Journal of Sedimentary Research*, *45*(3), 636–650. https://doi.org/10.1306/212F6E01-2B24-11D7-8648000102C1865D

Odom, I. E., Doe, T. W., & Dott, R. H. (1976). Nature of feldspar-grain size relations in some quartz-rich sandstones. *Journal of Sedimentary Research*, *46*(4), 862–870. https://doi.org/10.1306/212F7077-2B24-11D7-8648000102C1865D

Ojanuga, A. G. (1973). Weathering of Biotite in Soils of a Humid Tropical Climate. *Soil Science Society of America Journal*, *37*(4), 644–646. https://doi.org/10.2136/sssaj1973.03615995003700040046x

Oliva, P., Viers, J., Dupré, B., Fortuné, J. P., Martin, F., Braun, J. J., Nahon, D., & Robain, H. (1999). The effect of organic matter on chemical weathering: study of a small tropical watershed: nsimi-zoétélé site, cameroon. *Geochimica et Cosmochimica Acta*, *63*(23), 4013–4035. https://doi.org/10.1016/S0016-7037(99)00306-3

Oliveira, J. E. de, & Milheira, R. G. (2020). Ethnoarchaeology of two Guató mounds in the Pantanal: building dynamics and history in persistent places. *Mana*, *26*, e263208.

Olson, D. M., Dinerstein, E., Wikramanayake, E. D., Burgess, N. D., Powell, G. V. N., Underwood, E. C., D'amico, J. A., Itoua, I., Strand, H. E., Morrison, J. C., Loucks, C. J., Allnutt, T. F., Ricketts, T. H., Kura, Y., Lamoreux, J. F., Wettengel, W. W., Hedao, P., & Kassem, K. R. (2001). Terrestrial Ecoregions of the World:

A New Map of Life on Earth: A new global map of terrestrial ecoregions provides an innovative tool for conserving biodiversity. *BioScience*, *51*(11), 933–938. https://doi.org/10.1641/0006-3568(2001)051[0933:TEOTWA]2.0.CO;2

Orué, D. (1996). *Síntese da geologia do Paraguai oriental, com ênfase para o magmatismo alcalino associado* [Text, Universidade de São Paulo]. https://doi.org/10.11606/D.44.1996.tde-24092015-163805

Osborne, P. L., Humphreys, G. S., & Polunin, N. V. C. (1993). Sediment Deposition and Late Holocene Environmental Change in a Tropical Lowland Basin: Waigani Lake, Papua New Guinea. *Journal of Biogeography*, *20*(6), 599–613. https://doi.org/10.2307/2845517

Osborne, P. L., & Polunin, N. V. C. (1986). From Swamp to Lake: Recent Changes in a Lowland Tropical Swamp. *Journal of Ecology*, *74*(1), 197–210. https://doi.org/10.2307/2260358

Oste, J. T. F., Rodríguez-Berriguete, Á., & Dal' Bó, P. F. (2021). Depositional and environmental controlling factors on the genesis of Quaternary tufa deposits from Bonito region, Central-West Brazil. *Sedimentary Geology*, *413*, 105824. https://doi.org/10.1016/j.sedgeo.2020.105824

Owens, P. N. (2020). Soil erosion and sediment dynamics in the Anthropocene: a review of human impacts during a period of rapid global environmental change. *Journal of Soils and Sediments*, *20*(12), 4115–4143. https://doi.org/10.1007/s11368-020-02815-9

Owens, P. N., Batalla, R. J., Collins, A. J., Gomez, B., Hicks, D. M., Horowitz, A. J., Kondolf, G. M., Marden, M., Page, M. J., Peacock, D. H., Petticrew, E. L., Salomons, W., & Trustrum, N. A. (2005). Fine-grained sediment in river systems: environmental significance and management issues. *River Research and Applications*, *21*(7), 693–717. https://doi.org/10.1002/rra.878

Pacton, M., Ariztegui, D., Wacey, D., Kilburn, M. R., Rollion-Bard, C., Farah, R., & Vasconcelos, C. (2012). Going nano: A new step toward understanding the processes governing freshwater ooid formation. *Geology*, *40*(6), 547–550. https://doi.org/10.1130/G32846.1

Padisák, J., & Reynolds, C. S. (2003). Shallow lakes: the absolute, the relative, the functional and the pragmatic. *Hydrobiologia*, *506*(1), 1–11. https://doi.org/10.1023/B:HYDR.0000008630.49527.29

Papa, C. del, Payrola, P., Pingel, H., Hongn, F., Campo, M. D., Sobel, E. R., Lapiana, A., Cottle, J., Glodny, J., & Strecker, M. R. (2021). Stratigraphic response to fragmentation of the Miocene Andean foreland basin, NW Argentina. *Basin Research*, *33*(6), 2914–2937. https://doi.org/10.1111/bre.12589

Papangelakis, E., MacVicar, B., & Ashmore, P. (2019). Bedload Sediment Transport Regimes of Semi-alluvial Rivers Conditioned by Urbanization and Stormwater Management. *Water Resources Research*, *55*(12), 10565–10587. https://doi.org/10.1029/2019WR025126

Parinet, B., Lhote, A., & Legube, B. (2004). Principal component analysis: an appropriate tool for water quality evaluation and management—application to a tropical lake system. *Ecological Modelling*, *178*(3), 295–311. https://doi.org/10.1016/j.ecolmodel.2004.03.007

Park, E., Emadzadeh, A., Alcântara, E., Yang, X., & Ho, H. L. (2020). Inferring floodplain bathymetry using inundation frequency. *Journal of Environmental Management*, *273*, 111138. https://doi.org/10.1016/j.jenvman.2020.111138

Parker, A. (1970). An Index of Weathering for Silicate Rocks. *Geological Magazine*, *107*(6), 501–504. https://doi.org/10.1017/S0016756800058581

Pawlik, Ł., Phillips, J. D., & Šamonil, P. (2016). Roots, rock, and regolith: Biomechanical and biochemical weathering by trees and its impact on hillslopes—A critical literature review. *Earth-Science Reviews*, *159*, 142–159. https://doi.org/10.1016/j.earscirev.2016.06.002

Paz, A. R., Bravo, J. M., Allasia, D., Collischonn, W., & Tucci, C. E. M. (2010). Large-Scale Hydrodynamic Modeling of a Complex River Network and Floodplains. *Journal of Hydrologic Engineering*, *15*(2), 152–165. https://doi.org/10.1061/(ASCE)HE.1943-5584.0000162

Peixoto, J. L. dos S. (2009). Arqueologia na Região das Grandes Lagoas do Pantanal. *albuquerque: revista de história*, *1*(2), Article 2. https://doi.org/10.46401/ajh.2009.v1.3930

Penny, D., Cook, G., & Im, S. S. (2005). Long-term rates of sediment accumulation in the Tonle Sap, Cambodia: a threat to ecosystem health? *Journal of Paleolimnology*, *33*(1), 95–103. https://doi.org/10.1007/s10933-004-1323-2

Pettijohn, F. J. (1954). Classification of Sandstones. *The Journal of Geology*, *62*(4), 360–365. https://doi.org/10.1086/626172

Pivari, M. O., Pott, V. J., & Pott, A. (2008). Aquatic macrophytes of floating mats (" baceiros") in the Abobral and Miranda Pantanal Wetlands, Mato Grosso do Sul State, Brazil. *Acta Botanica Brasilica*, *22*, 563–571. https://doi.org/10.1590/S0102-33062008000200023

Pott, A., & da Silva, J. S. V. (2015). Terrestrial and Aquatic Vegetation Diversity of the Pantanal Wetland. In I. Bergier & M. L. Assine (Eds.), *Dynamics of the Pantanal Wetland in South America* (pp. 111–131). Springer International Publishing. https://doi.org/10.1007/698_2015_352

Potter, P. E. (1994). Modern sands of South America: composition, provenance and global significance. *Geologische Rundschau*, *83*(1), 212–232. https://doi.org/10.1007/BF00211904

Prado, A. L. do, Heckman, C. W., & Martins, F. R. (1994). The Seasonal Succession of Biotic Communities in Wetlands of the Tropical Wet-and-Dry Climatic Zone: II. The Aquatic Macrophyte Vegetation in the Pantanal of Mato Grosso, Brazil. *Internationale Revue Der Gesamten Hydrobiologie Und Hydrographie*, *79*(4), 569–589. https://doi.org/10.1002/iroh.19940790407

Prothero, D. R., & Schwab, F. (2004). *Sedimentary Geology*. Macmillan.

Pupim, F. do N., Assine, M. L., & Sawakuchi, A. O. (2017). Late Quaternary Cuiabá megafan, Brazilian Pantanal: Channel patterns and paleoenvironmental changes. *Quaternary International*, *438*, 108–125. https://doi.org/10.1016/j.quaint.2017.01.013

Quartero, E. M., Leier, A. L., Bentley, L. R., & Glombick, P. (2015). Basin-scale stratigraphic architecture and potential Paleocene distributive fluvial systems of the Cordilleran Foreland Basin, Alberta, Canada. *Sedimentary Geology*, *316*, 26–38. https://doi.org/10.1016/j.sedgeo.2014.11.005

RadamBrasil, P. (1982). *Projeto Radambrasil: levantamento de recursos naturais* [Map].

Rai, H., & Hill, G. (1980). Classification of central amazon lakes on the basis of their microbiological and physico-chemical characteristics. *Hydrobiologia*, *72*(1), 85–99. https://doi.org/10.1007/BF00016237

Räsänen, M. E., Salo, J. S., & Jungner, H. (1991). Holocene floodplain lake sediments in the Amazon: 14C dating and palaeoecological use. *Quaternary Science Reviews*, *10*(4), 363–372. https://doi.org/10.1016/0277-3791(91)90037-U

Rasbold, G. G., McGlue, M. M., Stevaux, J. C., Parolin, M., Silva, A., & Bergier, I. (2019). Sponge spicule and phytolith evidence for Late Quaternary environmental changes in the tropical Pantanal wetlands of western Brazil. *Palaeogeography, Palaeoclimatology, Palaeoecology*, *518*, 119–133. https://doi.org/10.1016/j.palaeo.2019.01.015

Rasbold, G. G., McGlue, M. M., Stevaux, J. C., Parolin, M., Silva, A., & Bergier, I. (2021). Enhanced middle Holocene organic carbon burial in tropical floodplain lakes of the Pantanal (South America). *Journal of Paleolimnology*, *65*(2), 181–199. https://doi.org/10.1007/s10933-020-00159-5

Reatto, A., Bruand, A., de Souza Martins, E., Muller, F., da Silva, E. M., Carvalho, O. A. de, & Brossard, M. (2008). Variation of the kaolinite and gibbsite content at regional and local scale in Latosols of the Brazilian Central Plateau. *Comptes Rendus Geoscience*, *340*(11), 741–748. https://doi.org/10.1016/j.crte.2008.07.006

Reimer, P. J., Austin, W. E. N., Bard, E., Bayliss, A., Blackwell, P. G., Ramsey, C. B., Butzin, M., Cheng, H., Edwards, R. L., Friedrich, M., Grootes, P. M., Guilderson, T. P., Hajdas, I., Heaton, T. J., Hogg, A. G., Hughen, K. A., Kromer, B., Manning, S. W., Muscheler, R., … Talamo, S. (2020). The IntCal20 Northern Hemisphere Radiocarbon Age Calibration Curve (0–55 cal kBP). *Radiocarbon*, *62*(4), 725–757. https://doi.org/10.1017/RDC.2020.41

Reimer, R., & Reimer, P. (Directors). (2004). *CALIBomb - calibration of post-bomb C-14 data*. Unknown Publisher.

Repasch, M., Scheingross, J. S., Hovius, N., Lupker, M., Wittmann, H., Haghipour, N., Gröcke, D. R., Orfeo, O., Eglinton, T. I., & Sachse, D. (2021). Fluvial organic carbon cycling regulated by sediment transit time and mineral protection. *Nature Geoscience*, *14*(11), Article 11. https://doi.org/10.1038/s41561-021-00845-7

Repasch, M., Wittmann, H., Scheingross, J. S., Sachse, D., Szupiany, R., Orfeo, O., Fuchs, M., & Hovius, N. (2020). Sediment Transit Time and Floodplain Storage Dynamics in Alluvial Rivers Revealed by Meteoric 10Be. *Journal of Geophysical Research: Earth Surface*, *125*(7), e2019JF005419. https://doi.org/10.1029/2019JF005419

Restrepo, J. D., Kettner, A. J., & Syvitski, J. P. M. (2015). Recent deforestation causes rapid increase in river sediment load in the Colombian Andes. *Anthropocene*, *10*, 13–28. https://doi.org/10.1016/j.ancene.2015.09.001

Reynolds, C. A., Jackson, T. J., & Rawls, W. J. (2000). Estimating soil water-holding capacities by linking the Food and Agriculture Organization Soil map of the world with global pedon databases and continuous pedotransfer functions. *Water Resources Research*, *36*(12), 3653–3662. https://doi.org/10.1029/2000WR900130

Ribeiro, F. B., Roque, A., Boggiani, P. C., & Flexor, J.-M. (2001). Uranium and thorium series disequilibrium in quaternary carbonate deposits from the Serra da Bodoquena and Pantanal do Miranda, Mato Grosso do Sul State, central Brazil. *Applied Radiation and Isotopes*, *54*(1), 153–173. https://doi.org/10.1016/S0969-8043(99)00265-1

Righi, D., & Meunier, A. (1995). Origin of Clays by Rock Weathering and Soil Formation. In B. Velde (Ed.), *Origin and Mineralogy of Clays: Clays and the Environment* (pp. 43–161). Springer. https://doi.org/10.1007/978-3-662-12648-6_3

Ritchie, J. C., & McHenry, J. R. (1990). Application of Radioactive Fallout Cesium-137 for Measuring Soil Erosion and Sediment Accumulation Rates and Patterns: A Review. *Journal of Environmental Quality*, *19*(2), 215–233. https://doi.org/10.2134/jeq1990.00472425001900020006x

Rivadeneyra-Vera, C., Bianchi, M., Assumpção, M., Cedraz, V., Julià, J., Rodríguez, M., Sánchez, L., Sánchez, G., Lopez-Murua, L., Fernandez, G., Fugarazzo, R., & Team, T. "3-B. P. (2019). An Updated Crustal Thickness Map of Central South America Based on Receiver Function Measurements in the Region of the Chaco, Pantanal, and Paraná Basins, Southwestern Brazil. *Journal of Geophysical Research: Solid Earth*, *124*(8), 8491–8505. https://doi.org/10.1029/2018JB016811

Rizzotto, G., & Hartmann, L. (2012). Geological and geochemical evolution of the Trincheira Complex, a Mesoproterozoic ophiolite in the southwestern Amazon craton, Brazil. *Lithos*, *148*, 277–295. https://doi.org/10.1016/j.lithos.2012.05.027

Rocha Junior, C. A. N. da, Costa, M. R. A. da, Menezes, R. F., Attayde, J. L., & Becker, V. (2018). Water volume reduction increases eutrophication risk in tropical semi-arid reservoirs. *Acta Limnologica Brasiliensia*, *30*, e106. https://doi.org/10.1590/S2179-975X2117

Rodrigues, A. A., Macedo, M. N., Silvério, D. V., Maracahipes, L., Coe, M. T., Brando, P. M., Shimbo, J. Z., Rajão, R., Soares-Filho, B., & Bustamante, M. M. C. (2022). Cerrado deforestation threatens regional climate and water availability for

agriculture and ecosystems. *Global Change Biology*, *28*(22), 6807–6822. https://doi.org/10.1111/gcb.16386

Rodríguez, M., Steiger, J., Rosales, J., Laraque, A., López, J. L., Castellanos, B., & Guerrero, O. A. (2019). Multi-annual contemporary flood event overbank sedimentation within the vegetated lower Orinoco floodplain, Venezuela. *River Research and Applications*, *35*(8), 1241–1256. https://doi.org/10.1002/rra.3510

Rodríguez-Zorro, P. A., Enters, D., Hermanowski, B., da Costa, M. L., & Behling, H. (2015). Vegetation changes and human impact inferred from an oxbow lake in southwestern Amazonia, Brazil since the 19th century. *Journal of South American Earth Sciences*, *62*, 186–194. https://doi.org/10.1016/j.jsames.2015.06.003

Rodríguez-Zorro, P. A., Turcq, B., Cordeiro, R. C., Moreira, L. S., Costa, R. L., McMichael, C. H., & Behling, H. (2018). Forest stability during the early and late Holocene in the igapó floodplains of the Rio Negro, northwestern Brazil. *Quaternary Research*, *89*(1), 75–89. https://doi.org/10.1017/qua.2017.99

Romans, B. W., Castelltort, S., Covault, J. A., Fildani, A., & Walsh, J. P. (2016). Environmental signal propagation in sedimentary systems across timescales. *Earth-Science Reviews*, *153*, 7–29. https://doi.org/10.1016/j.earscirev.2015.07.012

Ronco, A., Camilión, C., & Manassero, M. (2001). Geochemistry of heavy metals in bottom sediments from streams of the western coast of the rio de la plata estuary, Argentina. *Environmental Geochemistry and Health*, *23*(2), 89–103. https://doi.org/10.1023/A:1010956531415

Roulet, M., Lucotte, M., Canuel, R., Farella, N., Courcelles, M., Guimarães, J.-R. D., Mergler, D., & Amorim, M. (2000). Increase in mercury contamination recorded in lacustrine sediments following deforestation in the central Amazon1The present investigation is part of an ongoing study, the CARUSO project (CRDI-UFPa-UQAM), initiated to determine the sources, fate and health effects of the presence of MeHg in the area of the Lower Tapajós.1. *Chemical Geology*, *165*(3), 243–266. https://doi.org/10.1016/S0009-2541(99)00172-2

Ruddiman, W. F. (2001). *Earth's Climate: Past and Future*. Macmillan.

Ruiz-Fernández, A. C., Sprovieri, M., Piazza, R., Frignani, M., Sanchez-Cabeza, J.-A., Feo, M. L., Bellucci, L. G., Vecchiato, M., Pérez-Bernal, L. H., & Páez-Osuna, F. (2012). 210Pb-derived history of PAH and PCB accumulation in sediments of a tropical inner lagoon (Las Matas, Gulf of Mexico) near a major oil refinery. *Geochimica et Cosmochimica Acta*, *82*, 136–153. https://doi.org/10.1016/j.gca.2011.02.041

Ryken, N., Vanmaercke, M., Wanyama, J., Isabirye, M., Vanonckelen, S., Deckers, J., & Poesen, J. (2015). Impact of papyrus wetland encroachment on spatial and temporal variabilities of stream flow and sediment export from wet tropical catchments. *The Science of the Total Environment*, *511*, 756–766. https://doi.org/10.1016/j.scitotenv.2014.12.048

Sadler, P. M. (1981). Sediment Accumulation Rates and the Completeness of Stratigraphic Sections. *The Journal of Geology*, *89*(5), 569–584.

Salerno, J., Diem, J. E., Konecky, B. L., & Hartter, J. (2019). Recent intensification of the seasonal rainfall cycle in equatorial Africa revealed by farmer perceptions, satellite-based estimates, and ground-based station measurements. *Climatic Change*, *153*(1), 123–139. https://doi.org/10.1007/s10584-019-02370-4

Salzmann, U., & Hoelzmann, P. (2005). The Dahomey Gap: an abrupt climatically induced rain forest fragmentation in West Africa during the late Holocene. *The Holocene*, *15*(2), 190–199. https://doi.org/10.1191/0959683605hl799rp

Santos, K. R. de S., & Sant'anna, C. L. (2010). Cianobactérias de diferentes tipos de lagoas ("salina", "salitrada" e "baía") representativas do Pantanal da Nhecolândia, MS, Brasil. *Brazilian Journal of Botany*, *33*, 61–83. https://doi.org/10.1590/S0100-84042010000100007

Savage, K. M., & Potter, P. E. (1991). Petrology of Modern Sands of the Rios Guaviare and Inirida, Southern Colombia: Tropical Climate and Sand Composition. *The Journal of Geology*, *99*(2), 289–298.

Sawakuchi, A. O., Hartmann, G. A., Sawakuchi, H. O., Pupim, F. N., Bertassoli, D. J., Parra, M., Antinao, J. L., Sousa, L. M., Sabaj Pérez, M. H., Oliveira, P. E., Santos, R. A., Savian, J. F., Grohmann, C. H., Medeiros, V. B., McGlue, M. M., Bicudo, D. C., & Faustino, S. B. (2015). The Volta Grande do Xingu: reconstruction of past environments and forecasting of future scenarios of a unique Amazonian fluvial landscape. *Scientific Drilling*, *20*, 21–32. https://doi.org/10.5194/sd-20-21-2015

Schiavo, J. A., Pereira, M. G., Miranda, L. P. M. de, Dias Neto, A. H., & Fontana, A. (2010). Caracterização e classificação de solos desenvolvidos de arenitos da formação Aquidauana-MS. *Revista Brasileira de Ciência do Solo*, *34*, 881–889. https://doi.org/10.1590/S0100-06832010000300029

Schiefer, E., Petticrew, E. L., Immell, R., Hassan, M. A., & Sonderegger, D. L. (2013). Land use and climate change impacts on lake sedimentation rates in western Canada. *Anthropocene*, *3*, 61–71. https://doi.org/10.1016/j.ancene.2014.02.006

Schneider, T., Bischoff, T., & Haug, G. H. (2014). Migrations and dynamics of the intertropical convergence zone. *Nature*, *513*(7516), Article 7516. https://doi.org/10.1038/nature13636

Schulz, C., Whitney, B. S., Rossetto, O. C., Neves, D. M., Crabb, L., de Oliveira, E. C., Terra Lima, P. L., Afzal, M., Laing, A. F., de Souza Fernandes, L. C., da Silva, C. A., Steinke, V. A., Torres Steinke, E., & Saito, C. H. (2019). Physical, ecological and human dimensions of environmental change in Brazil's Pantanal wetland: Synthesis and research agenda. *Science of The Total Environment*, *687*, 1011–1027. https://doi.org/10.1016/j.scitotenv.2019.06.023

Sebag, D., Debret, M., M'voubou, M., Obame, R. M., Ngomanda, A., Oslisly, R., Bentaleb, I., Disnar, J.-R., & Giresse, P. (2013). Coupled Rock-Eval pyrolysis and

spectrophotometry for lacustrine sedimentary dynamics: Application for West Central African rainforests (Kamalété and Nguène lakes, Gabon). *The Holocene*, *23*(8), 1173–1183. https://doi.org/10.1177/0959683613483622

Selcer, P. (2015). Fabricating Unity: The FAO-UNESCO Soil Map of the World. *Historical Social Research / Historische Sozialforschung*, *40*(2 (152)), 174–201.

Selvaraj, K., & Chen, C. A. (2006). Moderate Chemical Weathering of Subtropical Taiwan: Constraints from Solid-Phase Geochemistry of Sediments and Sedimentary Rocks. *The Journal of Geology*, *114*(1), 101–116. https://doi.org/10.1086/498102

SERGEOMIN. (2005). *Geologia, Departamento de Santa Cruz (Ae-MAP-0005-B) Escala 1:1,000,000*. Servicio Geológico Técnico de Minas (SERGEOTECMIN), La Paz.

Settele, J. R., Scholes, R., Betts, R. A., Bunn, S., Leadley, P., Nepstad, D., Overpeck, J. T., & Taboada, M. A. (2014). 4 — Terrestrial and Inland Water Systems. In C. B. Field, V. R. Barros, D. J. Dokken, K. J. Mach, M. D. Mastrandrea, T. E. Bilir, M. Chatterjee, K. L. Ebi, Y. O. Estrada, R. C. Genova, B. Girma, E. S. Kissel, A. N. Levy, S. MacCracken, P. R. Mastrandrea, & L. L. White (Eds.), *Climate Change 2014: Impacts,Adaptation, and Vulnerability. Part A: Global and Sectoral Aspects. Contribution of Working Group II to the Fifth Assessment Report of the Intergovernmental Panel on Climate Change*. Cambridge University Press.

Setti, M., López-Galindo, A., Padoan, M., & Garzanti, E. (2014). Clay mineralogy in southern Africa river muds. *Clay Minerals*, *49*(5), 717–733. https://doi.org/10.1180/claymin.2014.049.5.08

Sharip, Z., Majizat, A., & Suratman, S. (2018). Socio-economic and institutional assessment of Malaysia's first biosphere reserve: Chini Lake. *Lakes & Reservoirs: Science, Policy and Management for Sustainable Use*, *23*(2), 104–116. https://doi.org/10.1111/lre.12217

Shepard Jr., G. H., Clement, C. R., Lima, H. P., Santos, G. M. dos, Moraes, C. de P., & Neves, E. G. (2020). Ancient and Traditional Agriculture in South America: Tropical Lowlands. In *Oxford Research Encyclopedia of Environmental Science*. https://doi.org/10.1093/acrefore/9780199389414.013.597

Shi, C., Zhang, D. D., & You, L. (2003). Sediment budget of the Yellow River delta, China: the importance of dry bulk density and implications to understanding of sediment dispersal. *Marine Geology*, *199*(1), 13–25. https://doi.org/10.1016/S0025-3227(03)00159-2

Shirzad, T., Assumpcao, M., & Bianchi, M. (2020). Ambient seismic noise tomography in west-central and Southern Brazil, characterizing the crustal structure of the Chaco-Paraná, Pantanal and Paraná basins. *Geophysical Journal International*, *220*(3), 2074–2085. https://doi.org/10.1093/gji/ggz548

Shover, E. F. (1963). Clay-Mineral Environmental Relationships in Cisco (U. Penn.) Clays and Shales, North Central Texas. *Clays and Clay Minerals*, *12*(1), 431–443. https://doi.org/10.1346/CCMN.1963.0120138

Sifeddine, A., Spadano Albuquerque, A. L., Ledru, M.-P., Turcq, B., Knoppers, B., Martin, L., Zamboni de Mello, W., Passenau, H., Landim Dominguez, J. M., Campello Cordeiro, R., Abrão, J. J., & da Silva Pinto Bittencourt, A. C. (2003). A 21 000 cal years paleoclimatic record from Caçó Lake, northern Brazil: evidence from sedimentary and pollen analyses. *Palaeogeography, Palaeoclimatology, Palaeoecology*, *189*(1), 25–34. https://doi.org/10.1016/S0031-0182(02)00591-6

Sileshi, G. W., Kihara, J., Tamene, L., Vanlauwe, B., Phiri, E., & Jama, B. (2022). Unravelling causes of poor crop response to applied N and P fertilizers on African soils‡. *Experimental Agriculture*, *58*, e7. https://doi.org/10.1017/S0014479721000247

Silio-Calzada, A., Barquín, J., Huszar, V. L. M., Mazzeo, N., Méndez, F., & Álvarez-Martínez, J. M. (2017). Long-term dynamics of a floodplain shallow lake in the Pantanal wetland: Is it all about climate? *Science of The Total Environment*, *605–606*, 527–540. https://doi.org/10.1016/j.scitotenv.2017.06.183

Silva, M. B., Anjos, L. H. C. dos, Pereira, M. G., Schiavo, J. A., Cooper, M., & Cavassani, R. de S. (2017). Soils in the karst landscape of Bodoquena plateau in cerrado region of Brazil. *CATENA*, *154*, 107–117. https://doi.org/10.1016/j.catena.2017.02.022

Singer, A. (1980). The paleoclimatic interpretation of clay minerals in soils and weathering profiles. *Earth-Science Reviews*, *15*(4), 303–326. https://doi.org/10.1016/0012-8252(80)90113-0

Sinha, R. K., Eldho, T. I., & Subimal, G. (2020). Assessing the impacts of historical and future land use and climate change on the streamflow and sediment yield of a tropical mountainous river basin in South India. *Environmental Monitoring and Assessment*, *192*(11), 679. https://doi.org/10.1007/s10661-020-08623-5

Sitoe, S. R., Risberg, J., Norström, E., & Westerberg, L.-O. (2017). Late Holocene sea-level changes and paleoclimate recorded in Lake Lungué, southern Mozambique. *Palaeogeography, Palaeoclimatology, Palaeoecology*, *485*, 305–315. https://doi.org/10.1016/j.palaeo.2017.06.022

Souza, E. B. de, Pott, A., Wittmann, F., Parolin, P., Markus-Michalczyk, H., Bueno, M. L., & Damasceno-Junior, G. A. (2021). Composition and Distribution of Woody and Palm Vegetation in the Pantanal Wetland. In G. A. Damasceno-Junior & A. Pott (Eds.), *Flora and Vegetation of the Pantanal Wetland* (pp. 443–469). Springer International Publishing. https://doi.org/10.1007/978-3-030-83375-6_9

Souza, E. S. de, Fernandes, A. R., De Souza Braz, A. M., Oliveira, F. J. de, Alleoni, L. R. F., & Campos, M. C. C. (2018). Physical, chemical, and mineralogical attributes of a representative group of soils from the eastern Amazon region in Brazil. *SOIL*, *4*(3), 195–212. https://doi.org/10.5194/soil-4-195-2018

Spinzi, Á. M., & Ramírez, H. M. (2014). *Mapa Geológico del Paraguay, Escala 1:1.000.000*. Viceministerio de Minas y Energía, Asunción.

Stallard, R. F., Koehnken, L., & Johnsson, M. J. (1991). Weathering processes and the composition of inorganic material transported through the orinoco river system,

Venezuela and Colombia. *Geoderma*, *51*(1), 133–165.
https://doi.org/10.1016/0016-7061(91)90069-6

Street, R. B., & Semenov, S. M. (1990). Chapter 3: Natural terrestrial ecosystems. In W.
J. M. Tegart, G. W. Sheldon, & D. C. Griffiths (Eds.), *Climate change: the IPCC
impacts assessment* (pp. 3–44). Australian Government Publishing Service.
https://www.ipcc.ch/site/assets/uploads/2018/03/ipcc_far_wg_II_chapter_03.pdf

Strey, S., Boy, J., Strey, R., Weber, O., & Guggenberger, G. (2016). Response of soil
organic carbon to land-use change in central Brazil: a large-scale comparison of
Ferralsols and Acrisols. *Plant and Soil*, *408*(1), 327–342.
https://doi.org/10.1007/s11104-016-2901-6

Stuiver, M., Reimer, P. J., & Reimer, R. W. (2021). *Calib 8.2*. Calib 8.2.
http://calib.org/calib/calib.html

Suttner, L. J., & Dutta, P. K. (1986). Alluvial sandstone composition and paleoclimate; I,
Framework mineralogy. *Journal of Sedimentary Research*, *56*(3), 329–345.
https://doi.org/10.1306/212F8909-2B24-11D7-8648000102C1865D

Syvitski, J. P. M., Cohen, S., Kettner, A. J., & Brakenridge, G. R. (2014). How important
and different are tropical rivers? — An overview. *Geomorphology*, *227*, 5–17.
https://doi.org/10.1016/j.geomorph.2014.02.029

Syvitski, J. P. M., & Kettner, A. (2011). Sediment flux and the Anthropocene.
*Philosophical Transactions of the Royal Society A: Mathematical, Physical and
Engineering Sciences*, *369*(1938), 957–975.
https://doi.org/10.1098/rsta.2010.0329

Talling, J. F. (2001). Environmental controls on the functioning of shallow tropical lakes.
Hydrobiologia, *458*(1), 1–8. https://doi.org/10.1023/A:1013121522321

Tan, Z., Melack, J., Li, Y., Liu, X., Chen, B., & Zhang, Q. (2020). Estimation of water
volume in ungauged, dynamic floodplain lakes. *Environmental Research Letters*,
15(5), 054021. https://doi.org/10.1088/1748-9326/ab82cb

Taylor, S. R., & McLennan, S. M. (1995). The geochemical evolution of the continental
crust. *Reviews of Geophysics*, *33*(2), 241–265.
https://doi.org/10.1029/95RG00262

Taylor, Z. P., Horn, S. P., Mora, C. I., Orvis, K. H., & Cooper, L. W. (2010). A multi-
proxy palaeoecological record of late-Holocene forest expansion in lowland
Bolivia. *Palaeogeography, Palaeoclimatology, Palaeoecology*, *293*(1), 98–107.
https://doi.org/10.1016/j.palaeo.2010.05.004

Terra, F. S., Demattê, J. A. M., & Viscarra Rossel, R. A. (2018). Proximal spectral
sensing in pedological assessments: vis–NIR spectra for soil classification based
on weathering and pedogenesis. *Geoderma*, *318*, 123–136.
https://doi.org/10.1016/j.geoderma.2017.10.053

Tineo, D. E. (2020). Facies model of a sedimentary record for a Pantanal-like inland
wetland. *Sedimentology*, *67*(7), 3683–3717. https://doi.org/10.1111/sed.12766

Tineo, D. E., Comerio, M. A., Vigiani, L. H., Kürten Moreno, G. S., & Poiré, D. G. (2022). Tectonic and paleoclimatic controls on the composition of inland wetland deposits, Chaco foreland basin, Central Andes. *Journal of Sedimentary Research*, *92*(2), 112–133. https://doi.org/10.2110/jsr.2021.033

Toledo, M. B. de, & Bush, M. B. (2008). Vegetation and hydrology changes in Eastern Amazonia inferred from a pollen record. *Anais Da Academia Brasileira de Ciências*, *80*, 191–203. https://doi.org/10.1590/S0001-37652008000100014

Truckenbrodt, W., Kotschoubey, B., & Schellmann, W. (1991). Composition and origin of the clay cover on North Brazilian laterites. *Geologische Rundschau*, *80*(3), 591–610. https://doi.org/10.1007/BF01803688

Tundisi, J. G., Forsberg, B. R., Devol, A. H., Zaret, T. M., Tundisi, T. M., Dos Santos, A., Ribeiro, J. S., & Hardy, E. R. (1984). Mixing patterns in Amazon lakes. *Hydrobiologia*, *108*(1), 3–15. https://doi.org/10.1007/BF02391627

Turcq, B., Albuquerque, A. L. S., Cordeiro, R. C., Sifeddine, A., Simoes Filho, F. F. L., Souza, A. G., Abrão, J. J., Oliveira, F. B. L., Silva, A. O., & Capitâneo, J. (2002). Accumulation of organic carbon in five Brazilian lakes during the Holocene. *Sedimentary Geology*, *148*(1), 319–342. https://doi.org/10.1016/S0037-0738(01)00224-X

USGS. (1996). *Global 30 Arc-Second Elevation (GTOPO30)*. https://doi.org/10.5066/F7DF6PQS

Ussami, N., Shiraiwa, S., & Dominguez, J. M. L. (1999). Basement reactivation in a sub-Andean foreland flexural bulge: The Pantanal wetland, SW Brazil. *Tectonics*, *18*(1), 25–39. https://doi.org/10.1029/1998TC900004

Vanderaveroet, P., Bout-Roumazeilles, V., Fagel, N., Chamley, H., & Deconinck, J. F. (2000). Significance of random illite-vermiculite mixed layers in Pleistocene sediments of the northwestern Atlantic Ocean. *Clay Minerals*, *35*(4), 679–691.

Vasconcelos, B. R., Ruiz, A. S., & Matos, J. B. de. (2015). Polyphase deformation and metamorphism of the Cuiabá group in the Poconé region (MT), Paraguay Fold and Thrust Belt: kinematic and tectonic implications. *Brazilian Journal of Geology*, *45*(1), 51–63. https://doi.org/10.1590/23174889201500010004

Veena, M. P., Achyuthan, H., Eastoe, C., & Farooqui, A. (2014). Human impact on lowland Vellayani Lake, south India: A record since 3000yrs BP. *Anthropocene*, *8*, 83–91. https://doi.org/10.1016/j.ancene.2015.04.001

Velde, B. B., & Meunier, A. (2008). *The Origin of Clay Minerals in Soils and Weathered Rocks*. Springer Science & Business Media.

Verdin, K. L. (2017). Hydrologic Derivatives for Modeling and Analysis—A new global high-resolution database. In *Data Series* (No. 1053). U.S. Geological Survey. https://doi.org/10.3133/ds1053

Vergotti, M. (2008). Uso do 210Pb no estudo de deposição de mercúrio em lagos da bacia do rio Madeira (RO). *Aleph*, 114 f. : il., tabs.

Vergotti, M., Bonotto, D. M., Silveira, E. G., & Bastos, W. R. (2009). INFLUÊNCIA DA MATÉRIA ORGÂNICA NA ADSORÇÃO DE Hg E OUTROS ELEMENTOS EM SEDIMENTOS DE LAGOS DA BACIA DO RIO MADEIRA (RO). *Geochimica Brasiliensis*, *23*(1), Article 1. https://www.geobrasiliensis.org.br/geobrasiliensis/article/view/297

Verstraeten, G., & Poesen, J. (2001). Variability of dry sediment bulk density between and within retention ponds and its impact on the calculation of sediment yields. *Earth Surface Processes and Landforms*, *26*(4), 375–394. https://doi.org/10.1002/esp.186

Vezzoli, G., Ghielmi, G., Mondaca, G., Resentini, A., Villarroel, E. K., Padoan, M., & Gentile, P. (2013). Quantifying modern erosion rates and river-sediment contamination in the Bolivian Andes. *Journal of South American Earth Sciences*, *45*, 42–55. https://doi.org/10.1016/j.jsames.2013.02.001

Viers, J., Dupré, B., Braun, J.-J., Deberdt, S., Angeletti, B., Ngoupayou, J. N., & Michard, A. (2000). Major and trace element abundances, and strontium isotopes in the Nyong basin rivers (Cameroon): constraints on chemical weathering processes and elements transport mechanisms in humid tropical environments. *Chemical Geology*, *169*(1), 211–241. https://doi.org/10.1016/S0009-2541(00)00298-9

Vincens, A., Schwartz, D., Bertaux, J., Elenga, H., & Namur, C. de. (1998). Late Holocene Climatic Changes in Western Equatorial Africa Inferred from Pollen from Lake Sinnda, Southern Congo. *Quaternary Research*, *50*(1), 34–45. https://doi.org/10.1006/qres.1998.1979

Walling, D. E. (1999). Linking land use, erosion and sediment yields in river basins. In J. Garnier & J.-M. Mouchel (Eds.), *Man and River Systems: The Functioning of River Systems at the Basin Scale* (pp. 223–240). Springer Netherlands. https://doi.org/10.1007/978-94-017-2163-9_24

Walling, D. E., & He, Q. (1998). The spatial variability of overbank sedimentation on river floodplains. *Geomorphology*, *24*(2), 209–223. https://doi.org/10.1016/S0169-555X(98)00017-8

Wang, H., Liu, Z., Sathiamurthy, E., Colin, C., Li, J., & Zhao, Y. (2011). Chemical weathering in Malay Peninsula and North Borneo: Clay mineralogy and element geochemistry of river surface sediments. *Science China Earth Sciences*, *54*(2), 272–282. https://doi.org/10.1007/s11430-010-4158-x

Wang, L., & Liu, H. (2006). An efficient method for identifying and filling surface depressions in digital elevation models for hydrologic analysis and modelling. *International Journal of Geographical Information Science*, *20*(2), 193–213. https://doi.org/10.1080/13658810500433453

Warr, L. N. (2022). Earth's clay mineral inventory and its climate interaction: A quantitative assessment. *Earth-Science Reviews*, *234*, 104198. https://doi.org/10.1016/j.earscirev.2022.104198

Webster, K. E., McCullough, I. M., & Soranno, P. A. (2022). Deeper by the Dozen: Diving into a Database of 17,675 Depths for U.S. Lakes and Reservoirs. *Limnology and Oceanography Bulletin*, *31*(1), 1–5. https://doi.org/10.1002/lob.10482

Weissmann, G. S., Hartley, A. J., Scuderi, L. A., Nichols, G. J., Owen, A., Wright, S., Felicia, A. L., Holland, F., & Anaya, F. M. L. (2015). Fluvial geomorphic elements in modern sedimentary basins and their potential preservation in the rock record: A review. *Geomorphology*, *250*, 187–219. https://doi.org/10.1016/j.geomorph.2015.09.005

Wetzel, R. G. (2001). *Limnology: Lake and River Ecosystems*. Gulf Professional Publishing.

Whitney, B. S., Dickau, R., Mayle, F. E., Soto, J. D., & Iriarte, J. (2013). Pre-Columbian landscape impact and agriculture in the Monumental Mound region of the Llanos de Moxos, lowland Bolivia. *Quaternary Research*, *80*(2), 207–217. https://doi.org/10.1016/j.yqres.2013.06.005

Wilson, M. D. (1992). Inherited Grain-Rimming Clays in Sandstones from Eolian and Shelf Environments: Their Origin and Control on Reservoir Properties. In D. W. Houseknecht & E. D. Pittman (Eds.), *Origin, Diagenesis, and Petrophysics of Clay Minerals in Sandstones* (Vol. 47, p. 0). SEPM Society for Sedimentary Geology. https://doi.org/10.2110/pec.92.47.0209

Wilson, M. J. (1999). The origin and formation of clay minerals in soils: past, present and future perspectives. *Clay Minerals*, *34*(1), 7–25. https://doi.org/10.1180/000985599545957

Wirrmann, D., Bertaux, J., & Kossoni, A. (2001). Late Holocene Paleoclimatic Changes in Western Central Africa Inferred from Mineral Abundance in Dated Sediments from Lake Ossa (Southwest Cameroon). *Quaternary Research*, *56*(2), 275–287. https://doi.org/10.1006/qres.2001.2240

Wolman, M. G., & Schick, A. P. (1967). Effects of construction on fluvial sediment, urban and suburban areas of Maryland. *Water Resources Research*, *3*(2), 451–464. https://doi.org/10.1029/WR003i002p00451

Wu, F.-T., & Caetano-Chang, M. R. (1992). Estudo mineralógico dos arenitos das formações Pirambóia e Botucatu no Centro-Leste do Estado de São Paulo. *Revista do Instituto Geológico*, *13*(1), Article 1. https://doi.org/10.5935/0100-929X.19920004

Xu, X., Jiang, B., Tan, Y., Costanza, R., & Yang, G. (2018). Lake-wetland ecosystem services modeling and valuation: Progress, gaps and future directions. *Ecosystem Services*, *33*, 19–28. https://doi.org/10.1016/j.ecoser.2018.08.001

Yuan, H., & Bish, D. L. (2010). NEWMOD+, a new version of the NEWMOD program for interpreting X-ray powder diffraction patterns from interstratified clay minerals. *Clays and Clay Minerals*, *58*(3), 318–326. https://doi.org/10.1346/CCMN.2010.0580303

Zani, H., Assine, M. L., & McGlue, M. M. (2012). Remote sensing analysis of depositional landforms in alluvial settings: Method development and application to the Taquari megafan, Pantanal (Brazil). *Geomorphology*, *161–162*, 82–92. https://doi.org/10.1016/j.geomorph.2012.04.003

Zeng, Z., Estes, L., Ziegler, A. D., Chen, A., Searchinger, T., Hua, F., Guan, K., Jintrawet, A., & F. Wood, E. (2018). Highland cropland expansion and forest loss in Southeast Asia in the twenty-first century. *Nature Geoscience*, *11*(8), Article 8. https://doi.org/10.1038/s41561-018-0166-9

Zocatelli, R., Moreira-Turcq, P., Bernardes, M., Turcq, B., Cordeiro, R. C., Gogo, S., Disnar, J. R., & Boussafir, M. (2013). Sedimentary evidence of soil organic matter input to the Curuai Amazonian floodplain. *Organic Geochemistry*, *63*, 40–47. https://doi.org/10.1016/j.orggeochem.2013.08.004

VITA

EDWARD LIMIN LO (羅力明)

Education

Master of Science, Geological Sciences, University of Kentucky (UK)	**Dec 2017**
Bachelor of Science, Geology, Louisiana State University (LSU)	**Dec 2013**

Professional Experience

Teaching Assistant, UK Appalachian Center	**Sept 2021-May 2022**
Teaching Assistant, LSU Geology Freshmen Field Camp	**Jun-Jul 2014**
SULI Intern, Lawrence Berkeley National Laboratory	**Jan-May 2013**

Scholastic and Professional Honors

Southern Regional Education Board Dissertation Award	**Aug 2021**
NSF Graduate Research Fellowship	**Mar 2016**
UK McNair Fellowship	**Aug 2014**
Fulbright Fellowship research grant, Brazil	**Apr 2014**
Louisiana State University Ronald McNair Postbaccalaureate Scholar	**Dec 2012**
Louisiana Sci., Tech., Eng. and Math (LA-STEM) Scholar	**Mar 2010**

Professional Publications (15)

Lo EL, Silva A, Kuerten S, Louzada RO, Rasbold GG, McGlue MM. 2023. Source-to-sink controls on modern fluvial sands in the Pantanal back-bulge basin (Brazil). *Sedimentologika, accepted August 16, 2023.*

McGlue MM, Dilworth JR, Johnson HL, Whitehead SJ, Thigpen JR, Yeager KM, Woolery EW, Brown SJ, Johnson SE, Cearley CS, Clark GM, Dixon TS, Goldsby RC, Helfrich AL, Hodelka BN, **Lo EL**, Domingos-Luz L, Powell NE, Rasbold GG, Swanger WR. 2023. Effect of Dam Emplacement and Water Level Changes on Sublacustrine Geomorphology and Recent Sedimentation in Jackson Lake, Grand Teton National Park (Wyoming, United States). *Earth Science, Systems and Society* 3: 10033. DOI: 10.3389/esss.2023.10066

Pereira LE, **Lo EL**, Paranhos Filho AC. 2022. Analysis of the Taquari Megafan through radiometric indices. *Journal of South American Earth Sciences* 119: 104034. DOI: 10.1016/j.jsames.2022.104034

Li J, Tang S, Ettensohn FR, Shen Y, Zu Z, **Lo EL**. 2022. Characterization of pore structure in Carboniferous-Permian gas shales and tight sandstones of the coal-bearing succession in the Qinshui Basin, north China. *Arabian Journal of Geosciences* 15(12): 1125. DOI: 10.1007/s12517-022-10325-w

Lo EL, Yeager KM, Bergier I, Domingos-Luz L, Silva A, McGlue MM. 2022. Sediment infill of tropical floodplain lakes: rates, controls, and implications for ecosystem services. *Frontiers in Earth Science* 10: 1-14. DOI: 10.3389/feart.2022.875919

Ettensohn FR, Seckinger DC, Eble CF, Clayton G, Li J, Martins GA, Hodelka BN, **Lo EL**, Harris FR, Taghizadeh N. 2020. Age and tectonic significance of diamictites at the Devonian-Mississippian transition in the central Appalachian Basin. In Swezey CS, Carter MW, eds., Geology Field Trips in and around the U.S. Capital: Geological Society of America Field Guide 57: 79-103. DOI: 10.1130/2020.0057(04)

Lo EL, McGlue MM, Silva A, Bergier I, Yeager KM, Macedo HA, Swallom M, Assine ML. 2019. Fluvio-lacustrine sedimentary processes and landforms on the distal Paraguay fluvial megafan (Brazil). *Geomorphology* 342: 163-175. DOI: 10.1016/j.geomorph.2019.06.001

Domingos-Luz L, Parolin M, Pessenda LCR, Rasbold GG, **Lo EL**. 2019. Multiproxy analysis (phytoliths, stable isotopes and C/N) as indicators of paleoenvironmental changes in a cerrado site, southern Brazil. *Revista Brasileira de Paleontologia* 22(1): 15-29. DOI: 10.4072/rbp.2019.1.02

Macedo HA, Stevaux J, Silva A, Merino ER, **Lo EL**, Assine ML. 2019. Hydrosedimentology of the Paraguay River in the Corumbá fluvial reach, Pantanal wetland. *Revista Brasileira de Geomorfologia* 20(2): 255-271. DOI: 10.20502/rbg.v20i2.1500

Stevanato M, Rasbold GG, Parolin M, Domingos-Luz L, **Lo EL**, Weber P, Trevisan R, Caxambu MG. 2019. New characteristics of the papillae phytolith morphotype recovered from eleven genera of cyperaceae. *Flora –Morphology Distribution Functional Ecology of Plants* 253: 49-55. DOI: 10.1016/j.flora.2019.03.012

Lo EL, Silva A, Bergier I, McGlue MM, Silva BLP, Silva APS, Pereira LE, Macedo HA, Assine ML, Silva ERS. 2017. Spatiotemporal evolution of the margins of Lake Uberaba, Pantanal floodplain (Brazil). *Geografia* 42(3): 159-173.

Silva ERS, Silva A, Silva BLP, Pereira LE, **Lo EL**, Fonseca TPL, Oliveira MR. 2017. Analysis of morphological and hydrological changes in the Correntes River. *Geografia* 42(3): 9-25.

Pereira LE, Lastoria G, Almeida BS, Haupenthal M, Júnior JM, **Lo EL**, Paranhos Filho AC. 2017. Application of aerial and orbital sensor photographs to identify and delineate water bodies. *Bulletin of Geodetic Sciences* 23(4): 591-605. DOI: 0.1590/S1982-21702017000400039

Macedo HA, Stevaux JC, Assine ML, Silva A, Pupim FN, Merino ER, **Lo EL**. 2017. Calculating bedload transport in rivers: concepts, calculus routines and application. *Revista Brasileira de Geormofologia* 18(4): 813-824. DOI: 10.20502/rbg.v18i4.1227

Lo EL, Bentley Sr. SJ, Xu K. 2014. Experimental study of cohesive sediment consolidation and resuspension identifies approaches for coastal restoration: Lake Lery, Louisiana. *Geo-Marine Letters*: 1-11. DOI: 10.1007/s00367-014-0381-3